UNIVERSITY OF
NEWCASTLE UPON TYNE

ELECTROCRYSTALLISATION AND RECOVERY OF GOLD FROM THIOSULPHATE-SULPHITE AGED ELECTROLYTE

A Thesis Submitted by

SHAFREEZA SOBRI

For the Degree of Doctor of Philosophy

School of Chemical Engineering and Advanced Materials
University of Newcastle upon Tyne

June 2006

ABSTRACT

Interest has grown in developing non-toxic electrolytes for gold electrodeposition to replace the conventional cyanide-based bath. The main driver for the development of this electrolyte is the long term sustainability. One electrolyte that is being examined is a solution containing thiosulphate and sulphite, which has been developed specially for microelectronics applications. However, at the end of the electrodeposition process, the spent electrolyte can contain a significant amount of gold in solution and low concentration in rinse waters. Since the discharge of gold along with the effluent is a major economic as well as environmental concern, this study has been initiated to investigate if gold can be recovered from a spent thiosulphate-sulphite electrolyte. The recovery process is expected to have an enhanced value if the recovered gold can be tailored for suitable applications, for example, gold nanoparticles are useful in catalysis, sensors, electronics etc.

In the initial work, we have used flat-plate glassy carbon and graphite electrodes to study the mechanism of nucleation and crystal growth of gold deposition from concentrated spent electrolyte. It was found that at the early stages of reduction process, the deposition of gold on glassy carbon exhibits an instantaneous nucleation of non-overlapping particles. At longer times, the particles begin to overlap and the deposition follows a classic progressive nucleation phenomenon. On the other hand, deposition of gold on graphite does not follow the classical nucleation phenomena. Microscopy observations demonstrate that the particle size and density of the deposited gold can be controlled by varying the deposition potentials and time.

A flow cell operated in a flow-by mode was constructed which used a three-dimensional reticulated vitreous carbon to recover gold from rinse waters. The reactor was tested by removing copper (II) from acidified copper sulphate solution near the mass transfer limiting rate. The gold removal process was then operated close to mass transport control at all times by adjusting the current to its limiting value, $I_L(t)$. It was found that the gold concentration depletes very slowly with time owing to the changes in electrolyte.

ACKNOWLEDGEMENT

The author would like to express her deepest gratitude to the following people:

- Professor Sudipta Roy for her excellent guidance and supervision throughout the research work.

- R. Dixon, P. Sterling, S. Latimer, J. Banks, I. Strong, B. E. Grover and J. Marshall for their brilliant technical support and assistance.

- K. Liddell for help with the XRD measurements and D. Dunbar for help with ICP analysis.

- G. Staines and P. Carrick for help with the SEM imaging.

- E. Kalman, M. Lakatos, B. Tury, P. Nagyp and D. Arranyi from Chemical Research Centre of the Hungarian Academy of Sciences for the AFM measurements and Short Term Scientific Mission (STSM) grant from COST D19-00935, which supported the travel to Hungary.

- Ministry of Science, Technology and Innovations (MOSTI), Malaysia for the financial support.

- Friends and colleagues in the School of Chemical Engineering and Advanced Materials especially Samaneh, Rachel, Nicola, Claire and Brijesh for their continuous inspiration and encouragement.

- Dilla Latiff and family for unconditional support and friendship throughout my years in Newcastle.

- Emak, Abah, Abang and Boy for their unconditional love and encouragement.

CONTENTS

Chapter 4: **EXPERIMENTAL SYSTEMS**

Chapter 5: **CHARACTERISATION OF AGED ELECTROLYTE**

NOMENCLATURE

A	nucleation rate constant	s^{-1}
A_e	electrode area	m^2
B	line width of diffraction profile	*radians*
c	concentration	$mol\ m^{-3}$
c_X^b	bulk concentration of species X	$mol\ m^{-3}$
c_Y^b	bulk concentration of species Y	$mol\ m^{-3}$
c_X^s	surface concentration of species X	$mol\ m^{-3}$
c_Y^s	surface concentration of species Y	$mol\ m^{-3}$
C	conductance	S
d	perpendicular distance between the reflecting planes of the crystals	nm
d_e	distance between electrodes	m
D	diffusion coefficient	$m^2\ s^{-1}$
e	voidage of porous electrode	*dimensionless*
E	electrode potential *vs.* a reference electrode	V
E_e	equilibrium (reversible) electrode potential	V
E_e^o	standard (formal) electrode potential	V
F	Faraday constant	$C\ mol^{-1}$
ΔG_c	critical free energy of a nucleus	$J\ mol^{-1}$
ΔG_v	free energy per unit volume	$J\ mol^{-1}$
ΔG_{bulk}	bulk free energy	$J\ mol^{-1}$
ΔG_{net}	total free energy change	$J\ mol^{-1}$
$\Delta G_{surface}$	surface free energy	$J\ mol^{-1}$
I	current	A
I_L	limiting current	A
$I_L(t)$	instantaneous limiting current	A
I_m	current maximum	A

I_p	peak current	A
j	current density	$A\ m^{-2}$
j_L	limiting current density	$A\ m^{-2}$
j_o	exchange current density	$A\ m^{-2}$
$\vec{j}$	partial cathodic current density	$A\ m^{-2}$
$\overleftarrow{j}$	partial anodic current density	$A\ m^{-2}$
K	Scherrer constant	*dimensionless*
k	rate constant	s^{-1}
$\vec{k}$	rate constant for cathodic reaction	$m\ s^{-1}$
$\overleftarrow{k}$	rate constant for anodic reaction	$m\ s^{-1}$
k_m	mass transport coefficient	$m\ s^{-1}$
$\vec{k}_o$	rate constant for cathodic reaction measured at 0 V *vs.* the reversible potential	$m\ s^{-1}$
$\overleftarrow{k}_o$	rate constant for anodic reaction measured at 0 V *vs.* the reversible potential	$m\ s^{-1}$
M	molar mass	$g\ mol^{-1}$
n	number of electrons exchanged in an electrochemical reaction	*dimensionless*
N	flux of a species	$mol\ m^{-2}\ s^{-1}$
N_o	number of active sites on electrode surface where nucleation can occur	cm^{-2}
$N(t)$	nuclei density at time t	cm^{-2}
p	penetration depth	m
R	universal gas constant	$J\ K^{-1}\ mol^{-1}$
R_e	resistance	Ω
r	radius of a hemispherical nuclei	m
r_c	critical radius of a hemispherical nuclei	m
r_d	radius of a hemispherical nuclei that grows under diffusion control	m

S	fractional surface coverage	*dimensionless*
S_{ex}	extended fractional surface coverage	*dimensionless*
t	time	*s*
t_m	time to maximum in $I-t$ transient	*s*
T	absolute temperature	*K*
u	time at which a nuclei is born on electrode surface	*s*
V_e	electrode volume	m^3
V_R	electrolyte volume	m^3
w	number of wavelengths in the path difference between scattered rays	*dimensionless*
X	reduced species	
Y	oxidised species	
x	perpendicular distance from the electrode surface	*m*
α_A	charge transfer coefficient for anodic reaction	*dimensionless*
α_C	charge transfer coefficient for cathodic reaction	*dimensionless*
σ	conductivity cell constant	m^{-1}
γ	molar surface free energy (surface tension)	$J\ m^{-2}$
η_{act}	activation overpotential	*V*
θ	angle of incidence	*dimensionless*
κ	electrolyte conductivity	$S\ m^{-1}$
λ	wavelength of light	*nm*
π	pi	*dimensionless*
δ	Nernst diffusion layer thickness	*m*
ρ	density	$kg\ m^{-3}$
υ	electrolyte velocity	$m\ s^{-1}$

ABBREVIATIONS

AFM	Atomic Force Microscopy
RVC	Reticulated Vitreous Carbon
SMSE	Saturated Mercurous Sulphate Electrode
SEM	Scanning Electron Microscopy
UV-Vis	Ultraviolet Visible
XRD	X-ray Diffraction

LIST OF FIGURES

LIST OF TABLES

CHAPTER 1:

INTRODUCTION

1.1 Background

Electrodeposition of soft gold has traditionally been performed using gold cyanide or gold sulphite electrolytes. The emergence of gold-based connectors in micro technology has initiated the need to search for new electrolytes because these existing electrolytes have inherent problems regarding long-term sustainability and was found to be incompatible with photoresists or other process steps [1.1-1.5].

For long term utility, interest has grown in developing non-toxic electrolytes in place of the conventional cyanide-based baths. However, the main problem encountered in replacing gold cyanide baths has been that the stability of the gold-cyanide complex is very high and all other ligands exhibit lower stability constants with gold in solutions [1.6]. One alternative electrolyte that is being examined is a solution containing thiosulphate and sulphite, which was initially proposed by Osaka and co-workers [1.1]. The bath was reported to be stable without additives and contained phosphoric acid as buffering agent. The electrolyte was proposed for electronics applications, specifically for the formation of gold bumps on silicon wafers. The gold bumps serve as sites for bonding silicon chips to the leads on an insulating tape carrier and are required to be soft enough to be easily deformable under applied pressure to achieved uniform bonding of a large number of bumps. For this reason, thallium ions were added to decrease hardness and improve surface morphology of the gold deposits. However, thallium raised the toxicity of the process, and an effort to reduce this was attempted by other researchers.

More recently, a bath containing only thiosulphate and sulphite as ligands was formulated by Newcastle University using aurochloric acid as the starting salt [1.2]. It was found that complexation by thiosulphate led to formation of $Au(S_2O_3)_2^{3-}$ a relatively stable complex, and the sulphite acted as a buffer and stabilized the solution [1.2]. The bath is found to be stable at near-neutral pH, showed good compatibility with positive photoresists and proved to be satisfactory for an industrial process [1.3].

At the end of a gold electrodeposition process, the spent electrolyte can contain a significant amount of gold in solution. Clearly, for economic and environmental reasons, it is crucial that gold can be recovered from the spent electrolyte. Under European Directive on Waste Electrical and Electronic Equipment (WEEE), scope exists for recovery of any precious metals from its scrap. The implementation of this WEEE legislation contributes towards the minimisation of waste and toxic compounds. Currently, there is no information available concerning gold recovery from thiosulphate-sulphite electrolytes. It can also be envisaged that the recovery process would have enhanced value if the recovered gold could have applications; for example, supported gold nanoparticles have great potential in the field of catalysis [1.7, 1.8]. In the electronics field, gold is used on connectors and contacts due to its high corrosion resistance [1.8, 1.9]. Applications have also been reported for gold nanoparticles as sensors in biomedical sector [1.8, 1.10] and broadly used in advanced coatings, exploiting its variation of colours depending on the particles sizes [1.10, 1.11]. Applications of gold nanoparticles are further discussed in section 1.2.

In this work, we have investigated the electrocrystallisation of gold on glassy carbon and graphite electrodes. Although relatively little information is available on electrodeposition from thiosulphate-sulphite solutions containing Au(I), there have been a number of electrocrystallisation studies using plating baths containing Au(III) in chloride [1.12, 1.13], citrate [1.14] and borate [1.15]. References 1.12-1.14 suggest that gold electrocrystallisation occurs by 3-dimensional nucleation followed by diffusion controlled growth. Examination of gold nucleation on glassy carbon from chloride solutions [1.12] indicated that in the early stages progressive nucleation occurs, whereas at longer times instantaneous nucleation takes place. On the other hand, electrodeposition on highly oriented pyrolytic graphite (HOPG) does not follow the classical nucleation phenomena [1.12]. Those electrocrystallisation studies showed that crystal size and density could be controlled by variation of deposition potentials and times [1.13].

We have also studied the recovery of gold from rinse waters by diluting the gold thiosulphate-sulphite aged electrolyte to below 200 ppm. Porous three-dimensional

electrode has been used for the study of gold ion removal due to its high surface area. Although there are numerous studies on cell configurations and electrolyte conditions for metal ion removal from waste stream, little information is found for gold removal. Among the examples of metal ion recovery which used three-dimensional electrode are copper [1.16-1.18], lead [1.19], cadmium [1.20] and silver [1.21], of which are discussed in section 1.3.4

1.2 Chemistry of Gold Thiosulphate-Sulphite Electrolyte

The existing gold plating baths that are commercially available can be classified as cyanide or non-cyanide baths [1.15]. The most common non-cyanide gold electrolyte is based on a gold-sulphite complex. Recently, a novel electrolyte consists of sulphite and thiosulphate as complexing agents has been proposed.

Sulphite is the most commonly used non-cyanide complex for gold deposition as it is non-toxic and suitable for plating soft gold in the microelectronics industry. Generally, the gold sulphite baths have the ability to produce fine, smooth, bright and ductile gold deposits [1.2]. The bath also exhibits better compatibility with the resists. In the sulphite-based baths, gold exists as $[Au(SO_3)_2]^{3-}$. There appears to be uncertainty about the stability constant, β, of the sulphite complex. In many electrodeposition literatures, it has been widely stated that the stability constant of the sulphite complex is approximately 10, which is 28 times less stable than the cyanide. However, this value has not been experimentally proved. Some researchers have calculated a value of 26-27 for $[Au(SO_3)_2]^{3-}$ [1.22, 1.23]. More recently, a speciation analysis by Green and Roy have found that the previous determination of the stability constant for sulphite baths indicating $\beta \approx 27$ are likely to be correct, while those claiming $\beta \approx 10$ are erroneous [1.24].

One of the major difficulties associated with the use of gold sulphite plating baths is their instability under neutral or acidic conditions. The principal cause of bath

instability has been attributed to the disproportionation of the free aurous ions and results in formation of colloidal gold [1.2].

$$Au(SO_3)_2^{3-} \leftrightarrow Au^+ + 2SO_3^{2-} \tag{1.1}$$

$$3Au^+ \rightarrow Au^{3+} + 2Au^0 \tag{1.2}$$

The sulphite ion itself can also decompose to form hydroxyl ions

$$SO_3^{2-} + H_2O \leftrightarrow SO_2 + 2OH^- \tag{1.3}$$

At neutral pH, the equilibrium of sulphurous acid in the above reaction starts to shift to the right, thereby releasing SO_2. Cathodic reduction of sulphite can lead to formation of dithionite ions, $S_2O_4^{2-}$,

$$SO_2^- + SO_2 \leftrightarrow S_2O_4^{2-} \tag{1.4}$$

Dithionite species is a strong reducing agent and can reduce $[Au(SO_3)_2]^{3-}$ to form colloidal gold. To counteract the stability problems of sulphite-based electrolyte at pH 4-8, many sulphite baths are operated at pH $\geq$ 8 as well as incorporating a proprietary stabilising additives such as organic amines.

Gold thiosulphate complex, $[Au(S_2O_3)_2]^{3-}$, offers better electrolyte stability, $\beta = 26$, than the sulphite bath. The relatively large stability constant for the thiosulphate complex ensures that it is stable over a wide range of pH. Thus, the thiosulphate complex is expected to be a viable alternative to the sulphite complex. Although the Au(I) thiosulphate complex is predicted to be stable even under mildly acidic conditions, they have never formed the basis for an electrodeposition process, mainly due to the tendency of free $S_2O_3^{2-}$ to disproportionate to form colloidal sulphur according to the following reaction [1.2, 1.24],

$$S_2O_3^{2-} \leftrightarrow S^0 + SO_3^{2-} \tag{1.5}$$

At neutral or mildly acidic conditions, protonation of excess $S_2O_3^{2-}$ forms HSO_3^- and colloidal sulphur, which hinders its industrial exploitation,

$$H^+ + S_2O_3^{2-} \leftrightarrow S^0 + HSO_3^- \tag{1.6}$$

The cathodic reduction of bisulphite ions can also lead to formation of dithionite ions, $S_2O_4^{2-}$.

Electrodeposition of soft gold from a non-cyanide bath containing both sulphite and thiosulphate as complexing agents was first proposed by Osaka and co-workers [1.1]. The formation of a mixed thiosulphate-sulphite complex made the bath more stable than only sulphite or thiosulphate complex. The addition of thallium ions in the form of Tl_2SO_4 as a grain refiner was found to decrease the hardness and improve the surface morphology of the gold deposits. However, the toxicity of the thallium is of concern. Based on the mixed ligand electrolyte developed by Osaka, Newcastle has developed an electrolyte for soft gold electrodeposition which eliminates the thallium ions [1.2]. The electrolyte formulation will be discussed in chapter 4.

According to the speciation analysis developed by Green and Roy [1.24], the model predicts that the dominant species in a mixed thiosulphate-sulphite electrolyte are $Au(S_2O_3)(SO_3)^{3-}$, $Au(S_2O_3)(SO_3)_2^{5-}$ and $Au(S_2O_3)_2^{3-}$. Under acidic conditions (pH <4), $Au(S_2O_3)_2^{3-}$ is the main complex exists in the solution. However, under neutral or alkaline conditions, $Au(S_2O_3)(SO_3)_2^{5-}$ complex predominates. The speciation analysis also predicts that in the intermediate pH range ($4 < pH < 6$), $Au(S_2O_3)(SO_3)^{3-}$ is also present but only at relatively low concentrations.

The mixed ligand bath developed by Newcastle is operated at a pH of 6-7.5. Based on the speciation model, the electrodeposition mechanism would involve the

$Au(S_2O_3)(SO_3)_2^{5-}$ complex. However, in a prior studies by Liew *et. al.* [1.6], UV-visible spectroscopy analysis carried out to determine the gold complex in solution revealed that the Au(I) was complexed with the thiosulphate and no evidence of a mixed complex was found. Cyclic voltammetry and limiting current data also showed that the electrochemical data for the thiosulphate-sulphite electrolyte is similar to that obtained for gold thiosulphate solution. These results strongly support that gold is deposited from a gold-thiosulphate complex.

$$2[Au(S_2O_3)_2]^{3-} \leftrightarrow Au_2S_2O_3 + 3S_2O_3^{2-} \tag{1.7}$$

On the other hand, sulphite ligand acts as the buffering agent which maintains a high level of bisulphite ions in the solution under neutral or mildly acidic conditions, making the formation of sulphur less favourable.

$$H^+ + (S_2O_3)^{2-} \leftrightarrow (HSO_3)^- \tag{1.8}$$

This means that gold is stabilised by the formation of $Au(S_2O_3)_2^{3-}$ ions and precipitation of sulphur is avoided by excess HSO_3^-.

The speciation analysis by Green and Roy has also identified that in the case of the thiosulphate-sulphite plating bath, the concentration of disproportionating Au(I) species is several orders of magnitude lower than the corresponding sulphite bath at all pH [1.24]. This shows that the thiosulphate-sulphite bath is more stable than the sulphite bath. The improved stability of the thiosulphate-sulphite bath can also be rationalized in terms of the formation of dithionite. In a mixed bath, electroreduction of the complex requires a less cathodic potential, therefore at the same pH and current density, the contribution of the dithionite reaction is expected to be less [1.24].

1.3 Applications of Gold Nanoparticles

In the search for new materials, nanoparticles research offers great potential. During the past decade, driven by the interest in unique physical and chemical properties of gold nanoparticles, the investigation of preparing gold particles and its use as a nanostructured material is becoming an existing area of interdisciplinary research. Based on the properties, gold nanoparticles have great potential for various applications ranging from catalysis, electronic and optical devices, sensors and many more.

Rapid growth of interest in catalytic properties of gold has manipulated its potential for applications in pollution control, chemical processing and fuel cells [1.8]. The preferred use of gold as catalyst is due to the lower 'light off' temperature (temperature at which catalysis become functional) and the stability of its price compared to platinum group metals (PGMs). Normally, gold catalyst will operate at temperature range 200-350K compared to platinum catalyst that will operate best at temperature 400-800K. In addition, the greater availability of gold compared to PGMs has explained the fluctuating prices of platinum and relatively stable value of gold prices [1.8]. In the area of pollution control, gold catalysis has been employed to design a prototype air purification unit, which removed carbon monoxide (CO) from the air at room temperature. Some patents have also been filed claiming use of gold catalyst in automotive emissions control. There are promising applications in vehicle emission devices such as the exhaust treatment for gasoline and diesel cars [1.25].

With respect to chemical processing, both homogeneous and heterogeneous applications are possible [1.8, 1.26]. Gold catalyst can be applied for synthesis of both heavy and specialty chemicals. Applications of gold catalyst include production of vinyl chloride and conversion of propene to propene oxide using gold on titanium catalyst in very high selectivities [1.7]. The most recent commercial use of gold catalyst is the production of vinyl acetate monomer (VAM) using gold palladium catalyst. In the field of fuel cells, gold catalyst is used in removal of carbon monoxide from the hydrogen feeds where carbon monoxide is oxidized at room

temperature [1.8]. Based on the lower activation temperature than copper or zinc oxide catalyst, gold catalyst has been used for production of H_2 supplies for fuel cells and other applications [1.26].

Gold is the material of choice in many electronics applications. The beneficial material properties of gold include outstanding resistance to tarnish or corrosion and high thermal and electrical conductivity [1.27]. Although silver and copper are better conductors of electricity, they do not have comparable resistance to tarnishing or corrosion. In addition, resistance of gold to environmental aspects is one of the important properties.

The most significant use of gold nanoparticles is the nanowires, which can be assembled by dielectrophoresis from suspension of gold nanoparticles [1.8]. These wires are used to connect parts of semiconductors such as transistors and integrated circuits to ensure reliable connections between components. Most semiconductor packages use very fine gold wires to make electrical connections between the semiconductor chip and the lead frame within the package. These wires are typically 2mm long and 25μm thick so only about 20 nanogram of gold is used per wire [1.27].

Gold is an indispensable element for nanoscale electronic devices because it is resistant to oxidation and mechanically robust at the incredibly small dimensions. The inertness of gold makes it invaluable as a solderable coating to maintain the solder wetting properties of PCBs and component leads. Applications have also been reported for gold nanoparticles as sensors in the biomedical sector. Metal particle arrays crosslinked by molecular receptor units act as selective sensing interfaces with controlled porosity and tuneable sensitivity.

Gold nanoparticles are also broadly used in advanced coatings, exploiting its variation of colours depending on the particle sizes. The red colour of gold-ruby glass is caused by small particles of metallic gold that form when gold containing colourless glass is annealed. The ruby colour is produced by metallic gold particles

with an optimum size of 5-60 nm [1.28]. In addition, metal gold inks have been used for decorative applications; containing nanoparticles precursors, thermally decompose to produce bright gold films. The best-known materials that contain nanoparticles of metallic gold are gold colloids. These lack the familiar metallic cluster, but show bright colours, which range from red, violet or blue, depending upon the size of the nanoparticles [1.29, 1.30]. Colloidal gold has traditionally been used to colour materials such as glass and enamels. Nippon Paint has developed the technology for use in paint for cars based on polymer-stabilized gold colloid [1.8].

1.4 Electrochemical Techniques for Metal Recovery

1.4.1 Electrochemical Technology in Environmental Treatment

Electrochemical process can provide valuable contributions to the protection of the environment through implementation of effluent treatment and production-integrated process for the minimisation of waste and toxic compounds. Examples of effluent treatment process include electrochemical reactors for removal of metal ions from waste water and anodic destruction of organic pollutants [1.31]. In pollution control, removal and destruction of pollutant species can be carried out directly or indirectly by electrochemical oxidation/reduction processes in an electrochemical cell. Examples of production integrated industrial process include recycling of valuable material and substitution of waste producing process by a cleaner electrochemical technology with little or no waste production [1.31]. The scope for electrochemical technology in environmental treatment is shown in table 1.1

Avoidance of pollution:	*Clean electrosynthesis*
Recycling of valuable materials:	*Precious metal deposition*
Remediation of polluted sites:	*Soil remediation by electrodialysis*
Monitoring and sensors:	*In the gas and liquid phase*
Efficient energy conversion:	*Fuel cells and redox flow cells*
Avoidance of corrosion:	*Choice of materials/protective coatings*
Removal of contaminants:	*Metal ions, organics and inorganics removal from water*
Disinfection of water:	*Chlorination, peroxidation, or ozonation*

Table 1.1: Scope for electrochemical technology in environmental treatment.

The choice of electrochemical method as an approach for environmental problems in the process industry is owing to its many advantages, as listed table 1.2. The inherent advantage is its environmental compatibility, due to the fact that the main reagent, the electron, is a 'clean reagent'. In addition, the high selectivity of many electrochemical processes helps to prevent the production of unwanted by-products, which in many cases have to be treated as waste. However, despite its many advantages, electrochemical processes are of a heterogeneous nature, which means that the reactions are taking place at the interface of an electrode and the electrolyte. This implies that the performance of electrochemical processes may suffer from limitations of mass transfer and the size of specific electrode area [1.31]. Another crucial point is the chemical stability of the cell components in contact with an aggressive medium and in particular the long term stability and activity of the electrode material. Damage to the electrode can restrict the cell performance and longevity.

Versatility:	
Applicability to a variety of media and pollutants in gases, liquids and solids, and treatment of small to large volumes.	
Energy efficiency:	
Electrochemical processes generally have lower temperature requirements. Electrodes and cells can be designed to minimise power losses caused by inhomogeneous current distribution, voltage drop and side reactions.	
Amenability to automation:	
The system inherent variables of electrochemical processes such as electrode potential and cell current are particularly suitable for facilitating process automation.	
Clean reagents:	
The main reagent, the electron, is a 'clean reagent'.	
Cost effectiveness:	
Cell construction and equipment are generally simple and, if properly designed, also inexpensive.	

Table 1.2: The advantages of electrochemical technology.

1.4.2 Electrochemical Techniques for Metal Ion Recovery

Waste water from different industrial sectors, such as electroplating, photographic development, printed circuit board production or battery technology, requires special treatment to remove toxic metal ions or recycling of valuable material. The sources of metal ion-containing process streams are shown in table 1.3 [1.32].

Hydrometallurgy: *primary ore leaching, solvent extraction liquors, electrowinning and eletrorefining, mine dump leaching and run-off waters.*
Surface engineering-metal finishing: *etching solutions, cleaning and other pre-treatment solution, passivation treatments, spent electroplating and electroless plating baths.*
Other applications: *scrap reprocessing and refining, catalyst liquors, redox reagents for chemical processing, photographic processing solutions and spent batteries.*

Table 1.3: The sources of metal ion-containing process streams.

A number of established techniques are available for treatment of waste streams containing heavy and precious metals, including precipitation, ion exchange, solvent extraction and adsorption. Controlled migration of ions through ion-exchange membranes can be used to remove some cations, while it is also possible to precipitate the metal as hydroxide due to an increasing near cathode pH. However, all the methods mention above have the disadvantage of producing a secondary effluent consisting of a more concentrated metal bearing solution which requires further treatment [1.32].

Electrowinning is a well established technology for metal deposition from solution. The technique of electrowinning is unique in that it can recover elemental metal directly from aqueous solution without the addition of reagents [1.31]. In cases such as precious and high value heavy metals, this allows the metal to be directly recycled. When the intrinsic toxicity of the metal is the problem, removal of the metal from the waste stream in a single stage process is a cost effective solution. When appropriate, electrochemical methods can also be used in conjunction with the other techniques in order to treat the secondary waste streams produced.

Different types of cell constructions have been design during recent years. Three examples of a reactor design and process strategy for metal ion recovery from waste stream may be given as [1.32]:

- Metal can be deposited on a high surface are per unit volume cathode having a porous, three-dimensional structure. Following deposition onto porous carbon materials, the metal may be recovered by furnace refining or by dissolution into a small volume of a corrosive electrolyte.
- Metal can be deposited as powder onto the surface of an inner rotating cathode cylinder. This allow metal to be scraped off the cathode drum and continuously fluidized out of the reactor followed by conventional methods of solid/liquid separation such as filtration and gravity settlement.
- Metal may be deposited onto the cathode surfaces of a thin electrolyte film reactor such as bipolar trickle tower reactor. Such reactors are readily constructed from alternating layers of porous carbon. The anode sites of this undivided cell allow other solution species to be oxidized.

1.5 Electrode Materials in Metal Ion Recovery

1.5.1 Gold Electrocrystallisation on Carbon Electrodes

The electrochemical deposition of metal nanocrystals onto carbon electrodes has been the subject of a large number of investigations. In most cases, investigations were done to study the utility of this type of interface in electrocatalysis and as a model system for studying the nucleation and growth mechanism of the metal phase on the substrate [1.33, 1.12-1.15].

Carbon-based electrodes have been chosen to study the deposition of gold mainly because they are easily available and inexpensive. It is one of the most frequently used substrates for studies of nucleation and growth phenomena [1.34]. In addition, the carbon electrodes provide high surface area for particle nucleation. In this work,

glassy carbon and graphite electrodes have been used. The two different forms of carbon were chosen due to the difference in their structures. The choice of glassy carbon allows us to examine the microstructure when the substrate has no preferred texture. It is very probable that the amorphous glassy carbon surface has randomly distributed active sites and therefore a random distribution should result from the particle nucleation on the surface. On the other hand, the choice of a graphite electrode allows us to examine when the substrate has a well established structure.

Although relatively little information is available on electrodeposition from thiosulphate-sulphite solutions containing Au(I), there have been a number of electrocrystallisation studies using plating baths containing Au(III) in chloride [1.12, 1.13], citrate [1.14] and borate [1.15]. Schmidt *et. al.* have investigated the deposition of gold from glassy carbon electrodes from concentrated LiCl electrolytes [1.12]. The analysis of current-time transients indicates that gold electrodeposition occurs by three-dimensional nucleation followed by diffusion controlled growth of nuclei. However, the nucleation mechanism is neither purely instantaneous nor progressive; in the early stages progressive nucleation occurs, whereas at longer times instantaneous nucleation takes place. McDermott *et. al.* also studied the characterisation of gold nanocrystals electrochemically deposited on glassy carbon from a chloride bath [1.13]. It was found that the nanocrystal size, density and surface texture can be controlled by variation of deposition conditions such as the overpotential and the solution concentration. Studies by Chrzanowski *et. al.* on gold electrodeposition from citrate bath shows that the nucleation mechanism changes from three-dimensional progressive at lower overpotentials to three-dimensional instantaneous at higher overpotentials [1.14]. On the other hand, electrodeposition on highly oriented pyrolytic graphite (HOPG) does not follow the classical nucleation phenomena [1.12].

1.5.2 Reticulated Vitreous Carbon as an Electrode Material

It is common to have a low reactant concentration in environmental treatment and to require compact treatment units in a restricted space. Under such conditions, the rate

of reactant removal is often mass transport limited, and a high performance reactor needs to have a high mass transport coefficient and enhanced electrode area in order to achieve high limiting current [1.32]. This can be achieved by the use of electrode movement or by the use of a three-dimensional electrode.

Over the past three decades, three-dimensional or porous electrodes have been used extensively for numerous industrial applications due to its remarkable properties compare to plane electrodes. There-dimensional electrodes are used to counteract the limitations of low space-time yield and low normalised space velocity obtained in electrochemical processes with two-dimensional electrodes [1.35]. Among the examples of three-dimensional electrodes are graphitised carbon felt and reticulated vitreous carbon (RVC). In this work, RVC has been used to study the recovery of gold from diluted gold thiosulphate-sulphite aged electrolyte.

RVC is an open pore foam material composed almost solely of glassy carbon which combines some of the properties of glass and normal industrial carbons [1.36]. The structure of RVC is achieved by polymerisation of a resin combined with foaming agents, followed by carbonisation. Besides polyurethane and phenolic resins, furfuryl and epoxy resins are also used for manufacturing RVC. The foam resin is dried and cured at 120 °C and then carbonised at 700-1100 °C [1.35].

RVC is available in several porosity grades ranging from 5 to 1400 pores per inch (ppi) [1.35-1.39]. The three dimensional porous structure offers high ratio of surface area to volume which allows the attainment of relatively high volumetric flow rates hence reducing mass transport problems. The rigid structure makes the material highly electroconductive and the high free void volume, between 90 % and 97 % depending on the porosity grades, results in low pressure drop in fluid flow. RVC is also inert to a wide range of reactive acids, bases and organic solvents. It is highly resistant to high temperature in non-oxidising environment and has a wide usable potential range, approximately between 1.20 V and – 1.0 V *vs.* SCE at pH 7. Moreover, this material is inexpensive and may easily be machined into various geometric shapes and mounted in various cell configurations.

1.5.3 Metal Ion Recovery using RVC

The properties mentioned previously have resulted in a steady diversification of its application both in research laboratories and in industrial applications [1.35-1.37]. Structural features make RVC an ideal electrode material for many electrochemical applications including sensors, synthesis of organics, studies of various anodic processes and the major application being metal ion removal from dilute process solution [1.35-1.37]. Various cell configurations and electrolyte conditions have been studied for the removal of metal ions from aqueous wastewater; among the examples are copper, lead, cadmium and silver.

Deposition of copper has been extensively studied and has also been used as a reference for more complex process solution. Copper ions are part of many industrial effluents, therefore finding efficient ways for effluent cleanup and treatment is vital. Pletcher *et. al.* investigated the removal of copper from acidified copper sulphate solution using several RVC porosity grades ranging from 10 to 100 ppi [1.16, 1.17]. The flow cell was operated in flow-by mode. It was found that the copper ion concentration are reduced to < 0.1 ppm and the concentration of copper decays faster as the porosity of the of the electrode increases. The current efficiencies for 90% removal of the copper ion were reported to be less than 80 % and decrease as higher ppi foams were used. This could be attributed to the difficulties in the nucleation of copper or to the reduction of surface oxide.

Reade *et. al.* examined the potentiostatic deposition of copper from sodium sulphate solution using RVC rotating cylinder electrode at four porosity grades, 10, 30, 60 and 100 ppi [1.18]. It was reported that the rate of decay of cupric ions are dependent upon the electrode potential, the highest rate of decay being achieved at more negative potential. The fastest rate of copper removal to < 0.1 ppm was achieved at 100 ppi RVC and the current efficiency was maintained at exceptionally high values, > 90 %.

Lead is one of the major pollutants in a number of important processes such as manufactures of paints, batteries and some alloys. Environmental legislation has increased pressure on these industries to reduce their lead effluent levels. Ponce-de-Leon and Pletcher [1.19] have studied the influence of several anions, $Cl^-, NO_3^-, ClO_4^-, BF_4^-$ and SO_4^-, on the removal of Pb(II) ions at different conditions on 10, 60 and 100 ppi RVC electrodes. It was shown that in all five electrolytes containing those anions at pH 2, it is possible to decreased Pb(II) to the level necessary for discharged of effluent into rivers and sea. However, the anions in solutions have different influences over the necessary conditions for satisfactory removal of the Pb(II) ion. The rate of removal from NO_3^-, ClO_4^- and BF_4^- media to a concentration of less than 1 ppm at 298 K is slower than that of Cl^- medium, indicating that lead deposition was not mass transport controlled in these media except for Cl^-. This suggests that addition of chloride ions to the solutions could be an option to improve the recovery process. It was also reported that the removal of Pb(II) from SO_4^- medium at 298 K was much slower than Cl^-, NO_3^-, ClO_4^- and BF_4^-, only 20% was removed after 3000 s of electrolysis. With increase of the temperature to 333 K, the removal of Pb(II) reached 90% in 2000-2500 s.

Cadmium is an example of heavy metal which has strong cumulative effect in living systems and its discharge limit has been continuously lowered over recent years. Dutra *et. al.* have developed a laboratory scale electrolytic flow-by cell with a RVC cathode operating in a mass transport regime [1.20]. The cell permitted the purification of aqueous solution containing cadmium ion from 200 to 0.1 ppm with current efficiencies up to 40% in 85 minutes of operation. Gonzalez and co-workers have studied the recovery of low concentrations of silver (10^{-4} M) from a simulated leaching solution containing high concentrations of copper and cyanide [1.21]. Studies were performed in a filter press electrochemical reactor (ElectroCell AB) with a 445 ppi RVC and a flow rate of 5 $cm^3\ s^{-1}$ at 25 °C. This study showed that high Cu (II) and CN^- concentrations do not interfere in the selective deposition of silver.

1.6 Aims and Objectives

The discharge of gold along with the effluent is a major economic as well as environmental concern. For this reason, the primary aim of this work is to study the feasibility of gold recovery from an aged thiosulphate-sulphite electrolyte using electrodeposition method. Currently, little information is available concerning gold electrodeposition from a thiosulphate-sulphite plating bath.

At first, a review of the aged plating bath was performed to study if there was any significant change in the electrochemical properties of the gold thiosulphate-sulphite electrolyte. In the initial work, gold has been deposited on glassy and graphitic carbons. The aim of this work is to elucidate information on the nucleation and growth behaviour of gold on carbon electrodes as well as studying their microstructural properties, which is likely to govern the utility of the recovered gold.

In order to study the effectiveness of gold removal process from rinse waters, a flow cell has been constructed which used a three-dimensional reticulated vitreous carbon as an electrode. This study is important to investigate the suitability of a batch decay model operated close to mass transport control condition to recover gold from the aged electrolyte.

1.7 References

1.1. T. Osaka, M. Kato, J. Sato, K. Yoshizawa, T. Homma, Y. Okinaka and O. Yushioka, *J. Electrochem. Soc.*, **148**, C659 (2001).

1.2 M. J. Liew, S. Roy and K. Scott, *Green Chem.*, **5,** 376 (2003).

1.3 T. A Green, M. J. Liew and S. Roy, *J. Electrochem. Soc.*, **150** C104 (2003).

1.4 M. J. Liew, *PhD Thesis*, University of Newcastle upon Tyne (July 2002).

1.5 H. Watanabe, S. Hayashi and H. Honma, *J. Electrochem. Soc.*, **146** 574 (1999).

1.6 M. J. Liew, S. Sobri and S. Roy, *Electrochim. Acta*, **51**, 877 (2005).

1.7 G. J. Hutchings, *Gold Bull.*, **29 (4)**, 123 (1996).

1.8 C. W. Corti, R. J. Holliday and D. T. Thompson, *Gold Bull.*, **35 (4)**, 111 (2002).

1.9 P. Goodman, *Gold Bull.*, **35 (1)**, 21 (2002).

1.10 C. W. Corti and R. J. Holliday, *Gold Bull.*, **37 (1-2)**, 20 (2004).

1.11 M. B. Cortie, *Gold Bull.*, **37 (1-2)**, 12(2004).

1.12 U. Schmidt, M. Donten and J. G. Osteryoung, *J. Electrochem. Soc.*, **144** 2013 (1997).

1.13 M. O. Finot, G. D. Braybrook, M. T. McDermott, *J. Electroanal. Chem.*, **466**, 234 (1999).

1.14 Y. G. Li, W. Chrzanowski and A. Lasia, *J. Appl Electrochem.*, **26**, 843 (1996).

1.15 X. Wang, N. Isaev and J. G. Osteryoung, *J. Electrochem. Soc.*, **143** 1201 (1996).

1.16 D. Pletcher, I. White, F. C. Walsh and J. P. Millington, *J. Appl. Electrochem.*, **21**, 659 (1991).

1.17 D. Pletcher, I. White, F. C. Walsh and J. P. Millington, *J. Appl. Electrochem.*, **21**, 667 (1991).

1.18 G. W. Reade, A. H. Nahle, P. Bond, J. M. Friedrich and F. C. Walsh, *J. Chem. Tech. and Biotech.*, **79**, 935 (2004).

1.19 C. Ponce-de-Leon and D. Pletcher, *Electrochim. Acta*, **41 (4)**, 533 (1996).

1.20 A. J. B. Dutra, A. Espinola and P. P. Borges, *Minerals Eng.*, **13 (10-11)**, 1139 (2000).

1.21 V. R. Cruz, M. T. Oropeza, I. Gonzalez and C. Ponce-de-Leon, *J. Appl. Electrochem.*, **32**, 473 (2002).

1.22 J. G. Webster, *Geochim. Cosmochim. Acta*, **50**, 1837 (1986).

1.23 G. Baltrunas, *Chemija*, **10**, 112 (1999).

1.24 T. A. Green and S. Roy, *J. Electrochem. Soc.*, **153** C157 (2006).

1.25 J. R. Mellor, A. N. Palazov, B. S. Grigorova, J. F. Greyling, K. Reddy, M. P. Lesoala and J. H. Marsh, *Catalyst Today*, **72**, 145 (2002).

1.26 G. C. Bond and D. T. Thompson, Cat. Rev. Sci. Eng., 41, 319 (1999).

1.27 Y. Okinaka, *Gold Bull.*, **33 (4)**, 117 (2000).

1.28 F. E. Wagner, S. Haslbeck, L. Stievano, S. Calogero, Q. A. Pankhurst and K. P. Martinek, *Nature*, **407**, 691 (2000).

1.29 J. Turkevich, *Gold Bull.*, **18**, 86 (2000).

1.30 J. Turkevich, *Gold Bull.*, **18**, 125 (2000).

1.31 K. Juttner, U. Galla and H. Schmieder, *Electrochim. Acta*, **45**, 2575 (2000).

1.32 F. C. Walsh, *Pure Appl. Chem.*, **73**, 1819 (2001).

1.33 M. S. El-Deab, T. Sotomura and T. Ohsaka, *J. Electrochem. Soc.*, **152** C730 (2005).

1.34 A. Milchev, E. Michailova and I. Lesigiarska, *Electrochem. Comm. 2*, 407 (2000).

1.35 J. M. Friedrich, C. Ponce-de-Leon, G. W. Reade and F. C. Walsh, *J. Electroanal. Chem.*, **561**, 203 (2004).

1.36 J. Wang, *Electrochim. Acta*, **26 (12)**, 1721 (1981).

1.37 Z. Rogulski, W. Lewdorowicz, W. Tokarz and A. Czerwinski, *Polish J. Chem.*, **78**, 1357 (2004).

1.38 T. Doherty, J. G. Sunderland, E. P. L. Roberts and D. J. Pickett, *Electrochim. Acta*, **41 (4)**, 519 (1996).

1.39 J. Newman and K. E. Thomas-Alyea, *Electrochemical Systems (3rd Edition)*, Wiley-Interscience (2004).

CHAPTER 2:

ELECTROCHEMICAL NUCLEATION THEORY

2.1 Deposition Process

2.1.1 Introduction

Electrodeposition is an electrode process which involves the reduction of metal ions from an electrolyte. The term electrodeposition is often used to describe reactions used in many technologies such as electroplating, electrowinning and electrorefining. The process is usually carried out in a three electrode electrochemical cell that consists of a working electrode, a counter electrode and a reference electrode. The working and counter electrodes are connected to a power supply. The deposition is achieved by applying a negative charge on the working electrode. The metallic ions carry a positive charge and thus attracted to the cathode. The ions next to the cathode accept electrons and reduce to their metallic form and are deposited on the electrode surface as a thin layer.

Often, the electrodeposition process at an electrode surface is presented as a simple electron transfer such as

$$X^{n+} + n\bar{e} \rightarrow Y \qquad (2.1)$$

However, electrochemical reduction and oxidation of metals is considerably more complex, which involves not only the electron transfer but also transport of reactants and products as well as chemical and phase transformations. Thus, the overall cathodic process in which a species X is reduced can be considered to take place in several stages as described below [2.1, 2.2]:

- Mass transport of electroactive ions from bulk solution to the electrode surface.
- Adsorption of electroactive species on the electrode surface.
- Electron transfer between the reactant and the electrode.

- Transport of anions away from the surface.
- Incorporation of adsorbed metal into a growing lattice.

The rate at which the overall reaction proceeds is determined by the slowest of these steps. In general, either the kinetics of electron transfer or the mass transport of electroactive species determines the rate of overall reaction. This effect can be typically seen in a polarisation curve, as shown in figure 2.1, which relates the current density, j_o, to the activation overpotential, η_{act}. From the figure, region (c) refers to a situation where the rate determining step is the charge transfer reaction. In consequence, the rate is potential dependent. The horizontal portion (a) is referred to as the diffusion limited region, which arises when the rate of reaction is governed by mass transfer to the electrode and therefore is independent of the electrode potential.

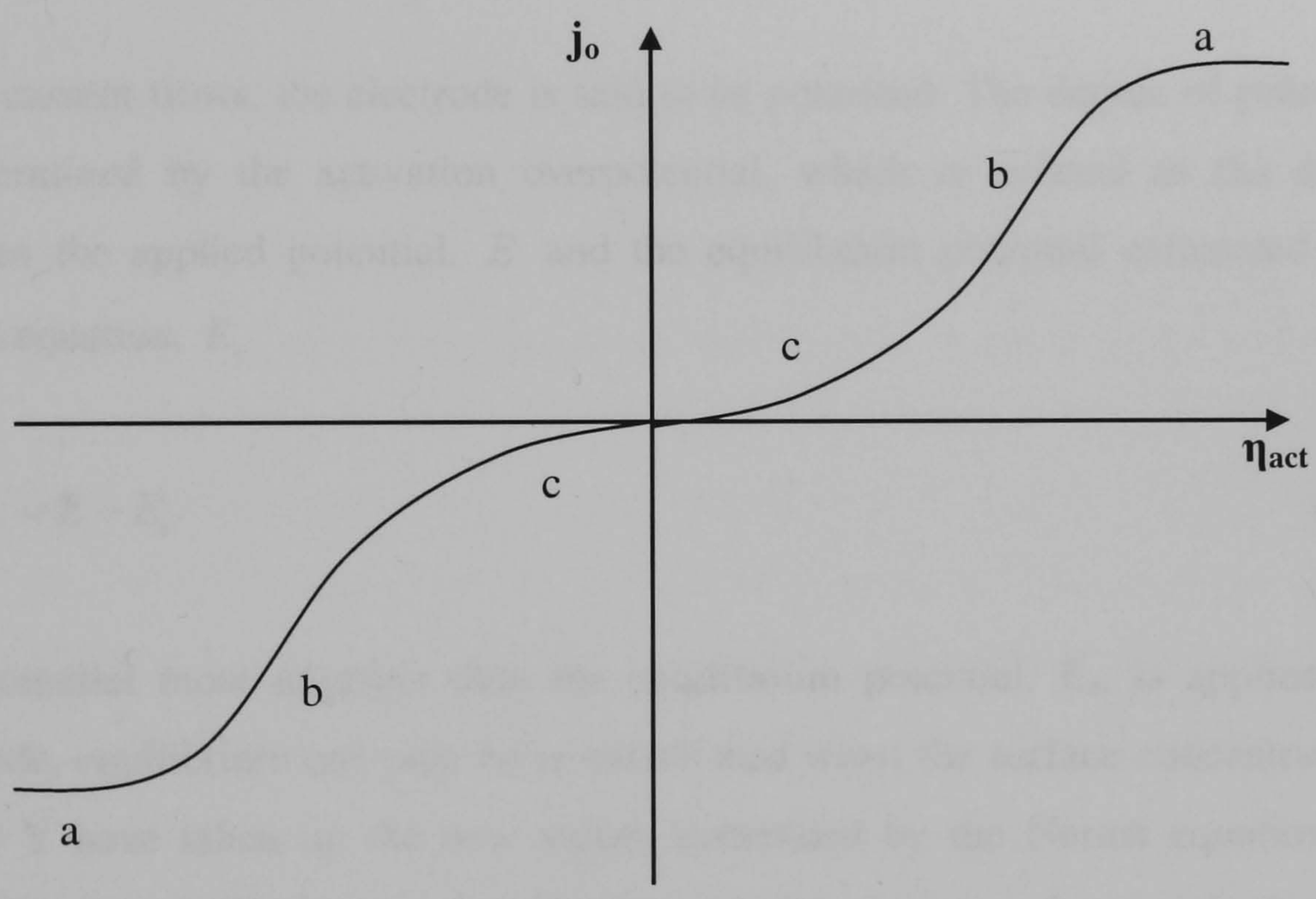

Figure 2.1: Schematic current vs. overpotential curve for a reaction $X^{n+} + n\bar{e} \rightarrow Y$

(a) mass transport control (b) mixed control and (c) charge transfer control

If the cell potential is monitored in the absence of current and no overall chemical change, the potential of the working electrode will eventually reach a value indicating that the cell is in equilibrium. At this state, the surface concentrations of species X, c_X^s, and Y, c_Y^s, are equal to their bulk concentrations. The equilibrium potential of the working electrode, E_e, is given by the Nernst equation

$$E_e = E_e^\theta + \frac{RT}{nF} \ln \frac{c_X^s}{c_Y^s} \qquad (2.2)$$

where E_e^o is the standard electrode potential, R is the universal gas constant, T is the absolute temperature, n is the number of electron, F is the Faraday's constant, c_X^s is the surface concentration of species X and c_Y^s is the surface concentration of species Y.

When current flows, the electrode is said to be polarised. The degree of polarisation is determined by the activation overpotential, which is defined as the different between the applied potential, E and the equilibrium potential calculated by the Nernst equation, E_e

$$\eta_{act} = E - E_e \qquad (2.3)$$

If a potential more negative than the equilibrium potential, E_e, is applied to the electrode, equilibrium can only be re-established when the surface concentrations of X and Y have taken up the new values demanded by the Nernst equation at the applied potential. The Nernst equation demands that there is a decrease in the ratio of surface concentrations, $\frac{c_X^s}{c_Y^s}$, and this can be achieved by the reduction of species X to Y by a passage of a cathodic current. Therefore, the cathodic current is defined as the flow of electrons into the electrode and from there into the reactant. Conversely, applying a positive potential relative to the equilibrium potential will drive the

reaction in the anodic direction, where electrons are transferred from the reactants to the electrode.

The most important aspect of a reversible reaction is that an equilibrium is established immediately. This concept can be explained in terms of the concentration profile of the electroactive species near the electrode surface during a during a liner potential sweep experiment. If a very slow linear potential sweep is applied to a system, the voltammogram follows a steady state I *vs.* E curve. The ratio of $\frac{C_X^s}{C_Y^s}$ is given by the Nernst equation and as the potential is made more negative, the surface concentration must be progressively decreased. The concentration gradient is thereby increased and hence the current also increases. Eventually the surface concentration of the reactant approaches zero and the steady state concentration profile cannot change further, therefore the current reaches a plateau value.

However, when the sweep rate is increased, the diffusion layer does not have sufficient time to relax to its equilibrium state and the concentration profiles are not yet linear. When the potential where X is reduced is reached, the surface concentration of X immediately decreases from its bulk value in order to satisfy the Nernst equation and a concentration gradient is set up. The electrode potential continuously changing and the surface concentration of X is further decreased until it effectively reaches zero. Once the surface concentration of X reaches zero, the concentration gradient starts to decrease and hence the current flowing must also decrease. Overall this behaviour gives rise to a peak-shaped current-potential response.

When the potential sweep is reversed, the species Y present near the electrode starts to be reoxidised back to X in order for the surface concentrations to be those required by the Nernst equation. With the changing electrode potential, the surface concentration of Y eventually reaches zero. Suing similar arguments as were used for the forward sweep, it can be shown that the current on the reverse sweep will also exhibit a peaked response of the opposite sign. It can be conclude that in a reversible

reaction, the current changes corresponding to the concentration gradient near the electrode and the Nernstian equilibrium is always maintained at the electrode surface. A typical I *vs.* E response at different sweep rates is shown in figure 2.2.

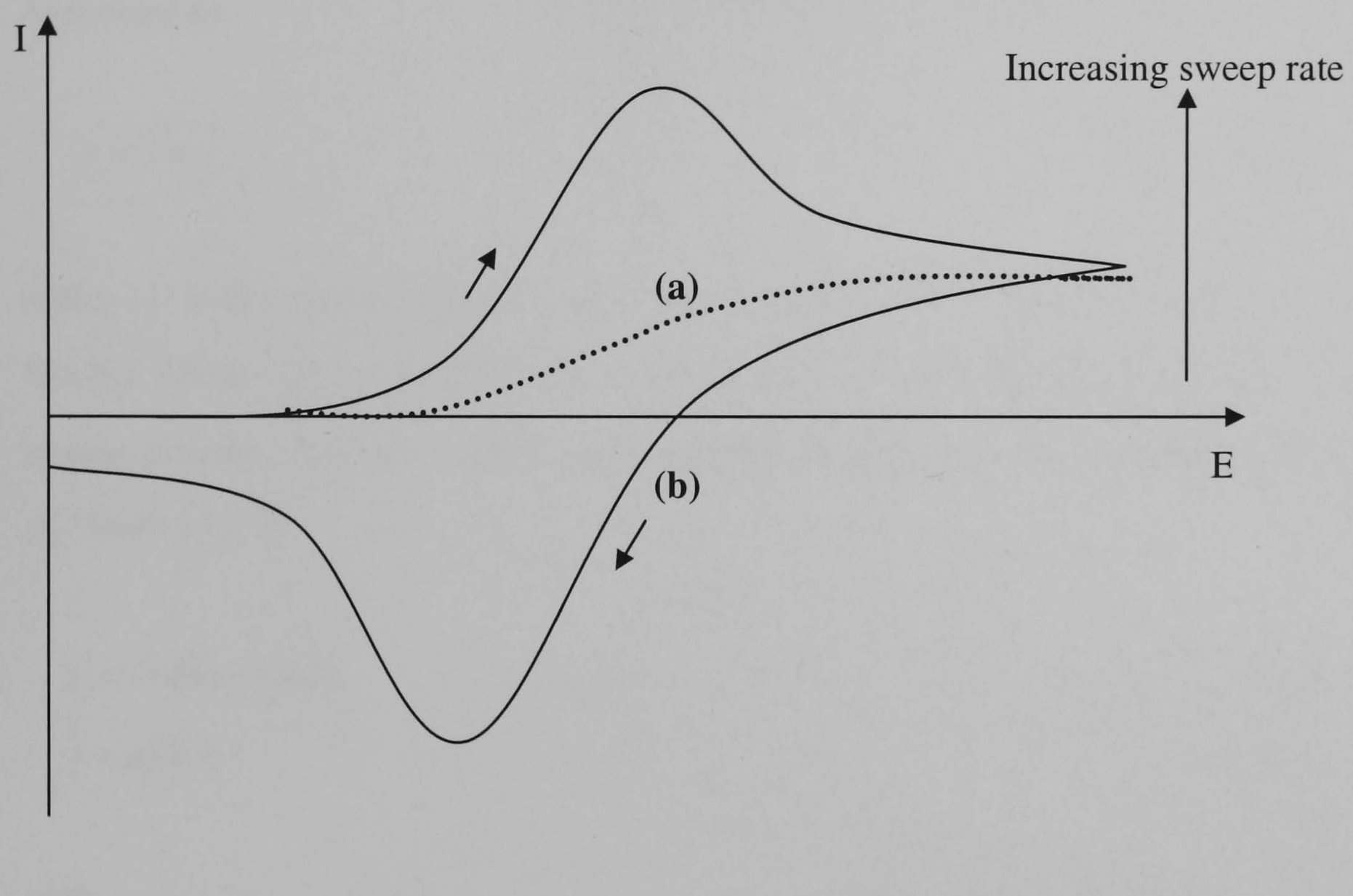

Figure 2.2: I-E response at different sweep rates (a) Steady state response (b) Cyclic voltammogram for a reversible process.

2.1.2 Charge Transfer Process

In the case where the overall rate of reaction is governed by the kinetics of electron transfer at an electrode, following assumptions are made [2.3]:

- The reaction is a simple electron transfer which follows equation 2.1 with no chemical complications.
- The rate of mass transport by diffusion and convection is so large that it is never the limiting rate.

- The concentrations at the electrode surface, c_X^s , are equal to those in the bulk solution, c_X^b .

When a reaction takes place at any potential, the measured current density can be expressed as

$$j = \vec{j} + \overleftarrow{j} \tag{2.4}$$

where $\vec{j}$ is the partial cathodic current density and $\overleftarrow{j}$ is the partial anodic current density. These current densities are each dependent on rate constants for cathodic and anodic process, $\vec{k}$ and $\overleftarrow{k}$, and the concentration of species at the electrode surface, c_X^s and c_Y^s [2.1].

$$\vec{j} = -nF\vec{k}c_X^s \text{ and} \tag{2.5 a}$$

$$\overleftarrow{j} = nF\overleftarrow{k}c_Y^s \tag{2.5 b}$$

with

$$\vec{k} = \vec{k}_o \exp\left(-\frac{\alpha_C nF}{RT}\eta_{act}\right) \text{ and} \tag{2.6 a}$$

$$\overleftarrow{k} = \overleftarrow{k}_o \exp\left(\frac{\alpha_A nF}{RT}\eta_{act}\right) \tag{2.6 b}$$

$\vec{k}_o$ and $\overleftarrow{k}_o$ are the rate constants for cathodic and anodic process respectively, measured at 0 V *vs.* the reversible potential. α_c and α_A are the cathodic and anodic charge transfer coefficients, regarded as the fraction of change in the overpotential which leads to a change in the rate constant for electron transfer. The values of α_c and α_A are related by

$$\alpha_A + \alpha_C = 1 \tag{2.7}$$

Equations 2.4 to 2.7 lead to the Butler-Volmer equation [2.1, 2.2]

$$j = j_o\left[\exp\left(\frac{\alpha_A nF}{RT}\eta_{act}\right) - \exp\left(\frac{\alpha_C nF}{RT}\eta_{act}\right)\right] \tag{2.8}$$

The Butler-Volmer equation shows how the current density varies with the exchange current density, overpotential and the transfer coefficients. There are two important limiting cases of equation 2.8. At high negative overpotential, $\vec{j} \gg \overleftarrow{j}$ and the cathodic current density is given by

$$\log|-j| = \log j_o - \frac{\alpha_C nF\eta_{act}}{2.3RT} \tag{2.9}$$

Conversely, at high positive overpotential, $\overleftarrow{j} \gg \vec{j}$ and the anodic current density is given by

$$\log|j| = \log j_o + \frac{\alpha_A nF\eta_{act}}{2.3RT} \tag{2.10}$$

These two equations are known as the Tafel equations, which are the basis for determining the exchange current density and the charge transfer coefficients.

2.1.3 Mass Transfer Process

In the above case where the electrochemical reaction is governed by the electron transfer kinetics, assumption was made that the concentration of an active species at the electrode surface is approximately equal to its bulk concentration. However, in most cases these surface concentrations can be significantly different from the concentration in the bulk of electrolyte. Since electrochemical reaction leads to consumption of reactant species at an electrode surface, this consumption must be balanced by transport of this species from the bulk to the electrode surface. Similarly,

product species are generated at the surface, and the generation rate must be balanced by transport of this species into the bulk electrolyte.

There are three mechanisms of mass transport of species in solution [2.1, 2.2]:

- Diffusion: transport of species due to concentration gradient between the electrode surface and the bulk solution. The flux of species is proportional to the concentration gradient at the surface and is given by the Fick`s first law

$$N_i = -D_i \frac{dc_i}{dx} \tag{2.11}$$

where N is the flux, i denotes the species, x is the length, D is the diffusion coefficient and c is the concentration of species in solution.

- Migration: transport of an ion under a potential gradient and it is the mechanism by which the current flows through electrolyte.
- Convection: transport of species due to gradient in pressure and density which leads to mechanical motion of the fluid. Density gradient can be caused by local variations in the solution concentration and temperature leading to natural convection. Forced convection by mechanical stirring or pumping can also be introduced in an electrochemical system.

Close to the electrode surface, diffusion is the main mechanism for mass transport at the electrode surface. Consider an electrode reaction which follows equation 2.1, at the electrode surface X will be depleted so that the surface concentration of X, c_X^s, will be less than the bulk concentration, c_X^b. Assuming steady state conditions at the electrode surface, the rate of consumption of X by electrochemical reaction must be balanced by the rate of transport of X to the surface. Thus, if diffusion is the only mechanism for mass transport of X at the surface,

$$\frac{\vec{j}}{nF} = -D_X \left(\frac{dc_o}{dx} \right)_s \tag{2.12}$$

It is apparent that the concentration gradient at the surface is dependent on the current density. At low current density, the concentration gradient will be small and the surface concentration will approach that of the bulk concentration. As the current density increases, the surface concentration of X will decrease so that the transport of X to the surface can balance the rate of reaction.

The minimum value for c_X^s is virtually zero, beyond which the current density cannot be increased further. The rate of reaction at the electrode is so fast that as soon as the species X reaches the surface, it immediately reacts such that the surface concentration is zero. This current maximum is called the mass transport limiting current density, j_L. The limiting current can be derived from equation 2.12 to yield the following, where δ is the mass transfer boundary layer.

$$\vec{j}_L = -\frac{nFD_X c_X}{\delta} \tag{2.13}$$

The concept of limiting current is important for electrochemical cell design. Many processes, particularly in metal recovery system where the reactant concentration is low, are operated under mass transport controlled conditions to ensure that the fractional conversion is high. In general, determination of mass transfer is important as it governs the maximum plating rate in a particular electrochemical system as well as influences the deposit uniformity and structure.

2.2 Electrocrystallisation of Metal

The term electrocrystallisation is used to describe the process which involved the formation of a new solid phase electrochemically. Examples of this process include reduction of ions from a solution, as in the case of cathodic deposition of metals, and the formation of anodic film by oxidation of metal ion in the solution. The mechanism of electrocrystallisation involves a number of distinct steps [2.2, 2.4], as illustrated schematically in figure 2.3. The steps in the overall process are:

1. Diffusion of metal ions through the solution to the electrode surface.
2. Reduction of a cation on the substrate surface.
3. Partial or complete loss of the hydration sheaths, resulting in formation of adatoms.
4. Surface diffusion or migration of adatoms to an energetically favourable site on the substrate surface.
5. Clustering of adatoms to form critical nuclei; a nucleus of sufficient size for it to be stable.
6. Incorporation of adatoms into a growing lattice.
7. Development of crystallographic and morphological characteristics of the deposit.

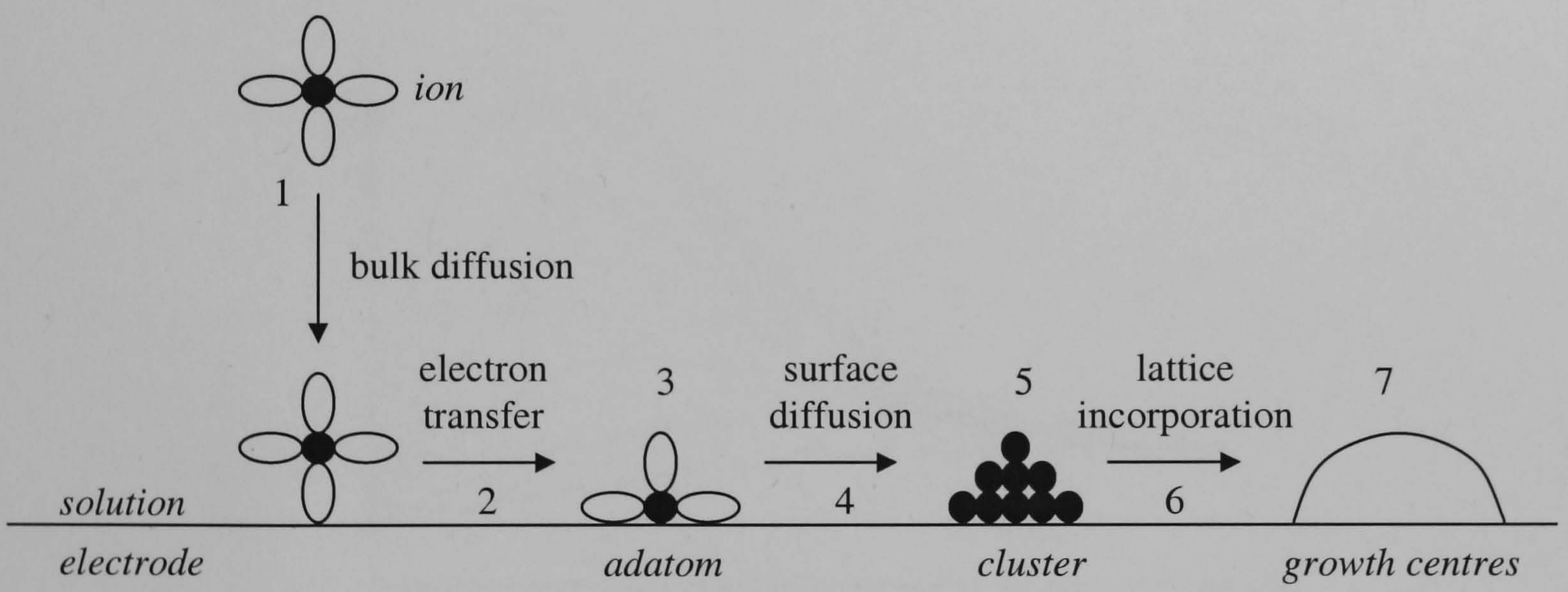

Figure 2.3: Steps involve in the electrocrystallisation of metal on a substrate.

Electrochemical techniques for studying the nucleation mechanism have been based on the observed response from current-potential-time relationships. The two most common methods are the current step and the potential step methods. The current step approach is mainly focused on the case of nucleation in dilute solutions where nuclei growth can be described in terms of pure diffusion control. The techniques

based on the analysis of potentiostatic current transient proved to be favourable as it can be applied over wide range of concentrations of electrodepositing species and provides direct control of the relevant thermodynamic parameters. They are experimentally simple and convenient because the determination of nucleation parameters is based exclusively on the information obtained from electrochemical measurements. In addition, microscopical information such as nuclei density and diameter can be obtained by direct counting from electron micrographs of the substrate surface.

A galvanostatic or potentiostatic plot obtained during the early stages of metal electrocrystallisation on a foreign substrate contains considerable information on the mechanism of nucleation. A typical set of transient is shown in figure 2.4 for potentiostatic technique.

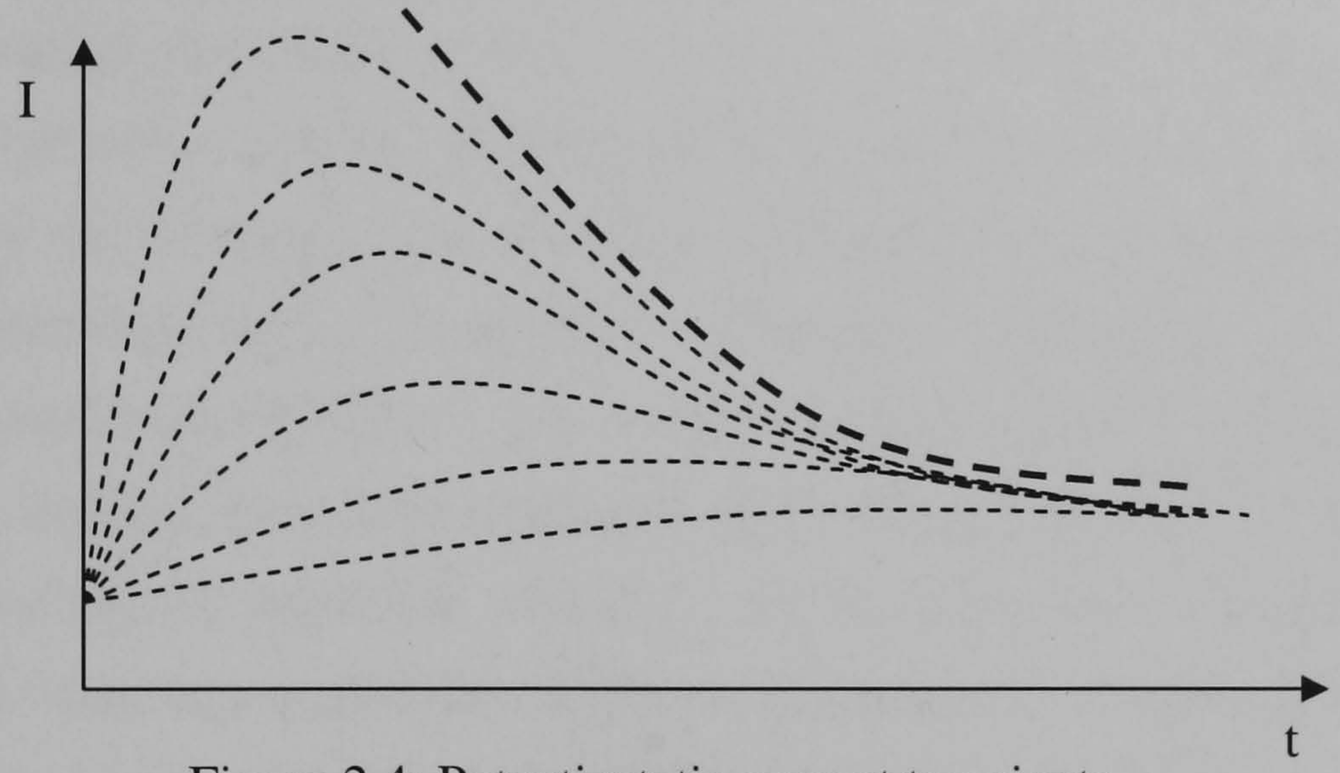

Figure 2.4: Potentiostatic current transients

The principal nature of the transient is the rising section corresponding to the nucleation process. During this stage, the electroactive area on the substrate surface increases due to the continuous formation of new nuclei as well as the increase in the size of existing nuclei [2.5-2.7]. The nuclei develop diffusion zones, and as the radii of each nuclei increases, this diffusion zones begin to overlap. This behaviour is responsible for the current maximum observed from the transient [2.5, 2.7, 2.8]. At

this point, the formation of new nuclei occurs on the metal being deposited rather than on the substrate, which leads to large particle aggregations. The height and position of the maximum increases with overpotential and the peaks become more pronounced at more cathodic overpotential. The clusters of nuclei continuously grow to form nuclei of a critical radius, which represents the minimum radius of stable nuclei. The current then gradually decrease due to the combined effect of the depletion of the diffusion layer as well as coagulation of nuclei. Thereafter, as more and more of the nuclei overlap to form "islands", the diffusion switches from quasi-spherical diffusion to semi-infinite planar diffusion. The current continues to drop until the entire surface is controlled by planar diffusion and natural convection effects take over. Theoretical concepts involved in characterising different stages of nucleation are described in more detail in section 2.3.

The formation of electrodeposits during electrodeposition is influenced by several factors such as the crystal structure and lattice orientation of the substrate, specific free surface energy and adhesion energy of the nuclei/substrate interface [2.9, 2.10]. The physical properties and the morphology of the deposits, however, are strongly influenced by the kinetics of the nucleation and growth, which depend on the deposition parameters such as overpotential, current and temperature as well as the solution composition and pH [2.11]. For example, during nucleation of particle under potentiostatic method, it has been observed that the potential applied to the electrode determines the rate of deposition and hence the structure of the deposit. At low overpotential, more time is available to form electrodeposits of perfectly crystalline structure, however, the low rate of electrodeposition does not compensate for using such low overpotentials. Generally it is best to apply a potential corresponding to the formation of polycrystalline deposits. Figure 2.5 shows the variation of electrodeposits structure with applied potential. Several aspects of studies which contribute to different nucleation characteristics and deposit morphology will be presented in chapters 6 and 7.

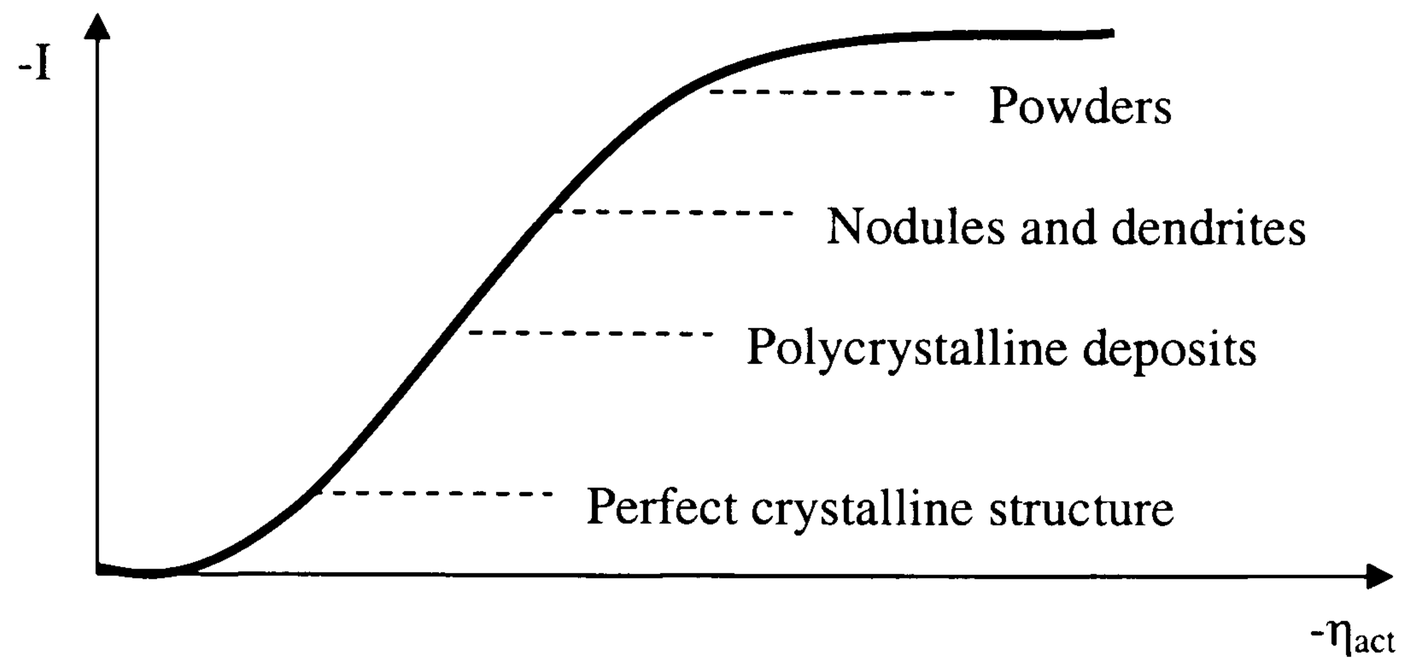

Figure 2.5: Variation of electrodeposits structure with applied potential.

2.3 Mechanism of Crystal Growth and Nucleation on Foreign Substrate

2.3.1 Geometries of Growth Centres

Equations describing two- or three-dimensional nucleation and crystal growth process occurring on a foreign substrate under potentiostatic conditions have been discussed extensively [2.2, 2.8, 2.12]. Several models have been developed for different shapes of growth centres. In many studies of the deposition of metals, the nucleation process is described in terms of localized hemispherical nucleus, where detailed examination has been given by Bosco and Rangarajan for the deposition of lead dioxide on platinum [2.13]. This growth model is particularly of interest since they are characterised by a maxima in the approach to the final current density. The transients then can be analysed in a more convenient form by using the coordinates of the maxima to obtain expressions in terms of reduced variable, $\frac{I}{I_m}$ and $\frac{t}{t_m}$, where I_m is the maximum current and t_m is the time corresponding to the maximum current.

Other geometries have also been considered using a similar approach. Abyaneh and Fleischmann have proposed an alternative model for right circular cone growth centres by considering the death and rebirth of the cone shaped centres for the case of

nickel deposition onto carbon substrate [2.14]. More recently, Li and Lasia have demonstrated the development of two-dimensional cylindrical growth model [2.15]. Figure 2.6 shows several geometries for three-dimensional growth discussed in this section. In our work, we focus only on hemispherical growth centres.

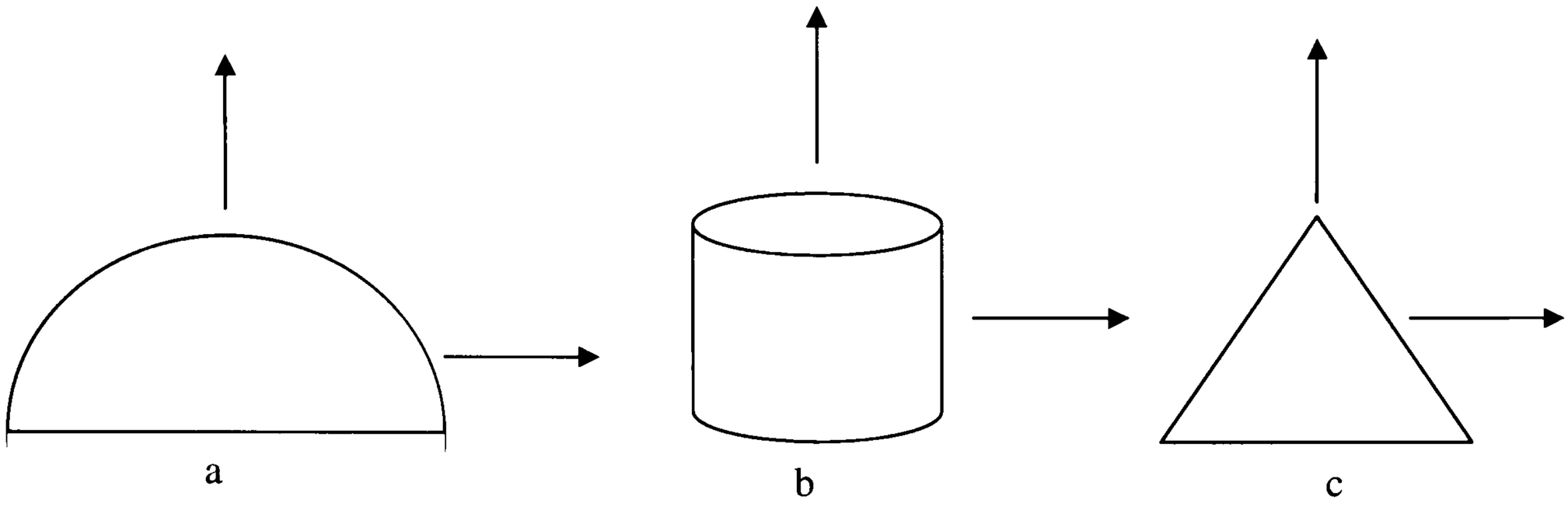

Figure 2.6: Several geometries for three-dimensional growth centres: (a) hemispherical (b) cylindrical (c) right circular cones.

2.3.2 Thermodynamic Driving Force

For a crystal to grow, some driving force is required. In the case of electrochemical reaction, the driving force transporting ionic material to the substrate is an applied electric field. Since the conditions in the system change according to the thermodynamics, the free energy of the whole system will decrease at the application of an electric field. This means that any decrease in free energy associated with the crystallisation process works to promote the growth of crystals [2.16].

The overall Gibbs' free energy associated with the formation of a new phase can be expressed in two parts; the surface free energy, $\Delta G_{surface}$, and the bulk free energy, ΔG_{bulk} [2.2, 2.17]. $\Delta G_{surface}$ is the energy required to form the surface and is compensated by the energy released by the formation of a new phase. Therefore, $\Delta G_{surface}$ is a positive quantity, the magnitude of which is proportional to r^2 and ΔG_{bulk} is a negative quantity proportional to r^3. These two parts are given by

$$\Delta G_{surface} = 4\pi r^2 \gamma \tag{2.14}$$

$$\Delta G_{bulk} = -\frac{4}{3}\pi r^3 \Delta G_V \tag{2.15}$$

where ΔG_V is the free energy of formation per unit volume and is given by

$$\Delta G_V = \frac{nF\rho\eta_{act}}{M} \tag{2.16}$$

The total free energy, ΔG_{net}, for a spherical nucleus resting on an electrode surface is therefore given by

$$\Delta G_{net} = \Delta G_{surface} + \Delta G_{bulk} \tag{2.17 a}$$

$$\Delta G_{net} = 4\pi r^2 \gamma - \frac{4\pi r^3 \rho n F \eta_{act}}{3M} \tag{2.17 b}$$

It is apparent that the total free energy depends on the size of nucleus, r, and the activation overpotential, η_{act}. Figure 2.7 shows the schematic illustration of the free energy curves for homogeneous nucleation and growth. The free energy curve will passes through a maximum value, ΔG_c, which corresponds to the critical nucleus, r_c, beyond which the ΔG of the crystal formation is negative and therefore, favoured thermodynamically. Differentiation of equation 2.17 b with respect to r gives the expression for the maximum in the free energy curve

$$\Delta G_c = \frac{16\pi M^2 \gamma^3}{3\pi\rho^2 n^2 F^2 \eta_{act}^{\ 2}} \tag{2.18}$$

and

$$r_c = \frac{-2M}{nF\eta_{act}} \tag{2.19}$$

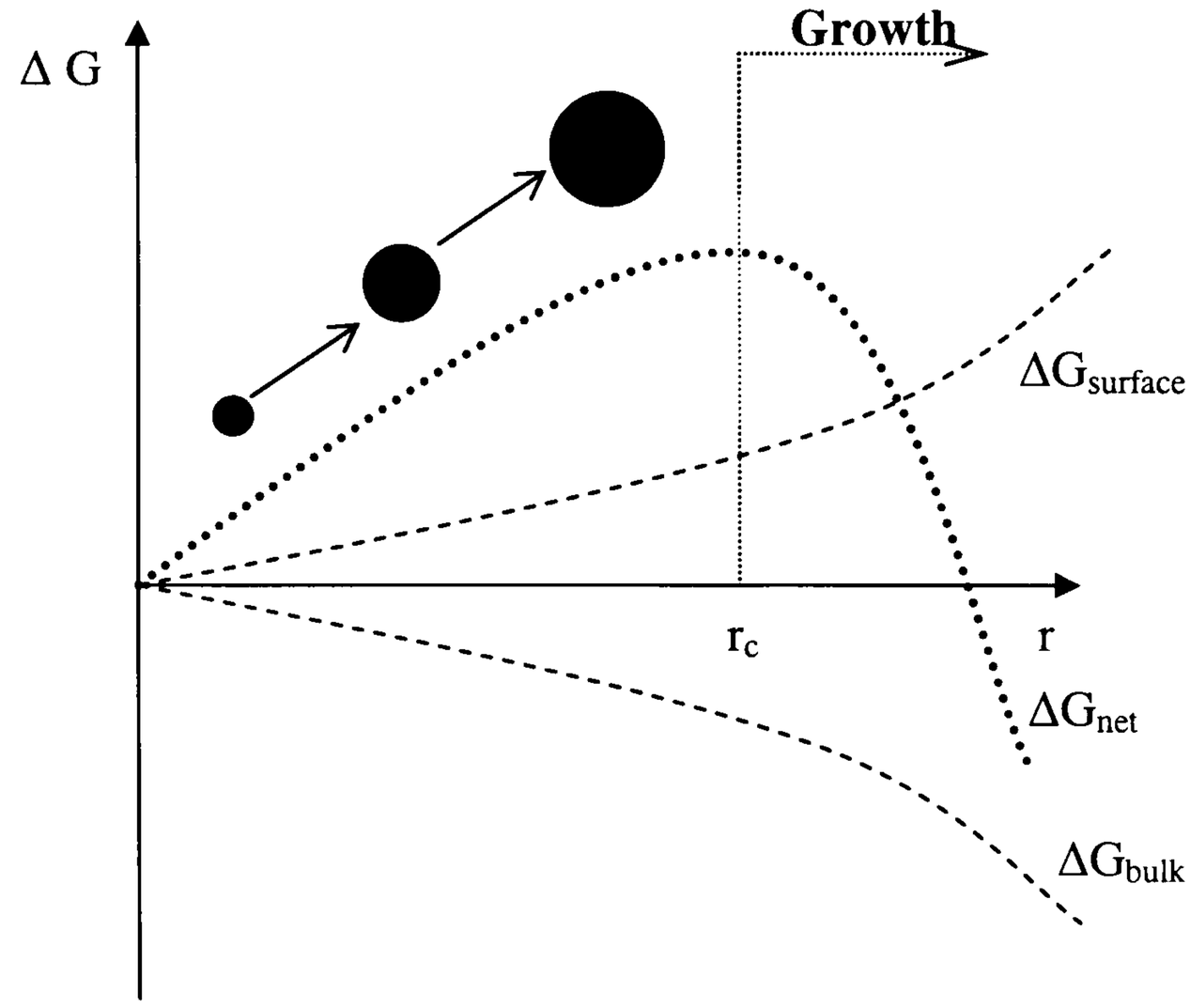

Figure 2.7: Schematic illustration of the free energy curves for homogeneous nucleation and growth

The behaviour of a newly created nuclei or crystal depends on its size; it can either grow or redissolve into the solution, but the process of which it undergoes should result in the decrease in the free energy of the particle [2.17]. The critical size, r_c, therefore represents the minimum size of a stable nuclei. Particles smaller than r_c will dissolve back into the liquid phase and particles larger than r_c will continue to grow. Therefore, for nuclei to evolve into a stable entity, its radius must exceed r_c. However, the free energy curve does not explain how the amount of energy necessary to form stable nuclei is produced. Although the energy of a fluid system at constant temperature and pressure is constant, this does not mean that the energy level is the same in all parts of the fluid. There will be statistical distribution of energy in the molecules constituting the system, and in those regions where the energy level rises temporarily to a high value, the nucleation will take place.

2.3.3 Mechanism of Crystal Growth

As soon as stable nuclei, nuclei larger than the critical size, have been created, they will grow readily unless the deposition conditions, such as the overpotential, are changed. The growth of nuclei may be either two-dimensional, where only a monolayer of nuclei can be deposited without further nucleation, or three-dimensional, where thick layers are formed continuously. A detailed understanding of the mechanisms involved in growth of nuclei is necessary for any attempts to specify the stability conditions. The stages involves in the process of crystal growth are illustrated in figure 2.8.

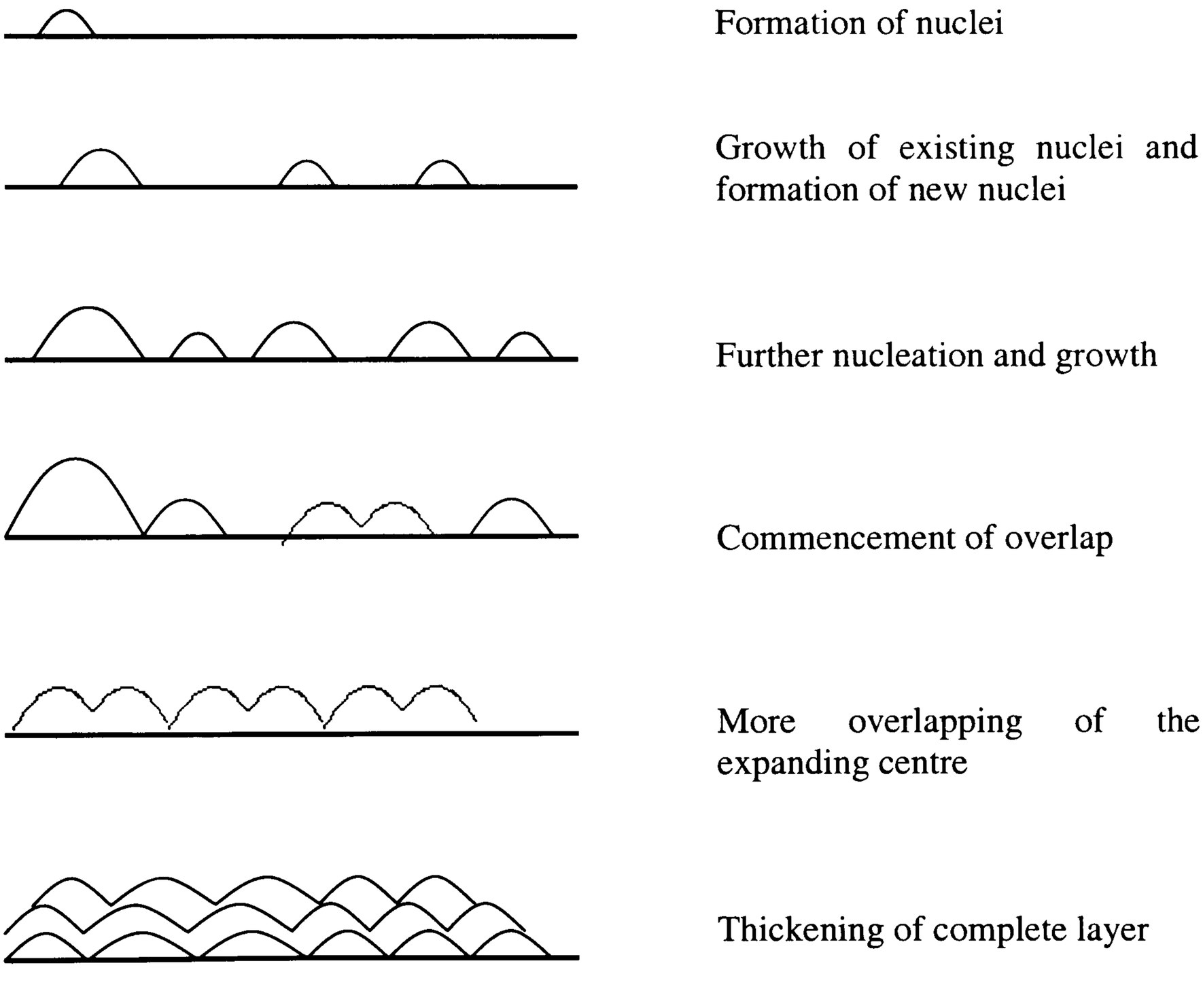

Figure 2.8: Stages involve in crystal growth

Once nuclei are formed on the substrate surface, each isolated centre of the nuclei will grow. At the same time, the appearances of new growth centres are continuously occurring. The cathode surface then reaches a stage where it is covered by a large number of growing centres and the current is the sum of the currents at all the centres. As the individual nuclei grow, they eventually become aware of the existence of the surrounding nuclei. Initially, there will be interference between neighbouring diffusion fields and then there will be physical overlap of the growing centres. The centres will no longer grow at the expected rate at the current will increase less rapidly than previously. The treatments of the overlap problem based on the Avrami theorem will be discuss in section 2.3.6. Once overlap of growing centres has occurred over the whole surface, the layer will thicken as deposition continues over the total area of the substrate surface. When a complete layer is formed, the current will eventually reach a plateau which signifies that the thickening of the electrodeposited layer is diffusion controlled.

Crystals are created when stable nuclei are formed and then growth. Several models or theories have been developed to describe the crystal growth mechanism from vapour or liquid phase systems which enable us to understand when the phase separation process takes place, how the crystal growth and the stability of the deposited crystals.

2.3.4 Limiting Cases Of Nucleation

The nucleation law N(t) generally follows Poisson distribution with the assumption that all sites on the substrate surface have uniform probability of being converted into nuclei [2.2, 2.5, 2.18]. The nucleation rate is defined as the rate of appearance of stable growth centres. It follows the first order kinetics and can be expressed as

$$\frac{dN(t)}{dt} = A[N_o - N(t)] \tag{2.20}$$

where N(t) is the nuclei density, t is time, A is the first order nucleation rate constant and N_o is the number of active sites on the substrate surface. A is known to be a function of overpotential, solution composition and the substrate surface free energy. Equation 2.20 can be integrated with N(t) = 0 and t = 0 to yield an expression for the nuclei density as a function of time

$$N(t) = N_o[1 - \exp(-At)] \tag{2.21}$$

Equation 2.21 gives two limiting cases. At large number of At, At » 1, which signifies an extreme situation of fast nucleation, equation 2.21 becomes

$$N(t) = N_o \tag{2.22}$$

The nucleation is instantaneous and the maximum number of nuclei, or the nuclei density, is formed immediately after the potential application. However, the size of each nuclei will continue to grow with time.

In the case where slow nucleation occurs, usually referred as progressive nucleation, the number density of nuclei that are formed on the surface is a function of time and the nuclei gradually grow and overlap. In this case, At « 1 and equation 2.21 reduces to

$$N(t) = N_o At \tag{2.23}$$

2.3.5 Formation of Single Nuclei

At the early stage of electrochemical nucleation, the nuclei are widely spaced, thus it is assume that each nucleus grows independently of each other [2.6, 2.18]. Under potentiostatic deposition, the deposition current at this stage can be described as

$$I(t) = \alpha t^{v} \tag{2.24}$$

It should be noted that this expression is valid only in the early stages of electrodeposition before the coalescence of nuclei and this is translated to the region well before the current maximum in the current-time transient such as in figure 2.3. The expressions for α and v are given in table 2.1 for different nucleation and growth mechanism. Equation 2.24 predicts that I (t) should be a linear function of t^{v}. At different overpotentials, the slopes of the plots will differ because each relates to a different value of N_o. N_o can be determined by substituting known values into the related equation from table 2.1. The values are then compared against the numbers obtained by manual calculation from the electron micrographs.

Growth	Shape of nuclei	Instantaneous		Progressive	
		v	α	v	α
Kinetically controlled	Cylinder	1	$\frac{2\pi nFMh}{\rho}N_o k^2$ (2.25 a)	2	$\frac{2\pi nFMh}{\rho}AN_o k^2$ (2.26 a)
	Hemisphere	2	$\frac{2\pi nFM^2}{\rho^2}N_o k^3$ (2.25 b)	3	$\frac{2\pi nFM^2}{3\rho^2}AN_o k^3$ (2.26 b)
Diffusion limited	Hemisphere planar diffusion	$\frac{1}{2}$	$\frac{8nFM^2c^3D^{3/2}}{\rho^2\pi^{1/2}}N_o$ (2.25 c)	$\frac{3}{2}$	$\frac{16nFM^2c^3D^{3/2}}{3\rho^2\pi^{1/2}}AN_o$ (2.26 c)
	Hemisphere spherical diffusion	$\frac{1}{2}$	$\frac{nF\pi M^{1/2}(2Dc)^{3/2}}{\rho^{1/2}}N_o$ (2.25 d)	$\frac{3}{2}$	$\frac{4nF\pi M^{1/2}(Dc)^{3/2}}{3\rho^{1/2}}AN_0$ (2.26 d)

Table 2.1: Expressions for v and α for various nucleation and growth mechanism.

2.3.6 Overlapping of Nuclei

After the initial stage, further growth of mature nuclei on the electrode surface cannot be considered entirely as independent of each other. This occurs when the diffusion zones around each nuclei begins to overlap with diffusion zones of neighbouring nuclei [2.5, 2.7], as shown in figure 2.9.

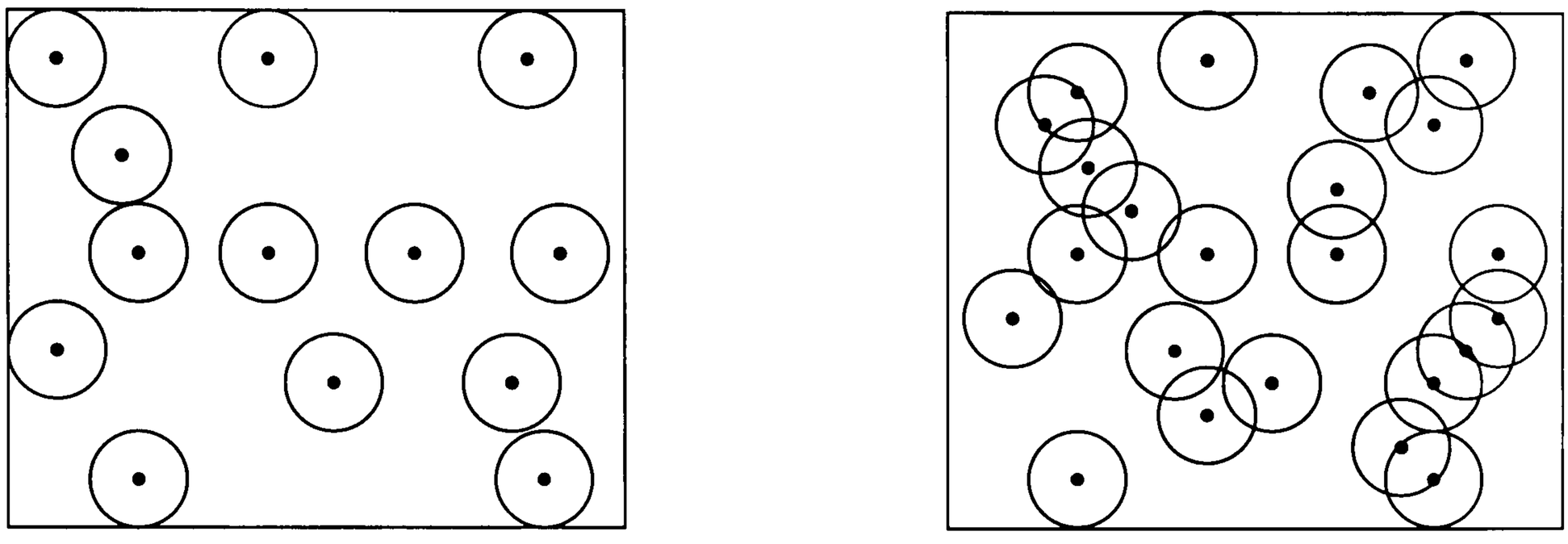

Figure 2.9: Schematic diagram of hemispherical nuclei, represent by the black dots, randomly distributed on the electrode surface. The surrounding circles represent their diffusion zones. (a) early stage of deposition before coalescence of nuclei (b) overlapping of nuclei

The theory of 3-dimensional overlap problem is described by the Avrami theorem [2.2, 2.5]. A concept of the extended area, S_{ex}, where S_{ex} is the area covered by the centres assuming that no overlapping of nuclei, is introduced. Because the centres are randomly distributed on the surface, the diffusion zone of each nuclei will eventually overlap and the area covered by the diffusion zones, S, can be related to S_{ex} by the expression given in equation 2.27. The concept of Avrami theorem is illustrated schematically in figure 2.10.

$$S = 1 - \exp(-S_{ex}) \tag{2.27}$$

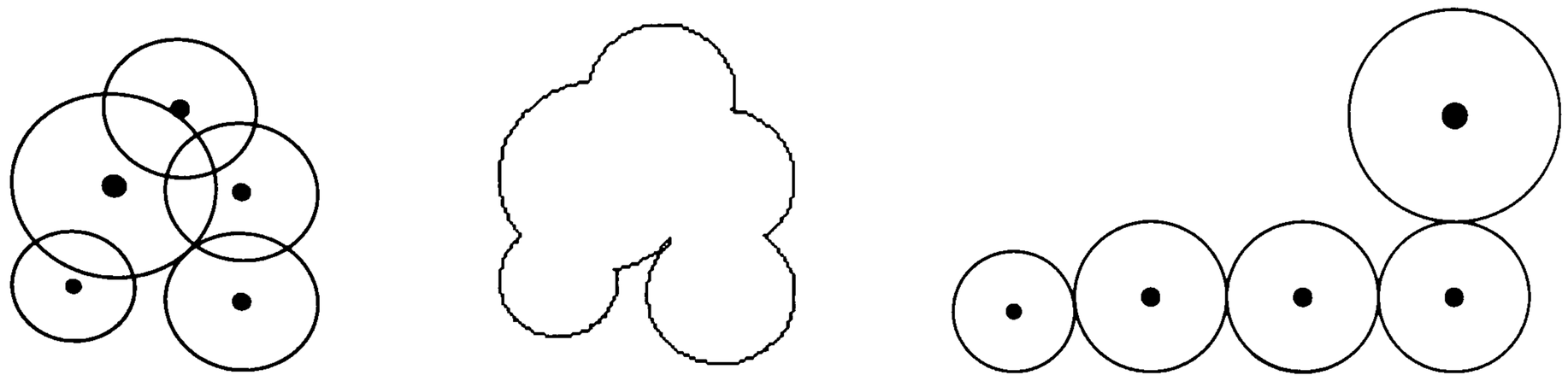

(a) (b) (c)

Figure 2.10: The Avrami theorem relates the true surface area, S, to the extended area, S_{ex}. (a) the overlapping nuclei (b) the true area (c) extended area.

Based on the law of conservation of mass, the amount of material entering the diffusion zones is equal to the amount being incorporated into the growing nuclei [2.7, 2.12]. In the model developed by Scharifker and Mostany, the mass balance is written as

$$nFDc\phi(t-u)^{1/2} = nFDc(\pi r_d^2)\frac{1}{[\pi D(t-u)]^{1/2}} \tag{2.28}$$

where $\phi = 2\pi(2MDc/\rho)^{1/2}$, u is the time at which the nuclei was born and r_d is the radius of a hemispherical nuclei that grows under diffusion control. Solving for the equivalent area, with

$$\frac{dN}{du} = AN_o \exp(-Au) \tag{2.29}$$

the extended area is calculated from

$$S_{ex} = \alpha\pi^{1/2} D_i^{1/2} AN_o \int_o^t (t-u)\exp(-Au)du \tag{2.30}$$

For the case of instantaneous nucleation, equation 2.30 can be solved to yield

$$S_{ex} = N_o \pi k' D_i t \tag{2.31}$$

For progressive nucleation, the number of nuclei increases linearly with time, therefore the area covered by diffusion zones is

$$S_{ex} = \frac{A N_o \pi k'' D_i t^2}{2} \tag{2.32}$$

The current density flowing to the whole electrode surface can be expressed as

$$I(t) = \frac{nFD^{1/2} c(1 - \exp(-S_{ex}))}{\pi^{1/2} t^{1/2}} \tag{2.33}$$

Substituting equation 2.31 into equation 2.33, we obtain the expression for current density for the case of instantaneous nucleation

$$I(t) = \frac{zFD^{1/2} c}{\pi^{1/2} t^{1/2}} \left[1 - \exp\left(-N_o \pi k' D t\right)\right] \tag{2.34 a}$$

with k' is defined as

$$k' = \left(\frac{8\pi c M}{\rho}\right)^{1/2} \tag{2.34 b}$$

On the other hand, if nucleation is progressive, the current density is

$$I(t) = \frac{nFD^{1/2} c}{\pi^{1/2} t^{1/2}} \left[1 - \exp\left(\frac{-A\pi k'' D t^2}{2}\right)\right] \tag{2.35 a}$$

where k'' is

$$k''=\frac{4}{3}\left(\frac{8\pi cM}{\rho}\right)^{1/2} \qquad (2.35\ b)$$

Thus, equations (2.34 a) and (2.35 a) can be used to described the nucleation mechanism of overlapping nuclei under instantaneous or progressive nucleation. In each case, the current passes through the maximum before it falls and approaches the limiting diffusion current. The current, I_m, and the time, t_m, corresponding to the maximum in each transient are given in table 2.2 for instantaneous and progressive nucleation [2.7, 2.19]. The transient then can be presented in a dimensionless form by plotting I^2/I_m^2 vs. $(t/t_m)^{-1}$ and compared against the theoretical plot of instantaneous and progressive nucleation.

Instantaneous nucleation	**Progressive nucleation**
$t_m=\frac{1.2564}{N\pi k'D}$ (2.36 a)	$t_m=\left(\frac{4.6733}{AN_\infty\pi k''D}\right)^{1/2}$ (2.37 a)
$I_m=0.6382\,nFD\left(k'N\right)^{1/2}$ (2.36 b)	$I_m=0.4615\,nFD^{3/4}c\left(k''AN_\infty\right)^{1/4}$ (2.37 b)
$I_m^2t_m=0.1629(nFc)^2D$ (2.36 c)	$I_m^2t_m=0.2598(nFc)^2D$ (2.37 c)
$\frac{I^2}{I_m^2}=\frac{1.9542}{t/t_m}\left\{1-\exp\left[-1.2564\left(t/t_m\right)\right]\right\}^2$ (2.36 d)	$\frac{I^2}{I_m^2}=\frac{1.2254}{t/t_m}\left\{1-\exp\left[-2.3367\left(t/t_m\right)^2\right]\right\}^2$ (2.37 d)

Table 2.2: Expressions for analysis of current maxima, I_m, and time maxima, t_m.

2.3.7 Dendritic Morphology

2.3.7.1 Dendritic Growth

In the growing field of nanoscience, the properties of nanocrystals, such as catalytic activity, are known to strongly depend not only on their composition, but also their structure, phase, shape and size distribution [2.20]. Therefore the understanding of different particle morphologies is significantly important and could be critical for their applications, especially when it involves the formation of complex aggregates such as dendrite.

During the process of crystallisation, nucleated crystals may grow preferentially in certain directions causing a dendritic pattern to form on the substrate surface. Presence of impurities in the solution and rapid crystallisation from supersaturated solutions are some of the contributing factors for its occurrence [2.21, 2.22]. It was found that the crystalline dendrite has a considerably increased surface free energy compared to the equilibrium shape of the crystal and is therefore thermodynamically unstable compared with this equilibrium shape. The origin of the dendrite therefore results from the kinetics of crystal growth under the condition where coupling between the surface phenomena (charge transfer reactions or crystal growth process) and the bulk transport in fluid phase occur in the system [2.22]. Under this condition, the growing crystal will generate temperature or concentration distribution along the solid/liquid interface, which influences the growth rate, shape and perfection of the crystals.

The formation of dendrites has been studied extensively with much of the interest is centred on the nature and morphology of the deposited metal [2.23-2.26]. Studies have shown that a large number of variables are involved in the growth mode of irregular topographies such as dendrites [2.23]. For example, the strength of electrolyte flow rate may significantly affect the growth velocity of the dendrite tips. It has also been found that the formations of dendritic branches were strongly

affected by the flow configuration. The formation of dendrites was also favoured at large applied potentials and high concentrations of electrolyte.

As stated above, the rapid growth of dendrite on substrate surface is depending on electrolyte composition, applied potential as well as hydrodynamics conditions. The dependence on hydrodynamics conditions signifies that the mass transport mechanism plays an important role in determining the final morphology of electrodeposits [2.23, 2.27, 2.28]. When current is supplied to the cell, the cations start to drift towards the cathode. When the cations reach the cathode, they are quickly reduced and plate out as metal. This results in a region in close vicinity to the cathode in which the ion concentration is lower than the bulk. As the concentration gradient becomes stronger, the diffusive transport of ions becomes higher. As a result, the perturbation on the cathode will grow, leading to the development of rough growth. The transport of cations becomes diffusion limited when the concentration of ions at the cathode becomes zero. After a while, an instability developed, triggering the formation of branches and tips splitting.

The diffusion limited aggregation (DLA) model has been widely used to explain and analyse the formation of dendrite. The DLA model was first introduced by Witten and Sander in 1981 [2.29]. It has attracted much attention because of the variety of growth shape that it can produce using Monte-Carlo simulation. The DLA model considers the growth of an aggregate by random walk of a particle on a lattice containing a seed. The particle was released at a point distant from the cluster and walks randomly until it found a site adjacent to the seed. The mobile particle then irreversibly sticks to the seed and becomes part of the cluster. As successive mobile particles repeat this process, the fractal aggregates are produced. Witten and Sander also showed that the exposed ends of the clusters tend to grow more rapidly than other perimeter sites.

2.3.7.2 Electrochemical Deposition of Dendrite

Electrochemical deposition was introduced to the field of pattern formation as a means of producing a wide range of morphologies including the dendrites. The growth of dendrites by electrochemical deposition is an interesting and complex example of non-equilibrium growth. Various studies on dendritic morphology produced by electrochemical metal deposition have been carried out; among the examples are silver, zinc and tin.

Qiu *et. al.* have studied the synthesis of silver dendritic nanostructured via an electroless metal deposition method from $AgNO_3$ solution [2.24]. They considered the synchronous growth of silver dendrites within the framework of the DLA model, in which the cluster was formed by the adhesion of a particle with a random path to a selected seed on contact and allows the particle to diffuse and stick to the growing structure. During the initial stage where the concentrations of the silver salt and the reduction agent, HF, are high, the mechanism of deposition of silver nanoclusters follows reduction-nucleation-growth at a lot of positions to form a chainlike network. With prolonging of the reaction duration, the concentrations of the silver salt and the reduction agent greatly decreased, the growth is mainly driven by decreasing surface energy, and thus the dendritic silver nanostructures are formed.

Carro *et. al.* examined the dependence of the growth mode of silver electrodeposits on the dominant mass transport mechanism [2.23]. They observed several transitions in the growth mode of silver electrodeposits and one of these transitions was related to the initiation of dendrite formation. The dendrite appeared when a critical amount of electrodeposited silver had been exceeded. They observed the initiation of dendrite at borders and angles of the hexagonal silver crystals formed initially when the average size of these crystals is smaller than the thickness of the diffusion layer around the working electrode.

Wang *et. al.* have studied the morphology of zinc deposits from alkaline zincate solutions under various deposition conditions [2.25]. They concluded that the

dendrite initiation and growth was observed only under diffusion control and not under activation control. At higher current density, the concentration gradient becomes significant and a mixed control of diffusion and activation was found. Under this condition, there was competition between the growth direction of the diffusion field and lateral layer growth. After further increase of the current density to the point when the concentration gradient is dominant, pure diffusion control takes place and deposits grow in the diffusion direction perpendicular to the electrode surface. This controlling factor forms the dominant dendritic shape of zinc. They also found out that lead, bismuth and indium are among the additives that suppress the formation of dendrites.

Devers *et. al.* studied the electrodeposition operating conditions for the preparation of dendritic tin nanoaggregates composed of small grains of the size 50-100 nm [2.26]. At low current density, a uniform carpet of very small tin grains was observed coating the substrate surface. In the high current regime, the deposit shows a very rapid growth. It was found that the formation of dendritic tin aggregates was preceded by the formation of smaller tin grains. Therefore, the coating texture is said to be bi-model, it is a dendrite with grains of the order of 0.1 μm, which is covering a uniform deposit of grains 5-10 nm thick.

2.3.7.3 Formation of Dendrite

The dendrites are formed from a nucleus or a 'centre of crystallisation' [2.30-2.32]. The nucleus is composed of a small unit of atom oriented into a crystal pattern and each nucleus has a potential to grow. The nucleus will proceed to send out radial arms. From these primary arms, secondary and tertiary axes begin to sprout at angles determined by the crystal structure. This is repeated until the dendritic patterns are formed on the surface.

These dendrites developed by the addition of nuclei onto its branches. The arms will grow outward and thicken as the deposition time increased. They continue to grow until its outer arms begin to make contact with those of neighbouring dendrites which

have been developing independently at the same time. This contact acts as a boundary of the grain. When contact has taken place, growth outwards is impossible, therefore further growth results in thickening of the existing dendrite arms. At the end of the dendritic growth, the crystal gradually fills up the spaces between the dendrite arms. The dendrite growth of crystals is illustrated in figure 2.11.

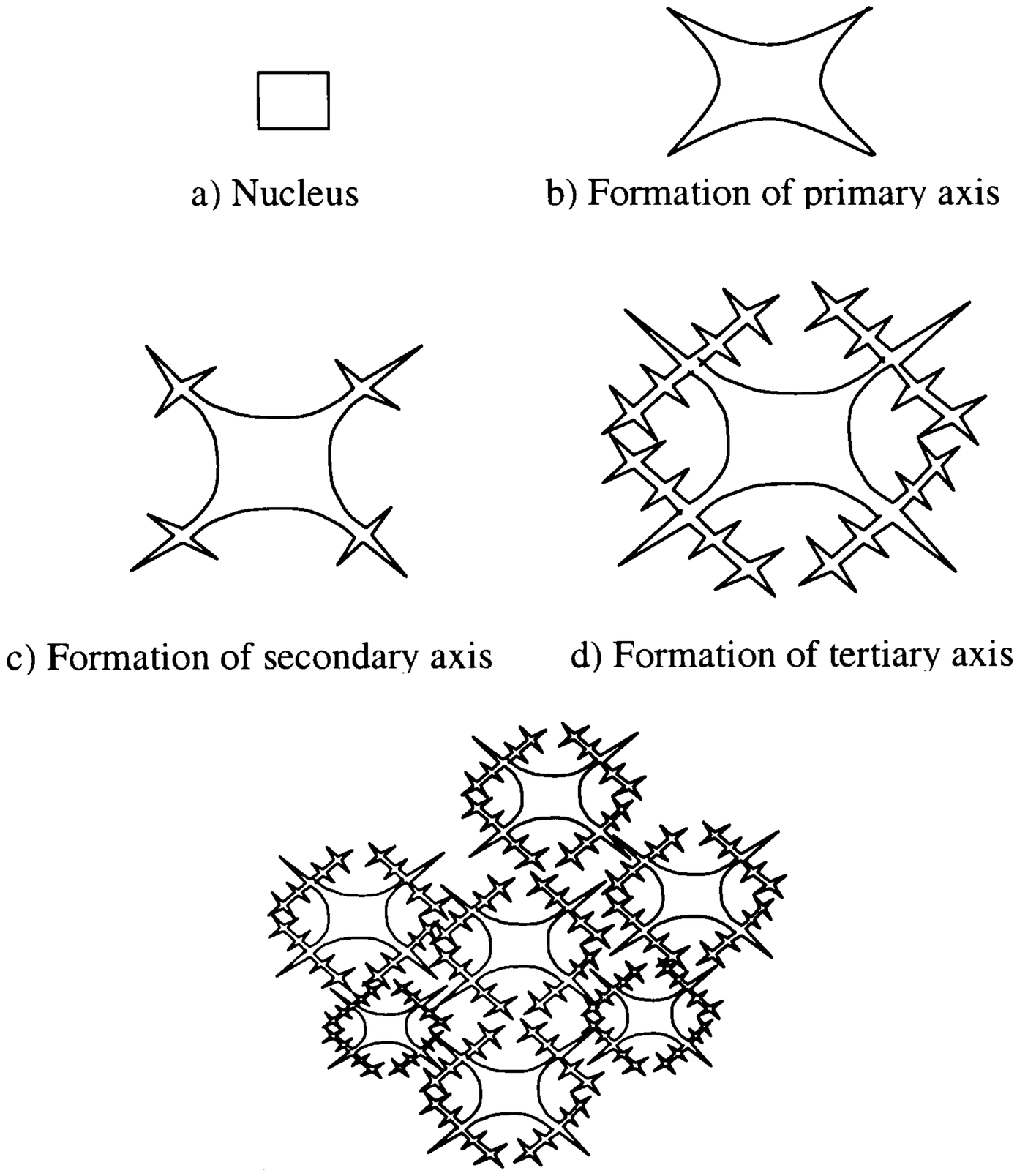

Figure 2.11: Formation of Dendritic Growth

2.4 References

2.1. F. Walsh, *A First Course in Electrochemical Engineering*, The Electrochemical Consultancy Ltd. (1993).

2.2. D. Pletcher, R. Greef, R. Peat, L. M. Peter and J. Robinson, *Instrumental Methods in Electrochemistry*, Horwood Publishing Ltd. (1985).

2.3. B. R. Horrocks, Lecture notes on 'Kinetics of Electrochemical System'. Spring School on Development of Electrochemical Process (2004).

2.4 L. Uziel, Y. Earnest and D. Kortan, *Electrochemistry in Industry: New Directions*, Plenum Press New York (1982).

2.5. R. Varma and J. R. Selman, *Techniques for Characterisation of Electrodes and Electrochemical Process*, John Wiley and Sons (1991).

2.6. G. A. Gunawardena, G. J. Hills and I. Montenegro, *Electrochim. Acta*, **23**, 693 (1978).

2.7. B. Scharifker and G. Hills, *Electrochim. Acta*, **28**, 879 (1983).

2.8 G. Gunawardena, G. Hills, I. Montenegro and B. Scharifker, *J. Electroanal. Chem.*, **138**, 225 (1982).

2.9 R. E. Panzer and P. J. Elving, *Electrochim. Acta*, **20**, 635 (1975).

2.10. H. S. Nalwa, *Handbook of Thin Film Materials: Deposition and Processing of Thin Films*, Academic Press (2002).

2.11 D. Bera, S. C. Kuiry and S. Seal, *JOM Online: Overview on Nanoscale Surfaces*, January 2004.

2.12. B. Scharifker and J. Mostany, *J. Electroanal. Chem.*, **177**, 13 (1984).

2.13. E. Bosco and S. K. Rangarajan, *J. Electroanal. Chem.*, **134**, 213 (1985).

2.14. M. Y. Abyaneh and M. Fleischmann, *J. Electroanal. Chem.*, **119**, 187 (1981).

2.15 Y. G. Li and A. Lasia, *J. Electrochem. Soc.*, **144**, 1979 (1997).

2.16 B. Byrappa, *Crystal Growth Technology*, William Andrew Publishing (2003).

2.17 J. W. Mullin, *Crystallisation (2nd Edition)*, Butterworth and Co. Publishers (1972).

2.18 P. Allongue and E. Souteyrand, *J. Electroanal. Chem.*, **286**, 217 (1990).

2.19 A. J. Bard, *Electroanalytical Chemistry*, Vol. 5, Marcel and Dekker, Inc., New York (1971).

2.20 Z. Kang, E. Wang, S. Lian, B. Mao, L. Chen and L. Xu, *Mater. Lett.*, **59**, 2289 (2005).

2.21 W. Bardsley, D. T. J. Hurle and J. B. Mullin, *Crystal Growth: A Tutorial Approach*, North–Holland Publishing Company (1979).

2.22 B. R. Pamplin, *Crystal Growth*, Pergamon Press Limited (1975).

2.23 P. Carro, S. Ambrosolio, S. L. Marchinao, A. Hernandez Creus, R. C. Salvarezza and A. J. Arvia, *J. Electroanal. Chem.*, **396**, 183 (1995).

2.24 T. Qiu, X. L. Wu, Y. F. Mei, P. K. Chu and G. G. Siu, *Appl. Phys. A*, **81**, 669 (2005).

2.25 R. Y. Wang, D. W. Kirk and G. X. Zhang, *J. Electrochem. Soc.*, **153** C357 (2006).

2.26 T. Devers, I. Kante, L. Allam and V. Fleury, J. Non-Cryst. Solids, **321**, 73 (2003).

2.27 J. R. de Bruyn, *Phys. Rev. E*, **56**, 3326 (1997).

2.28 G. Marshall, E. Mocskos, G. Gonzalez, S. Dengra, F. V. Molina and C. Iemmi, *Electrochim. Acta*, **51**, 3058 (2006).

2.29 T. A. Written and L. M. Sander, *Phys. Rev. Lett.*, **47**, 1400 (1981).

2.30 I. Tarjan and M. Matrai, *Laboratory Manual on Crystal Growth*, Akademiai Kiado, Budapest (1972).

2.31 E. C. Rollason, *Metallurgy for Engineers*, Edward Arnold UK (1973).

2.32 R. A. Higgins, *Engineering Metallurgy*: Applied Physical Metallurgy, Edward Arnold UK (1993).

CHAPTER 3:

DESIGN CONSIDERATIONS OF ELECTROCHEMICAL REACTOR

3.1 Electrochemical Reactor Design for Metal Ion Removal

3.1.1 Important Factors in Reactor Performance

Electrochemical techniques are used in a wide range of applications due to its advantages over other available techniques [3.1, 3.2]. Among the applications that received major attention is metal ion recovery from industrial effluents. For this application, some of the essential features required in the process of reactor design are listed in table 3.1.

• reactor type and configuration
• high surface area electrode, A_e
• high mass transport to electrode, k_m
• uniform current density distribution
• low potential drop across the electrode
• simplicity of electrode design, installation and maintenance
• moderate costs

Table 3.1: The essential features required in designing electrochemical reactor for metal ion recovery process.

It is crucial to design an electrochemical reactor for a specific process in order to achieve high conversion of reactant to product or, in the case of metal ion removal, high rate of concentration decreased as well as high current efficiency for the desired reaction. Adequate attention must be paid in selecting the type of reactor, the flow configuration, the mode of operation and design equations when designing electrochemical reactors for metal recovery process.

3.1.2 Reactor Types

There are three ideal reactor types; batch reactor (BR), continuous stirred tank reactor (CSTR) and plug flow reactor (PFR). Schematic representations of the three reactor types are presented in figure 3.1.

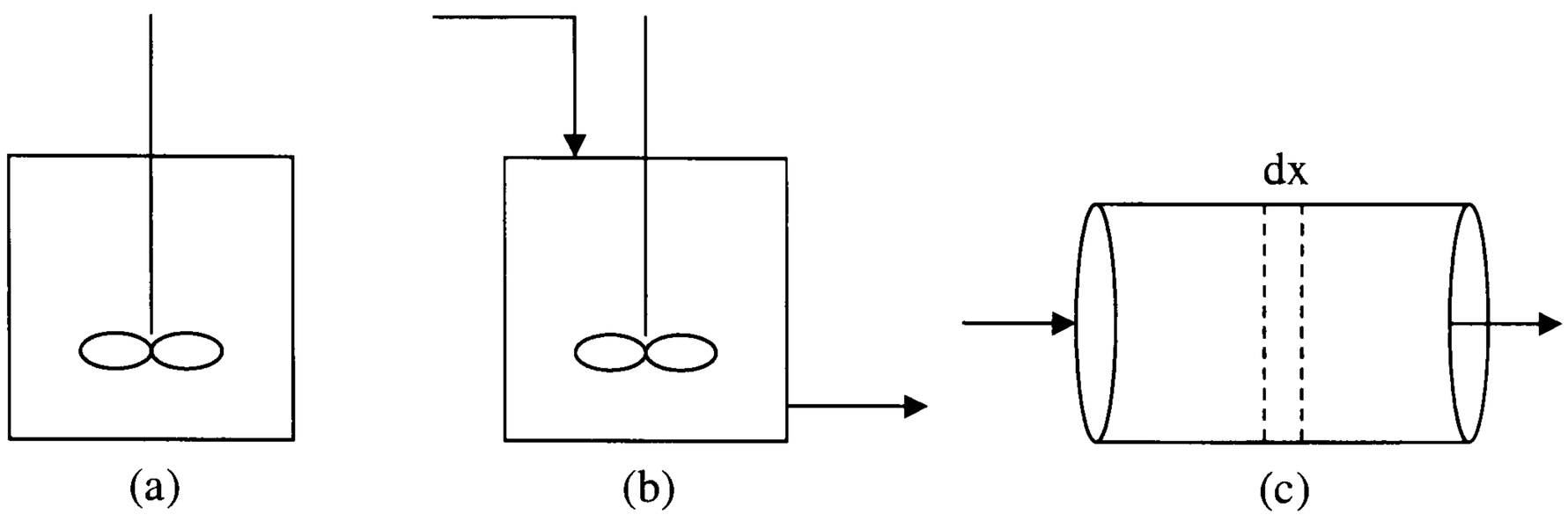

Figure 3.1: Reactor types (a) batch reactor (b) continuous stirred tank reactor (c) plug flow reactor.

In a continuous stirred tank reactor (CSTR), the electrolyte is perfectly stirred so that the concentrations of reactants and products are uniform throughout the reactor. The significant feature of CSTR is that the operating parameters are time and space dependent, therefore operations at constant current or potential will result in similar outcomes [3.3]. The plug flow reactor (PFR) operates under steady state condition and there is no mixing along the direction of electrolyte flow. The reactor concentration therefore is a function of the distance into the reactor from the inlet end [3.3]. Among the three reactors, batch reactor system is commonly employed in metal deposition or recovery process as they enable performance data to be evaluated as a function of reactant concentration or conversion [3.4]. Furthermore, batch reactors are useful when the inlet metal ion concentration is variable and are the most economical way to operate small units of production.

The simple batch reactor often presents design problems associated with the non-uniform distribution of reaction within the electrolyte [3.4]. To overcome this,

recirculating batch flow systems are often used, in which the electrolyte circulates from a vessel through the reactor. In this way, high mass transfer rates can be attained in reactors with low interelectrode spaces. The schematic diagram of a recirculating batch flow reactor is presented in figure 3.2.

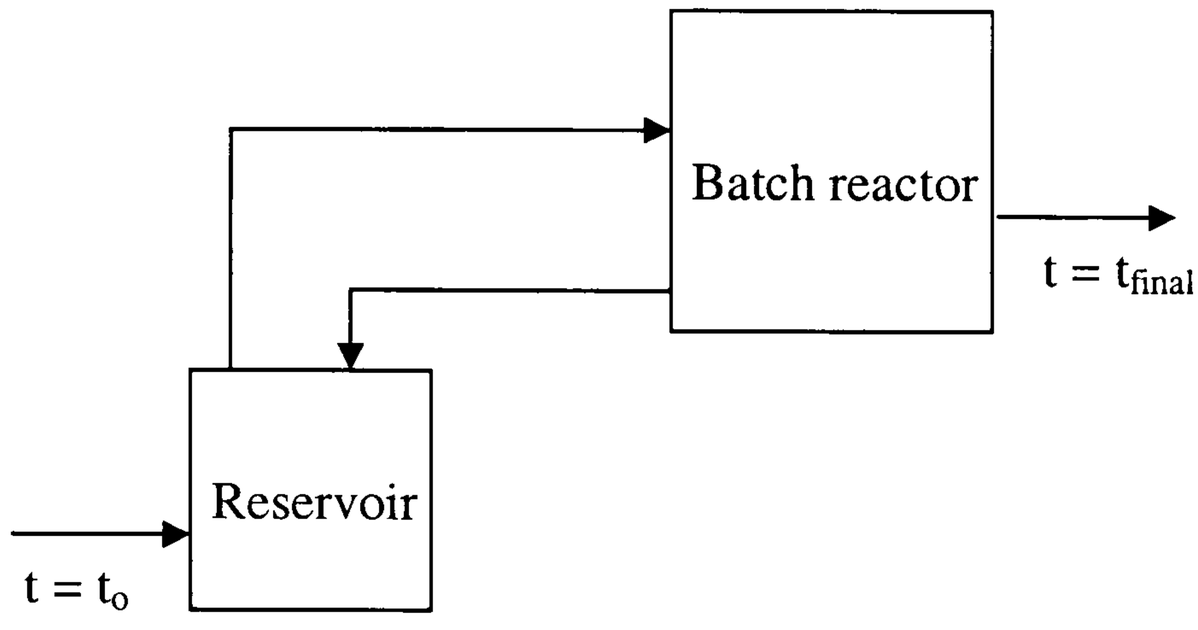

Figure 3.2: Schematic diagram of a recirculating batch flow reactor.

3.1.3 Reactor Configuration

Studies have shown that flowing a solution through porous electrode possesses inherent advantages over non-porous electrodes with flowing solution or porous electrodes without flow. By flowing a solution through a porous electrode, the mass transport limitations could be diminished. Kalnoki-Kis and Brodd have demonstrated that the current increases by factors of 10^2 to 10^4 at a given overpotential in a porous flow-through electrode [3.7].

There are two possible reactor configurations for porous electrodes; flow-through and flow-by configurations [3.5]. In flow-through configuration, the current flow is parallel to electrolyte flow. Although this configuration is preferred for laboratory scale studies, it is often associated with large potential drop occurring within the electrode matrix. Therefore, in our analysis, flow-by configuration is employed in which the current flow perpendicular to the electrolyte flow. With this arrangement,

high fractional conversion is achievable and the reactor can be easily scale-up by increasing the electrode width and length or by duplicating the electrode modules. Figure 3.3 illustrates the two types of flow configurations.

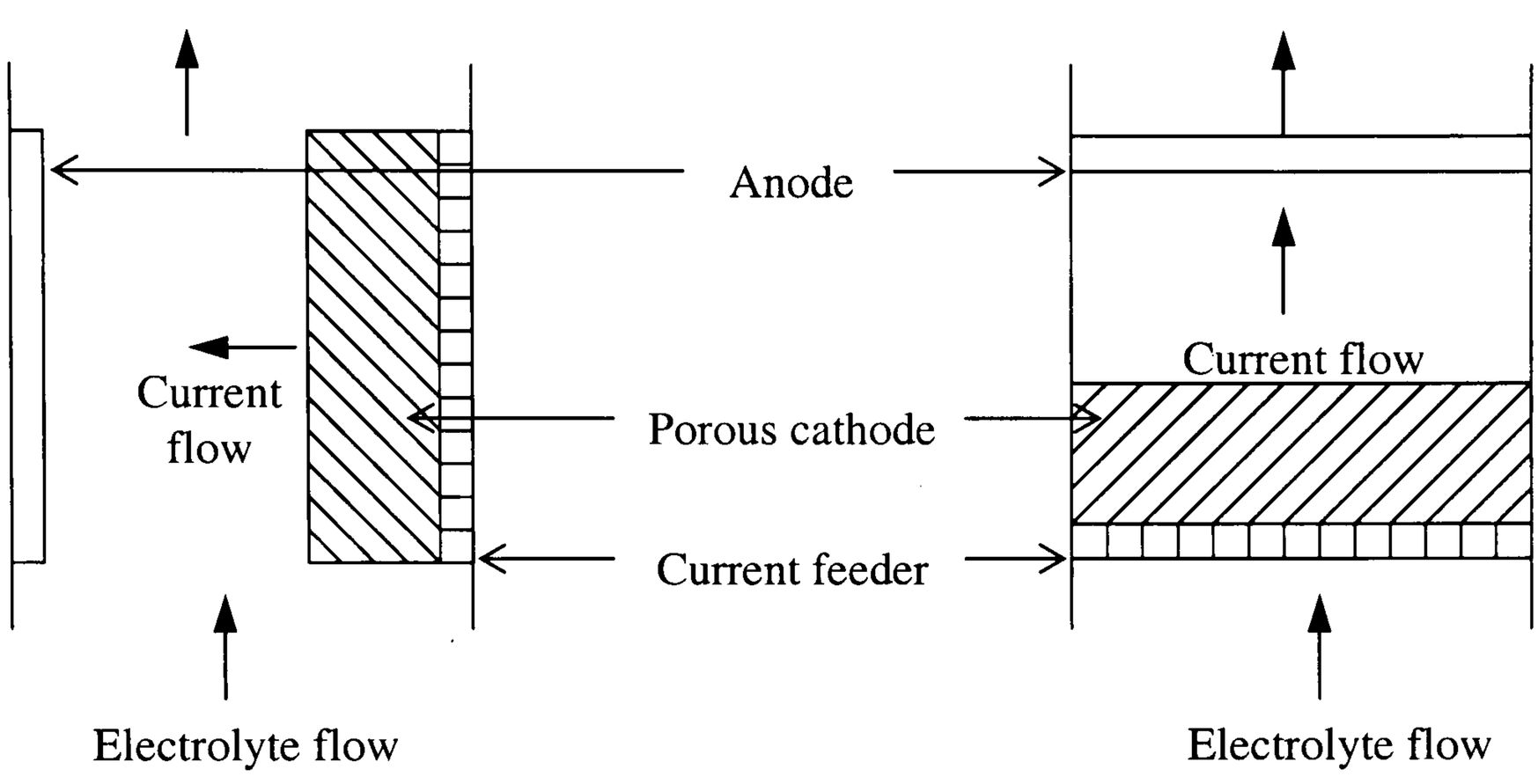

Figure 3.3: Cell configurations: (a) flow-by (b) flow-through.

3.1.4 Mass Transport Characteristics at a Flow-by Porous Electrode

For a two-dimensional electrode, the limiting current is given by

$$I_L = \frac{AnFD_o c_o}{\delta} \tag{3.1}$$

δ is defined as the Nernst diffusion layer thickness which describes the concentration profile near the electrode surface in an agitated solution or in the presence of natural convection, as shown in figure 3.4.

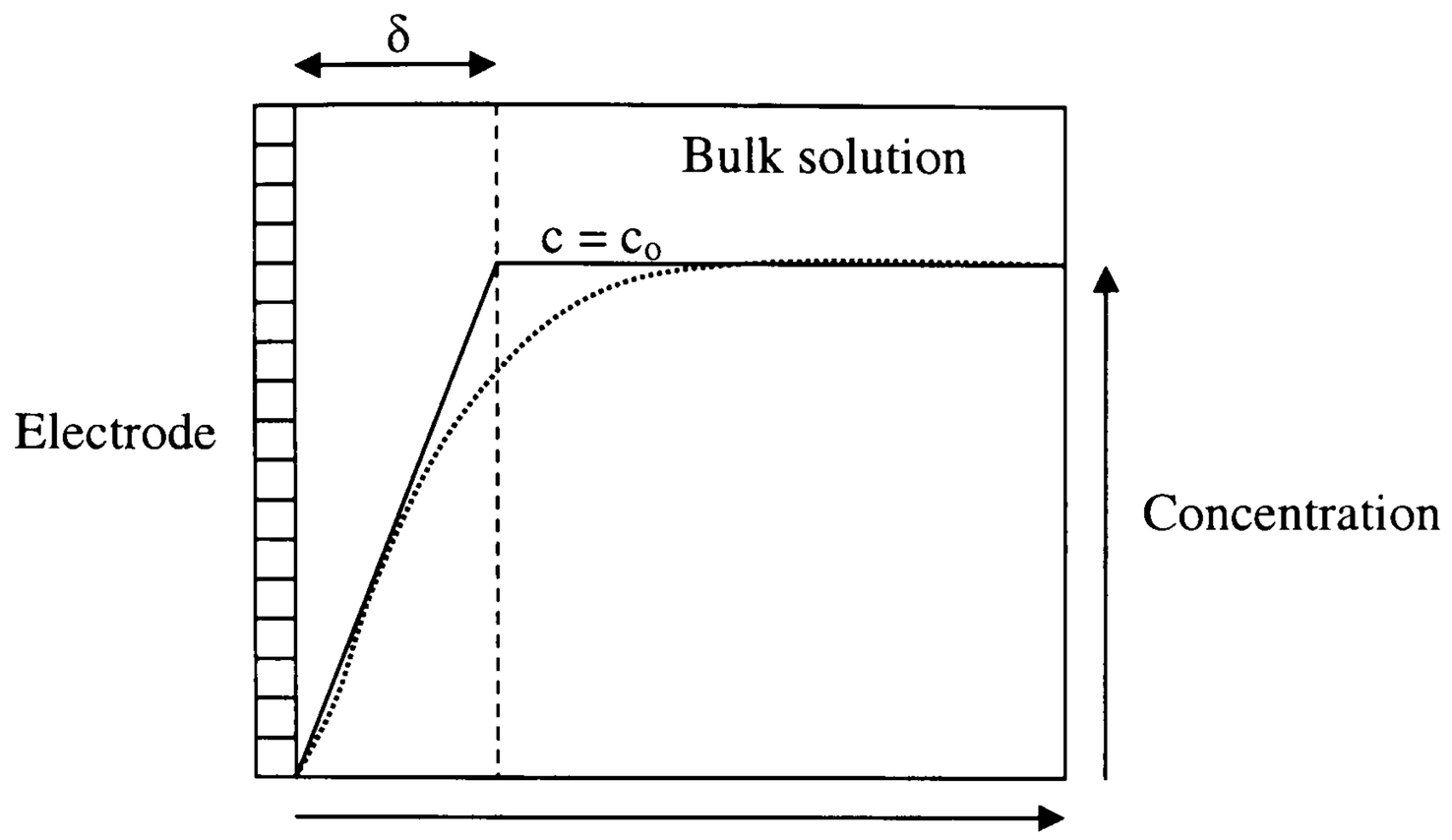

Figure 3.4: Nernst diffusion layer profile.

The Nernst diffusion layer model assumes that the electrolyte near the electrode surface is divided into two regions [3.8]. The combination of convection and diffusion produce velocity and concentration profiles near the electrode surface. In the bulk region, strong convection occurs and the concentration is uniform, $c = c_o$. Adjacent to the electrode surface, a thin stationary layer of thickness δ exists and diffusion is the only mode of transport of reactant to electrode. When an electrode is polarised, the surface concentration of the reactant falls. The concentration gradient will be at a maximum when the concentration of the reactant at the electrode is zero. At this point, the rate of diffusion transport reaches a maximum. The corresponding current is called the limiting current density.

Equation 3.1 indicates that for a given electrode reaction and electrolyte, the limiting current may be increased by increasing the active electrode area, the ionic diffusion coefficient or the reactant concentration, as well as decreasing the Nernst diffusion layer The use of porous electrode not only provides high specific surface area, A_e (m^2/m^3), but its porous structure also acts as a turbulence promoter, giving rise to electrolyte velocities near the electrode surface [3.9]. The enhancement in

hydrodynamic effects reduces the diffusion layer thickness near the electrode surface, resulting in moderately high values of the mass transport coefficients. The limiting current for three-dimensional electrode is given by

$$I_L = nFV_e k_m A_e c_o \tag{3.2}$$

where I_L is the limiting current, V_e is the electrode volume, k_m is the mass transport coefficient, A_e is the specific electrode area and c_o is the bulk concentration. In many reactors operating under mass transport controlled conditions, it is often difficult to separate the individual contributions of mass transport coefficient, k_m and the specific surface area, A_e, therefore these values are usually present as $k_m A_e$. Hence equation 3.2 is used to calculate the product of $k_m A_e$ under the conditions where the reduction of metal is mass transport controlled over the porous electrode surface and the potential or current distribution is sufficiently uniform through the electrode. The quantity $k_m A_e$ can also be estimated by monitoring the decay in metal concentration as a function of time during the deposition process, which will be described in section 3.2 of design equations.

Due to secondary reactions in a gold thiosulphate-sulphite aged electrolyte, the limiting current for gold reduction is difficult to obtain. For this reason, acidified copper sulphate solution has been used in this study as a reference electrolyte in characterising the mass transport properties at two- and three-dimensional electrodes, as has been done by other researchers [3.9]. Using equation 3.1 from Nernst diffusion layer model, the limiting current for gold can be derived using the diffusion limiting current of copper for similar Cu^{2+} and Au^{+} concentrations from the following

$$\frac{I_{L,Au}}{I_{L,Cu}} = \frac{n_{Au} D_{Au}}{n_{Cu} D_{Cu}} \tag{3.3}$$

with $n_{Au} = 1$, $n_{Cu} = 2$, $D_{Au} = 1.835 \times 10^{-10}$ m^2/s [3.10] and $D_{Cu} = 5.8 \times 10^{-10}$ m^2/s [3.9]. The diffusion coefficient of gold is obtained from the voltammetry studies while the diffusion coefficient of copper was found from the literature. Substitution of all values into equation 3.3, we found that the limiting current of gold is about 16% of limiting current of copper

$$I_{L,Au} = 0.158 I_{L,Cu} \tag{3.4}$$

Equations 3.2 and 3.4 are further used to characterise the mass transport properties at porous electrode.

3.1.5 Potential Drop within the Electrode

The effective operation of an electrochemical cell utilising a porous electrode is critically dependent on the potential distribution generated within its structure [3.11]. Despite its many electrochemical advantages, the use of porous electrode is often associated with non-uniform potential distribution across the matrix [3.7]. This non-uniformity results in reduced current efficiency and uneven utilisation of the electrode material, hence non-uniform deposition of metals [3.5]. Roberts *et al.* have developed a model of flow-through porous electrode system which takes into consideration the effect of electrode thickness and both electrode and electrolyte conductivity on the current and potential distribution within the porous electrode [3.11]. They reported that in order to achieve a maximum deposition rate within the electrode material under limiting current conditions, the thickness of the electrode must not exceed the penetration depth of the current through the electrode matrix [3.11]. The numerical model was developed for graphite felt with 95% porosity and inlet concentration of 0.5 mM. The electrode thicknesses were varied at a fixed applied potential and the total current density obtained were then observed. It was found that for thin electrode, < 7 mm, the limiting current plateau is clearly observed and the total current increases linearly with thickness for large cathodic potentials. However, for thick electrodes, most part of the electrode is operating under electron transfer control and the total current decreases with electrode thickness due to the

potential drop within the electrode material. From this study, it is clear that the choice of electrode thickness plays a major role in determining the performance of the metal recovery process. The choice of electrode thickness for our study is given in the next section.

3.1.6 Choice of Electrode Material

To clarify the problems associated with potential drop across the electrode matrix, we conducted a series of resistance measurements across the electrode thickness and length, as shown in figure 3.5. The results are summarised in table 3.2. It was found that the electrode resistance increases with increasing thickness and length. This will promote higher potential drop across its matrix and lead to a dramatic decrease in performance. Therefore, electrode A, with 3 cm length, 5 cm width and 0. 5 cm thickness, is chosen for our experiments.

Points	Resistance (Ω)		
	Electrode A	Electrode B	Electrode C
a	6.5	6.8	6.9
b	10.1	12.2	16.9
c	10.5	11.8	13.5
d	9.1	11.5	13.6
e	9.5	11.0	14.0

Table 3.2: Resistance across the electrode thickness and length.

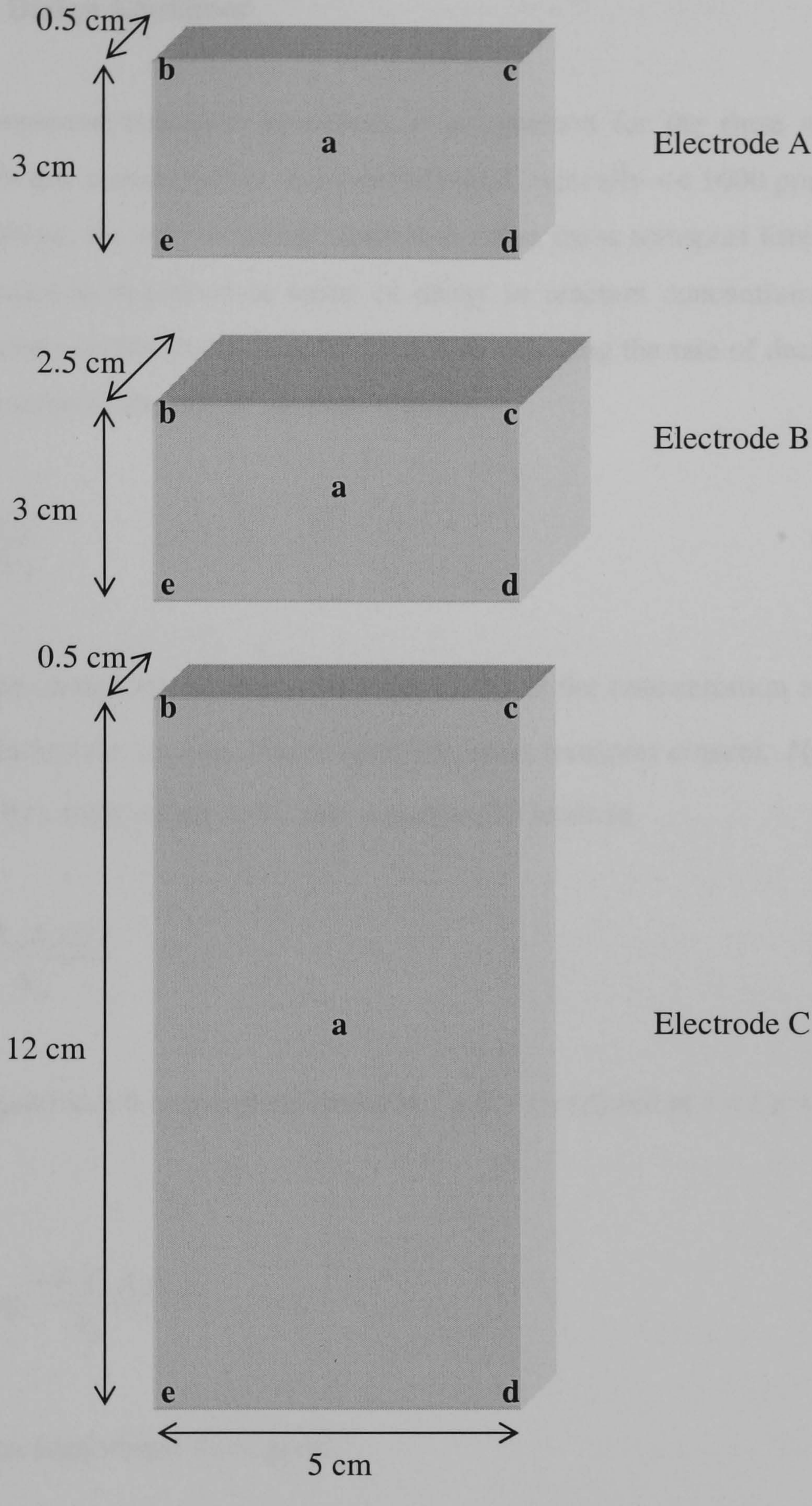

Figure 3.5: Electrode resistance measurements.

3.2 Reactor Design Equations

In many environmental treatment processes, it is common for the rinse water to contain relatively low concentration of dissolved metal, typically << 1000 ppm [3.1]. Under this condition, the rate of metal removal is often mass transport limited and reactor performance is described in terms of decay in reactant concentration with time. A mass balance in the reactor can be written by equating the rate of decrease in reactant concentration to the rate of electron transfer

$$-\frac{dc(t)}{dt} = \frac{I(t)}{nFV_R} \tag{3.5}$$

where $I(t)$ is the instantaneous current at time t, $c(t)$ is the concentration at time t and V_R is the electrolyte volume. Under complete mass transport control, $I(t) = I_L$. Substitution of $I(t)$ from equation 3.2 into equation 3.5 leads to

$$-\frac{dc(t)}{dt} = \frac{V_e k_m A_e c(t)}{V_R} \tag{3.6}$$

Integration of equation 3.6 between the limits at $t = 0, c = c(o)$ and at $t = t, c = c(t)$ gives

$$c(t) = c(o)\exp\frac{-V_e k_m A_e t}{V_R} \tag{3.7}$$

or rearranged into logarithmic form gives

$$\ln\frac{c(t)}{c(o)} = \frac{-V_e k_m A_e t}{V_R} \tag{3.8}$$

It must be noted that this treatment is only valid under the condition where the current applied to the system is equal to or greater than the limiting current at all concentrations experienced during the electrolysis. Equation 3.7 clearly indicates that the reactor performance depends strongly upon the product of mass transport coefficient and the electrode area, $k_m A_e$. This equation was derived by F. C. Walsh and tested for copper (II) removal from acidified copper sulphate electrolyte. However, potentiostatic deposition was chosen for his work, and we found out that this can lead to uneven deposition of metal ion on the electrode due to non-uniform potential distribution generated within the porous electrode. Therefore, in our work, galvanostatic deposition mode has been chosen.

In order to carry the reaction to a highest possible gold recovery from a dilute waste stream, here we use a new approach to recovery method. In this work, a constant current analysis was carried out to recover metal at close to the mass transport control condition, by adjusting the current to its limiting value , $I_L(t)$, corresponding to the instantaneous gold (I) concentration at time t, $c(t)$. Initially, we used equation 3.7 to construct the theoretical plot of normalised gold concentration against time at different electrolyte flow velocities, as is shown in figure 3.6. This plot provides information on the estimated time required for removal of at least 80% of gold in 6 litres of 1 mM gold thiosulphate-sulphite aged electrolyte. Figure 3.6 clearly shows that the rate of concentration decay is an exponential function of time and that the rate of gold removal is faster at higher electrolyte flow rates.

Subsequently, the theoretical plot in figure 3.6 is used to construct a series of stepwise changes in current which reflect the changes in gold concentration within the reactor. The limiting current values for each step were calculated using equation 3.9 by substituting the values of concentration, $c(t)$, measured at several points on time scale, t, from figure 3.6.

$$I_L(t) = nFV_e k_m A_e c(t) \tag{3.9}$$

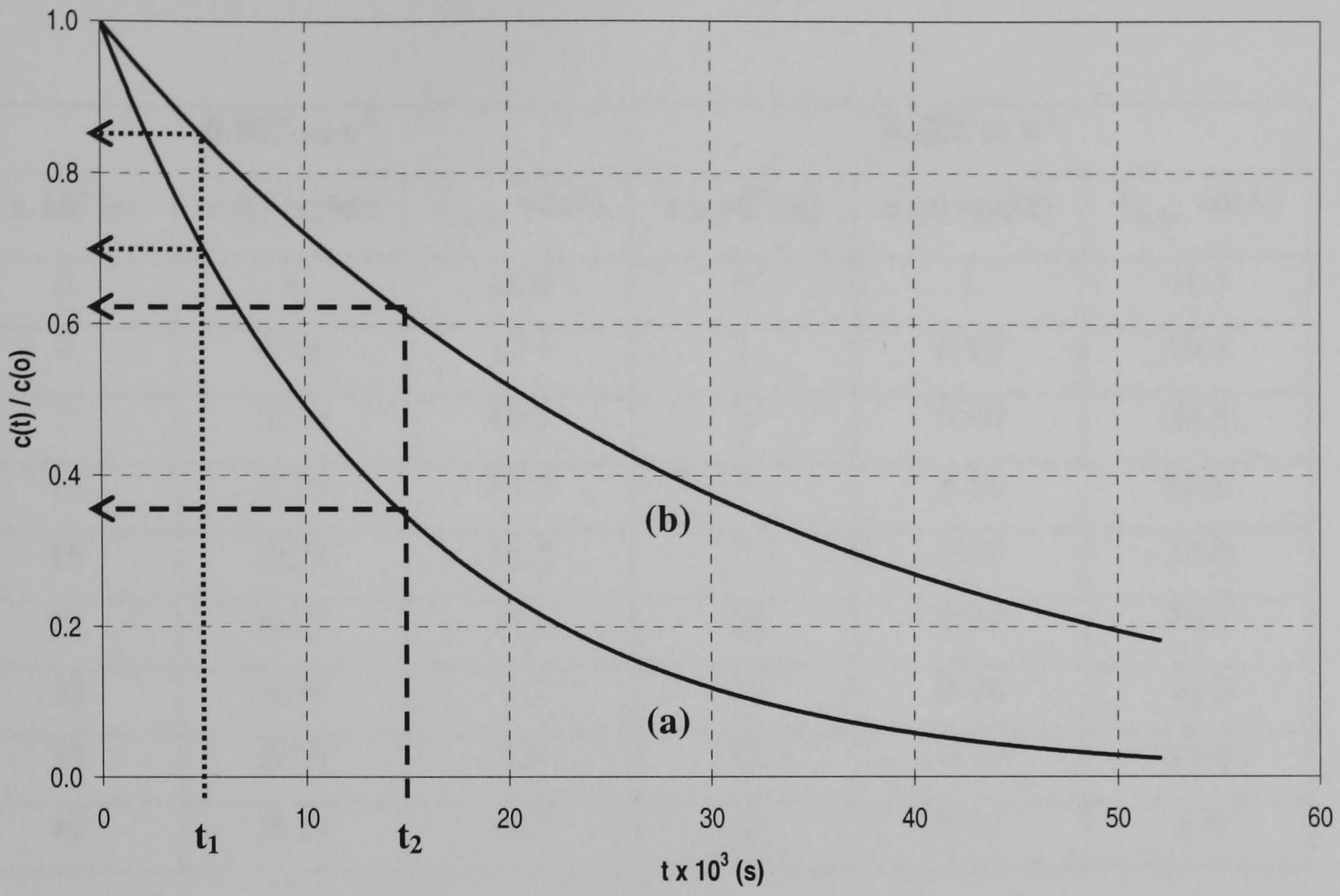

Figure 3.6: Theoretical plot of normalised gold concentration against time at electrolyte velocities of (a) 0.222 m s^{-1} and (b) 0.037 m s^{-1}.

As the concentration of gold within the reactor decreases, the limiting current is also decreases. The values of limiting current applied throughout the removal process are listed in table 3.3. As an example, when a current of 18.9 mA is applied at an electrolyte velocity of 0.037 m s^{-1} for duration of 3000 s, the concentration of gold is expected to reduce to 0.91 mM. In order to reduce this concentration to 0.79 mM, a current of 17.1 mA is then needed to be applied. In this experiment, overall eight steps were taken in order to reduce the concentration to below 0.2 mM. Samples of electrolyte were taken at predetermined intervals during the experiment and the remaining concentration of gold (I) ions in the electrolyte was monitored as a function of time. It is evident that to follow the theoretical decay curve, an infinite amount of steps is required. However, in practice, usually 8-10 steps should follow the concentration decay sufficiently closely such that high current efficiencies are achieved.

0.037 m s^{-1}			0.222 m s^{-1}		
t x 10^3 (s)	c (t) (mM)	$I_{L,Au}$ (mA)	t x 10^3 (s)	c (t) (mM)	$I_{L,Au}$ (mA)
0	1	18.9	0	1	41.1
3	0.91	17.1	1	0.93	39.1
7	0.79	15.1	3	0.80	34.5
11	0.70	13.2	5	0.70	28.9
16	0.59	11.2	7	0.61	25.0
21	0.49	9.5	10	0.49	20.2
28	0.39	7.5	13	0.40	16.3
37	0.29	5.5	17	0.30	12.3
49	0.19	3.7	22	0.21	8.6

Table 3.3: Estimated limiting currents of 1 mM gold thiosulphate-sulphite aged electrolyte at electrolyte velocities of 0.037 m $s^{-1}$and 0.222 m s^{-1}.

The current efficiency for this process can be described as

$$\vartheta = \frac{nFV_e k_m A_e c(t)}{I_L(t)} \tag{3.10}$$

By adjusting the current to its limiting value, a high current efficiency could be maintained throughout the removal process. Also, by operating in galvanostatic mode, the process can be considerably simplified and applied to a large scale of electrochemical reactor.

To summarise, the overall steps involved in the design and interpretation of the recovery process of gold from thiosulphate-sulphite aged electrolyte are illustrated in figure 3.7.

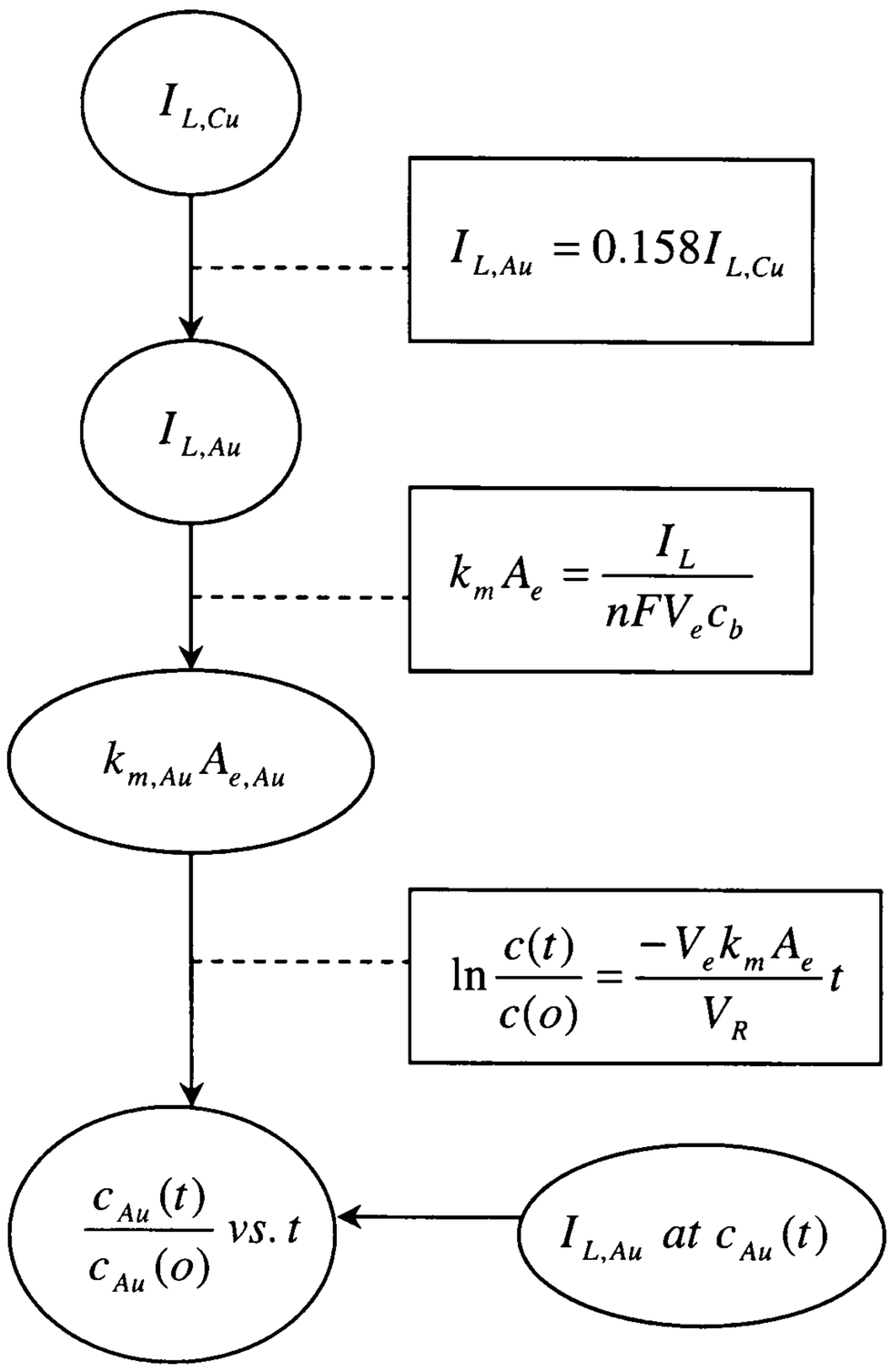

Figure 3.7: Steps involved in recovery process of gold.

As shown above, one needs to go through the following design steps in order to recover gold from an aged thiosulphate-sulphite electrolyte:

1. Determination of the limiting current of copper at different electrolyte velocities.
2. Estimation of limiting current of gold using a correlation derived from Nernst diffusion layer model using the diffusion limiting current of copper.
3. Calculation of the product of mass transport coefficient and specific surface area, $k_m A_e$, for the gold system.

4. Construction of a theoretical plot of normalised gold concentration against time, $\ln\frac{c(t)}{c(o)}$ *vs.* t.

5. Calculation of the limiting current, $I_L(t)$, corresponding to the instantaneous gold concentration at time t, $c(t)$.

3.3 References

3.1 F. C. Walsh, *Pure Appl. Chem.*, **73 (12)**, 1819 (2001).

3.2 K. Juttner, U. Galla and H. Schmieder, *Electrochim. Acta*, **45**, 2575 (2000).

3.3 P. Trinidad and D. Gilroy, *Int. J. Engng. Ed.*, **14 (6)**, 431 (1998).

3.4 K. Scott, *J. Chem. Tech. Biotech.*, **54**, 257 (1992).

3.5 F. C. Walsh, *A First Course in Electrochemical Engineering*, Alresford Press Ltd. (1993).

3.6 K. I. Popov, S. M. Pesic and P. M. Zivkovic, *J. Serb. Chem. Soc.*, **67 (4)**, 273 (2002).

3.7 J. Newman and K. E. Thomas-Alyea, *Electrochemical Systems (3rd Edition)*, Wiley-Interscience (2004).

3.8 C. H. Hamann, A. Hamnett and W. Vielstich, *Electrochemistry*, Wiley-VCH (1998).

3.9 D. Pletcher, I. White, F. C. Walsh and J. P. Millington, *J. Appl. Electrochem.*, **21**, 659 (1991).

3.10 S. Sobri and S. Roy, *J. Electrochem. Soc.*, **152**, C593 (2005).

3.11 T. Doherty, J. G. Sunderland, E. P. L. Roberts and D. J. Pickett, *Electrochim. Acta*, **41 (4)**, 519 (1996).

CHAPTER 4:

EXPERIMENTAL SYSTEMS

4.1 Electrolytes

4.1.1 Gold Thiosulphate-Sulphite Aged Plating Bath

Basic composition of fresh gold thiosulphate-sulphite fresh plating bath is shown in table 4.1. The electrolyte was developed in Newcastle University by Liew *et. al.* [4.1]. The plating bath was prepared using ACS reagents by first dissolving both the complexing agents, 0.42 M Na_2SO_3 and 0.42 M $Na_2S_2O_3$, with deionised water and constantly stirred with a magnetic stirring unit. Once dissolved, 0.05 M aurochloric acid, $HAu(III)Cl_4$, was slowly added into the solution containing the mixed ligand. In order to avoid disproportionation of the thiosulphate ions at pH 6.0, pH of the electrolyte was monitored through the formulation process and maintained at about pH 7.5. pH of the bath was adjusted using dilute H_2SO_4 or $NaOH$ solution.

Composition	(M)
$HAuCl_4$	0.05
Na_2SO_3	0.42
$Na_2S_2O_3$	0.42

Table 4.1: Basic composition of fresh gold thiosulphate-sulphite plating bath

The $Au(III)Cl_4^-$ subsequently undergoes complexation by thiosulphate which led to formation of $Au(S_2O_3)_2^{3-}$, a relatively stable complex while the sulphite acted as a buffer and stabilised the solution [4.1]. This was proved by chemical and electrochemical experiments performed with the gold thiosulphate-sulphite electrolyte which shows similar characteristic to that obtained for gold thiosulphate solution [4.2]. The bath is found to be stable at near-neutral pH, showed good

compatibility with positive photoresists and proved to be satisfactory for an industrial process [4.3].

An important aspect to consider is the aging process of gold thiosulphate-sulphite electrolyte. The fresh thiosulphate-sulphite electrolyte was used extensively in microelectronics industry for over 2-3 weeks. The process involved during this period was equivalent to 2 months of total production. At the end of the process, significant change was observed in the electrodeposits obtained. The smooth and bright electrodeposited gold were becoming rough, dark and were beginning to become powdery. The gold deposits obtained were of unacceptable quality due to the lower quantity of sulphite presence in the solution. The electrolyte was then collected and left to age for more than 6 months. This plating bath, now referred as aged electrolyte, was then collected and the concentration and pH of the electrolyte was then measured. It should be noted that the composition of electrolyte has slightly changed over the period of aging; however the basic chemicals remain similar.

Initially, chemical and electrochemical properties of the aged electrolyte were characterised. The aged electrolyte was then used for studying the nucleation and growth behaviour of gold onto carbon plate electrodes. The electrolyte was then diluted to 1 mM using Millipore water for studying the recovery of gold from rinse waters using reticulated vitreous carbon electrode in a flow-by cell.

4.1.2 Acidified Copper Sulphate Solution

1, 5 and 10 mM acidified copper sulphate solutions were prepared with Milipore water and Fluka reagents. Initially, the amounts of $CuSO_4.5H_2O$ powder needed for each copper concentration were weighted. The $CuSO_4.5H_2O$ powder is then dissolved with 0.05 M H_2SO_4 prepared earlier using 97% sulphuric acid. The solution was made up to approximately 6 litres for each specified concentration of copper sulphate.

4.2 Electrochemical Systems

4.2.1 H-cell System

An H-cell was used to study the electrochemical characteristics of the aged thiosulphate-sulphite plating bath as well as the nucleation and growth mechanism of gold. The schematic diagram of a three-electrode H-cell is shown in figure 4.1.

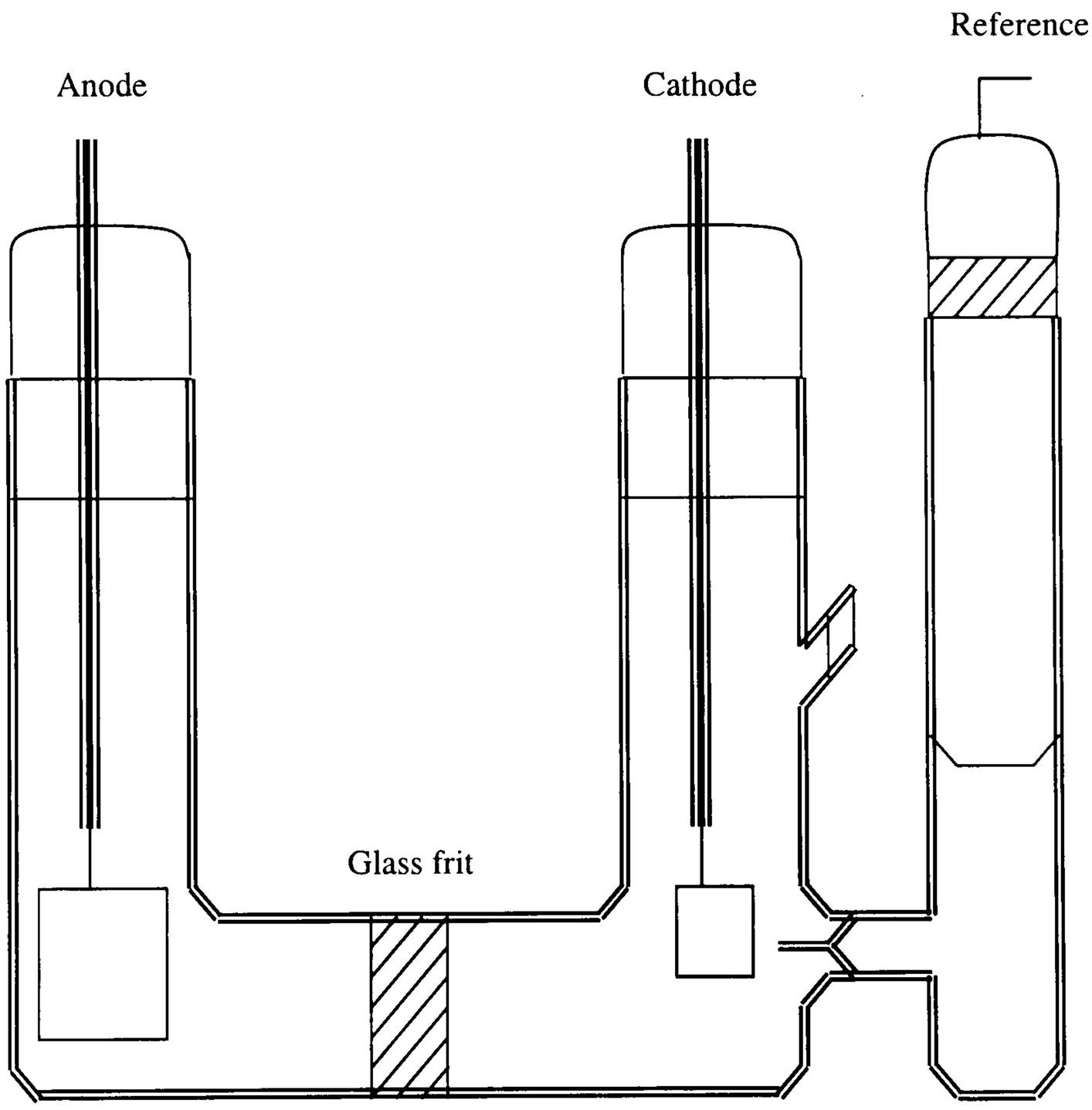

Figure 4.1: Schematic diagram of the H-cell.

Gold foil (Goodfellow Ltd., UK) was employed for electrochemical studies of aged electrolyte while carbon electrodes (Goodfellow Ltd., UK) were used for studying the electrocrystallisation of gold deposits. All electrodes had a surface area of 1.0 x 1.0 cm^2. The anode was a 2.5 x 2.0 cm^2 platinised-titanium sheet. The anolyte and

catholyte compartments were separated by a glass frit and were each filled with a volume of approximately 35 mL of aged thiosulphate-sulphite electrolyte.

A saturated mercurous sulphate electrode (Thermo Electron), Hg/Hg_2SO_4 in saturated K_2SO_4 reference was used throughout the study. The SMSE was connected to a Luggin-Haber tip filled with the aged electrolyte and placed 0.2 cm from the surface of the cathode. All potential measurements were made with respect to this reference electrode. The potential of SMSE is 0.6 V vs. the standard hydrogen electrode (SHE) and 0.4 V vs. saturated calomel electrode (SCE) at 25°C. A potentiostat (Sycopel Scientific) controlled by a computer was used to carry out the experiment.

Figure 4.2: The H-cell

4.2.2 Flow Cell System

A laboratory scale flow cell operated in a flow-by mode has been constructed to study the performance of gold recovery at recycle or continuous modes of operation. The schematic diagram of the flow cell is shown in figure 4.3.

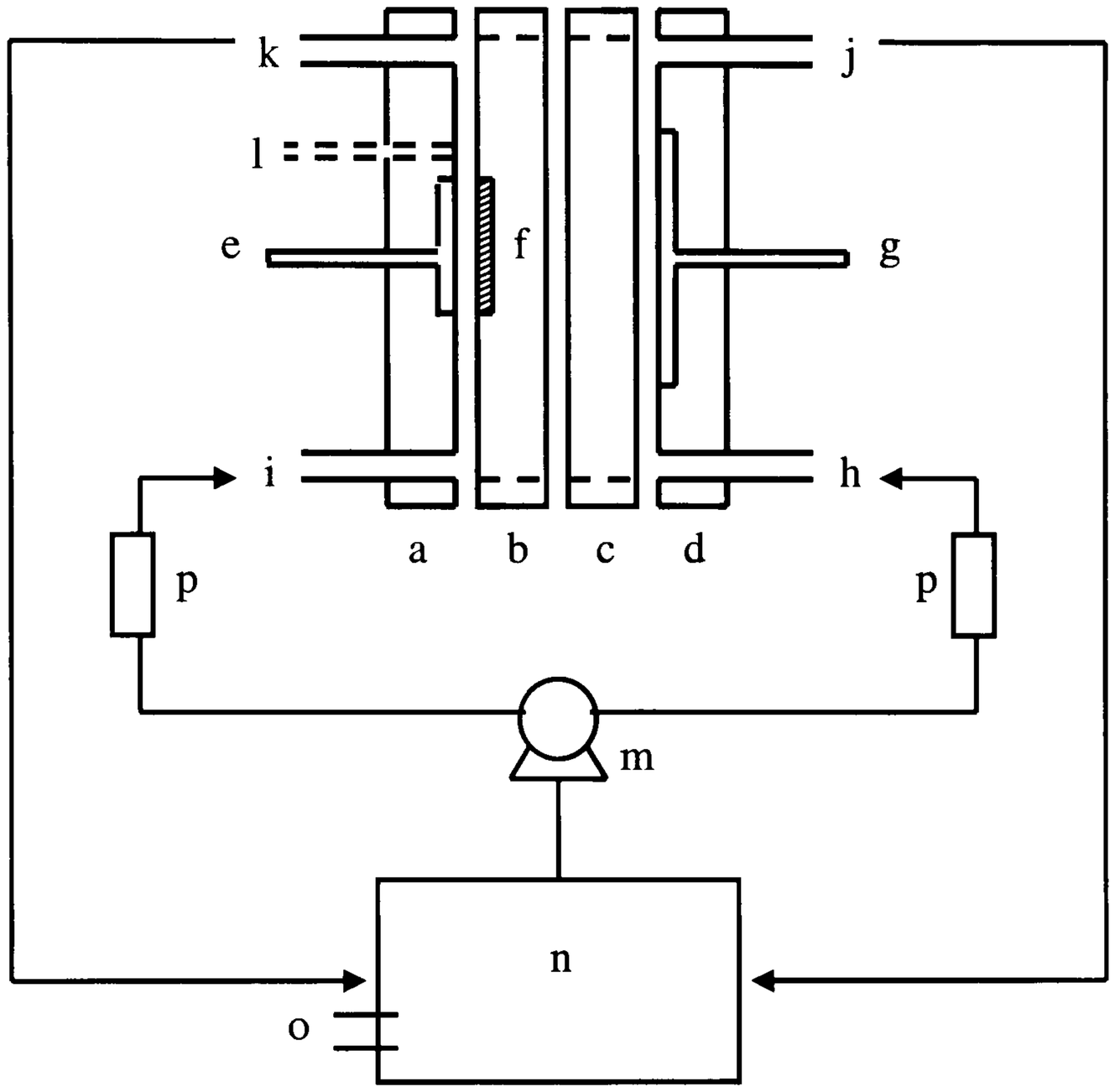

Figure 4.3: Schematic view of the electrolytic flow-by cell.

a, **d**: outer Perspex blocks, **b**, **c**: inner Perspex blocks with flow channel, **e**: stainless steel cathodic current collector, **f**: reticulated vitreous carbon (RVC) cathode, **g**: copper plate anode, **h**, **i**: electrolyte inlets, **j**, **k**: electrolyte outlets, **l**: copper wire reference electrode, **m**: pump, **n**: electrolyte reservoir, **o**: drain pipe, **p**: flow meters.

The cell was a modified form of a design proposed by Pletcher *et. al.*[4.4]. It was fabricated from four blocks of Perspex, each is 280 mm length, 100 mm width and

25 mm thick. The cathode and anode were mounted into the outer blocks while the inner blocks were machined to form the electrolyte channel. To prevent electrolyte leakage, O-ring grooves were placed in between each of the blocks. The cell had two electrolyte entrances and exits.

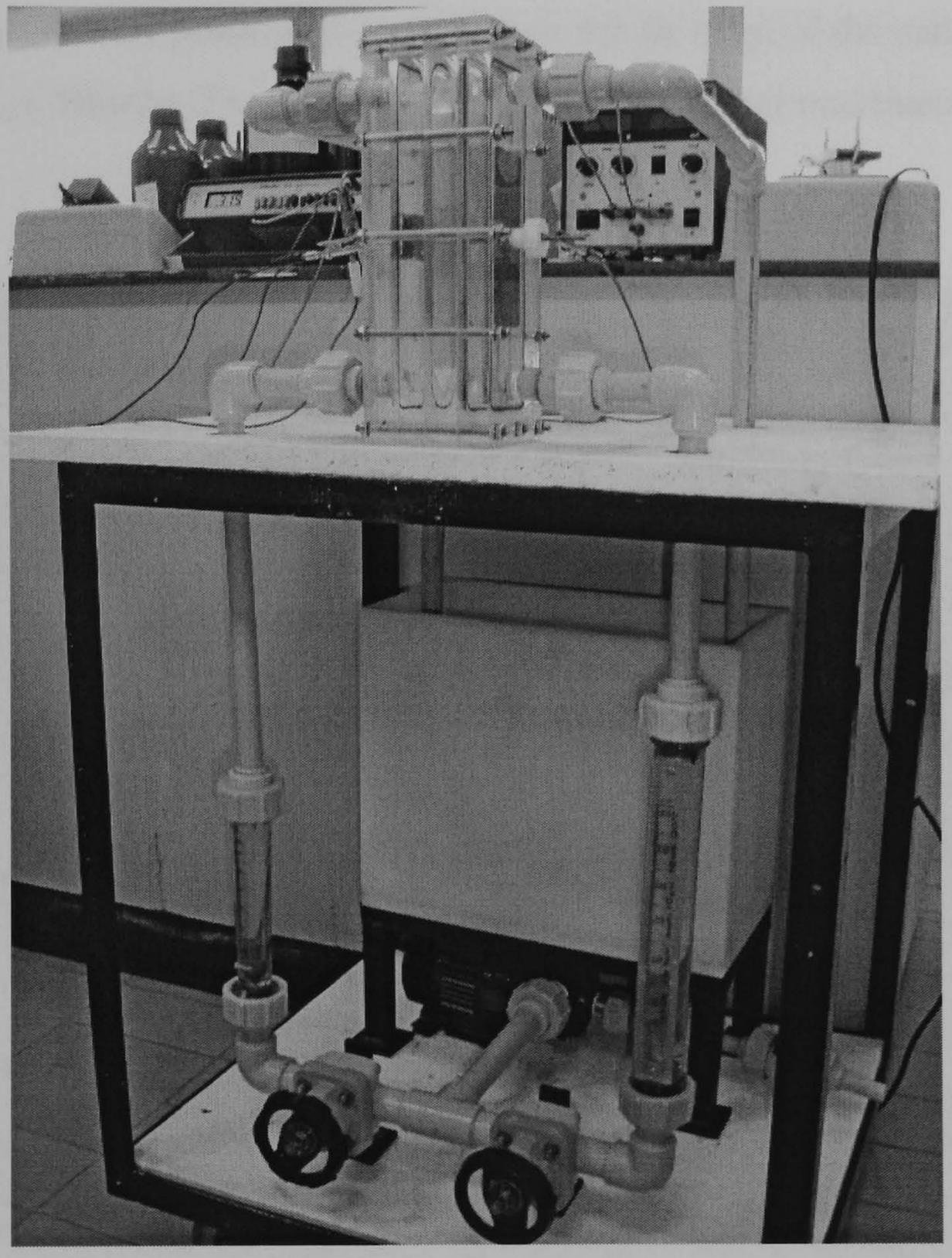

Figure 4.4: The flow cell system.

A 120 mm x 50 mm rectangular copper plate cathode with identical anode placed flushed against the outer Perspex blocks were used in a set of experiment carried out to characterise the mass transport at flat plate electrode. Studies on metal ion recovery from rinse waters were performed with a reticulated vitreous carbon (RVC)

electrode. The RVC was cut into 3 cm x 5 cm x 0.5 cm and attached to a 3 x 5 cm^2 stainless steel current collector using silver loaded epoxy adhesive and hardener (RS Components, UK) and a silver conductive paint (RS Components, UK). The contact was left for 24 hours to dry in ambient condition before being mounted into the outer Perspex block. 12 mm x 5 mm platinised titanium mesh served as an anode. All potential measurements were recorded against a copper reference electrode. The reference electrode was positioned 10 mm from the far edge of the cathode. The cell is connected to a Thurlby-Thandar power supply and a digital multimeter.

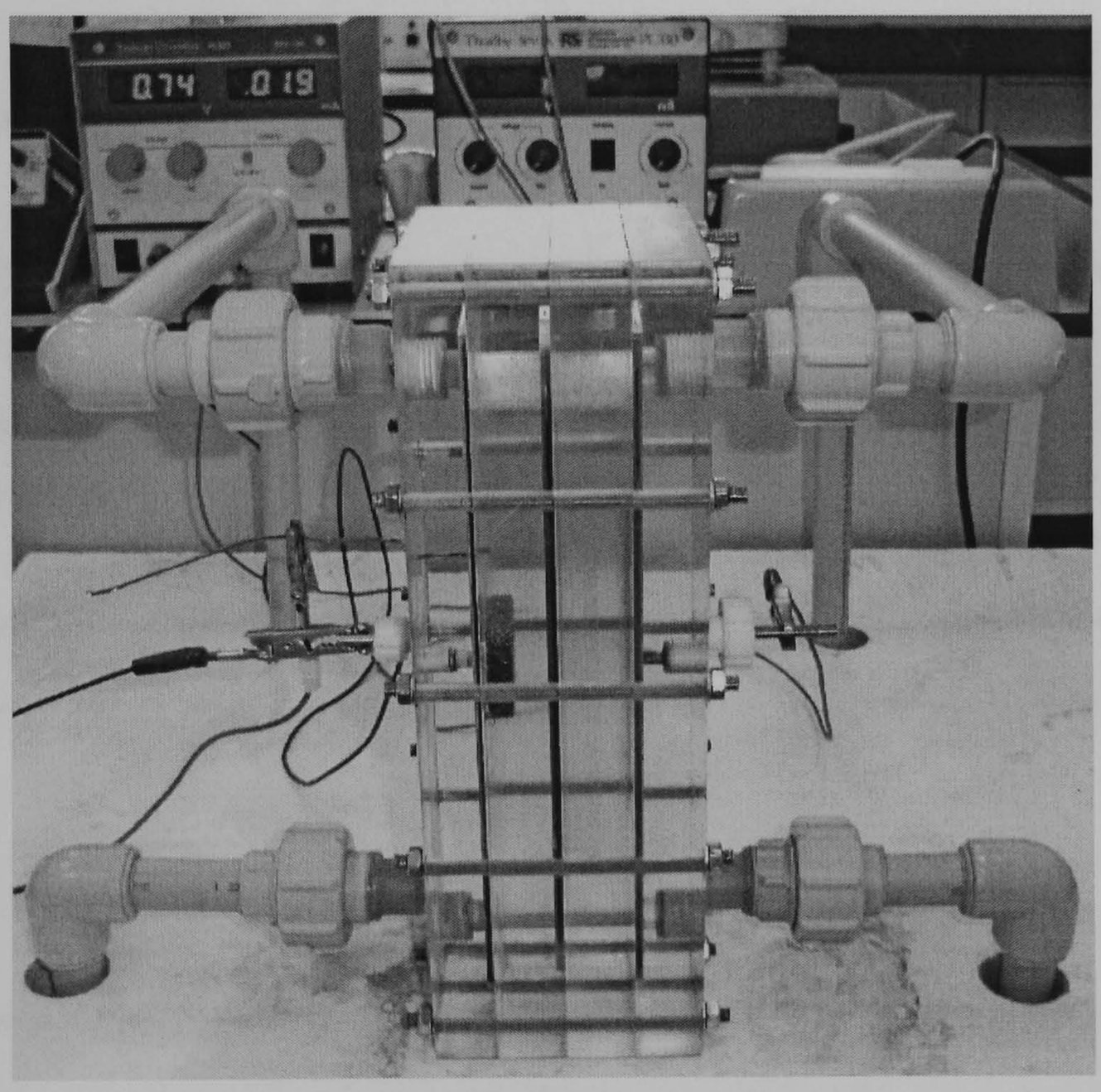

Figure 4.5: The Perspex blocks.

The reservoir was made of polypropylene blocks and could contain up to 10 litres of electrolyte. Electrolytes comprising of acidified copper sulphate solution (5mM and 10 mM $CuSO_4$ in 0.1 M H_2SO_4) or 1 mM aged gold thiosulphate-sulphite were employed in the experiments. Electrolytes were pumped (Totton Pumps Ltd., UK)

through the channel at velocities between 60 L/h (0.022 m s^{-1}) and 600 L/h (0.222 m s^{-1}) controlled using two flow meters (Nixon Flowmeters Ltd.).

Electric power was supplied to the anode and cathode using a Thurlby-Thandar power supply. For any experiment, the pump was started and set to the desired electrolyte flow velocity. The current was then switched on. A digital multimeter was used to measure the potential difference between the cathode and a copper reference electrode when necessary.

4.3 Electrode Material

4.3.1 Gold Foil

The working electrode employed in electrochemical studies of aged electrolyte was a 1.0 cm x 1.0 cm gold foil (Goodfellow Cambridge Ltd, UK), mounted into the H-cell. The electrode was 99.5% pure with 0.05 mm thickness. Properties of the gold foil are listed in table 4.2.

Properties	Value
Density (g cm^{-3})	19.30
Resistivity (μΩ cm)	2.20
Thermal Conductivity (W m^{-1} K^{-1})	318
Coefficient of Thermal Expansion (K^{-1})	14.1 x 10^{-6}

Table 4.2: Properties of gold foil.

The gold foil was chosen for this experiment because the electrochemical characteristics of the aged electrolyte needed to be compared with that of a fresh electrolyte. In an earlier study, a gold foil electrode was used [4.2, 4.3], and therefore we also used a gold foil.

4.3.2 Carbon Plate Electrodes : Glassy Carbon and Graphite

Carbon electrodes were chosen for studying the nucleation and growth mechanism of gold onto foreign surfaces. Two types of carbon electrodes were used, glassy carbon and rigid graphite (Goodfellow Cambridge Ltd., UK). The two different forms of carbon were chosen due to the difference in their structure. The choice of glassy carbon allows us to examine the microstructure of gold deposits when the substrate had no preferred texture, whereas the choice of graphitic electrode allows us to examine the microstructure when the substrate has a well-established structure. These two carbon electrodes are the most frequently used substrates for studying the electrocrystallisation process and are also used for metal recovery in industry [4.5-4.8]. Furthermore, they are easily available and inexpensive. Properties of both glassy carbon and rigid graphite are listed in table 4.3.

Properties	Glassy Carbon	Rigid Graphite
Density (g cm^{-3})	14	1.8
Resistivity (μOhm cm)	400	1200
Thermal Conductivity (W m^{-1} K^{-1})	6.3	150
Coefficient of Thermal Expansion (K^{-1})	2.6 x 10^{-6}	7 x 10^{-6}

Table 4.3: Properties of carbon vitreous and rigid graphite.

Both types of electrodes were 99.95% pure with 1 mm thickness. The electrode was cut into 1 cm^2 squares and attached to a copper wire using silver loaded epoxy adhesive and hardener (RS Components, UK). In order to avoid metal deposition on copper wire and silver contact paste used for contact, this area was covered using a multipurpose silicone sealant (Dow Corning Ltd., UK). The electrode was then mounted in the H-cell and held in place by the use of a metal clip. After each electrochemical measurements, the carbon surface was gently polished using wet silicone carbide paper grit 4000 (Struers Ltd., UK), washed thoroughly with distilled

water and then wiped with a clean cloth before being transferred to the experimental cell for the next experiment. The electrode was used immediately after being polished.

4.3.3 Porous Electrode: Reticulated Vitreous Carbon

In order to evaluate the performance of gold recovery in a laboratory flow cell as constructed in section 4.2.2, we used reticulated vitreous carbon (RVC- Goodfellow Cambridge Ltd., UK) as an electrode. The RVC is an open pore foam material which available in several porosity grades ranging from 10 to 100 pores per inch (ppi). In this study, we have used the RVC with 60 ppi (24 pores cm^{-1}) and 97% porosity. The properties of the RVC are summarised in table 4.4. In addition to the known properties, we conducted a series of resistance measurements in our laboratory. The measurement was done using a digital multimeter across the electrode thickness and length and has been shown in section 3.1.6 of chapter 3.

Properties	Value
Bulk density (g cm^{-3})	0.05
Pores (cm^{-1})	24
Porosity	96.5

Table 4.4: Properties of reticulated vitreous carbon.

This three-dimensional material was selected due to its regular structure, high specific surface area, high porosity and relatively good electrical conductivity [4.10-4.12]. Its high ratio of surface area to volume promotes turbulence thus increases the mass transport rate in the system. The RVC is also inert over wide range of very reactive acids, bases and organic solvents. In addition, its ability to operate at a wide range of potentials made it the preferred choice for metal ion removal in industry.

4.4 Electrochemical Instrumentation

All electrochemical experiments performed with the H-cell, such as linear sweep, cyclic voltammetry and chronoamperometry, were carried out using a potentiostat (Sycopel Scientific Scanning Ministat) and PCI-100 data acquisition system operated with a PC using Sycopel ECPROG software, as shown in figure 4.6. The potentiostat can operate at scan rates between 10 nV/s to 10 V/s with output current 1 Amp ± 5% and output voltage 25 V ± 10%. The current-potential data on the experiments was collected and then interpreted using Microsoft Excel.

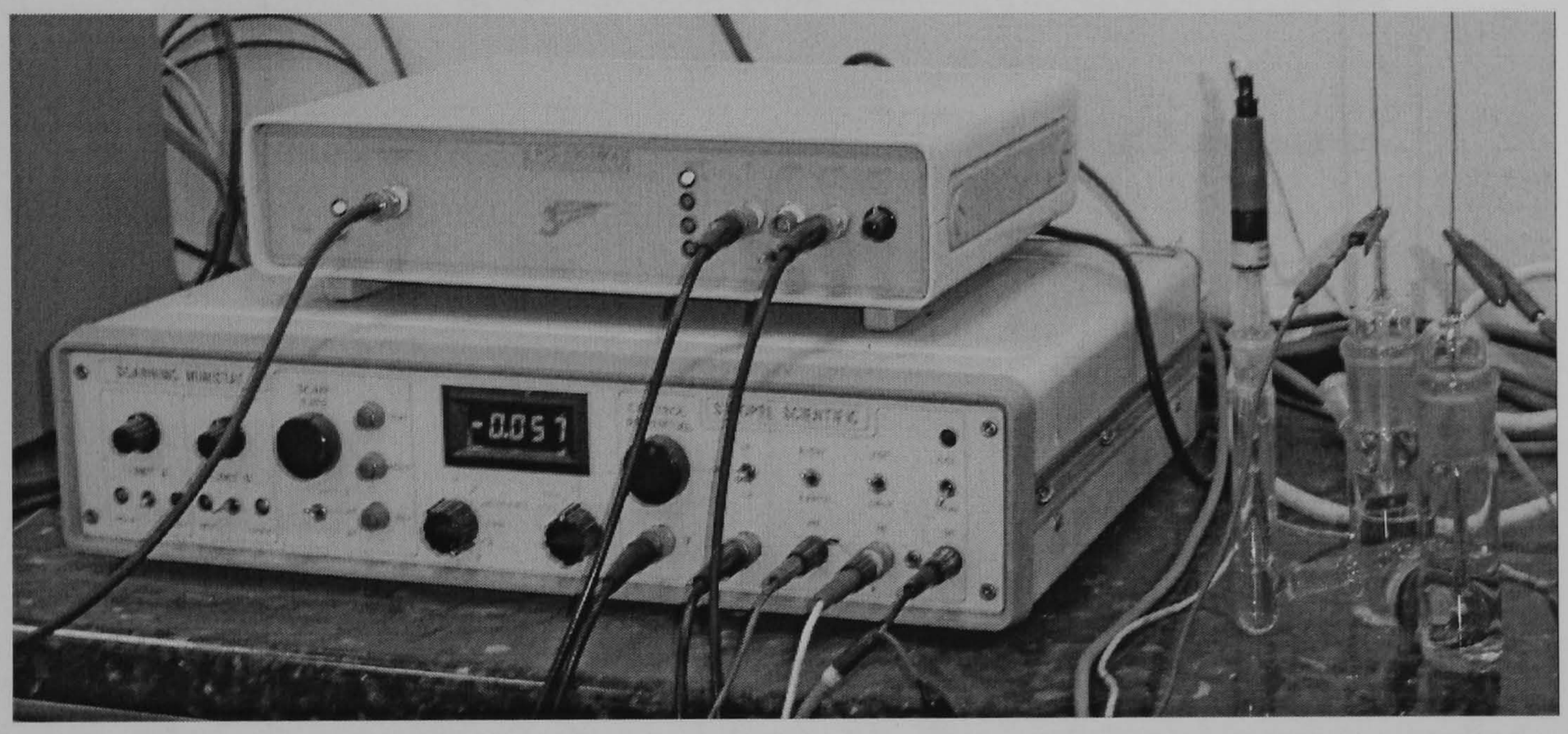

Figure 4.6: The potentiostat and PCI-100 data acquisition system.

A Thurlby-Thandar PL320 power supply was connected to the flow cell described in section 4.2.2. It was used for both constant voltage and constant current operations, which covered voltages up to 32 V and currents up to 2 A. A Thandar TM351 digital multimeter (DMM) was used to measure the potential difference between the cathode and a copper reference electrode when necessary. Current and potential data was recorded manually in these experiments.

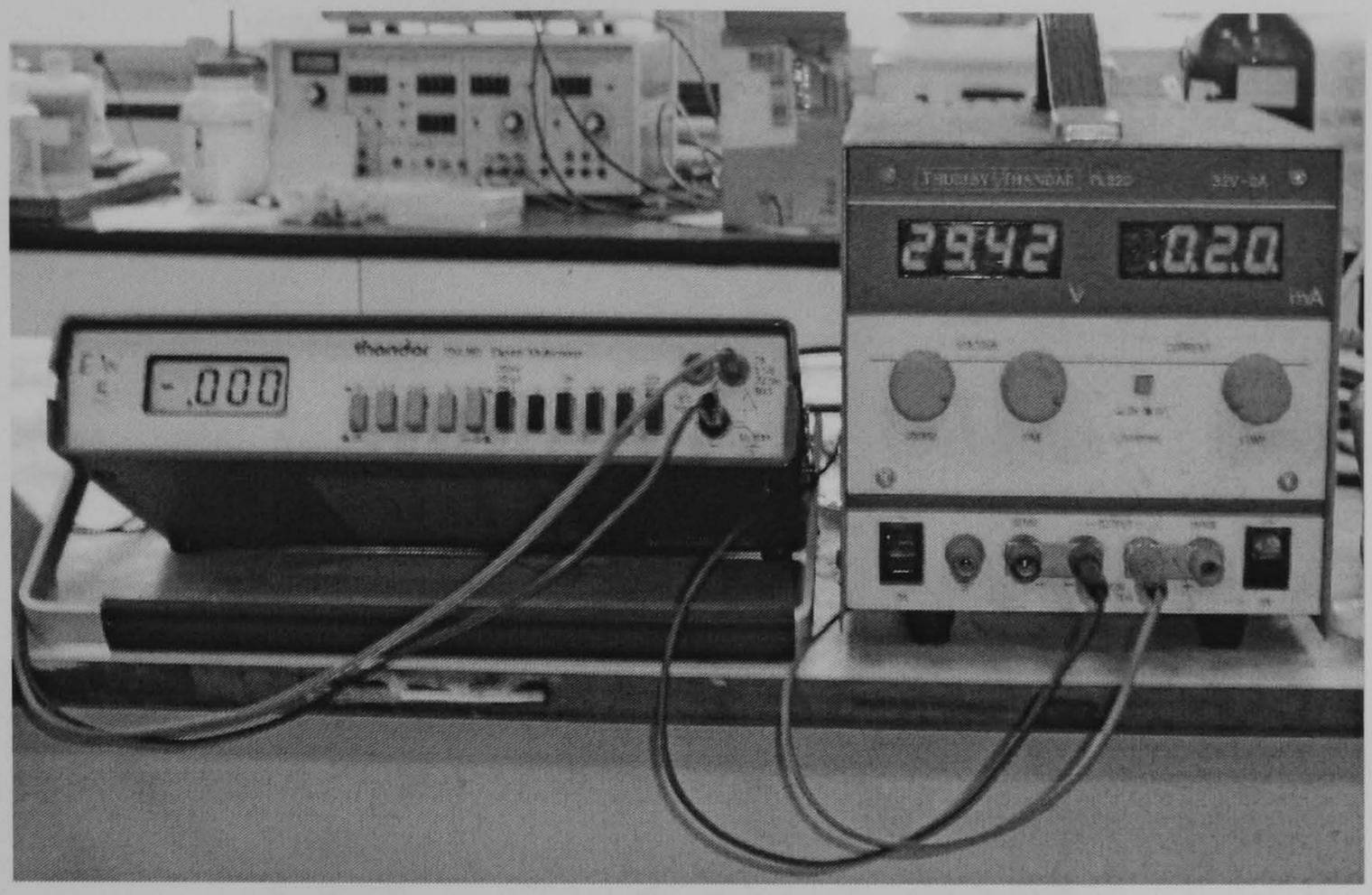

Figure 4.7: A Thurlby-Thandar power supply and a digital multimeter.

4.5 Chemical and Material Analysis

4.5.1 Conductivity Measurements

Measurement of electrolytic conductivity was performed with HI 8633 conductivity meter (Hanna Instrument), as shown in figure 4.8. The conductivity meter is supplied with a 4-ring potentiometric HI 7630ID probe with 1 m cable. The probe was rinsed with distilled water before being transferred to a beaker containing the electrolyte. The meter was then switched on and measurement was performed by switching the conductivity range between 0-199.9 μS, 0-1999 μS, 0-19.99 mS or 0-199.9 mS.

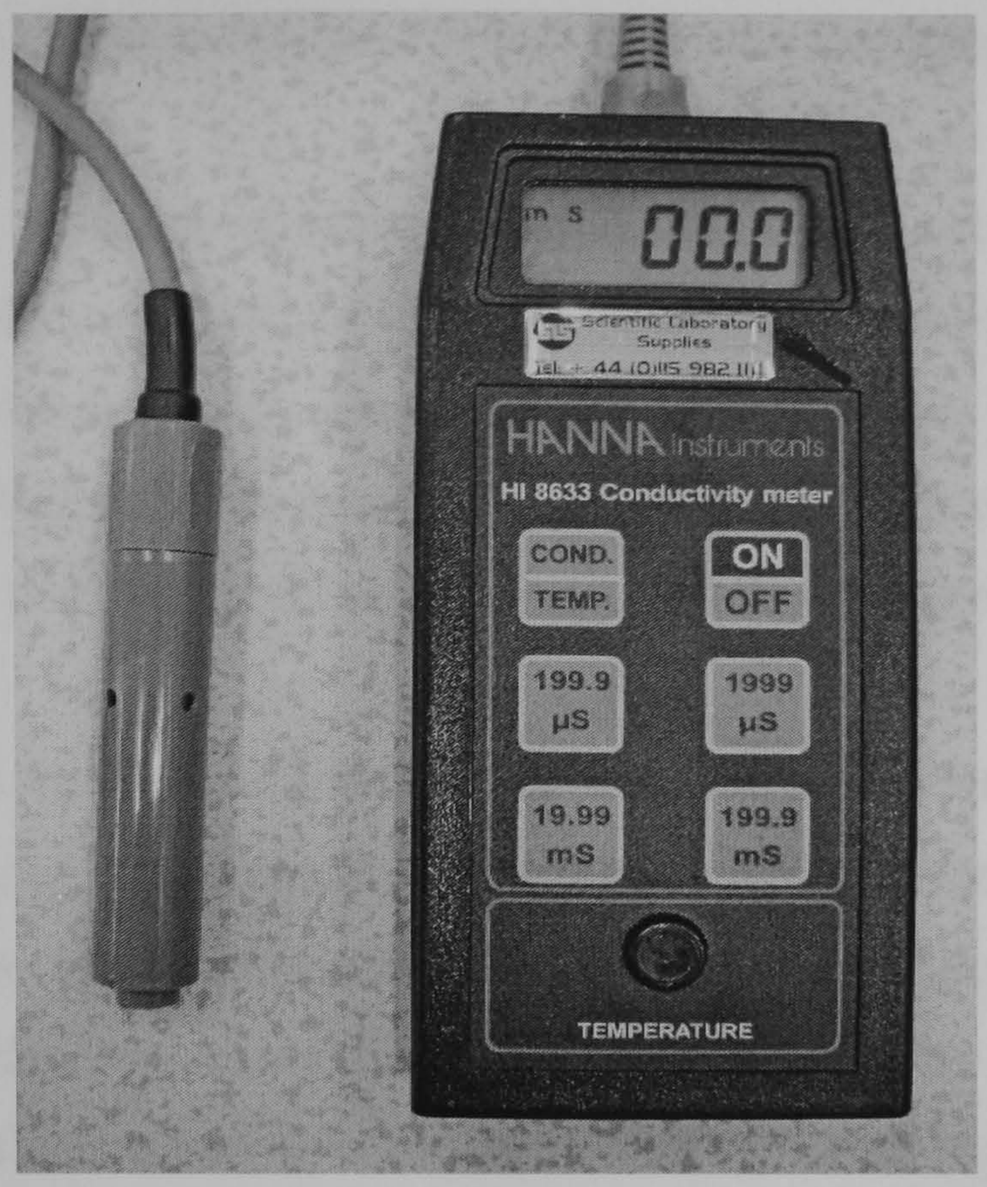

Figure 4.8: Hanna Instrument conductivity meter.

Conductivity measurements were done to study the ability of the aged electrolyte to conduct electrical current by means of ionic motion under the influence of a potential gradient. The specific conductivity, κ, is measured in S/cm or $\Omega^{-1}cm^{-1}$ and is determined as the product of conductance, C, and a calibration factor known as cell constant, σ as derived through equations 4.1 and 4.2 [4.9]. The cell constant is a ratio of d_e and the electrode area, A_e, which can be determined by calibrating the conductivity meter using a substance of known conductivity, 0.1 M KCl (potassium chloride), prior to the conductivity measurements. From this calibration, the cell constant was calculated and found to be 0.1362 cm^{-1}. This value was then used to calculate the specific conductivity of the gold plating bath.

$$\kappa = \sigma C \tag{4.1}$$

$$\kappa = \frac{d_e}{A_e}\frac{1}{R_e} \tag{4.2}$$

4.5.2 Inductively Coupled Plasma-Optical Emission Spectroscopy (ICP-OES)

A UNICAM 701 Series Emission Spectrometer was used to determine the concentration of gold species in the thiosulphate-sulphite aged electrolyte. The ICP-OES measures elements in the concentration range of 1 ppb to 1000 ppm. It is particularly useful technique for measuring samples with high dissolved solids and samples containing both high and low concentration elements in the same solution.

The instrument was initially calibrated with a series of appropriate solution standard. Prior to each sample measurement, the sample submitted for ICP analysis was usually prepared to ensure it match the acidity and background matrix of the calibration standards. Typical methods of sample preparation include extraction, dissolution or acidification and should result in a solution free of particulates.

The electrolyte sample is drawn into the ICP and pumped using a peristaltic pump to a nebulizer where it is converted to a fine spray and mixed with argon plasma in a spray chamber. The purpose of the spray chamber is to make sure that only droplets in a narrow size range make it through into the plasma. The sample carried into the plasma is then instantly excited by the sufficiently high temperature (near 10,000 K) to break the chemical bonds and transform into atomic state. The atoms emit their characteristic ultraviolet and visible radiation. The emitted radiation is separated by wavelengths using a monochrometer and the separated light is focused onto a solid-state detector which measures individual ions in the sample. Radiation wavelength is use to identify the element and radiation intensity is used to determine the concentration range of a species present in the sample. Elemental determination of ICP are typically reported in ppm (parts per million) on a sample weight or sample volume basis.

4.5.3 X-Ray Diffractometer (XRD)

In order to determine the phases present on the electrode surface as well as the crystalline structure of gold deposits, x-ray diffraction patterns were obtained using a

Philips X'Pert Pro diffractometer. The analysis was done by K. Liddell in Newcastle University Materials Analysis Unit.

The X-ray diffractometer used a Cu Kα radiation (wavelength = 0.154 nm) as an incident beam. When the x–ray beam of wavelength λ is directed towards the crystalline material at an angle θ, called the Bragg angle, the beam will be scattered by the crystal atoms, as shown in figure 4.9. Some of these scattered beams will be completely in phase and so reinforce each other to form diffracted beams. The diffracted beam, therefore, may be defined as a beam composed of a large number of scattered rays mutually reinforcing each other.

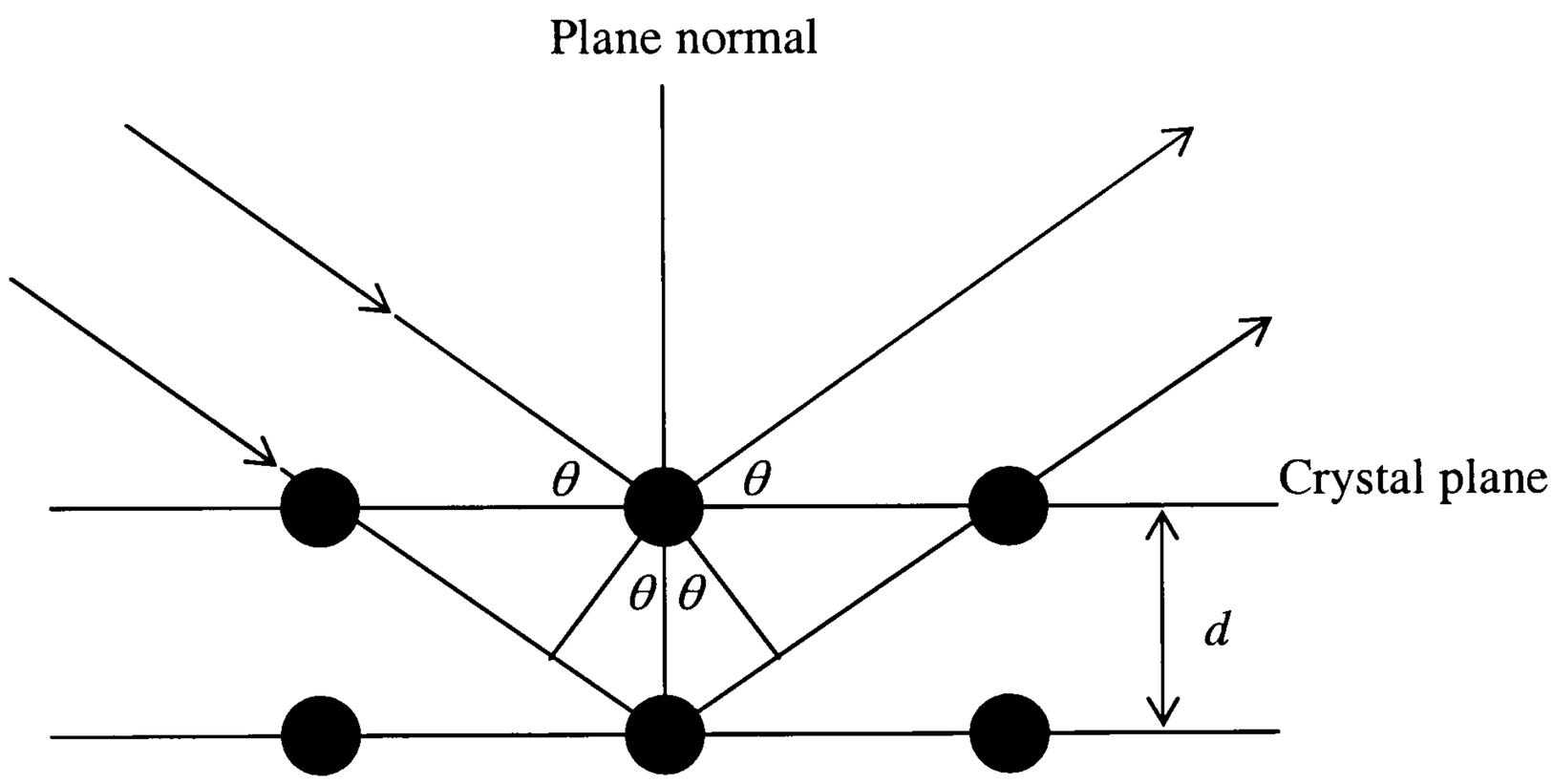

Figure 4.9: Diffraction of x-rays by crystals.

The scattered rays can only be completely in phase if their path length difference is equal to a whole number w of wavelengths, obeying the Bragg equation [4.13, 4.14]

$$w\lambda = 2\,d\sin\theta \qquad (4.3)$$

where λ is the wavelength, d is the perpendicular distance between the reflecting planes of the crystals and θ is the angle between the incident beam and the reflecting

planes. The Bragg's Law states the essential condition which must be met in order for the rays scattered by all the atoms in all the crystal planes to be completely in phase and interfere constructively to form the diffracted beam. At angles of incident other than the Bragg angle, the reflected beams are out of phase and destructive interference occurs.

The machine is also fitted with Philips Analytical X'Celerator, offering a 100-fold of increase in recording speed with better resolution as compared to traditional powder diffractometer. A secondary monochromator is used in combination with the X'Celerator to eliminate fluorescent scattering from the specimen. In this work, scans were carried out at 50 kV and 25 mA, between 2θ values of 20° to 140° with a step size of 0.033° and time per step of 50 seconds. Intensities were recorded and plotted against the diffraction angles using Microsoft Excel program. Patterns were then interpreted using standard methods for powder diffraction from JCPDSC (Joint Committee on Powder Diffraction Standards) data bank. The average crystallite size can also be calculated according to the Scherrer formula which will be described in section 6.4.

4.5.4 Scanning Electron Microscopy (SEM)

Deposit characterisation was performed to investigate the influence of deposition overpotential and time. Scanning electron microscopy (SEM) analysis for the gold deposits was recorded using a JEOL model 5300 LV SEM at an acceleration voltage of 25kV. The samples were mounted on a specimen stub. All images are obtained using the secondary electron detector. Micrographs were recorded in the magnification range 3500 to 10000. Analysis was done by G. Staines and P. Carrick from the Newcastle University Advanced Chemical and Materials Analysis (ACMA) Unit.

The SEM uses an electron beam instead of light to form an image. The beam is produced from a metallic filament; the most commonly used is the tungsten hairpin gun, which functions as the cathode. When a voltage is applied to the filament, it

causes the filament to heat up. The anode forms powerful attractive forces, which causes the electron beam to accelerate towards the anode through a vertical path. A magnetic lens focuses and directs the beam towards the sample. This magnetic lens is designed to focus the electrons to a very fine spot. A set of scanning coils moves the focus beam back and forth across the specimen row by row. As the electron beam hits each spot on the sample, secondary electrons are produced from its surface. A detector counts these electrons and sends the signals to an amplifier. The final image is built up from the number of electrons emitted from each spot on the sample.

When the electron beam strikes the sample, a number of interactions can occur, as described in figure 4.10. However, not all of the signals are detected. The signals most commonly used are the secondary electrons and the backscattered electrons.

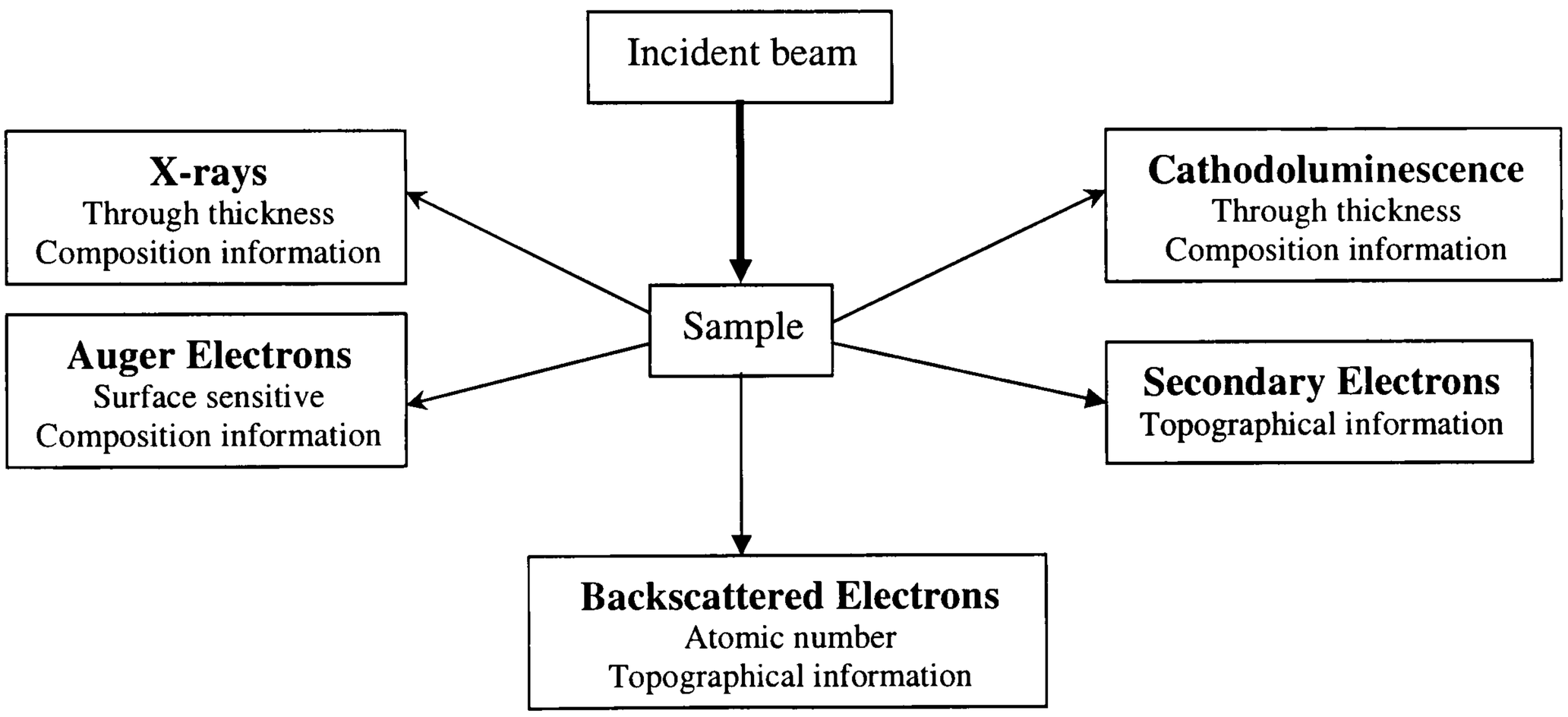

Figure 4.10: Interactions between electron beams and sample.

Secondary electrons are produced predominantly by the interactions between the energetic electron beams and the weakly-bonded specimen electrons. Since there is a great difference between the amounts of energy contained by beam electrons compared to specimen electrons, only a small amount of kinetic energy can be

transferred to the secondary electron. Because of this, only those secondary electrons that are produced within a very short distance of the surface are able to escape from the sample. These electrons are then collected by an electron detector which converts the radiation into an electrical signal and a high resolution topographical image is produced.

The backscattered electrons are produced when the negatively charged beam electrons interact with the positive nucleus. This is known as the Rutherford scattering. The scattering angle is strongly dependent on the atomic number of the nucleus; thus the electrons arriving at the electron detector can be used to obtain not only the topographical images but also the different elements present in a sample based on the atomic mass constant.

4.5.5 Atomic Force Microscopy (AFM)

The Atomic Force Microscopy (AFM) analysis for gold deposits was done in collaboration with the Chemical Research Centre of the Hungarian Academy of Sciences with the help from P. Nagyp and D. Arranyi. The instrument used was a Nanoscope Dimension™ 3100 with operational frequency of 2 Hz. It was operated in contact mode, scanning at 25, 10, 5 and 1 μm imaging scales. Prior to scanning, sample is placed on a magnetic holder. Figure 4.11 shows schematically how the AFM works.

The Dimension 3100 produces high-resolution, three-dimensional images by scanning a sharp probe over the sample surface [4.16]. The probe is part of a flexible cantilever which is mounted on one end of a cylindrical piezoelectric tube. The AFM works by measuring the forces between the probe and sample. In response to the forces between the tip and the sample, the cantilever flexes or bends. As the cantilever flexes, the light from the laser is reflected onto a split photo-diode. By measuring the different signal, changes in the bending of the cantilever can be measured and translated into topographical images.

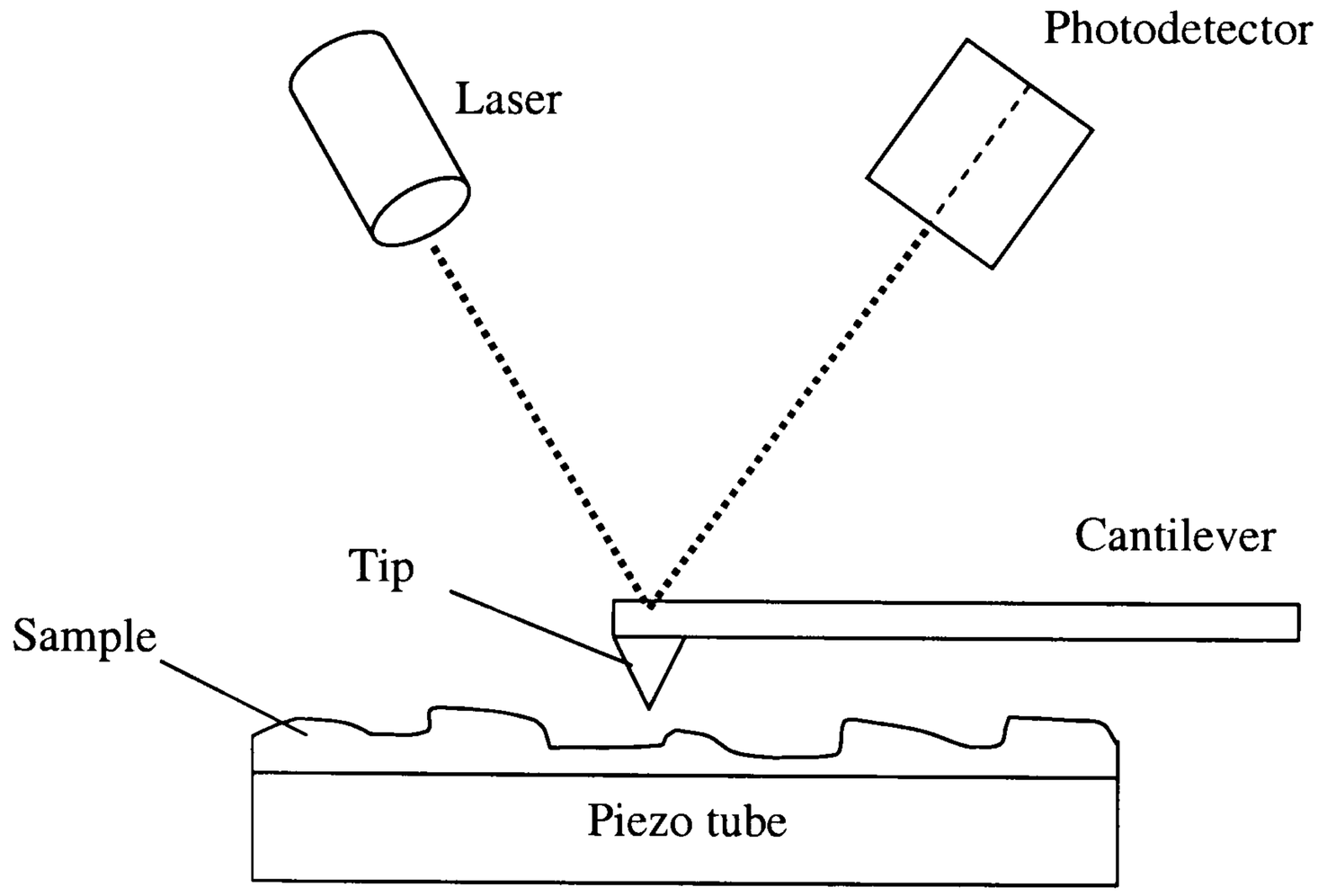

Figure 4.11: How AFM works.

The piezo tube is rigidly mounted near the top of the microscope. Voltages applied to the X and Y electrodes on the piezoelectric tube deflect the tube horizontally to produce a precise raster scan over the sample surface. The vertical height of the probe is controlled by a voltage applied to the Z electrode on the piezo tube. A stepper motor coupled to a lead screw translates a slide to which the sample is attached. A separate motor drive allows the height of the microscope and probe to be adjusted relative to the sample surface.

The AFM imaging modes can be classified as contact or non-contact depending on the net forces between the probe and sample as the probe approaches the sample surface, as shown in figure 4.12. The curve can be measured by moving the probe toward the sample surface and measuring its deflection.

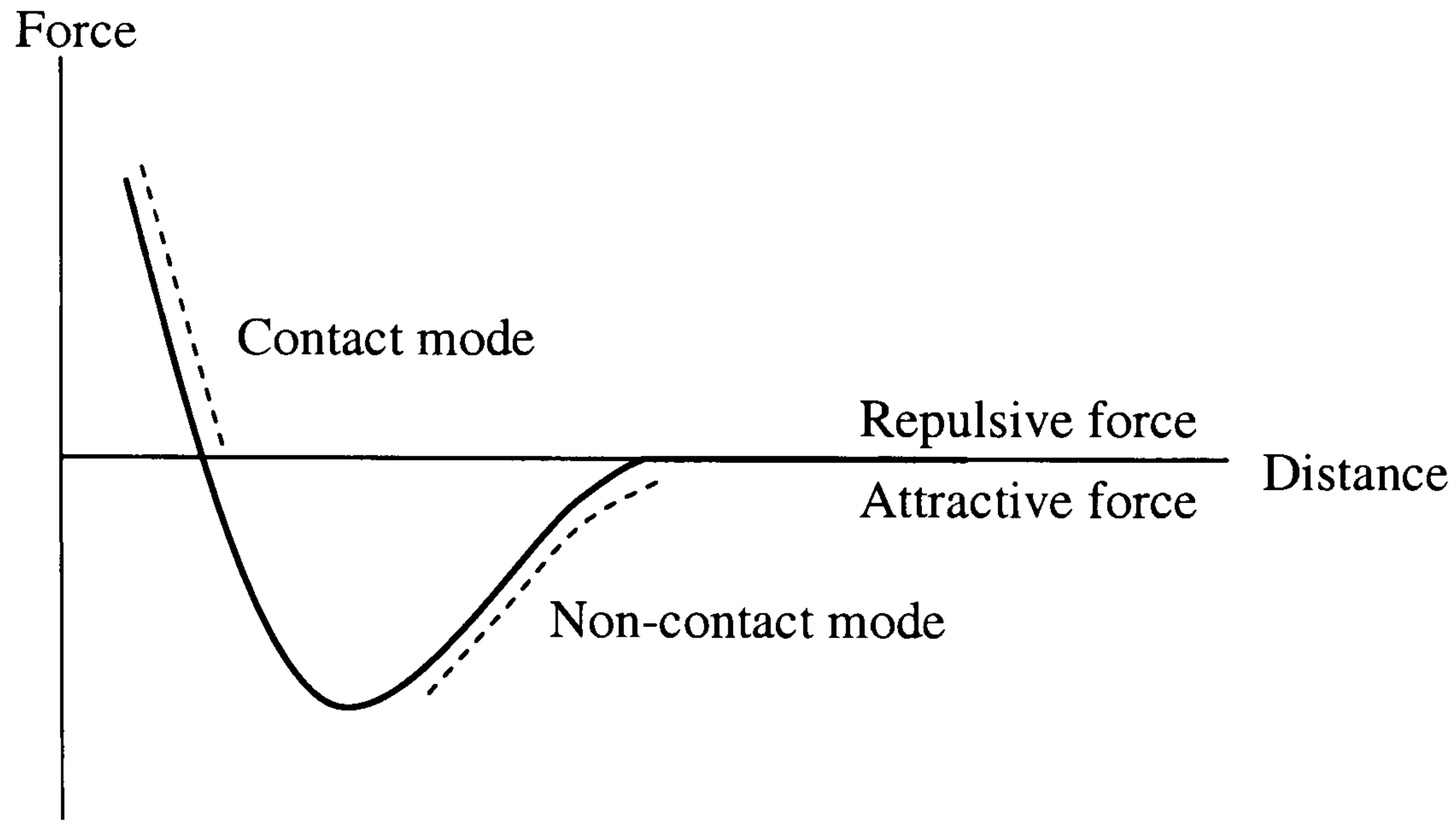

Figure 4.12: Forces between the probe and the sample.

Non-contact AFM is one of several vibrating cantilever techniques in which an AFM cantilever is vibrated near the surface of a sample with little or no contact between the tip and the sample. The total force between the tip and the sample in the non-contact regime is very low and in addition, cantilevers used for non-contact mode must be stiffer than those used for contact mode because soft cantilevers can be pulled into contact with the sample surface. The small force values in the non-contact regime and the greater stiffness of the cantilevers used for non-contact AFM are both factors that make its signal small, and therefore difficult to measure. In contact mode, the tip-sample interaction is much greater which produces large force than that in non-contact mode. This force is set by pushing the cantilever against the sample surface with a piezoelectric tube. When the probe touches the surface, the cantilever is pulled by surface tension toward the sample surface. The deflection of the cantilever is sensed and compared in a DC feedback amplifier to some desired value of deflection.

4.6 Electrochemical Measurement

4.6.1 Analysis of Aged Plating Bath

In order to determine if there was any significant change in the electrochemical properties of the aged electrolyte, cyclic voltammetry experiments were carried out in a three-electrode H-cell connected to a potentiostat. Prior to the voltammetry experiments, concentration and pH of the aged electrolyte was measured. Cathodic potential was swept between 0 and -1.0 V at scan rates 2, 10 and 20 mV/s. All experiments were carried out at room temperature. Tafel analysis was also performed in order to obtain the charge transfer coefficient. Comparison was made on the electrochemical characteristics between aged and fresh gold thiosulphate-sulphite electrolyte.

4.6.2 Gold Electrocrystallisation onto Carbon Electrodes

Nucleation and growth phenomena of gold from aged thiosulphate-sulphite electrolyte were studied at stationary glassy carbon and graphite electrodes in an H-cell. A set of cyclic voltammograms at scan rates varying between 5 to 100 mV s^{-1} was carried out to determine the potential for gold nucleation. Visual observation was also carried out to see if there were any changes to the colour of the aged plating solution.

Current-time transients for studying the nucleation behaviour of gold were accomplished by applying the potentials from the rest potential to the deposition potentials of lower than – 0.7 V for duration of 60 seconds. Cottrell analysis was applied to obtain the diffusion coefficient of gold. Nucleation characteristics of gold were analysed from the experimental current-time data at different overpotentials. The plots can also be used to calculate the nuclei density of gold and the calculated values are compared with results obtained from microscopy images. In order to study the growth of gold with time, a set of current transient were accomplished at different overpotentials for duration of 1, 10, 100, 500 and 1000 seconds. Samples were sent

for scanning electron microscopy (SEM) and atomic force microscopy (AFM) analysis.

4.6.3 Gold Recovery Using Reticulated Vitreous Carbon

At first, acidified copper sulphate solution was used as the reference electrolyte to characterise the mass transport properties at a copper plate and RVC electrode. 1, 5 and 10 mM of $CuSO_4$ in 0.1 M H_2SO_4 were used to test the effect of concentration on mass transport properties. Limiting current of the cathodic deposition of copper was determined by increasing the current stepwise using a Thurlby Thandar power supply and measuring the cathode potential against the copper reference electrode using a digital multimeter. The product of mass transport coefficient, $k_m A_e$, were determined as a function of electrolyte flow velocity.

In the next stage, removal of copper (II) from 1 mM copper sulphate was carried out under controlled current analysis, in which the current was adjusted to its limiting value corresponding to the estimated copper concentration at that instant. Samples of electrolyte were periodically collected during the experiment and the remaining copper concentration was quantified using ICP spectroscopy in order to monitor the effectiveness of the removal process.

Subsequently, the mass transport properties for the copper (II) system were updated for the gold thiosulphate-sulphite system. Removal of gold from aged gold electrolyte was then performed using similar experimental method to that performed with copper (II) removal.

4.7 References

4.1 M. J. Liew, S. Roy, and K. Scott, *Green Chem.*, **5**, 376 (2003).

4.2 M. J. Liew, S. Sobri, and S. Roy, *Electrochim. Acta*, **51**, 877 (2005).

4.3 T. A. Green, M. J. Liew, and S. Roy, *J. Electrochem. Soc.*, **150**, C104 (2003).

4.4 D. Pletcher, I. White, F. C. Walsh, and J. P. Millington, *J. Appl. Electrochem.*, **21**, 659 (1991).

4.5 U. Schmidt, M. Donten, and J. G. Osteryoung, *J. Electrochem. Soc.*, **144**, 2013 (1997).

4.6 M. O. Finot, G. D. Braybrook, and M. T. McDermott, *J. Electroanal. Chem.*, **466**, 234 (1999).

4.7 Y. G. Li, W. Chrzanowski, and A. Lasia, *J. Appl. Electrochem.*, **26**, 843 (1996).

4.8 X. Wang, N. Isaev, and J. G. Osteryoung, *J. Electrochem. Soc.*, **143**, 1201 (1996).

4.9 F. C. Walsh, *A First Course in Electrochemical Engineering*, Alresford Press Ltd. (1993).

4.10 Z. Rogulski, W. Lewdorowicz, W. Tokarz, and A. Czerwinski, *Polish J. Chem.*, **78**, 1357 (2004).

4.11 J. Wang, *Electrochim. Acta*, **26**, 1721 (1981).

4.12 J. M. Friedrich, C. Ponce-de-Leon, G. W. Reade, and F. C. Walsh, *J. Electroanal. Chem.*, **561**, 203 (2004).

4.13 A. R. West, *Basic Solid State Chemistry*, John Wiley and Sons (1984).

4.14 B. D. Cullity, *Elements of X-Ray Diffraction*, 2nd Edition, Addison-Wesley Publishing Company, Inc. (1978).

4.15 A. J. Bard and L. R. Faulkner, *Electrochemical Methods: Fundamentals and Applications*, John Wiley and Sons (1980).

4.16 Dimension™ 3100 Instruction Manual.

CHAPTER 5:

RESULTS:

CHARACTERISATION OF AGED ELECTROLYTE

5.1 Chemical Characterisation

The gold thiosulphate-sulphite electrolyte was formulated from 0.05 M of chloroauric acid ($Au(III)Cl_4$) slowly added into a solution containing two complexing agents, 0.42 M sodium sulphate (Na_2SO_3) and 0.42 M sodium thiosulphate ($Na_2S_2O_3$), dissolved in deionised water [5.1]. The concentration of Au^+ species in the fresh thiosulphate-sulphite electrolyte was 10 g/L. During the electrolyte formulation, pH of the electrolyte was monitored and maintained at about pH 7.5. The electrolyte was then used extensively in an industrial process for over 2-3 weeks which was equivalent to two months of total production. At the end of the process, a significant change was observed in the electrodeposits. The deposits were rough, dark and were beginning to become powdery. The electrolyte was then collected and left to age for more than 6 months [5.2].

After the period of 6 months, the aged electrolyte was collected and the concentration of Au^+ species was measured. It was found that the concentration decreased between 10-20 % from the fresh electrolyte, which gave a concentration of 8-9 g/L (~ 0.04 - 0.045 M). pH of the electrolyte was determined to be 5.23 and this value was found to be stable throughout the electrochemical analysis. Although the pH decreased very slowly over the aging period, this rendered the electrolyte less stable and prone to precipitation. However, precipitates were not visible to the naked eye and no turbidity was detected, as is usually observed when gold disproportionates. This indicates that a slow homogeneous reaction occurs within the solution which leads to a decrease in pH. In this work, it was observed that the aged plating bath remains colourless and transparent throughout the analysis.

Conductivity measurements were carried out to measure the ability of the solution to conduct an electric current [5.3]. The conductance cell was first calibrated by measuring the conductance of a standard solution, 0.1 M KCl, with known specific conductivity. From this calibration, the cell constant was calculated and found to be

0.1362 cm^{-1}. This value was then used to calculate the specific conductivity of the gold plating bath.

Table 5.1 shows the values of electrolyte resistivity and specific conductivity for aged gold thiosulphate-sulphite electrolytes. The electrolyte was diluted from its initial concentration of approximately 45 mM to 10, 5 and 1 mM. It was found that the conductivity of the electrolyte is lower at lower electrolyte concentration, which indicates that there are fewer ions to carry the electric current in the diluted solution.

Concentration (mM)	Specific conductivity (Ω^{-1} cm^{-1})	Electrolyte resistance (Ω)
45	76.2×10^{-3}	1.70
10	28.1×10^{-3}	4.80
5	9.45×10^{-3}	14.3
1	3.77×10^{-3}	35.7

Table 5.1: Measurements of electrolyte specific conductivities and resistance.

5.2 Electrochemical Characterisation

5.2.1 Polarisation Curves

Cyclic voltammetry experiments were carried out in an H-cell with gold foil as the cathode. Surface area available for the deposition was 1.0 cm^2. Figures 5.1 shows the polarisation curves for gold thiosulphate-sulphite aged electrolyte when polarised from 0 to – 0.8 V at scan rates of 2, 5 and 10 mV/s.

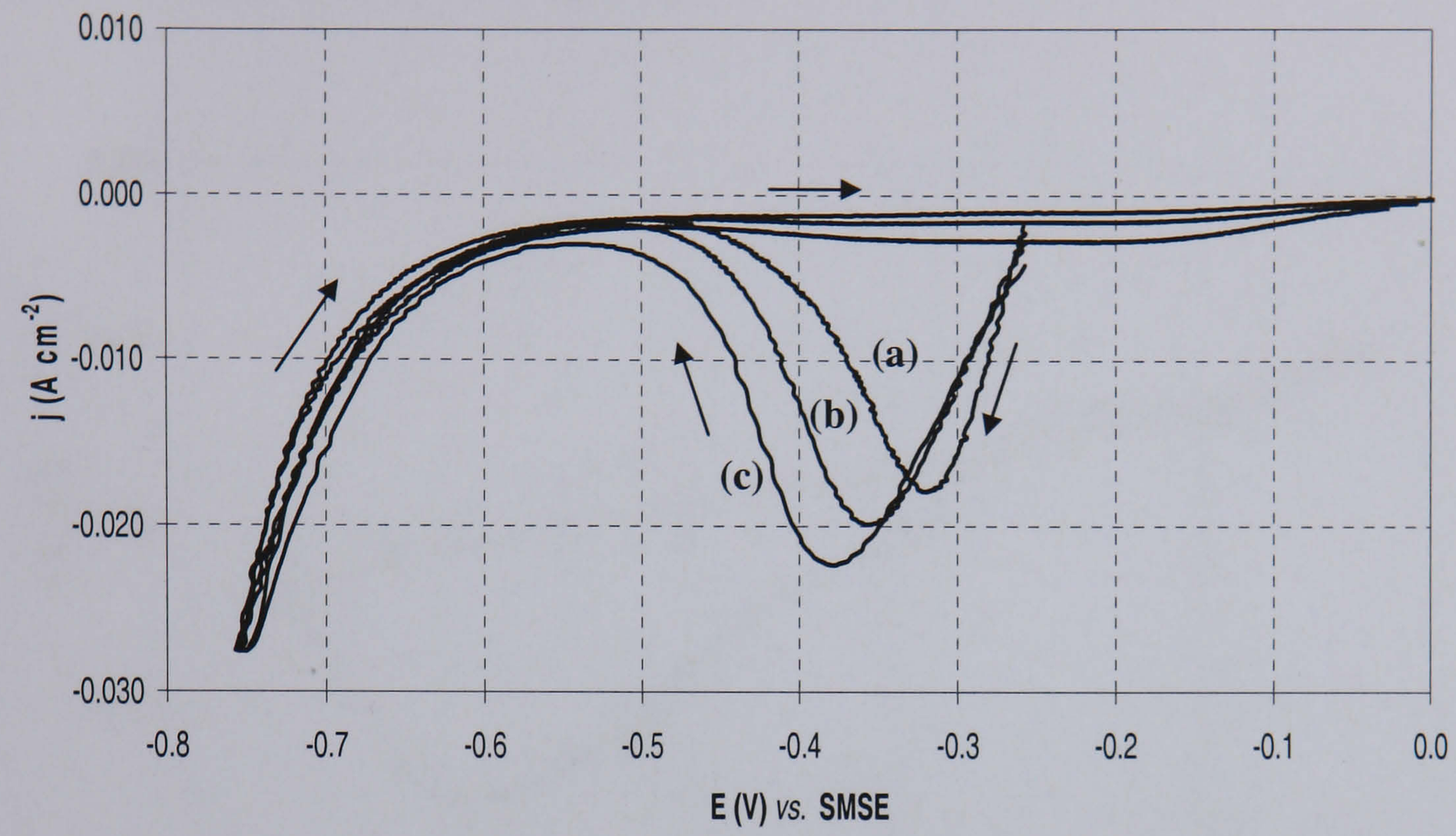

Figure 5.1: Cyclic voltammogram obtained for gold thiosulphate-sulphite aged electrolyte at (a) 2 mV s^{-1} (b) 5 mV s^{-1} and (c) 10 mV s^{-1}.

Figure 5.1 shows that as the scan rate is increased, the total current also increases and the reduction peak shifts to more negative overpotentials. This could be due to slow electron transfer kinetics at the electrode surface, ohmic drop in the solution or the kinetics of the nucleation and growth process [5.4]. Reduction of gold occurs between – 0.3 to – 0.4 V and no peaks were observed for the anodic cycle. Hydrogen evolution in this system starts at around – 0.5 V. Both the anode and cathode compartment were observed to see if any changes occurred during the electrolysis. No significant visible effects were found and the plating solution remains colourless and transparent towards the end of the experiments.

Since the cyclic voltammograms shown in figure 5.1 were obtained in large potential scan, it is difficult to observe where gold deposits. For this reason, the voltammetry

experiment was repeated at a scan rate of 2 mV s^{-1} for potential range 0 to – 0.5 V. The voltammogram is shown in figure 5.2.

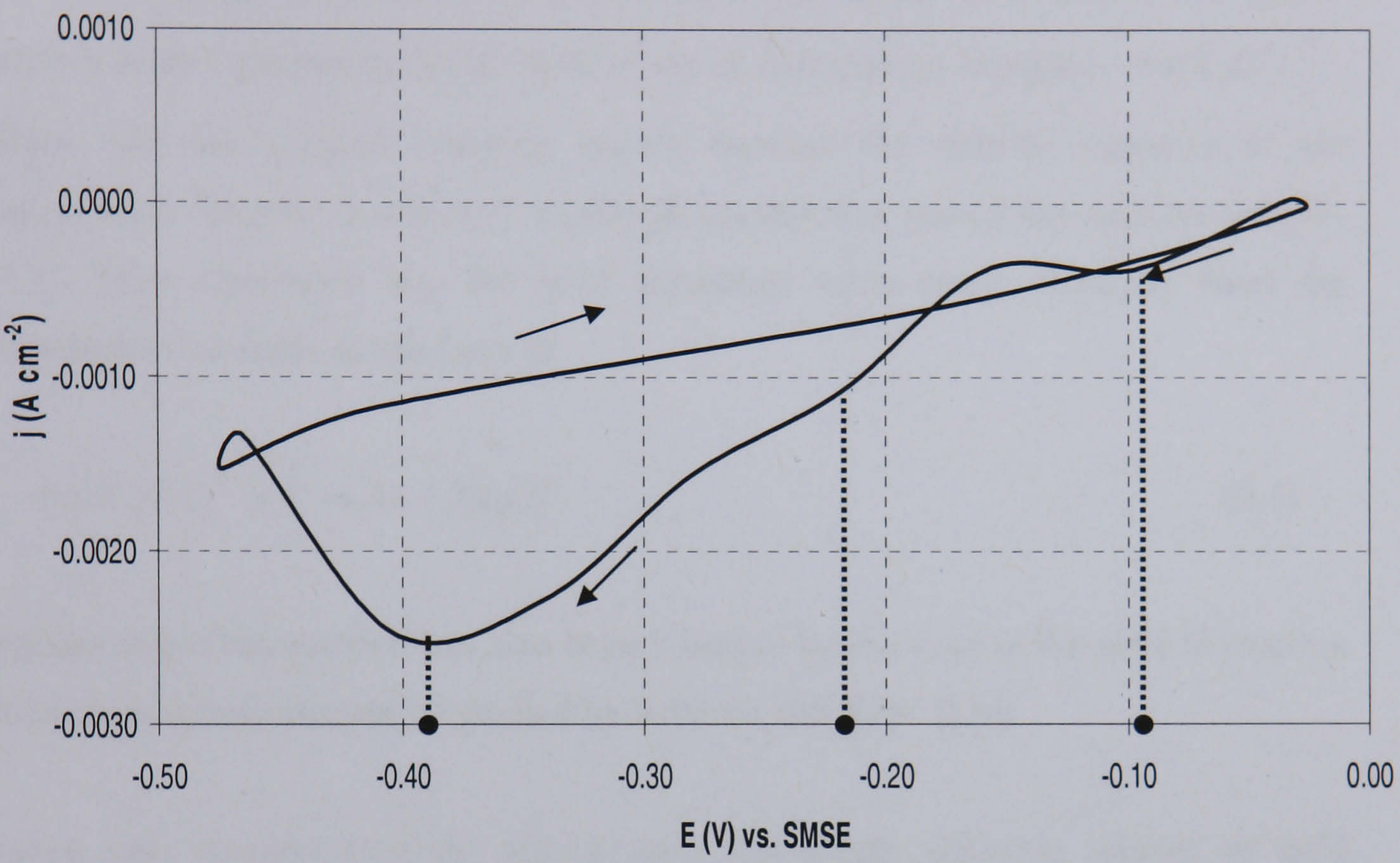

Figure 5.2: Cyclic voltammogram obtained for gold thiosulphate-sulphite aged electrolyte at 2 mV s^{-1}.

There are clearly three peaks observed from the voltammogram. An initial hump was observed at - 0.09 V followed by a shoulder at - 0.22 V. The third peak was observed at a potential close to – 0.40 V which exhibits a bigger peak in comparison to the two peaks. In our experiments, when the electrode potential was held at the first two overpotentials for a certain period of time, no traces of deposited gold was observed on the substrate surface. Therefore, it is apparent that direct reduction of the complex Au^{+} occurs at an overpotential of more negative than - 0.4 V and for this reason, the Tafel analysis was performed only for overpotential below – 0.4 V. The voltammogram in figure 5.2 also exhibits nucleation loops in the reverse scan. As was observed in many studies involving metal deposition on foreign substrate, the

nucleation loops observed from the voltammogram suggest that the metal deposition occurred by potential-driven nucleation mechanism [5.5-5.7].

An earlier study by Liew *et. al.* found that Au(I) in the fresh gold thiosulphate-sulphite bath exist preferentially in the form of thiosulphate complex, $Au(S_2O_3)_2^{3-}$, rather than the sulphite complex mainly because the stability constant of the thiosulphate complex is orders of magnitude greater than that of the sulphite complex [5.2]. They concluded that the gold deposition takes place primarily from the thiosulphate complex in the form of

$$Au(S_2O_3)_2^{3-} + \bar{e} \rightarrow Au + 2S_2O_3^{2-} \qquad (5.1)$$

Similar reduction reaction has also been found to be the case in the gold deposition from thiosulphate electrolyte studied by Sullivan and Kohl [5.8].

Taken into consideration the pH of aged electrolyte, different species of gold complex may present in the electrolyte. According to the speciation analysis of Au(I) electroplating baths containing sulphite and thiosulphate, the species $Au(S_2O_3)(SO_3)^{3-}$ and $Au(S_2O_3)(SO_3)_2^{5-}$ also present in the electrolyte and may participate in the gold deposition according to the following reaction [5.9],

$$Au(S_2O_3)(SO_3)^{3-} + \bar{e} \rightarrow Au + SO_3^{2-} + S_2O_3^{2-} \qquad (5.2)$$

$$Au(S_2O_3)(SO_3)_2^{5-} + \bar{e} \rightarrow Au + 2SO_3^{2-} + S_2O_3^{2-} \qquad (5.3)$$

Therefore, the first two peaks observed in figure 5.2 may be attributed to the reduction of gold from these complexes.

Prior studies of gold deposition from fresh thiosulphate-sulphite electrolyte on a gold surface have shown that two reduction peaks are observed at potentials – 0.6 V and – 1.0 V [5.10]. Clearly, the overpotential for the commencement of gold deposition was at lower cathodic overpotentials in the aged electrolyte.

The difference in potential for gold electrodeposition could be due to the presence of adsorbed species in fresh electrolyte. This adsorbed species is believed to be sulphite, since sulphite electrolytes are characterised by high cathodic overpotentials for gold reduction and anodic currents are entirely absent [5.1, 5.10]. The presence of a significant quantity of sulphite in the electrolyte also contributes to good quality of gold deposits obtained from the fresh electrolyte [5.2, 5.11, 5.12].

5.2.2 Tafel Analysis

Despite the complex kinetics of gold discharge and the presence of multiple reactions on the electrode surface, an effort was made to estimate the kinetics of the system. Electrochemical kinetics of the system was determined by the Tafel slope analysis in which the charge transfer coefficients are determined. Experiments were carried out at slow scan rates, 2 mV s^{-1} and 10 mV s^{-1}. Although 10 mV s^{-1} may be somewhat fast scanning rate, a comparison of Tafel constants at these two different scan rates provides an assessment of scan rate which is appropriate for our system.

Tafel plots, log $|i/i_o|$ against overpotential η are shown in figures 5.3 and 5.4. As seen in the figures, two Tafel slopes were observed for both the scan rates. Slopes A and B were designated for scan rate 2 mV $s^{-1}$and A' and B' for 10 mV s^{-1}.

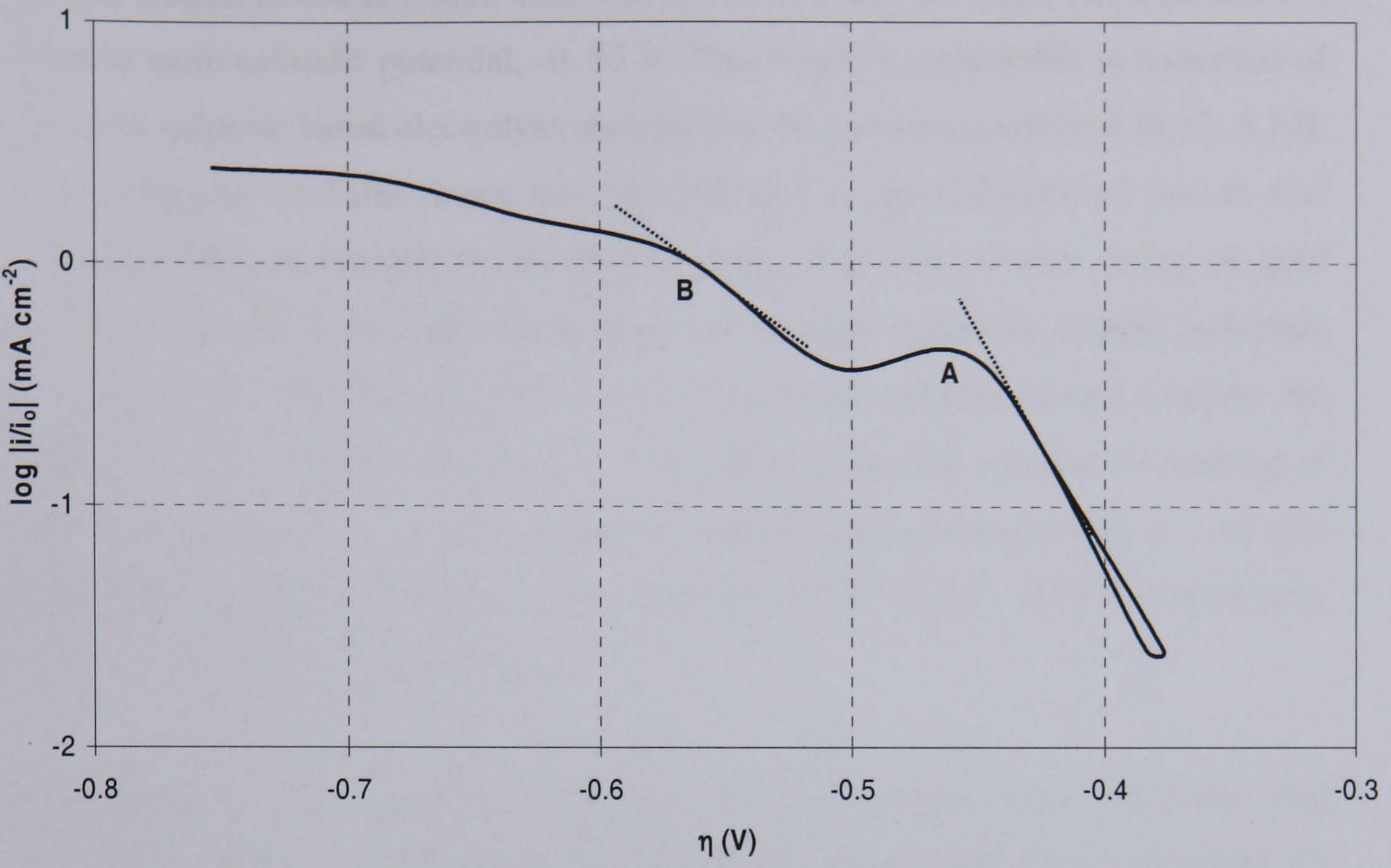

Figure 5.3: Tafel plot for gold thiosulphate-sulphite aged electrolyte at scan rate 2 mV s^{-1}.

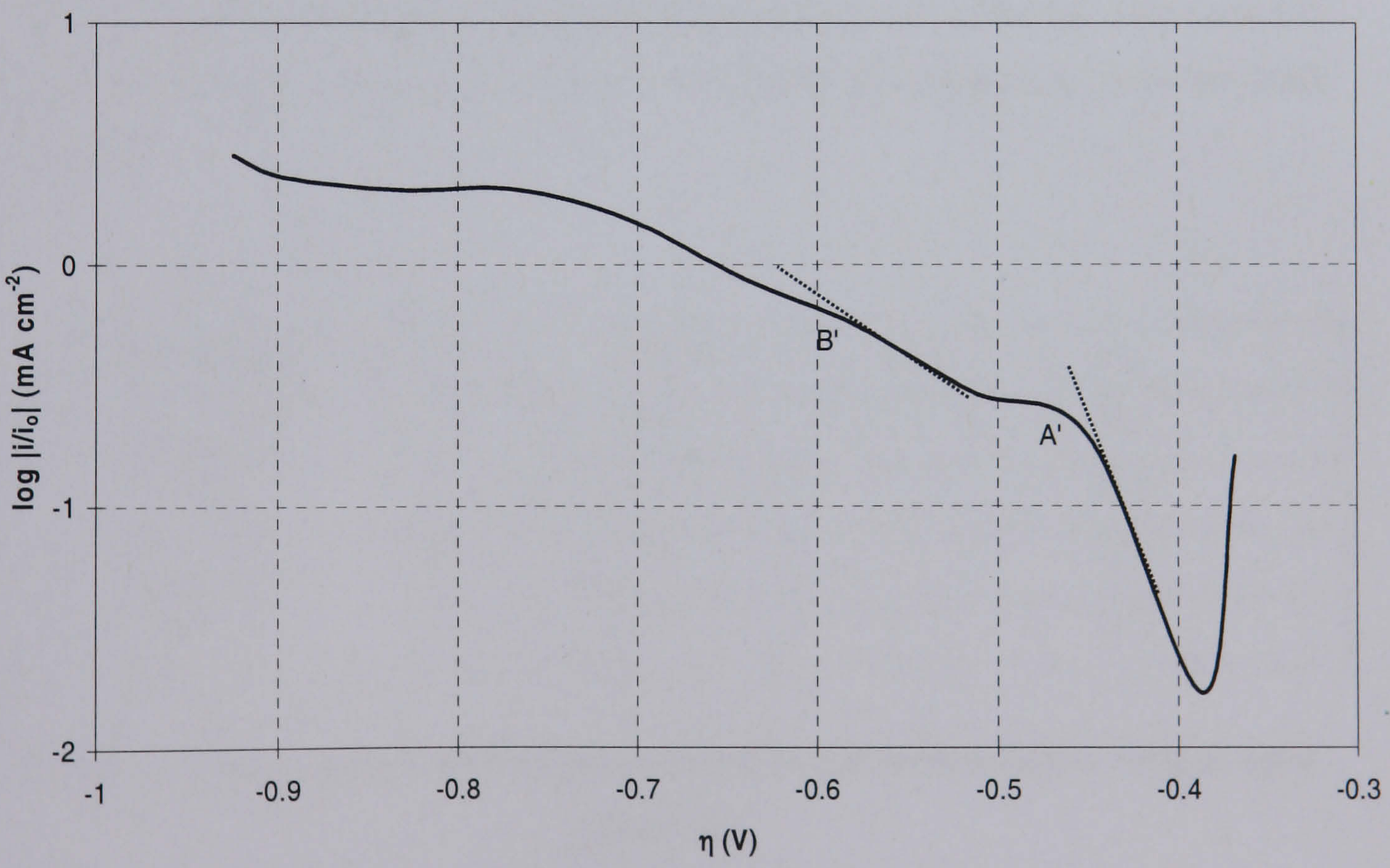

Figure 5.4: Tafel plot for gold thiosulphate-sulphite aged electrolyte at scan rate 10 mV/s.

The first slopes, A and A', were observed at – 0.43 V and the latter slope (B and B') occurs at more cathodic potential, -0. 55 V. This result is comparable to reduction of gold from sulphite based electrolyte, as reported from other researchers [5.13, 5.14]. The two regions of Tafel slopes may be attributed to the reduction of Au^{+} to Au^{0} from two different complexes. As stated earlier, there are several forms of gold complexes present in the aged electrolyte and multiple reactions of gold reduction can occur from different complexes. Although Tafel analysis cannot confirm the exact reaction, it is clear that there are two electrochemical reactions occurring at different overpotentials in the thiosulphate-sulphite aged plating system. It was also found that the current density reaches a plateau at – 0.70 V and – 0.75 V at scan rates 2 mV s^{-1} and 10 mV s^{-1}, respectively.

The cathodic charge transfer coefficients for both slopes were calculated and presented in table 5.2. It was found that the charge transfer coefficient calculated for the first slope at 10 mV s^{-1}, A', was higher than that obtained for 2 mV s^{-1}. However, the scan rate of 10 mV s^{-1} could be too fast for the system and therefore there is a slight mismatch in the charge transfer coefficient for the two different scan rates. For this reason, results obtained at 2 mV s^{-1} were used for comparison with the fresh electrolyte.

Scan rates	Slopes	α_c
2 mV s^{-1}	A	0.7
	B	0.4
10 mV s^{-1}	A'	0.9
	B'	0.3

Table 5.2: Charge transfer coefficients obtained for gold thiosulphate-sulphite aged electrolyte.

Table 5.3 shows the comparison of charge transfer coefficients between the aged and fresh thiosulphate-sulphite plating bath at a scan rate of 2 mV s^{-1}. The values of charge transfer coefficients for fresh electrolyte was taken from reference [5.10]. It was found that the charge transfer coefficient for aged electrolyte was higher, presumably due to irreversible changes within the electrolyte. The changes were due the decrease in gold concentration and pH as well as the existence of some impurities in the electrolyte.

Slopes	Gold Thiosulphate-Sulphite Electrolyte	
	α_c, fresh	α_c, aged
A	0.6	0.7
B	0.3	0.4

Table 5.3: Comparison of charge transfer coefficients between fresh and aged gold thiosulphate-sulphite electrolyte at scan rate 2 mV s^{-1}.

5.3 References

5.1 M. J. Liew, S. Roy and K. Scott, *Green Chem.*, **5**, 376 (2003).

5.2. M. J. Liew, S. Sobri and S. Roy, *Electrochim. Acta*, **51**, 877 (2005).

5.3 F. Walsh, *A First Course in Electrochemical Engineering*, Alresford Press Ltd. (1993).

5.4 D. Pletcher, R. Greef, R. Peat, L. M. Peter and J. Robinson, *Instrumental Methods in Electrochemistry*, Horwood Publishing (2001).

5.5 M. L. Munford, M. L. Sartorelli, L. Seligman and A. A. Pasa, *J. Electrochem. Soc.*, **149** (5), C274 (2002).

5.6 L. A. Carlos, C. A. Souza, E. M. J. A. Pallone, R. H. P. Francisco, V. Cardosa and B. S. Lima-Neto, *J. Appl. Electrochem.*, **30**, 987 (2000).

5.7 S. Fletcher, C. S. Halliday, D. Gates, M. Wescott, T. Lwin and G. Nelson, *J. Electroanal. Chem.*, **159**, 267 (1983).

5.8 A. M. Sullivan and P. A. Kohl, *J. Electrochem. Soc.*, **144** (5), 1686 (2006).

5.9 T. A. Green and S. Roy, *J. Electrochem. Soc.*, **153** C157 (2006).

5.10 M. J. Liew, *Novel Gold Electrodeposition Process for Micro and Opto Electronics*, PhD Thesis, University of Newcastle upon Tyne (2002).

5.11 H. Honma and Y. Kagaya, *J. Electrochem. Soc.*, **140** (9), L135 (1993).

5.12 H. Honma and K. Hagiwara, *J. Electrochem. Soc.*, **142** (1), 81 (1993).

5.13 K. Wang, R. Beica and N. Brown, *Electronics Manufacturing Technical Symposium*, (2004).

5.14 C. Zur and M. Ariel, *J. Appl. Electrochem.*, **12**, 231 (1982).

CHAPTER 6:

RESULTS:

NUCLEATION STUDIES

OF GOLD ON

CARBON ELECTRODES

In this work, we have investigated the electrocrystallisation of gold on glassy and graphitic carbon electrodes. The two different forms of carbon were chosen due to the difference in their structure. The choice of glassy carbon allows us to examine the microstructure when the substrate has no preferred texture, whereas the graphitic electrode allows us to examine when the substrate has a well established structure. We have examined the effect of electrode potential on particle size, nucleation density and microstructure. This work was carried out mainly to investigate of gold can be recovered from a spent thiosulphate-sulphite electrolyte, and to determine the microstructure of the obtained deposits or particles.

6.1 Voltammetry Curves

Cyclic voltammetry was performed to determine the potential for gold nucleation on carbon electrodes. The voltammetry experiments were carried out for three cycles from 0 to – 1.4 V at scan rates ranging from 5 to 100 mV s^{-1}. Figures 6.1 and 6.2 show cyclic voltammograms for glassy carbon and graphite electrodes respectively, taken from the second cycle of the scan at of 5 mV s^{-1}. Both voltammograms are characterized by two cathodic peaks or shoulders – a first peak close to - 0.5 V (vs. SMSE) followed by another peak close to - 0.85 V for the glassy carbon and - 0.9 V for the graphite. It is worth noting that, unlike deposition on gold substrates [6.1, 6.2], the peaks are not sharp.

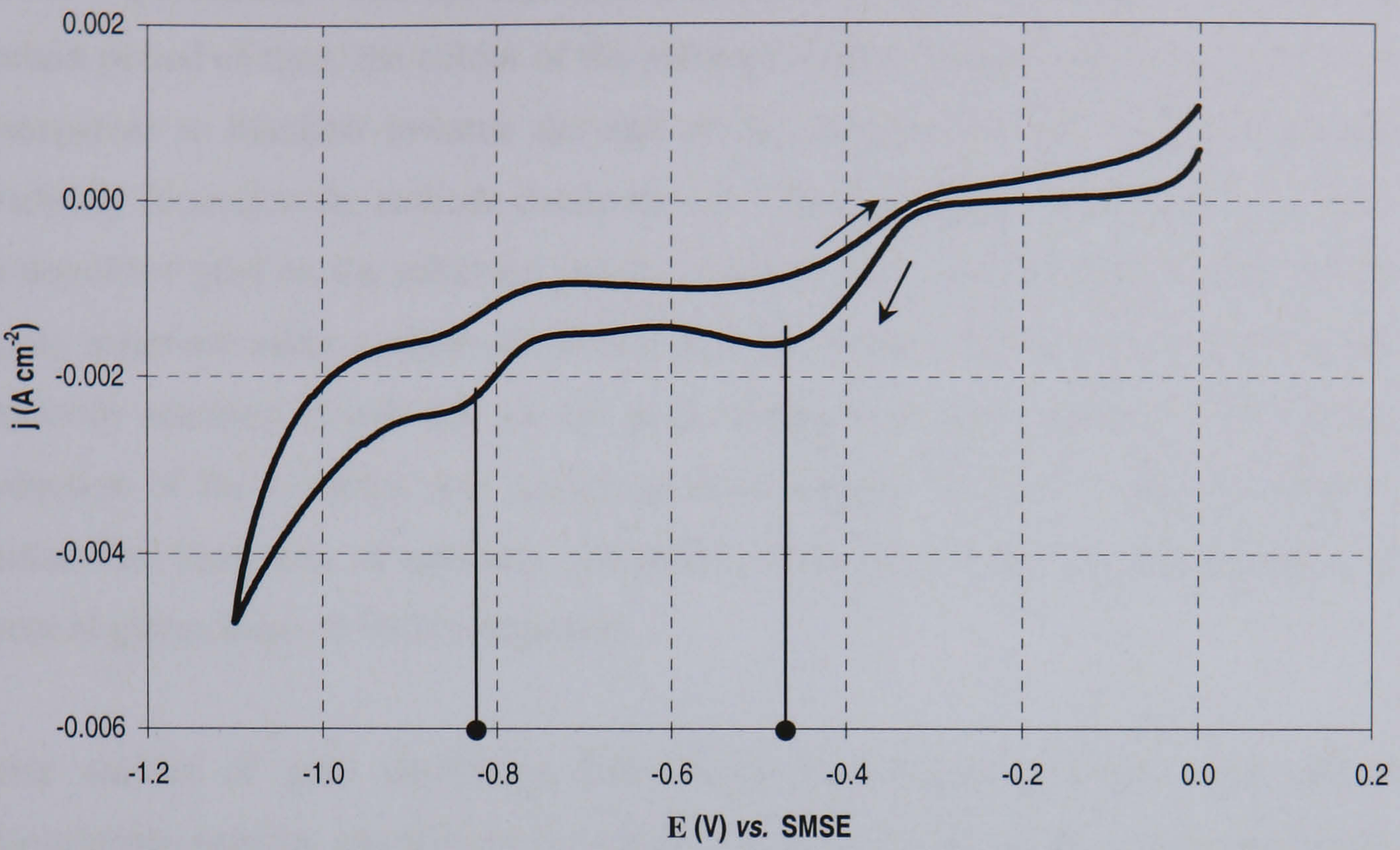

Figure 6.1: Cyclic voltammetry of gold on stationary glassy carbon at 5 mV s^{-1} from an aged thiosulphate-sulphite electrolyte.

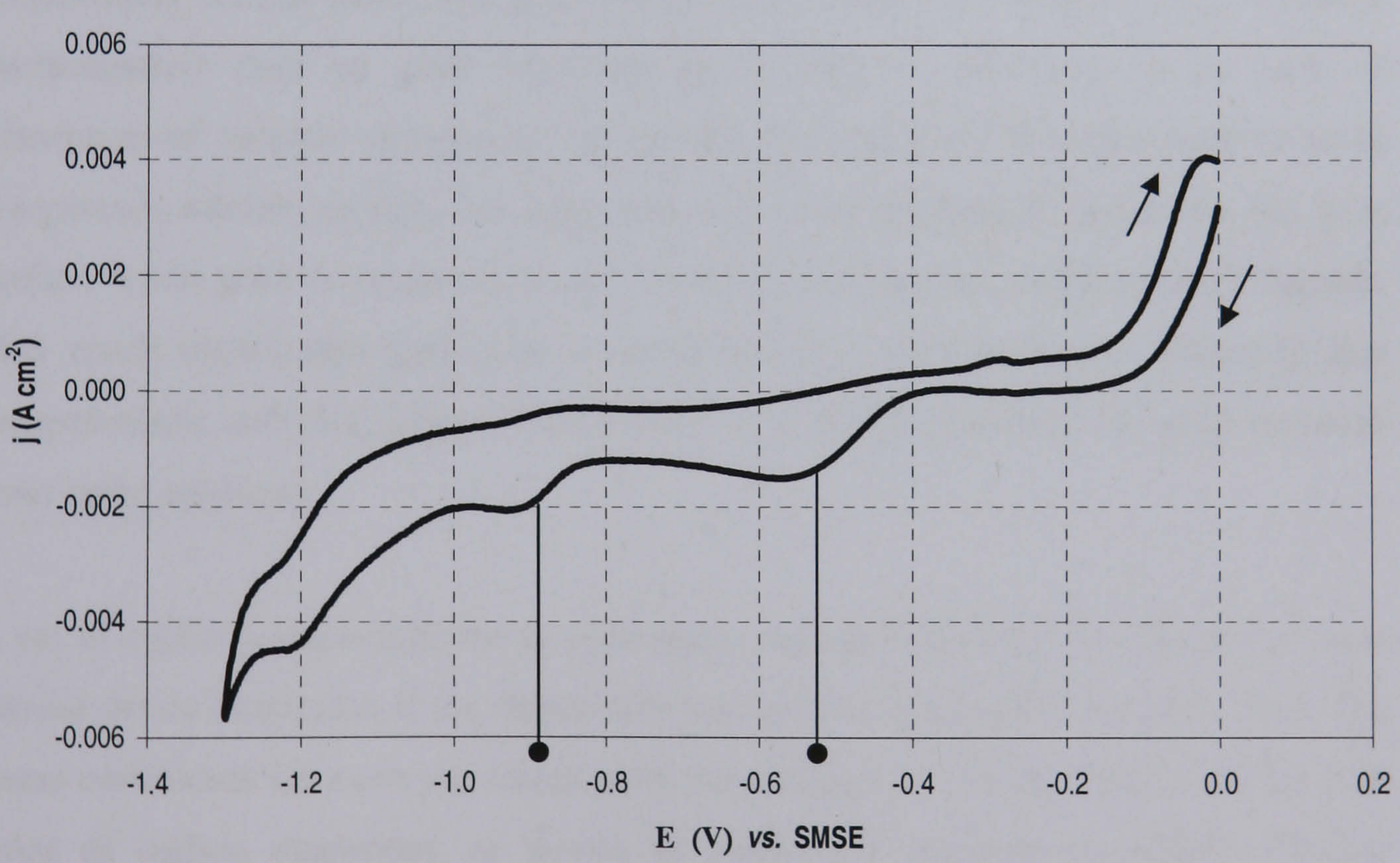

Figure 6.2: Cyclic voltammetry of gold on stationary graphite at 5 mV s^{-1} from an aged thiosulphate-sulphite electrolyte.

In our experiments, when the electrode potential was held just above - 0.5 V for a certain period of time, the colour of the plating solution changed from colourless and transparent to blackish towards the end of the experiment and black precipitates gradually formed in the cathode compartment. Visual observations revealed no traces of deposited gold on the substrate and the blackish layer on electrode surface can be easily removed using a clean cloth and distilled water. Therefore, at – 0.5 V, the electrode reaction is not due to the gold discharge from a complex. The direct reduction of the complex Au^{+} occurs at more negative potentials and in order to initiate the formation of adherent and stable nuclei on carbon, an overpotential of more negative than - 0.75 V is required.

Prior studies of gold deposition from fresh thiosulphate, sulphite, and mixed thiosulphate-sulphite electrolytes on a gold surface have shown that a reduction peak is observed at potentials below - 0.8 V [6.1, 6.3, 6.4]. However, gold deposition was observed only at significantly lower potentials, i.e. - 1.5 V. Clearly, our cyclic voltammetry results show that gold reduction proceeds on carbon at less cathodic overpotentials than on gold substrates [6.1]. This is attributed to the lack of adsorption of sulphur compounds on carbon. It is well known that sulphur-based compounds adsorb strongly on gold, and that some adsorption occurs on the gold surface when gold is polarized in an electrolyte containing sulphur-based ligands. This result shows that gold can be reduced from the solution at relatively low overpotentials and that carbon would serve as a useful electrode for gold recovery from spent solutions.

A set of cyclic voltammograms at scan rates varying between 5 to 100 mV s^{-1} was carried out to determine if the deposition was governed by diffusion [6.5, 6.6]. The linear correlation between the return peak current density and the scan rates for both types of carbon electrodes, as shown in figure 6.3, suggests a diffusion-limited process.

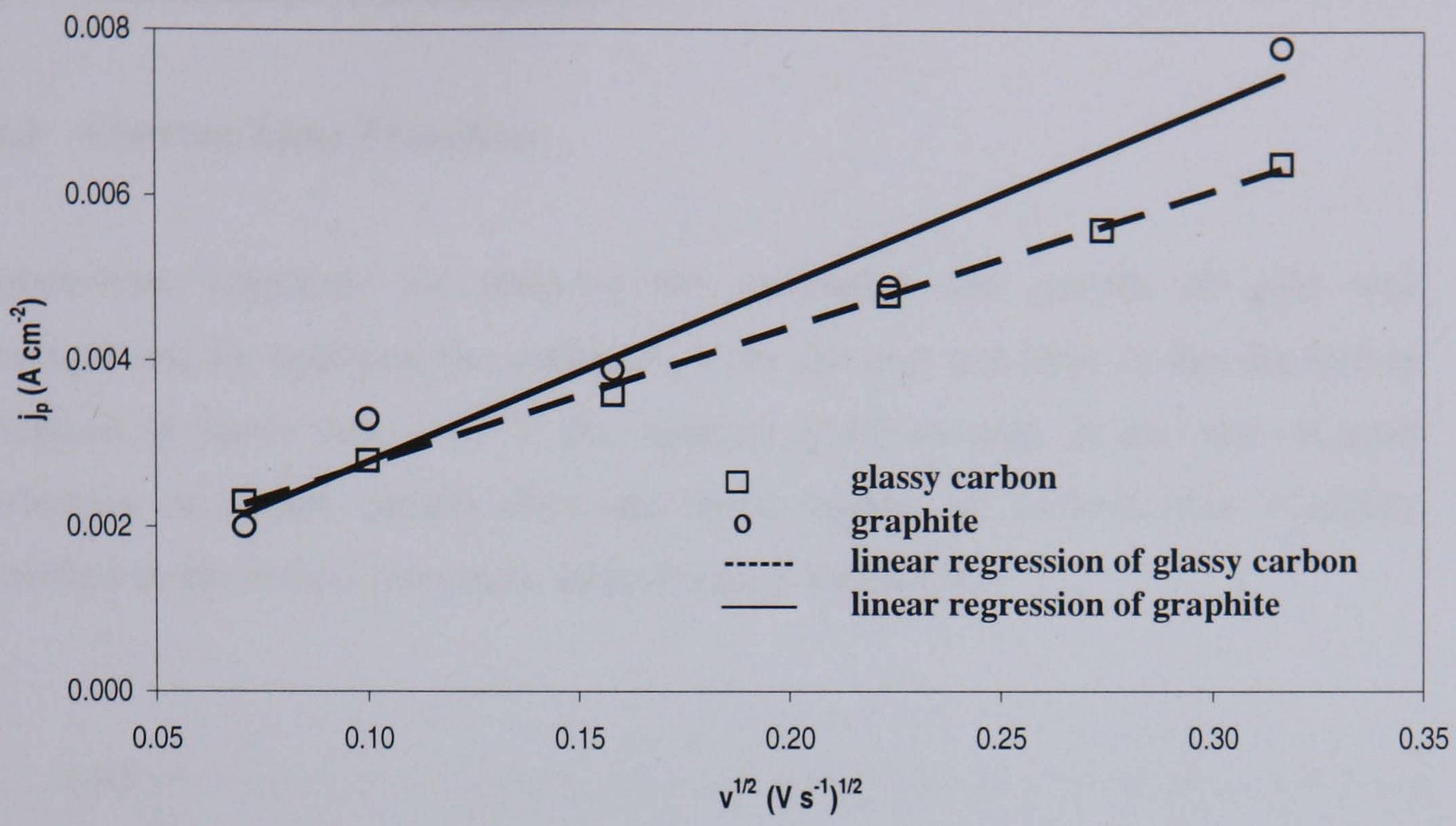

Figure 6.3: Randles-Sevcik plots of gold on glassy carbon and graphite electrodes

The diffusion coefficient was calculated using Randles-Sevcik equation, as presented in equation 6.1 [6.5].

$$I_p = (2.69 x 10^{-5}) n^{3/2} c_o D^{1/2} \upsilon^{1/2} \qquad (6.1)$$

The best-fit line for each data set is determined by linear regression analysis and yielded diffusion coefficients of 1.84 x 10^{-6} cm^2 s^{-1} for gold deposition on glassy carbon and 3.37 x 10^{-6} cm^2 s^{-1} for gold on graphite. The different values of diffusion coefficients were due to the different in nucleation mechanism of gold at the two carbon electrodes. These values were also found to be nearly an order of magnitude greater than those observed in the fresh electrolyte [6.1]. This could be due the reduction of different species of gold within the aged solution.

6.2 Chronoamperometric Studies

6.2.1 Current-Time Transients

Current-time transients for studying the nucleation and growth of gold was accomplished by applying the potentials from the rest potential to the deposition potentials of lower than – 0.7 V for duration of 60 seconds. In the case of gold nucleation on glassy carbon electrode, three regions of interest were typically identified in the current transients, as is shown in figure 6.4.

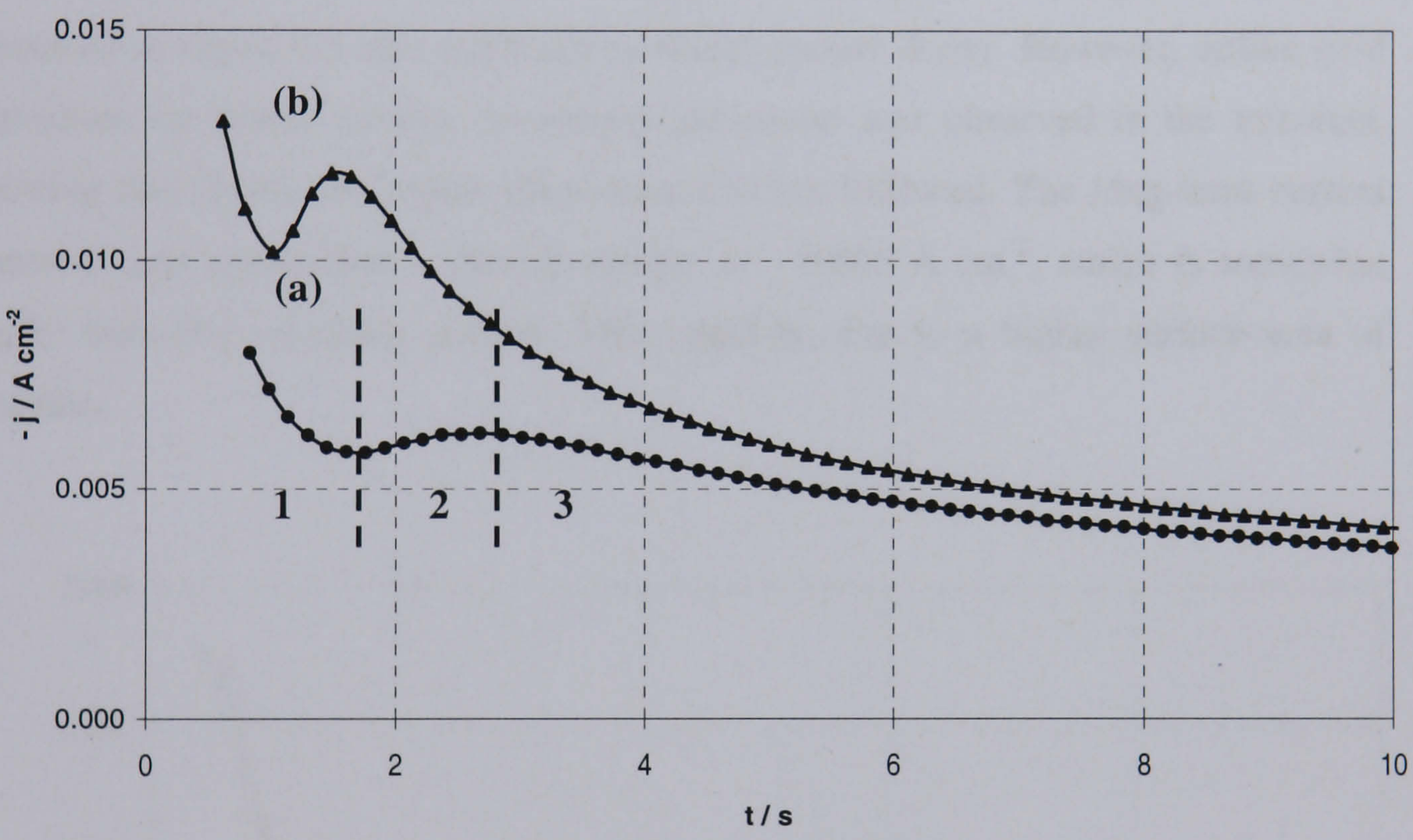

Figure 6.4: Current-time transient for nucleation of gold on glassy carbon at (a) – 850 V and (b) – 0.925 V

For the first two seconds after application of a potential, there is a sharp decay in the current, mainly due to capacitive charging [6.7, 6.8] and decay of local currents [6.7]. The capacitive current increased with applied potential, but the time required for the

decay decreased. In our analysis, current data for the first two seconds were, therefore, not used.

After the initial decay, the current transient exhibited a hump or a shoulder (for potentials greater than - 0.850 V). As the applied potential is lowered, this current maximum became more pronounced and its height and position increased as the applied potential became more cathodic, as predicted by classic nucleation phenomena [6.8-6.11]. At longer time intervals, the current reached a plateau of - 0.003 A cm^{-2}.

The potentiostatic current transient of gold on graphite, an example of which is presented in figure 6.5 also exhibited an initial current decay. However, unlike gold deposition on glassy carbon, no current maximum was observed in the transient, showing that classic nucleation phenomenon is not followed. The long-term current transient data approached a current density of - 0.005 A cm^{-2}, which is somewhat higher than that of glassy carbon. This could be due to a higher surface area of graphite.

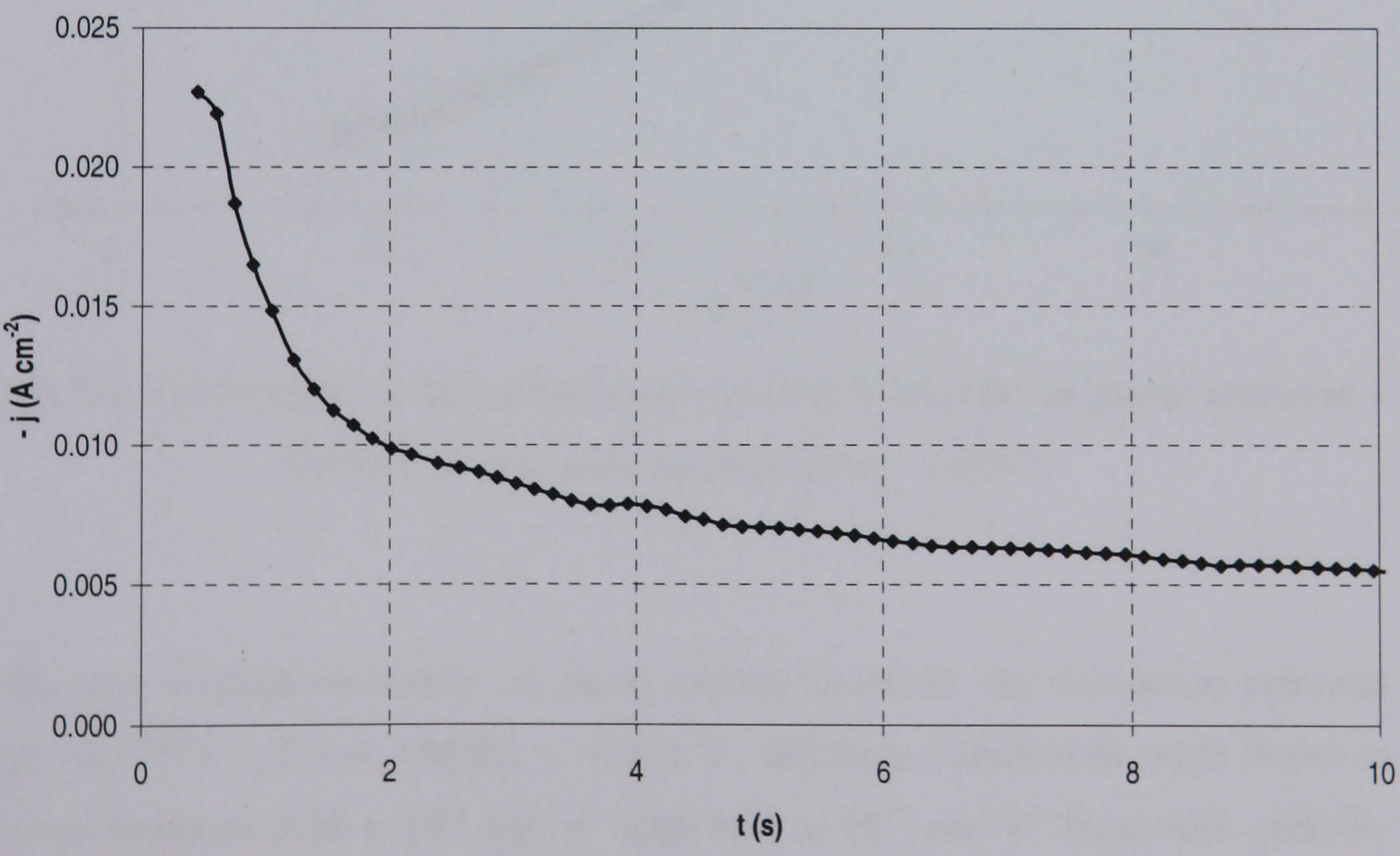

Figure 6.5: Current-time transient for nucleation of gold on graphite at – 1.05 V

6.2.2 Diffusion Phenomena

The chronoamperometry results from the steady state region of j *vs.* t data (region 3 of figure 6.4) can be used to calculate diffusion coefficients at various overpotentials using the Cottrell equation. Figure 6.6 shows that for glassy carbon and graphite electrodes, the current is indeed found to be linear with respect to $t^{-1/2}$ for glassy carbon, as predicted by the Cottrell equation.

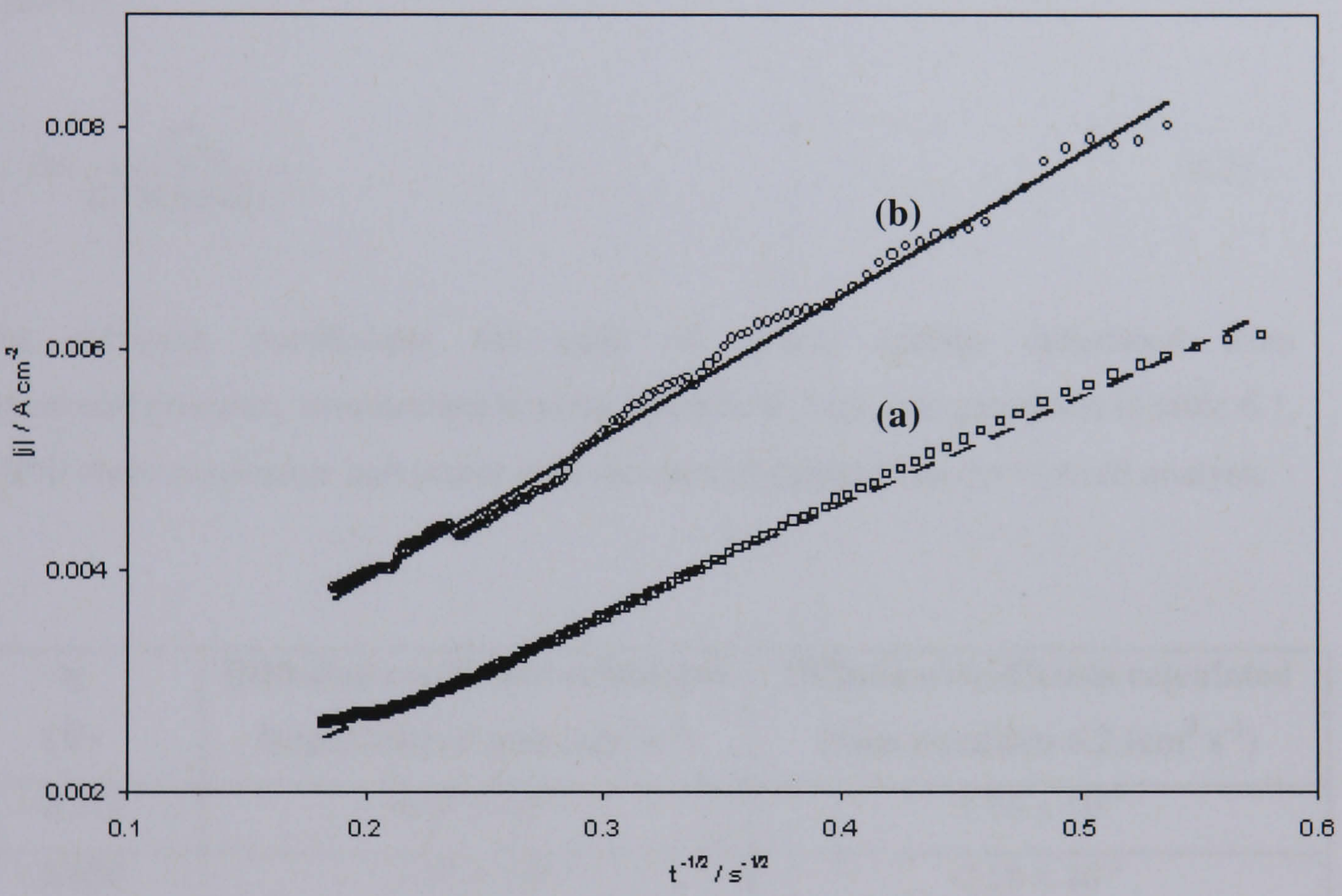

Figure 6.6: Cottrell plot of the current-time transient of (a) gold on glassy carbon at – 0.850 V and (b) gold on graphite at – 1.050 V

In the case of gold nucleation on glassy carbon electrode, for deposition potential range -0.775 V < E (*vs.* SMSE) < -0.925 V, diffusion coefficients were found to increase between 6.24 x 10^{-6} cm^2 s^{-1} and 3.00 x 10^{-5} cm^2 s^{-1} from low cathodic overpotentials to the higher values, as is shown in table 6.1. While the lower value is

similar in magnitude to the value obtained from the Randles-Sevcik equation. difference between the diffusivity at low and high overpotentials is nearly an order of magnitude. It can be conceived that there are different species of gold within the aged solution, which reduce at different overpotentials, although we assume that only $Au(S_2O_3)_2^{3-}$ species are involved in the reduction process. This assumption, in turn, could be reflected through changing diffusivity.

The diffusivity of gold can also be calculated from the current maximum and the time at which the maximum is observed [6.8] in region 2, using the following equation:

$$D = \frac{I_m^2 t_m}{0.1629 (nFc)^2} \qquad (6.2)$$

The diffusion coefficients for gold on glassy carbon calculated from chronoamperometry measurements using equation 6.2 are also presented in table 6.1, which show reasonable agreement with the ones obtained from the Cottrell analysis.

η (V)	**Diffusion coefficient calculated from Cottrell plot ($cm^2\ s^{-1}$)**	**Diffusion coefficient calculated from equation 6.2 ($cm^2\ s^{-1}$)**
- 0.775	6.24×10^{-6}	1.76×10^{-5}
- 0.850	1.53×10^{-5}	2.18×10^{-5}
- 0.925	3.00×10^{-5}	4.57×10^{-5}

Table 6.1: Values of diffusion coefficients of gold deposition on glassy carbon calculated by different methods.

In the absence of a classic nucleation curve for graphite, the current transient data for gold deposition after 3 seconds was used to determine diffusion coefficient of gold species. As shown in figure 6.6, the dependence of j is linear with respect to $t^{-1/2}$. as

was found for glassy carbon. When a Cottrell analysis was applied for deposition potential range -0.80 V < E (*vs.* SMSE) < -1.35 V, diffusion coefficients ranging from 4.06 x 10^{-6} to 3.13 x 10^{-5} cm^2 s^{-1}, were obtained, which are in agreement with the values obtained for glassy carbon.

6.2.3 Nucleation Phenomena

The nucleation characteristics of gold on glassy carbon were analysed using data from the rising part as well as the current maximum observed in region 2 of the current time transient. At the early stage of electrochemical nucleation on glassy carbon, the nuclei are widely spaced, thus it was assumed that there was no interaction between nuclei during this time. The experimental j *vs.* t data, therefore, can be described by equation 6.3 for the regime well before the maximum in the observed current transient.

$$I(t) = \alpha t^{v} \tag{6.3}$$

For the case of instantaneous nucleation, v is ½ and α is described by equations 6.4 and 6.5 for hemispherical nuclei growing under planar and spherical diffusion, respectively.

$$\alpha = \frac{8nFM^2c^3D^{3/2}}{\rho^2\pi^{1/2}}N_o \tag{6.4}$$

$$\alpha = \frac{nF\pi M^{1/2}(2Dc)^{3/2}}{\rho^{1/2}}N_o \tag{6.5}$$

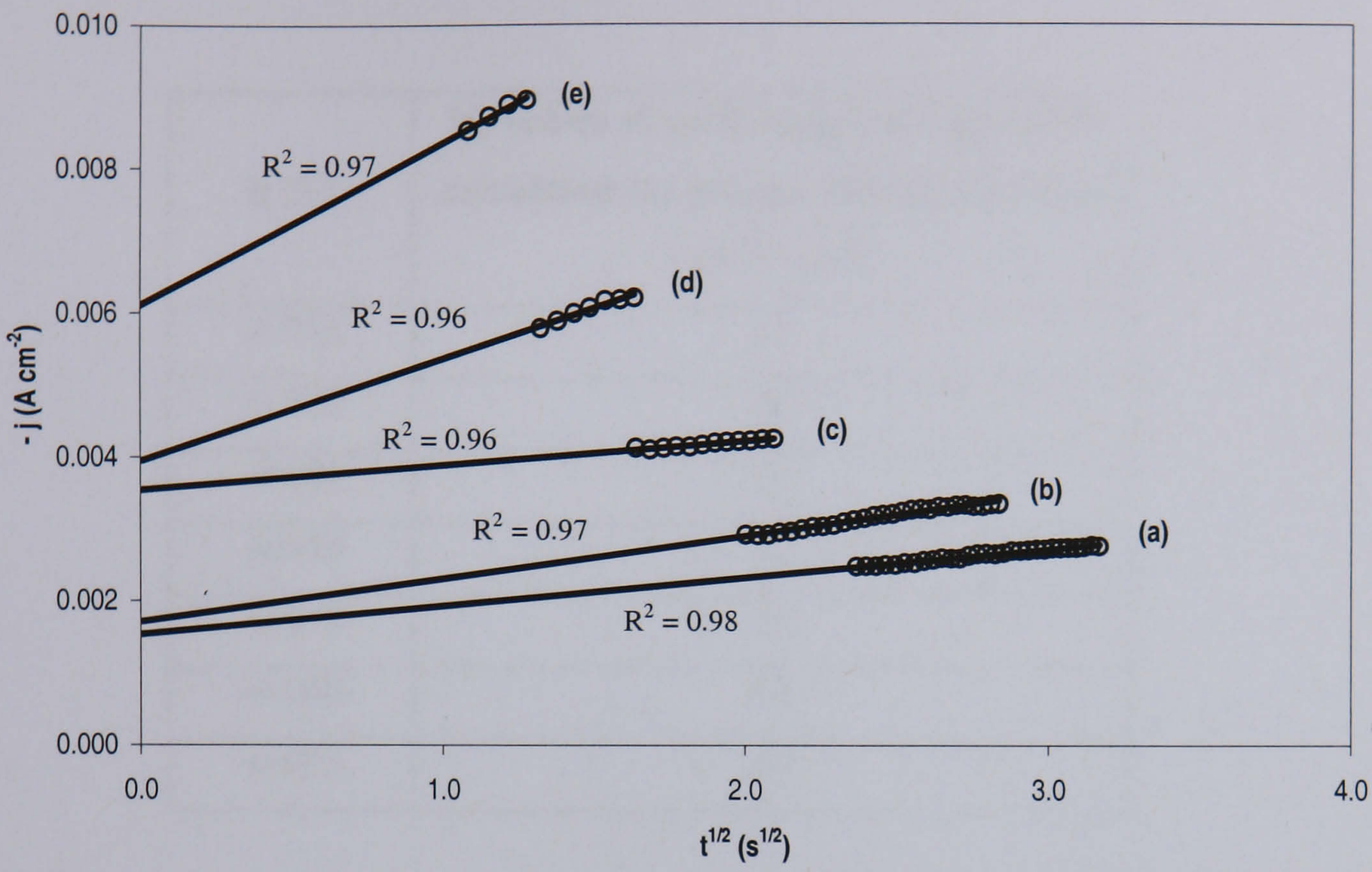

Figure 6.7: Linear dependence between j and $t^{1/2}$ corresponds to the early stage of gold deposition on glassy carbon at overpotentials (a) – 0.775 V (b) – 0.800 V (c) – 0.825 V (d) – 0.850 V and (e) – 0.875 V.

The result in figure 6.7 shows that a plot of j *vs.* $t^{1/2}$ observes linearity in region well before the current maximum in the current transient, indicative of hemispherical growth under instantaneous nucleation. The slopes of j *vs.* $t^{1/2}$ plots can be used to determine the nuclei density, N_o, using equations 6.4 and 6.5 for planar and spherical diffusion, respectively, and the diffusivity at the respective overpotential. However, this analysis does not allow us to distinguish between the two diffusion processes, and therefore a second check against electron micrographs has to be made. Microscopy analysis of gold on glassy carbon are shown in section 6.4, and it is apparent that the nuclei density calculated using equation 6.4, i.e., for planar diffusion, is in good agreement with the results obtained from microscopy. The values of the absolute number of nuclei at particular overpotentials calculated for planar diffusion are shown in table 6.2.

η (V)	**N_o values at early stages of deposition calculated for planar diffusion process (10^{-8} / cm^2)**
-0.775	13
-0.800	18
-0.825	13
-0.850	32
-0.875	39
-0.900	63
-0.925	50

Table 6.2: N_o values of gold deposition on glassy carbon under planar diffusion process.

As the radii of nuclei increase, diffusion zones begin to overlap [6.8, 6.12]. This part of the current transient is represent by the current maximum, which is located between regions 2 and 3. This portion of the current transient is interpreted by plotting a dimensionless (or reduced) current transient, I^2 / I_m^2 *vs.* the dimensionless inverse time, $(t/t_m)^{-1}$. Such a plot for glassy carbon at an overpotential of - 0.85 V is shown in figure 6.8. It should be noted that since the dimensionless current is plotted as a function of dimensionless inverse time, the short time data of figure 6.4 translates to the larger values of $(t/t_m)^{-1}$ in figure 6.8.

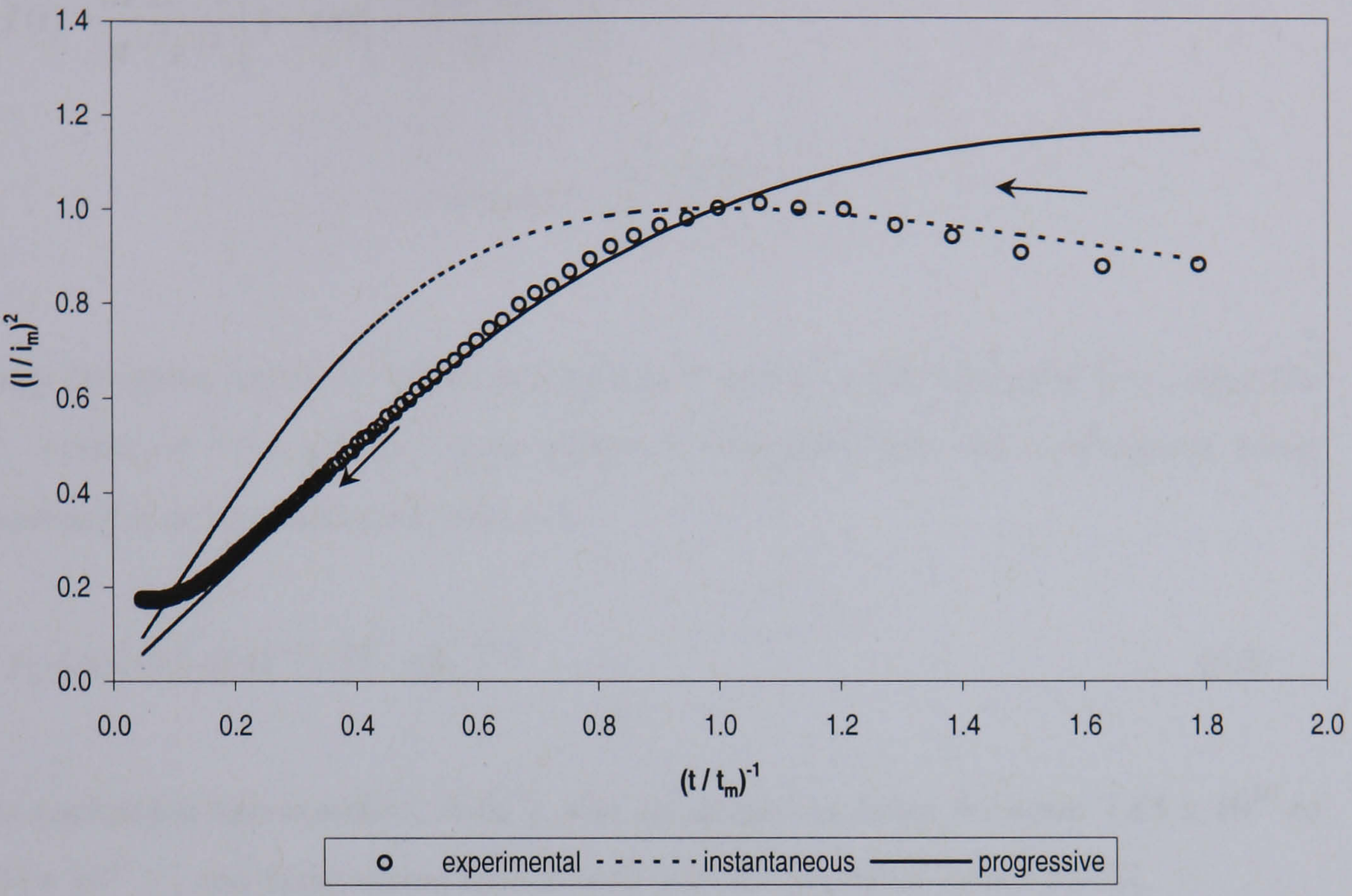

Figure 6.8: Dimensionless current-time transient for nucleation of gold on glassy carbon at – 0.850 V and corresponding theoretical curves for instantaneous and progressive nucleation

As shown in figure 6.8, the reduced data for short time current transient is well represented by equation 6.4, which described instantaneous nucleation under planar diffusion. However, the data representing current maximum of the dimensionless current transient, is best represented by equation 6.6 below, which describes progressive nucleation.

$$\frac{I^2}{I_m^2} = \frac{1.2254}{t/t_m}\left\{1 - \exp\left[-2.3367\left(t/t_m\right)^2\right]\right\}^2 \qquad (6.6)$$

This equation is derived from

$$I(t)=\frac{nFD^{1/2}c}{\pi^{1/2}t^{1/2}}\left[1-\exp\left(\frac{-A\pi k' Dt^2}{2}\right)\right] \qquad (6.7)$$

$$\text{where } k''=\frac{4}{3}\left(\frac{8\pi cM}{\rho}\right)^{1/2}$$

Using the mean value of diffusion coefficient and k' value obtained from equation 6.7, values of AN_o for the entire range of overpotentials were calculated using equation 6.8 and presented in table 6.3.

$$I_m=0.4615\,nFD^{3/4}c\left(k''AN_o\right)^{1/4} \qquad (6.8)$$

The nucleation rate constant, A (s^{-1}), was calculated to range between 7.85×10^{10} to 6.24×10^{12} s^{-1} and these values agrees well with the reported values [6.13].

η (V)	**AN_o values calculated from dimensionless transient ($cm^{-2}s^{-1}$)**
-0.775	1.57×10^{3}
-0.800	3.29×10^{3}
-0.825	8.53×10^{3}
-0.850	3.76×10^{4}
-0.875	1.64×10^{5}
-0.900	1.93×10^{5}
-0.925	4.99×10^{5}

Table 6.3: AN_o values of gold deposition on glassy carbon.

These analyses indicate that the early stages of nucleation of gold is characterised by instantaneous nucleation, which changes to progressive nucleation as time proceeds.

Different behaviour was observed for gold reduction from other electrolytes. In the case of gold nucleation from plating baths containing Au (III) in chloride [6.14, 6.15] and citrate [6.7], the electrocrystallisation mechanism changes from progressive nucleation at the early stages to three-dimensional instantaneous nucleation at longer times.

As shown in the potentiostatic current transient of gold on graphite, figure 6.5, no current maximum was observed in the transient therefore no classic nucleation analyses could be carried out. This characteristic was affirmed by the observed microscopy images of graphite, shown in the next section.

6.3 Deposit Characterisation

Figure 6.9 shows the scanning electron micrographs of gold nanoparticles on glassy carbon after 60 seconds of potential application. These images illustrate the influence of overpotentials on crystal distribution and size.

As shown in the images of gold nucleation on glassy carbon, deposition at - 0.775 V yields a smaller number of nuclei. Notably, the nuclei are of nearly the same size, the average size being 680$\pm$10 nm. At intermediate overpotential, two distinct nuclei sizes are visible, with average particle sizes of 650 nm and 160 nm. As the applied potential is lowered, homogeneous nanocrystals ranging in diameter from 80 to 100 nm are obtained. A manual image analysis showed that the range of crystal diameter had a relative deviation of less than 1% for potentials below -1.0 V.

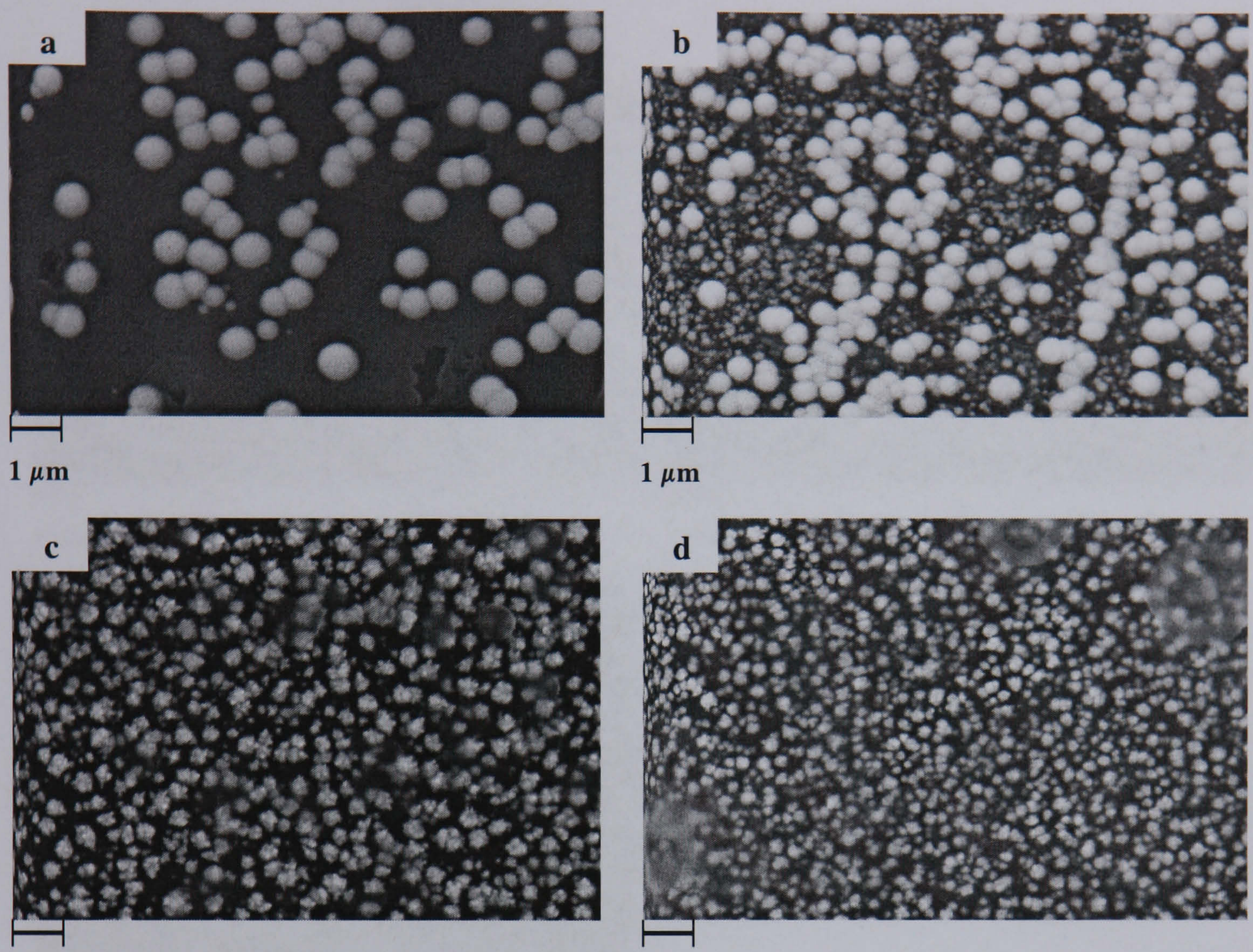

Figure 6.9: SEM images of gold on glassy carbon at deposition overpotentials: (a) – 0.775 V (b) – 0.925 V (c) – 1.075 V and (d) – 1.200 V

Figure 6.10 contains representative scanning electron micrographs of gold nanoparticles on graphite electrodes. The figure shows the deposits after 60 seconds of potential application. When a constant potential within the range $-0.9 < \eta < -1.2$ V is applied to the electrode, the average size of the particles on graphite remained more or less uniform, at about 100-110 nm throughout the potential range. In the same potential range, electrodeposited gold nuclei obtained on glassy carbon were less uniform, and decreased from 200 nm to 85 nm as the potential was lowered. This result shows that the size of gold nuclei deposited on graphite surface is not strongly influenced by potentiostatic pulse.

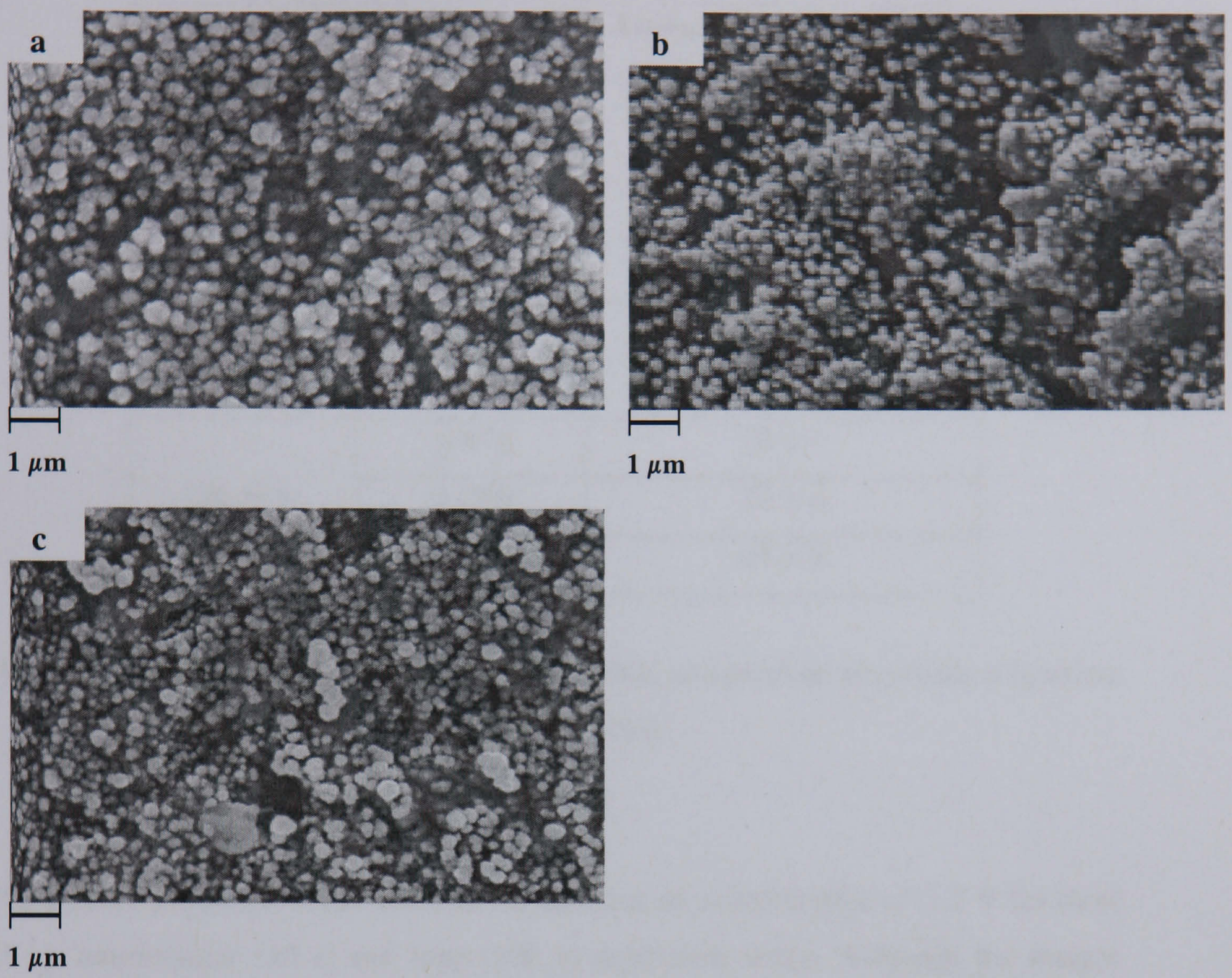

Figure 6.10: SEM images of gold on graphite as a function of deposition overpotentials: (a) – 0.950 V (b) – 1.20 V and (c) – 1.350 V.

In order to determine the density of gold nuclei, 15 areas were randomly chosen from the micrographs of the substrate surface with each of the area being 1 μm^2. The values, as a function of overpotential, are listed in table 6.4. As expected, the density of nuclei increased with increasing overpotential for gold reduction. These nuclei density values are an order of magnitude 10^1-10^2 smaller compared to those reported for gold deposition from chlorides [6.14], which could be due to the difficulty of reduction from sulphite based electrolytes.

Substrates	η (V)	Average particle density calculated from SEM (10^{-8} / cm^{-2})
Glassy Carbon	-0.775	4 ± 3
	-0.925	8 ± 3
	-1.075	13 ± 4
	-1.200	19 ± 6
Graphite	-0.950	20 ± 7
	-1.200	22 ± 6
	-1.350	25 ± 6

Table 6.4: Nuclei density of gold on glassy carbon and graphite electrodes a function of overpotentials.

Figure 6.11 shows the distribution of Au nuclei at an overpotential of -1.2 V for short (1 s), intermediate (10 s) and long (100 s) deposition times. Although the images obtained at short time were during the current decay, it can be seen that nuclei are deposited during the period of capacitive charging. The images presented indicate that the electrodeposition of Au on glassy carbon for 1 s results in uniform coverage of Au nuclei having a relatively uniform size of 80 ± 5 nm. It is also observed that each nuclei grows independently during this stage. At the intermediate period, there is some coalescence of Au crystals and at longer times, large aggregates having diameter ranging from 100 to 300 nm are obtained.

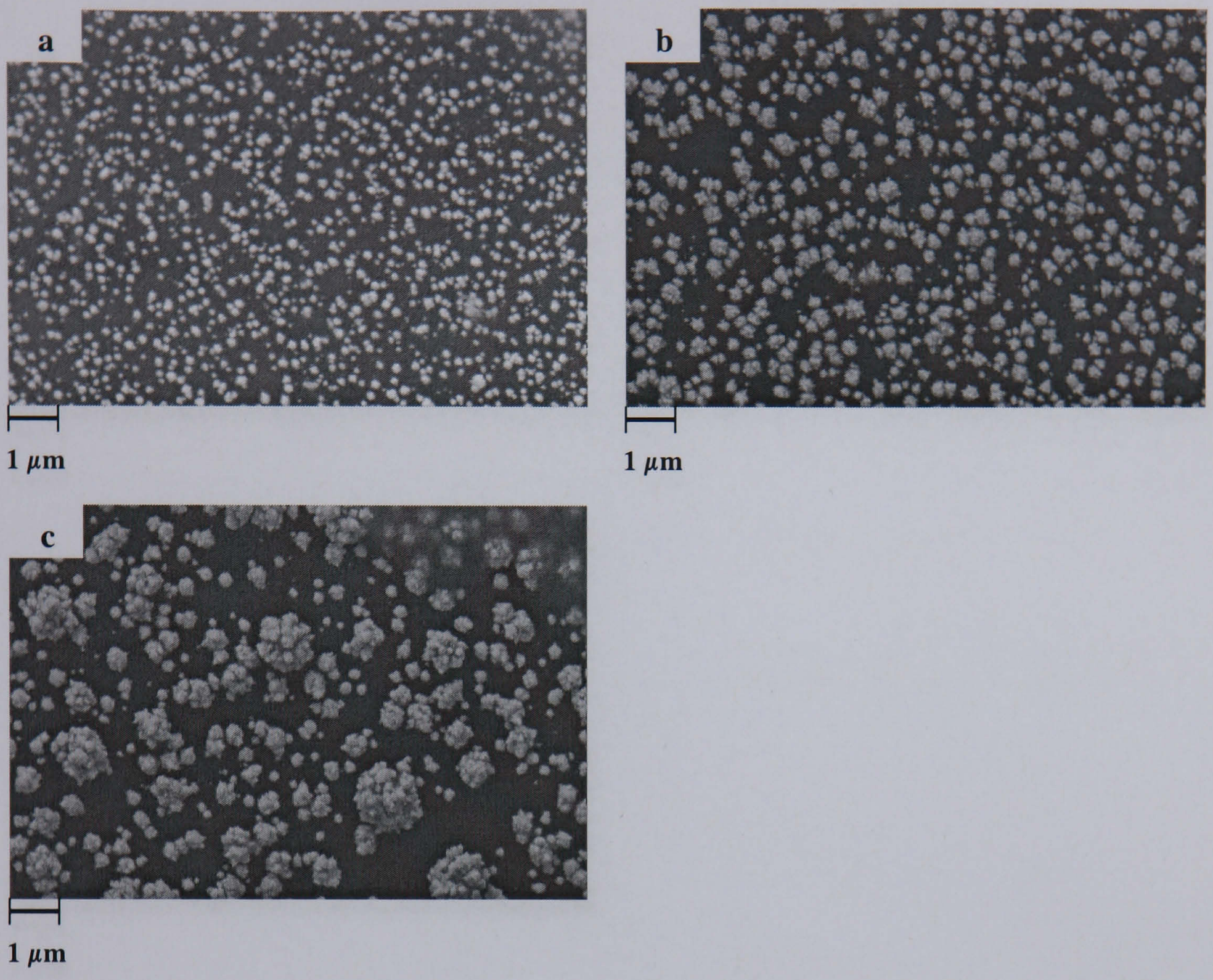

Figure 6.11: SEM images of gold on glassy carbon as a function of deposition time: (a) 1 s (b) 10 s and (c) 100 s.

On the other hand, figure 6.12 shows that the graphite electrode itself is rough and is characterized by craters. Gold was distributed unevenly on the surface, which is indicative that some part of the electrode behaved as a non-planar surface. This observation confirmed that the nucleation of gold on graphite does not follow the classical nucleation phenomena.

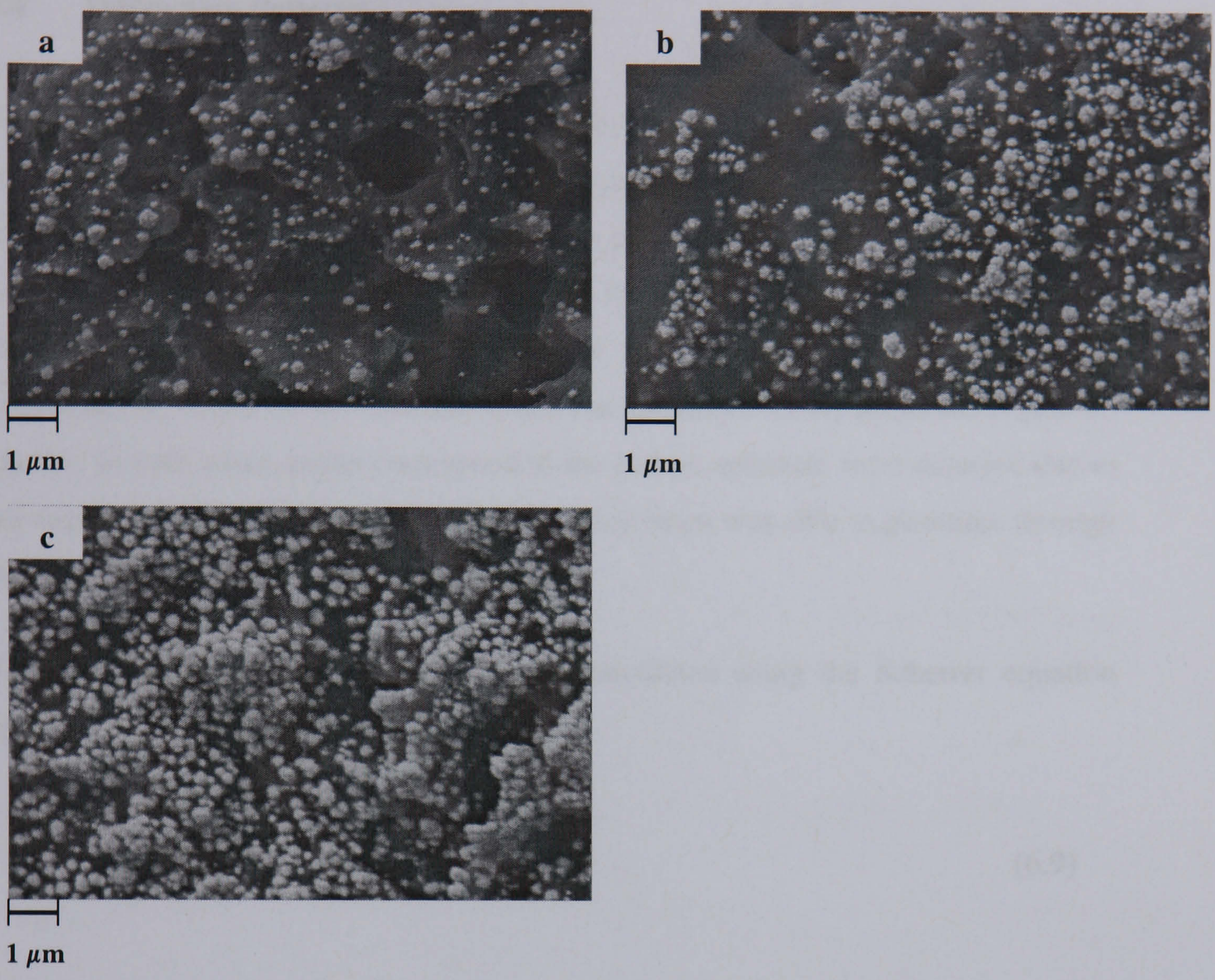

Figure 6.12: SEM images of gold on graphite as a function of deposition time: (a) 1 s (b) 10 s and (c) 100 s.

Figure 6.12 also shows that numerous nuclei are formed on the planar areas, and it is clear that coalescence of the nuclei occurs even before the first second has elapsed. Between 1 and 10 s, a fraction of the Au nanoparticles continues to grow to over 90 nm while other nuclei remain in the range between 80-90 nm. After 100 s, the graphite surface is almost completely covered by Au nuclei of 100-300 nm, which have clearly coalesced from smaller nuclei. The appearance of gold deposited on graphite is more powdery than that observed for glassy carbon.

6.4 Diffraction Patterns

X-ray diffraction patterns of the polycrystalline gold thin film are shown in figures 6.13 and 6.14 obtained for glassy carbon and graphite, respectively. Crystallographic structure of the x-ray diffraction patterns show peaks characteristics of a face-centred cubic (FCC). Au (111) is the preferred texture for gold deposits as the intensity of the (111) peak was the highest. Both deposits were obtained at the same plating conditions (η = -1.2 V, T = 298 K), hence the intensities of all major Au peaks are similar. In both cases, peaks correspond to the carbon substrate were detected due to the fact that the gold film was thin that the x-ray beam was able to penetrate through the thin film, thus producing the peaks.

The average size of the Au particles was calculated using the Scherrer equation [6.16, 617], as given in equation 6.9 below.

$$Crystallite\ size = K\frac{\lambda}{B\cos\theta} \tag{6.9}$$

K is a constant which related to the crystallite shape and approximately equal to unity. In this calculation, K was taken as 0.89 corresponds to the hemispherical shape of the nuclei. λ is the x-ray wavelength, 0.154 nm, B is the line width of the diffraction profile and θ is the diffraction angle. The average size of the Au deposits was found to be between 15-30 nm, somewhat smaller than those obtained by SEM. Since the diffraction beam is capable of detecting the smallest particle produced on the layer closer to the electrode surface, the values obtained therefore does not represent the average size of the whole particles.

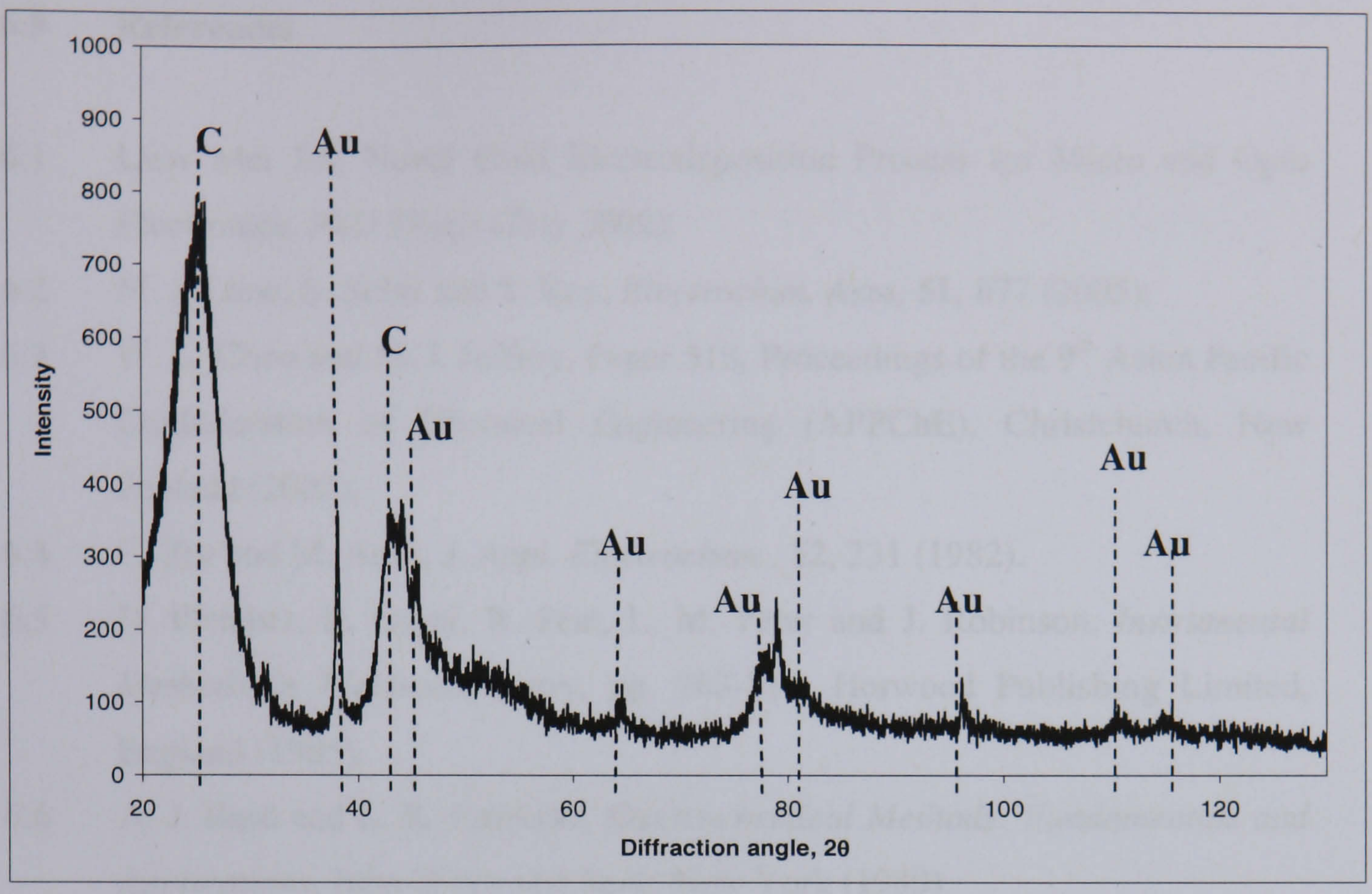

Figure 6.13: X-ray diffraction pattern of gold on glassy carbon at – 1.20 V.

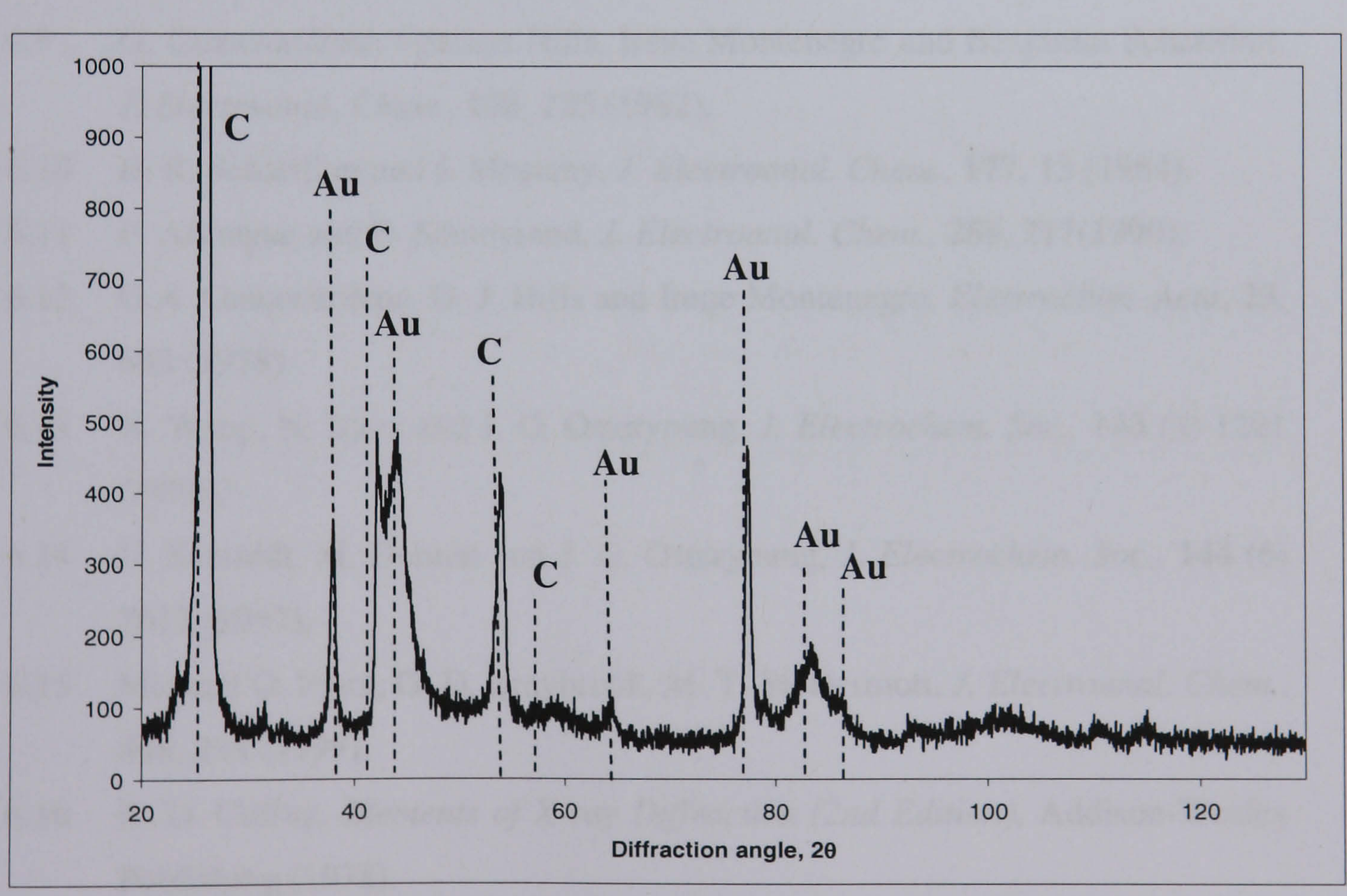

Figure 6.14: X-ray diffraction pattern of gold on graphite at – 1.20 V.

6.5 References

6.1 Liew Mei Jin, Novel Gold Electrodeposition Process for Micro and Opto Electronics, *PhD Thesis* (July 2002).

6.2 M. J. Liew, S. Sobri and S. Roy, *Electrochim. Acta*, **51**, 877 (2005).

6.3 W. L. Choo and M. I. Jeffrey, Paper 518, Proceedings of the 9th Asian Pacific Confederation of Chemical Engineering (APPChE), Christchurch, New Zealand (2002).

6.4 C. Zur and M. Ariel, *J. Appl. Electrochem.*, **12**, 231 (1982).

6.5 D. Pletcher, R. Greef, R. Peat, L. M. Peter and J. Robinson, *Instrumental Methods in Electrochemistry*, pp. 283-316, Horwood Publishing Limited, England (1985).

6.6 A. J. Bard and L. R. Faulkner, *Electrochemical Methods: Fundamentals and Applications*, John Wiley and Sons, New York (1980).

6.7 Y. G. Li, W. Chrzanowski and A. Lasia, . *Appl. Electrochem.*, **26**, 843 (1996).

6.8 B. Scharifker, *Electrochim. Acta*, **28** (7), 879 (1983).

6.9 G. Gunawardena, Graham Hills, Irene Montenegro and Benjamin Scharifker, *J. Electroanal. Chem.*, **138**, 225 (1982).

6.10 B. R. Scharifker and J. Mostany, *J. Electroanal. Chem.*, **177**, 13 (1984).

6.11 P. Allongue and E. Souteyrand, *J. Electroanal. Chem.*, **286**, 217(1990).

6.12 G.A. Gunawardena, G. J. Hills and Irene Montenegro, *Electrochim. Acta*, **23**, 693 (1978).

6.13 X. Wang, N. Isaev and J. G. Osteryoung, *J. Electrochem. Soc.,* **143** (4) 1201 (1996).

6.14 U. Schmidt, M. Donten and J. G. Osteryoung, *J. Electrochem. Soc.*, **144** (6) 2013 (1997).

6.15 Michael O. Finot, G. D. Braybrook, M. T. McDermott, *J. Electroanal. Chem.*, **466**, 234 (1999).

6.16 B. D. Cullity, *Elements of X-ray Diffraction (2nd Edition)*, Addison-Wesley Publishing (1978).

6.17 A. Authier, *Dynamical Theory of X-Ray Diffraction*, Oxford University Press (2004).

CHAPTER 7:

RESULTS:

GROWTH OF GOLD PARTICLES ON GLASSY CARBON

7.1 Analysis Using Atomic Force Microscopy

In previous chapter, scanning electron microscopy (SEM) analysis of gold deposits has been reported in terms of particle density and diameter as well as its growth behaviour corresponding to the current-time transients. Although SEM can resolve surface feature as small as a few nanometres, it does not give high contrast images on flat surface or directly generate three-dimensional surface images. Therefore, further analysis using atomic force microscopy (AFM) is crucial in order to elucidate the surface morphology of gold deposits. In this chapter, focus will be given in elucidating the growth pattern of gold at longer period of time.

Images were simultaneously recorded in height and deflection modes. In height mode, the local height variations are measured while the probe-sample interaction force is kept constant. The height variations are presented by means of colour contrast, as shown in figure 7.1. Regions of high and low particle heights are identified using darker shades for low features and bright for high features. In deflection mode, the deflection of the cantilever is measured while the probe scanned at a constant height. While height images provided quantitative information on surface topography, deflection images exhibited higher contrast of the morphological details and were more sensitive to fine surface features than the height signal. Images obtained could be presented as two-dimensional or three-dimensional representations. Using a wide variety of image manipulation, quantitative topographical information such as features size, thickness and height, surface roughness and area, and cross sectional plots could be obtained. For example, a line profile could be extracted from the image, from which the height and width of the features are measured.

In this work, current-time transients were accomplished for durations of 1, 10, 100, 500 and 1000 seconds. Electrode potentials of – 0.925 V and – 1.20 V were chosen as the deposition potentials mainly because it showed the transition between the formation of single particulates and aggregates. Current-time transients recorded at these two overpotentials were found to be reproducible and similar to those shown in

figure 6.4 of chapter 6. The AFM was operated in contact mode with operational frequency of 2 Hz, scanning between 1 μm to 25 μm imaging scales. Scans carried out at low imaging scale, 1 μm, produced large noise and are, therefore, not used in our analysis.

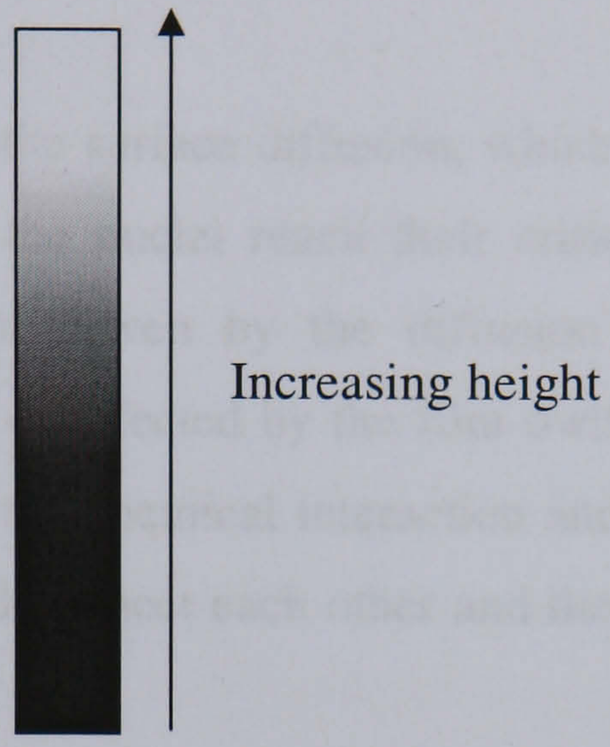

Figure 7.1: Colour coding for height images

7.2 Particle Distribution and Growth Pattern

Figures 7.2 to 7.5 show atomic force micrographs of gold on glassy carbon at – 0.925 V with 5 μm and 25 μm imaging scales. In agreement with results obtained in figure 6.9 of chapter 6, the initial stage of growth exhibits the appearance of nuclei which grow independently of each other. It was observed in figure 7.2 (a) that the initial morphology of nuclei at low particle coverage is spherical and the average size of the nuclei is 120 nm. The gold nuclei started depositing in one direction; preferentially at the grain boundaries or the crystallographic plane of the substrate, mainly because these sites are thermodynamically favourable for deposition [7.1]. The scratches observed on the surface are mainly due to surface polishing using silicone carbide paper, although fine grit paper has been used throughout the experiments.

As time proceeds, the isolated nuclei continue to grow and at the same time, new growth centres are formed on the substrate surface. However, the isolated nuclei

expanded isotropically for a limited time, i.e. during induction time. The cathode surface then reached a point where it is covered by large number of growing centres and there is interference between neighbouring diffusion zones. Therefore, in figure 7.2 (b), one observes a coarsening process whereby adjacent nuclei coalesce to form larger aggregates whilst some still remain as single particles. The aggregates are of nearly the same size, the average size being 550 nm.

The clustering of particle is due to the surface diffusion, which is expected to be a mass transfer controlled [7.2]. As the nuclei reach their critical size, the mature nuclei begin to move on the film driven by the diffusion force. During this movement, the crystal is controlled or affected by the film owing to the interaction between crystal and substrate. It is the chemical interaction and the diffusion force that drive the crystals to contact and connect each other and they coalesce regularly to form larger aggregates.

Figure 7.2 (c) shows that deposition for longer periods results in complete coverage of gold aggregates on the substrate surface. At this point, particles are clustered into large aggregates and measurement of diameter is no longer possible. The continuous clustering of nuclei results in formation of a three-dimensional growth. We find that the attachment between the deposits and carbon substrate was weak and the deposits could be easily removed using fine grit paper, distilled water and a cloth. This suggests that in three-dimensional growth, the adatoms interact weakly with the surface but strongly with one another [7.3].

The spherical morphology of a growing particle became unstable at a particular value of concentration gradient. Figure 7.2 (d) and (e) show that approaching 500 s and 1000 s deposition times, surface morphology exhibit formation of dendritic aggregates. The morphological transition from spherical geometry at the initial stage of deposition to dendritic growth at longer times may arise from the size dependent amorphous to crystalline phase transition. The continuous growth of the amorphous particle leads to a concentration depletion which then acts as the driving force for dendritic crystallisation. Although from the thermodynamic view a spherical shape

should be the most stable configuration, but microscopic diffusion kinetics might favour configurations that have a large surface area, such as dendritic growth.

Figure 7.3 shows three-dimensional images of gold particles at – 0.925 V. The scan range in the entire X and Y is 5 micrometers and the Z range varies depending upon the thickness of gold layer. It clearly demonstrates that surface features of gold deposits change from single particulates at 1 s to smooth gold deposits at 1000 s as a result of the dendritic growth. The intensity of the colour reflects the height of the particle on the surface which is more clearly specified in figure 7.4. At the early stage of deposition, i.e. 1 s, the height of the deposited particles was 70 nm and increases to 1000 nm at the point where particles begin to overlap. It was also observed that particle aggregation is more pronounced at 100 s (figure 7.4 (b)) than that at 10 s (figure 7.4 (c)), although the height of the deposited particle remains at 1000 nm. This indicates that the nuclei grow preferentially along their length or width as opposed to their height, indicating growth along the side facets is favoured. When dendritic aggregates are produced, the height drastically increases to 2200 nm and the pattern becomes denser at higher deposition time, indicating that growth is favoured in all directions.

Figure 7.5 shows similar deflection images to that of figure 7.2 but at lower imaging scale, 5 μm. It is important to note from this figure that the images shown do not represent the true shape of gold nuclei or aggregates due to the distortion caused by the probe, which is a tip at the end of a cantilever. Since the AFM was operated in contact mode, the tip and the sample remain in close contact as the scanning proceeds. In response to the force between the tip and the gold sample, the cantilever flexes toward the sample and dragged the tip over the substrate surface. As a result, we observed that the gold pattern appears as triangles (figure 7.5 (c) – (e)), which reflects the shape of the tip rather than the true geometry of the gold nuclei.

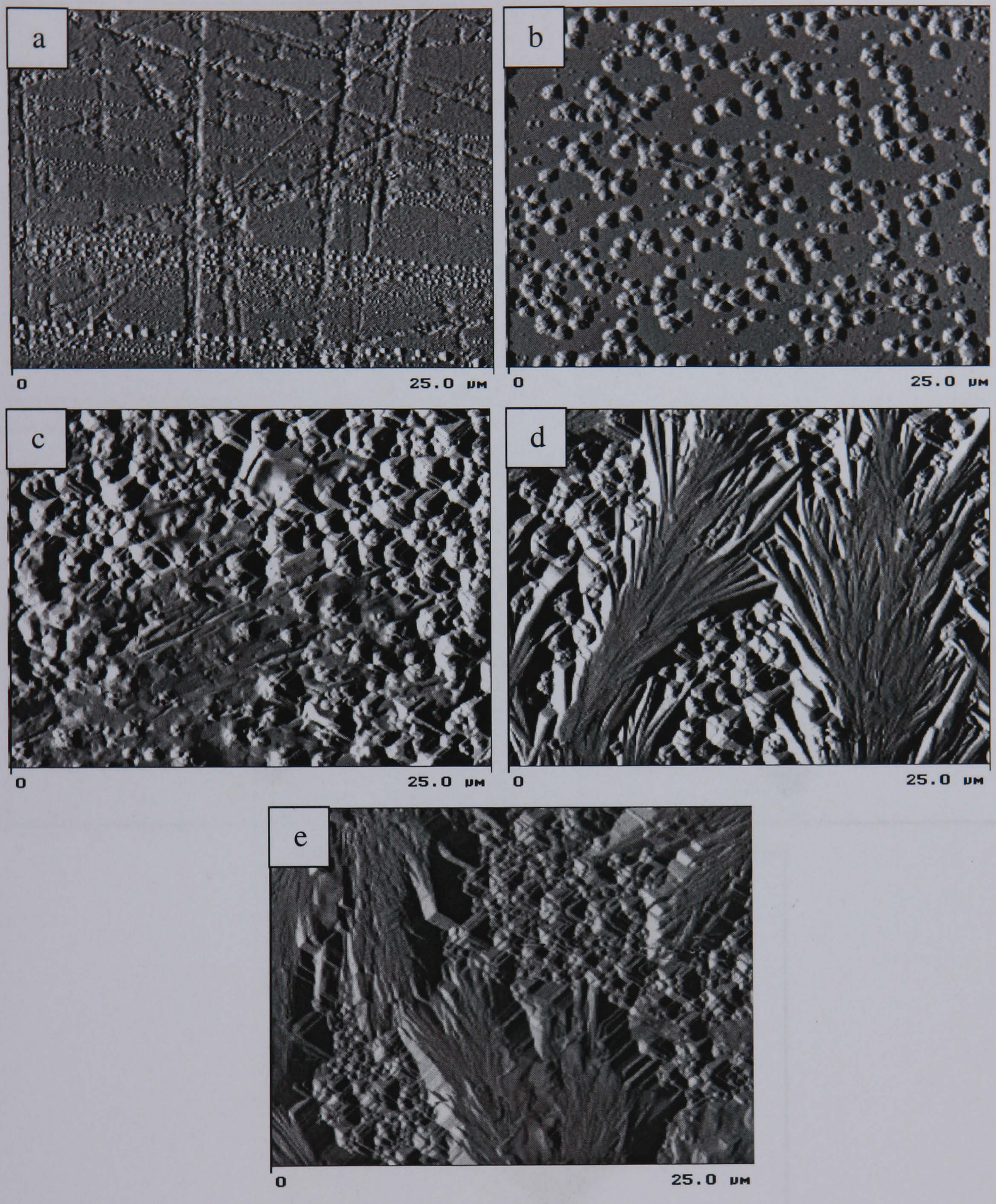

Figure 7.2: AFM deflection images of gold on glassy carbon at – 0.925 V and 25 µm imaging scale (a) 1 s (b) 10 s (c) 100 s (d) 500 s (e) 1000 s.

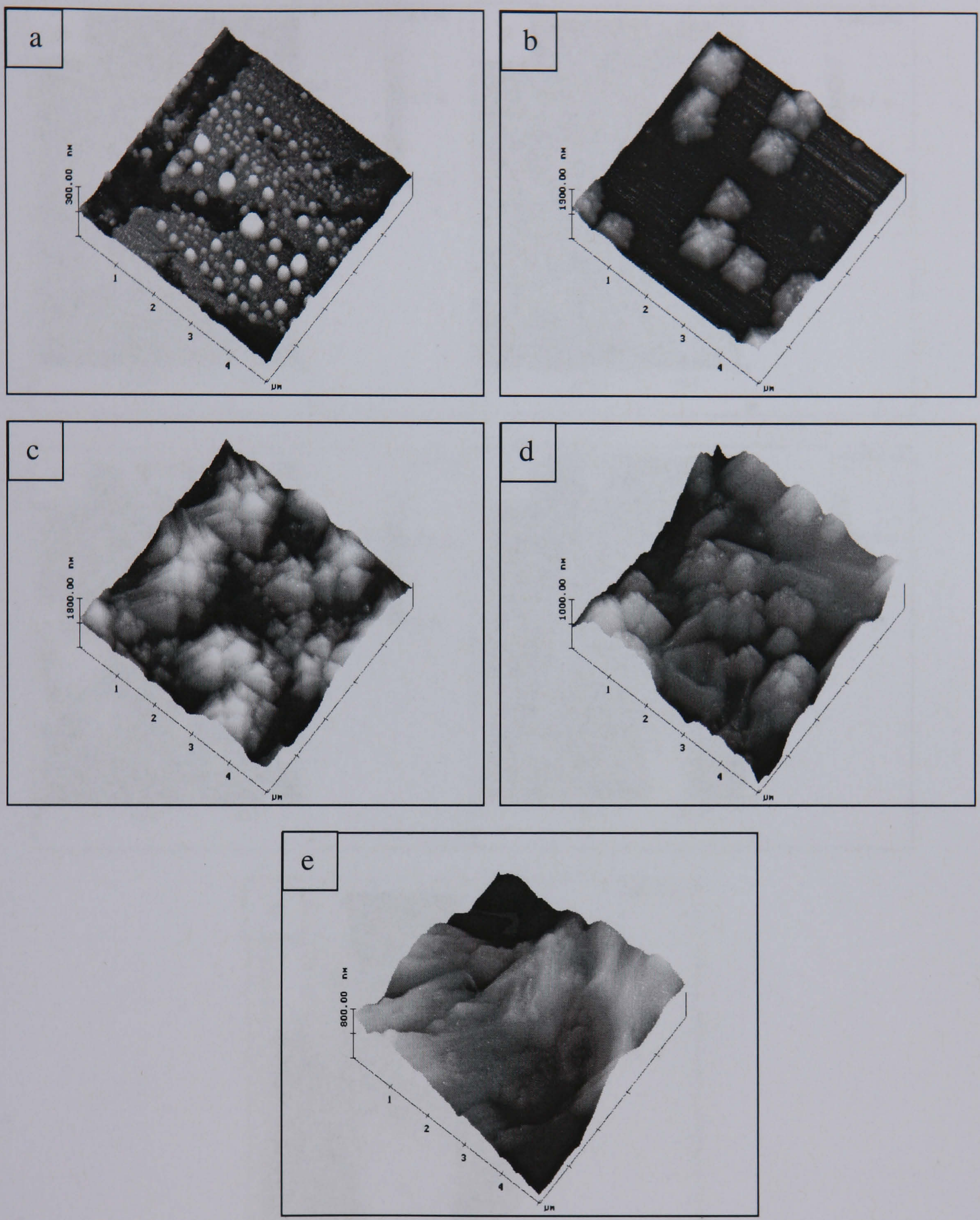

Figure 7.3: AFM 3-dimensional images of gold on glassy carbon at – 0.925 V at 5 µm imaging scale (a) 1s (b) 10s (c) 100s (d) 500s (e) 1000s

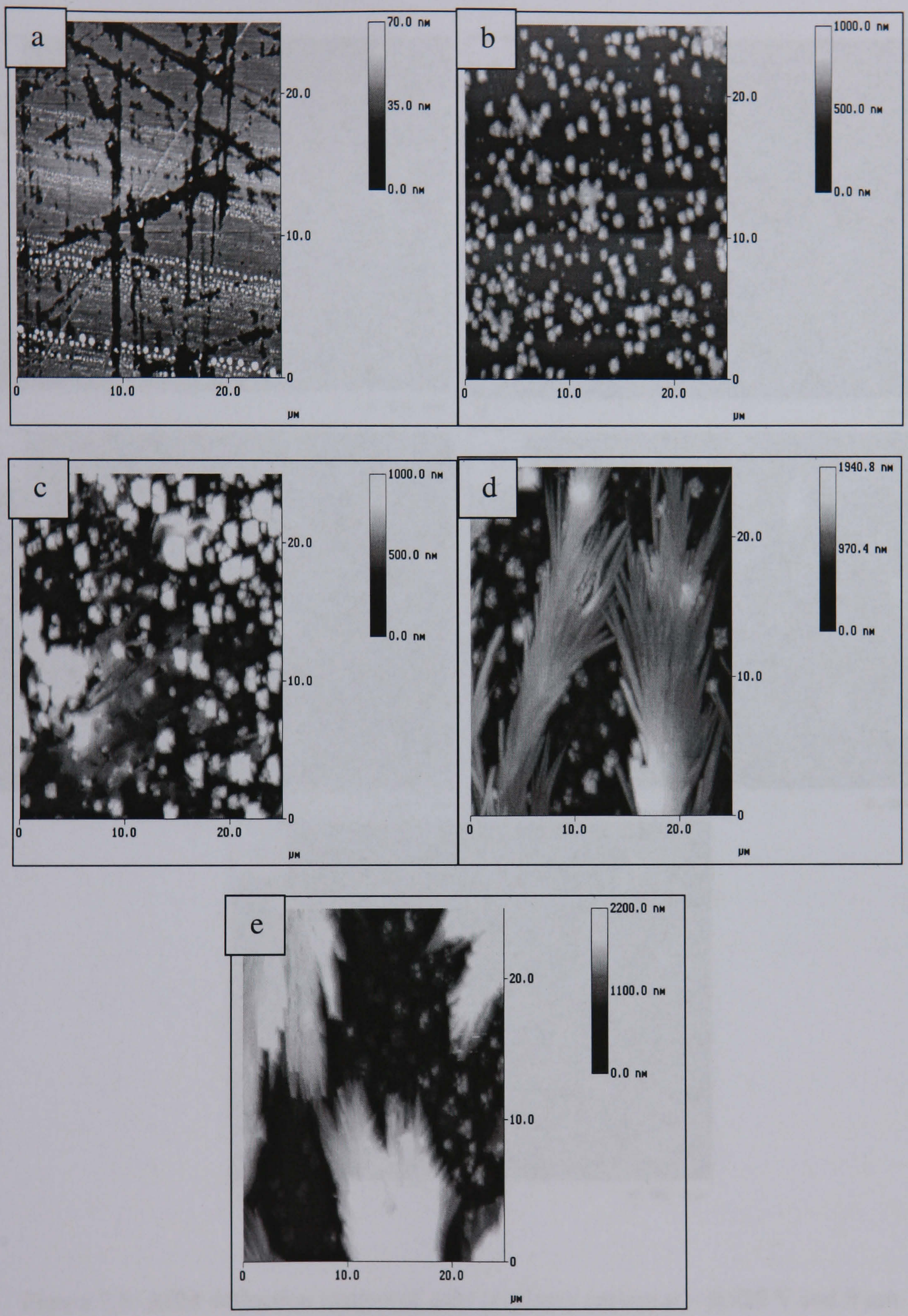

Figure 7.4: AFM height images of gold on glassy carbon at – 0.925 V at 25 μm imaging scale (a) 1s (b) 10s (c) 100s (d) 500s (e) 1000

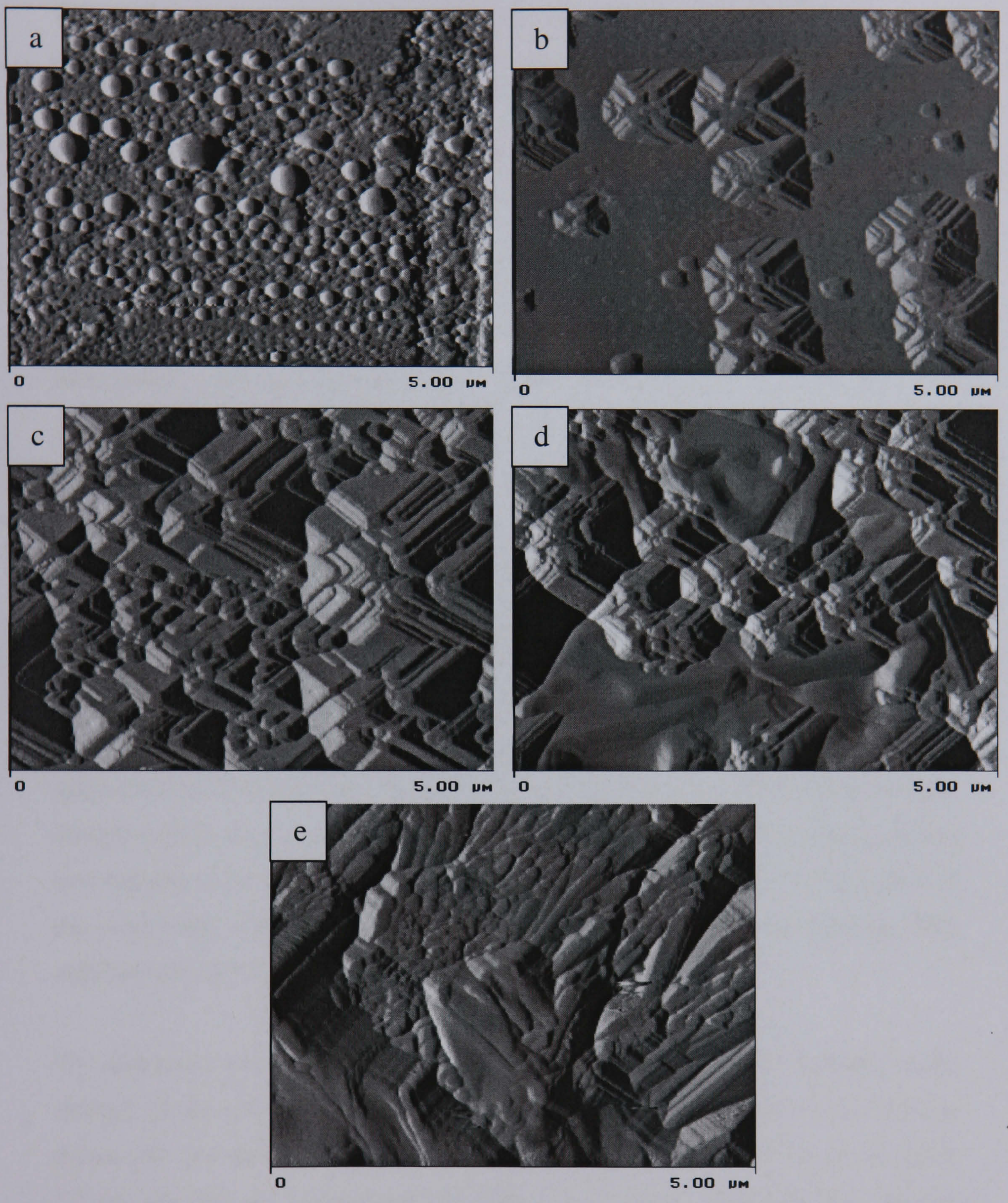

Figure 7.5: AFM deflection images of gold on glassy carbon at – 0.925 V and 5 μm imaging scale (a) 1 s (b) 10 s (c) 100 s (d) 500 s (e) 1000 s.

Figures 7.6 to 7.9 represent the atomic force micrographs of gold nanoparticles deposited at an overpotential of – 1.20 V with 5 μm and 25 μm imaging scales. As can be seen in figure 7.6, the images presented indicate that the deposition of gold nuclei at more cathodic overpotential exhibits the dendritic growth. Due to the high overpotential applied to the electrode, the dendrite growth velocity is high. Therefore we observed the formation of dendrites occurring even before the first second has elapse. The structure of the dendrites generally follows a pattern consisting of a main branch with many appendages. Figure 7.6 also illustrates that the dendritic form coexists with the spherical particle which eventually fills up the spaces between the dendritic arms. Similar observation was also found by other researcher in the case of dendritic tin nanoaggregates, where the dendritic grains of the order of 0.1 μm were preceded by the formation of smaller tin grains [7.4].

One of the important aspects of dendritic growth is the formation of branches. Figure 7.7 (a) demonstrates the formation of finger-type structures at the early stage of dendritic formation. This behaviour can be explained in terms of the current-time behaviour which corresponds to figure 6.4 in chapter 6. Initially the current increased very rapidly as the surface area of the deposit increased. Due to the high current applied to the electrode, the driving force for the formation of dendrites is high; therefore the emergence of branches was fast. The growth centres frequently emitted new branches with different growth directions. It was also observed that the radius of the branch tips was smaller and the deposit was dominated by tip splitting. This signifies that the rate of growth is relatively fast in the beginning.

The deposition process depletes the concentration of gold nuclei available in the vicinity of the electrode. Since new nuclei are formed only when gold discharge occurs, the driving force for the system therefore becomes low. As shown in figure 7.7 (b), the tips are characterised by wide curved shape, signifying that the tips velocity reduces and the rate of tips splitting has becoming slow. The dendritic arms grow until they eventually become large enough to contact each other. The lines of contact between the outer arms of neighbouring dendrites acts as a grain boundary

and further growth results in thickening of the existing dendrites arms, as shown in figure 7.7 (c) and (d).

Apart from the formation of branches, another important aspect of dendritic growth is the spacing between dendrite arms. Figure 7.8 reveals that these spaces crystallise to yield more regular spherical particles. Isolated spherical particles were observed at 1 s (figure 7.8 (a)), which slowly coalesces to form aggregates at longer deposition time. As time proceeds, these spaces ultimately filled with particles. Although both the dendrites and spherical particles were evidently found coexisting on the substrate surface, it was found that the time taken for the emergence of spherical particles is much longer than the dendrites. This signifies that both morphologies grow at different rates from each other and that the dendrites grow much faster than the spherical particles. Since the systems adopt faster growing morphology [7.5], the dendritic growth is seen to be dominating the overall growth rate.

Figure 7.9 shows the height images of gold particles at an applied potential of – 1.20 V. Since the growth rates of dendrites varied at different points on the substrate surface, it was observed that the thickness of deposited gold layer fluctuates between 800 nm to 2500 nm regardless the increasing deposition time. Therefore measurements of the thickness of dendrites are worthless as different directions of dendritic growth occur at different rates. However, the thickness of the deposited gold layer was found to be higher than that observed at lower overpotentials, which shows that the overpotential plays an important role as the driving force to enhance the growth rate.

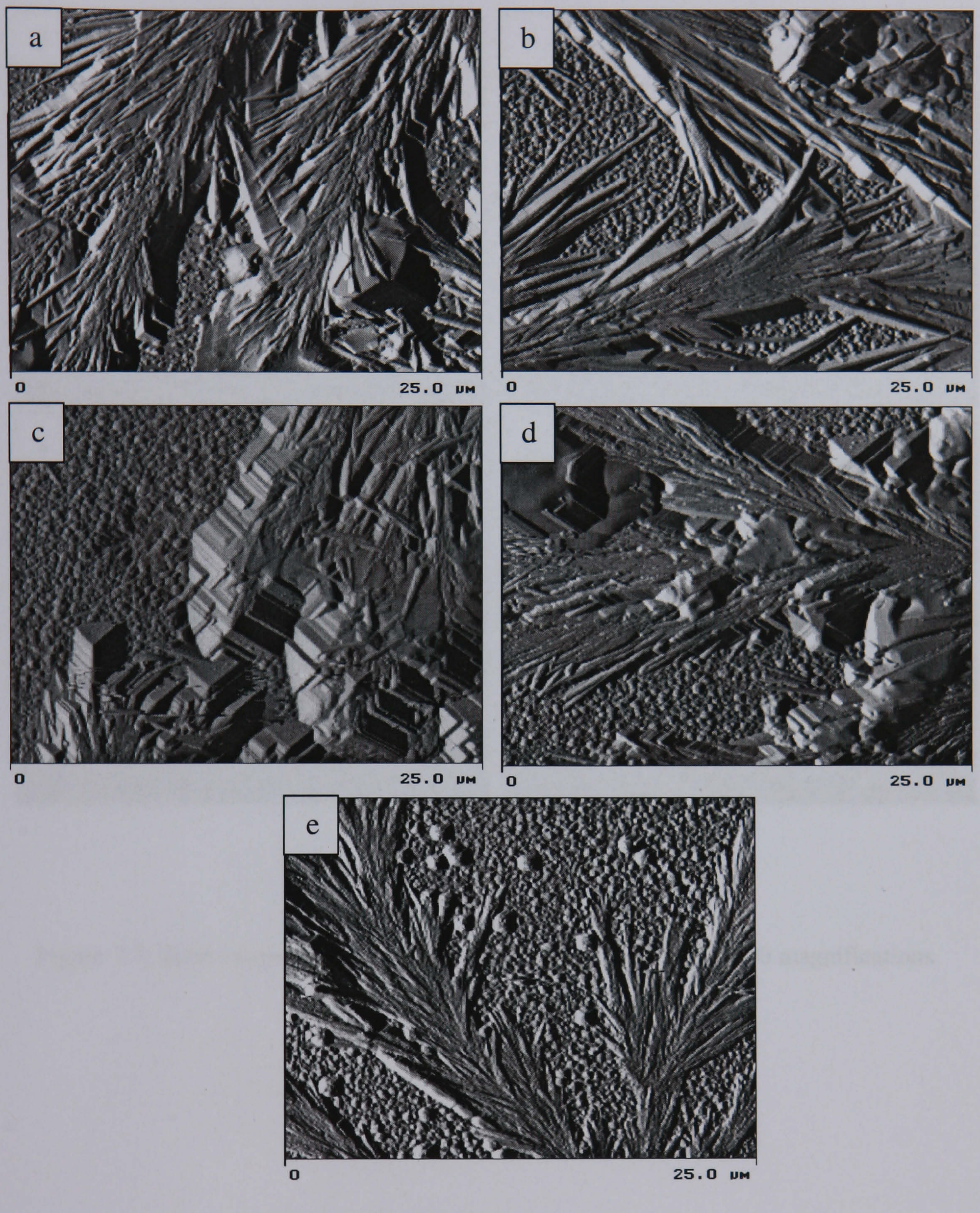

Figure 7.6: AFM deflection images of gold on glassy carbon at – 1.20 V and 25 μm imaging scale (a) 1 s (b) 10 s (c) 100 s (d) 500 s (e) 1000 s.

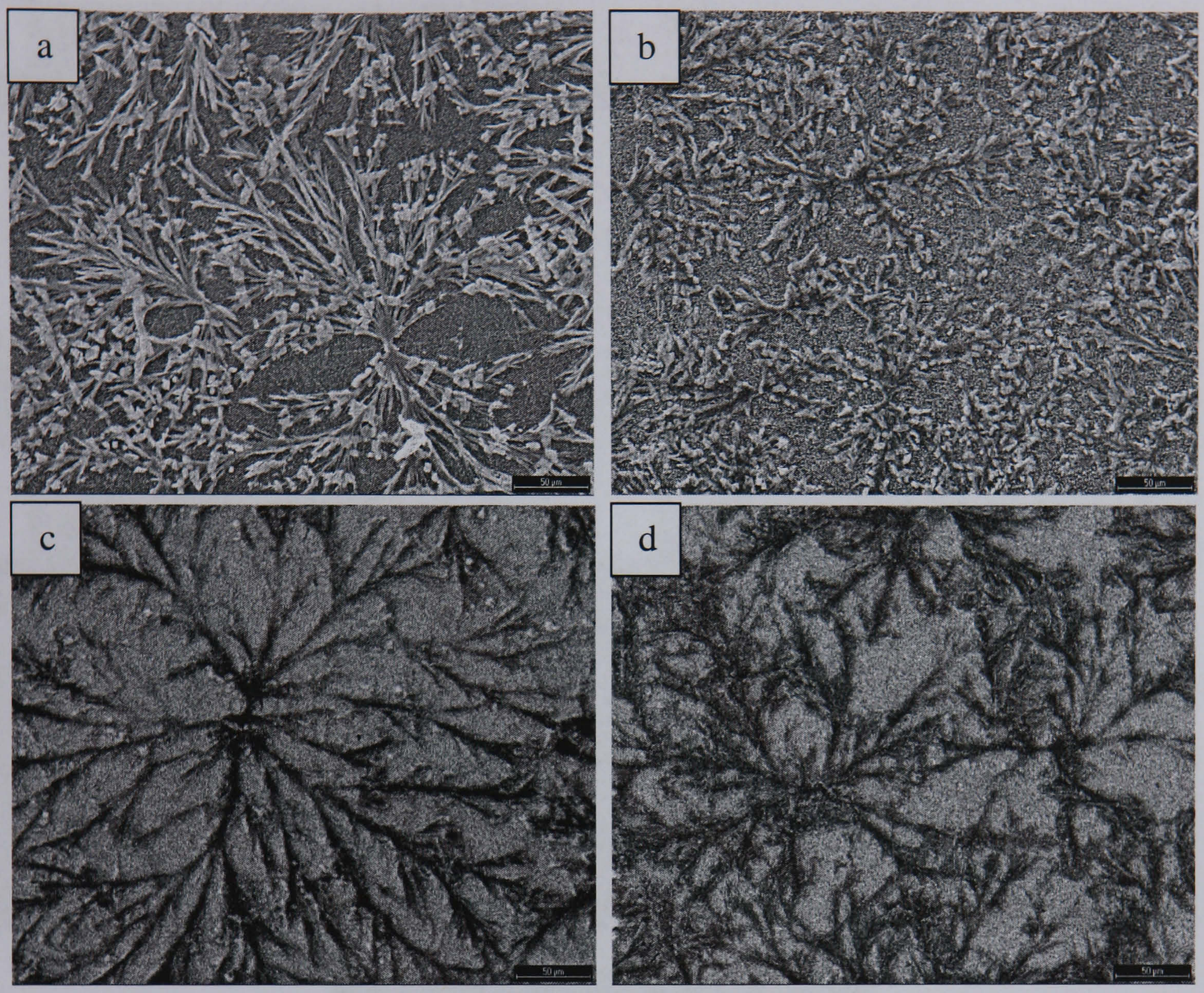

Figure 7.7: SEM images of gold on glassy carbon at – 1.20 V and 200 magnifications
(a) 10 s (b) 100 s (c) 500 s (d) 1000 s

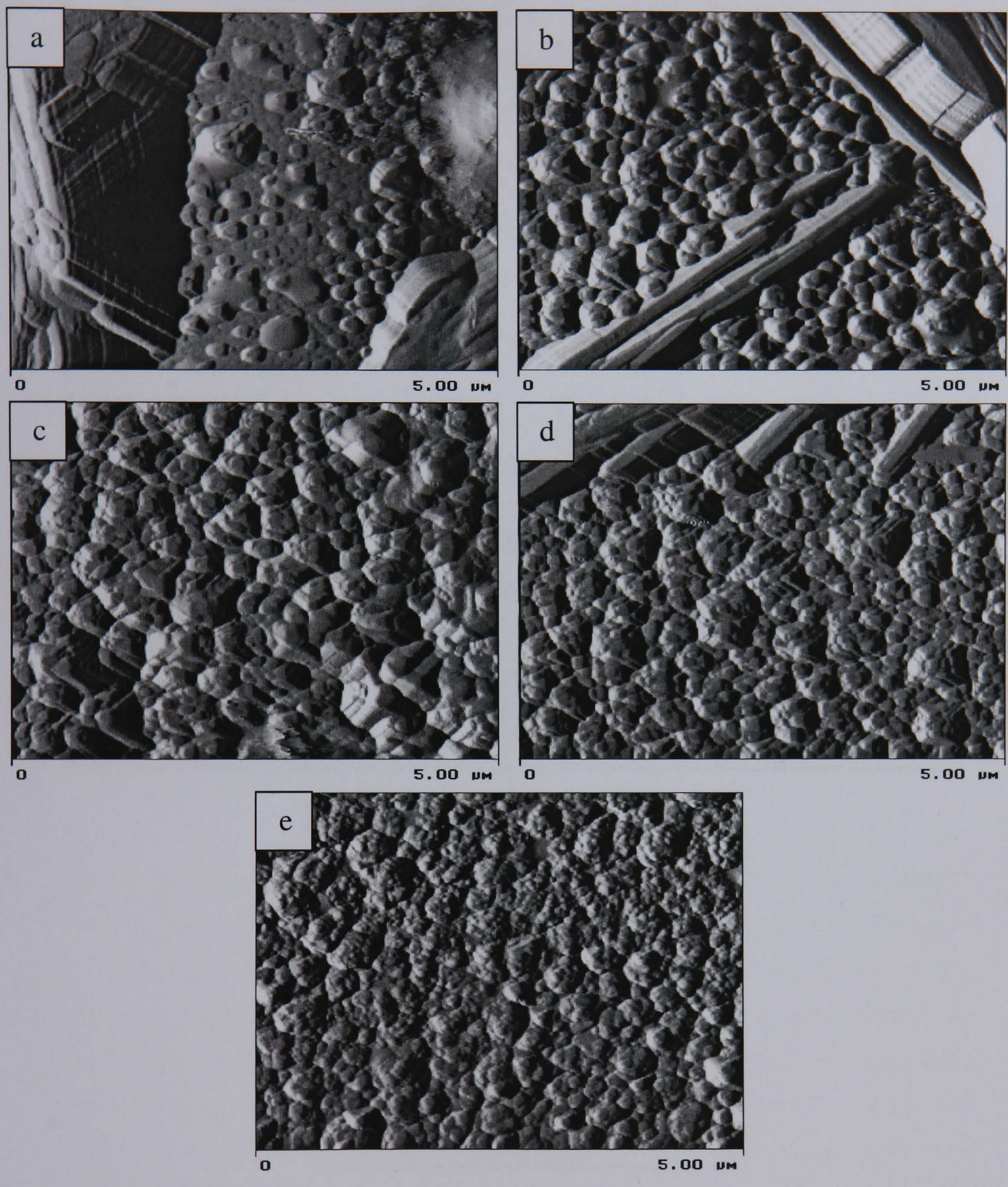

Figure 7.8: AFM deflection images of gold on glassy carbon at – 1.20 V and 5 µm imaging scale (a) 1 s (b) 10 s (c) 100 s (d) 500 s (e) 1000 s.

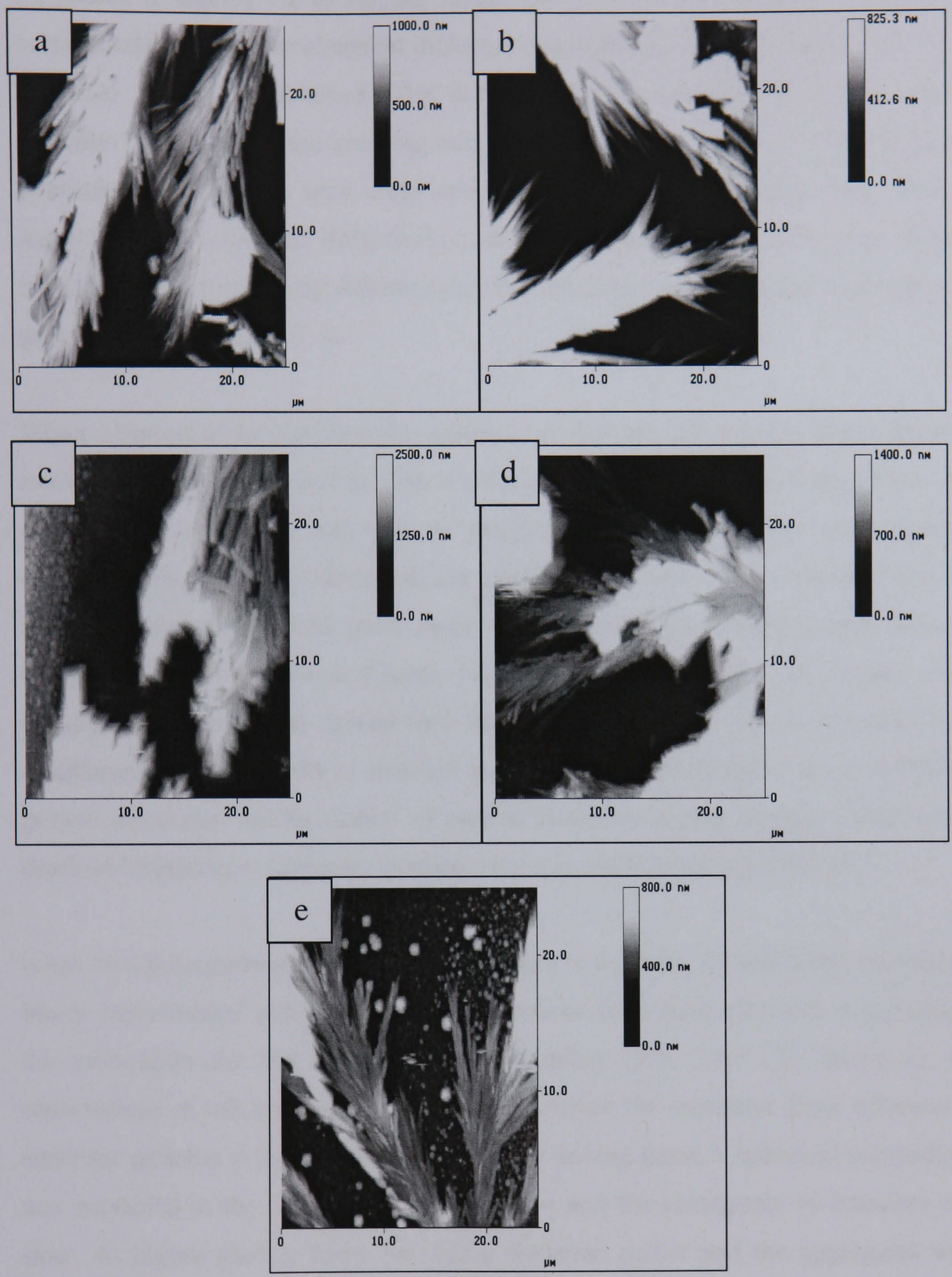

Figure 7.9: AFM height images of gold on glassy carbon at – 1.20 V at 25 μm imaging scale (a) 1s (b) 10s (c) 100s (d) 500s (e) 1000s.

As shown in figures 7.2 to 7.5, the initial deposition of Au at lower overpotential corresponds to an electrochemical diffusion controlled of Au^+ discharge from which spherical nuclei are obtained. The deposits evolve isotropically and develop a diffusion layer around the growing nuclei. The diffusion layers of adjacent nuclei gradually overlap with each other and three-dimensional aggregates are formed. According to the classical diffusion limited aggregation (DLA) model, these clusters are formed when randomly diffusing particles stick irreversibly to the perimeter of a growing aggregate [7.6, 7.7].

When a certain induction time for spherical growth has passed, the initial growing nuclei become unstable and the thin Au deposit begins to developed tips. These tips grow larger with time and split to produce more branches. At more cathodic overpotentials, however, dendrites are produced as soon as the driving force is applied to the system and grew much faster than those formed at less cathodic overpotentials, as shown in figures 7.6 to 7.9. New branches are emitted more frequently and gradually spread and shielded one another. This continuous non-equilibrium process results in dendritic patterns which are characterised by preferred growth directions. In the studies of pattern formation during electrocrystallisation, dendrite formation is a primary example of a non-equilibrium growth [7.5].

It has now been generally accepted that the key to dendritic growth is the anisotropy. Many experimental and theoretical examinations have been directed to investigate the motivation for this morphological instability [7.5, 7.8-7.12]. Based on the observations in our work, the parameter that drives the crossover from spherical to dendritic patterns is the overpotential. At low driving force, a spherical morphology was produced at the early stage of deposition and the emergence of branches was slow. At higher driving force, branching occurred earlier and the aggregates were made up of fine dendrites with regular side branches. Other researchers have also concluded that the overpotential acts as the driving force for dendritic growth and plays an important role in determining the final morphology of the particles [7.5, 7.10, 7.13].

Up until now, discussion about dendritic formation focused on the effects of concentration gradient and applied potential. However, we also believe that the presence of heterogeneity, *i.e.* sulphur adsorption, may also have significant influence on the morphology of deposited particles. In our case, the adsorption of sulphur creates changes in microscopic interfacial dynamics due to its accumulation and depletion in front of the growing interface. At the beginning of experiment, the effect of sulphur adsorption is low and the morphology maintains dendritic shape due to the enhancement of anisotropy by the applied potential. However, as the dendritic branch grows forward, sulphur adsorption in front of the growing interface increases. The interference of sulphur adsorption on the interfacial growth may change the interfacial growth dynamics and cause a decreasing of anisotropy. This leads to the instability of the growing interface and promotes more tips splitting. As the growth of the dendrites continues, the sulphur adsorption in front of the growing interface is gradually eliminated. The anisotropy in the interfacial growth may again be enhanced and the process described above will be repeated. This results in further formation of dendrites on the substrate surface.

The transition from diffusion limited aggregates to dendritic growth can also be an indication that the time for surface diffusion along the surface to a more energetically favourable site becomes greater than the time between incorporation of molecules. Since dendrites grow much faster than the spherical morphology, it suggests that in diffusion limited growth, faster morphology is selected as it sustains a higher global flux and hence a more rapid approach to equilibrium.

One important aspect of dendrite formation is the deterioration of electrolyte. After a period of processing, the gold content in the plating bath was reduced, and combined with high driving force applied to the system, dendrites were easily formed. Therefore, dendritic growth is one phenomenon that marked the decay in solution as well as bath lifetime, which is important for maintaining high quality of gold deposits.

7.3 Section Analysis and Height Distribution

Vertical height and horizontal distance measurements were carried out using section analysis along selected reference line on the surface. The section analysis was performed between the top of the particle and the surface of the substrate. The particle heights obtained from this analysis are summarised in Table 7.1.

Deposition time, s	**Overpotentials, V**	
	- 0.925	**- 1.20**
1	26 ± 6	43 ± 11
10	350 ± 22	155 ± 27
100	365 ± 12	176 ±15
500	599 ± 8	145 ±11
1000	645 ± 15	139 ± 13

Table 7.1: Average particle height in nanometres.

Figure 7.10 shows the section analysis performed for overpotential – 0.925 V. It was found that the height increases with increasing deposition time when depositing at -0.925 V. The peaks obtained at 1 s are sharp and the width of each peaks are narrow and well-separated from each other, indicating the initial formation of growth centres with small, isolated nuclei. The particle height significantly increase from 25 nm to 350 nm after 10 s of deposition signifying the growth of larger nuclei, as indicated by larger isolated peaks in figure 7.11 (b). Peaks obtained after 100 s show characteristic feature of large particle aggregation, resulting from the coalescence of nuclei, by the emergence of overlap peaks. The resulting particle height reaches 645 nm.

On the other hand, section analysis performed at – 1.20 V shows inconsistency in particle heights. The heights were found to be ranging from 40 nm to 180 nm, in no particular order. However, this range is smaller than that was observed at - 0.925 V. As dendritic growth dominates surface features, the rate of which they are formed

differs at different point on the substrate surface, which contributes to poor interpretation of particle heights due to variations in baseline.

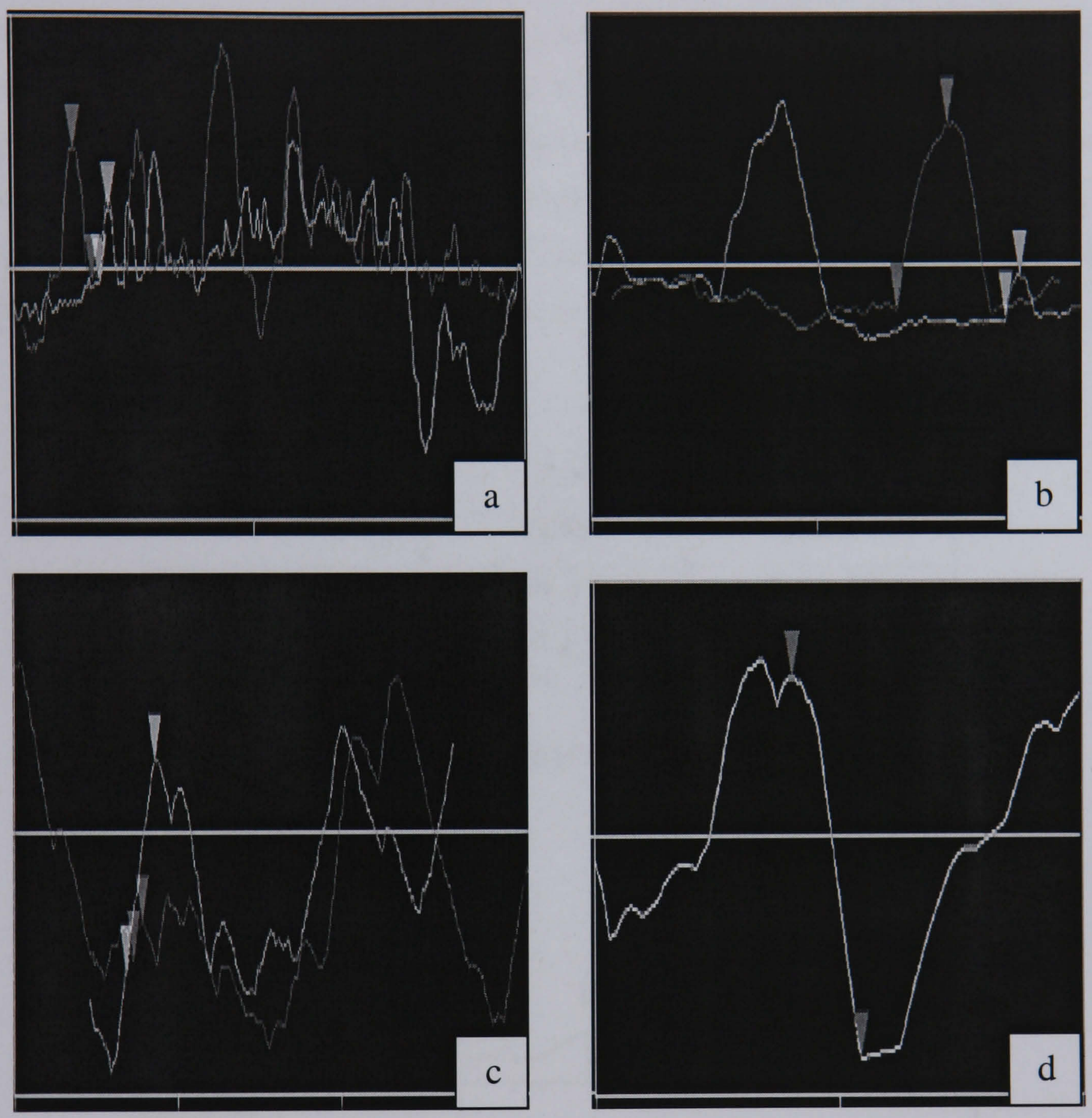

Figure 7.10: Section analysis of gold deposits on glassy carbon at – 0.925V.

Table 7.2 listed the averages particle diameters obtained by AFM and SEM analysis under the same plating conditions. It was found that the particle diameters obtained by AFM cross-section analysis are larger that that obtained from SEM analysis. This may be due to an error associated with the probe tip, which results in an overestimate of the lateral dimension. Although cross-section analysis provides precise measurements of the particle heights, the horizontal distance, which corresponds to particle diameter, however, is distorted due to a tip convolution effect caused by the triangular shape of the tip. Figure 7.11 illustrates the motion of an AFM probe (the tip and the cantilever) as it goes over a particle on a substrate surface. In such a measurement, the side of the probe will cause a broadening of features in the image.

Overpotential, V	**Particle diameter, nm**	
	SEM	**AFM**
- 0.925	160 ± 8	365 ± 10
- 1.20	86 ± 5	175 ± 7

Table 7.2: Particle diameter obtained from AFM and SEM analysis

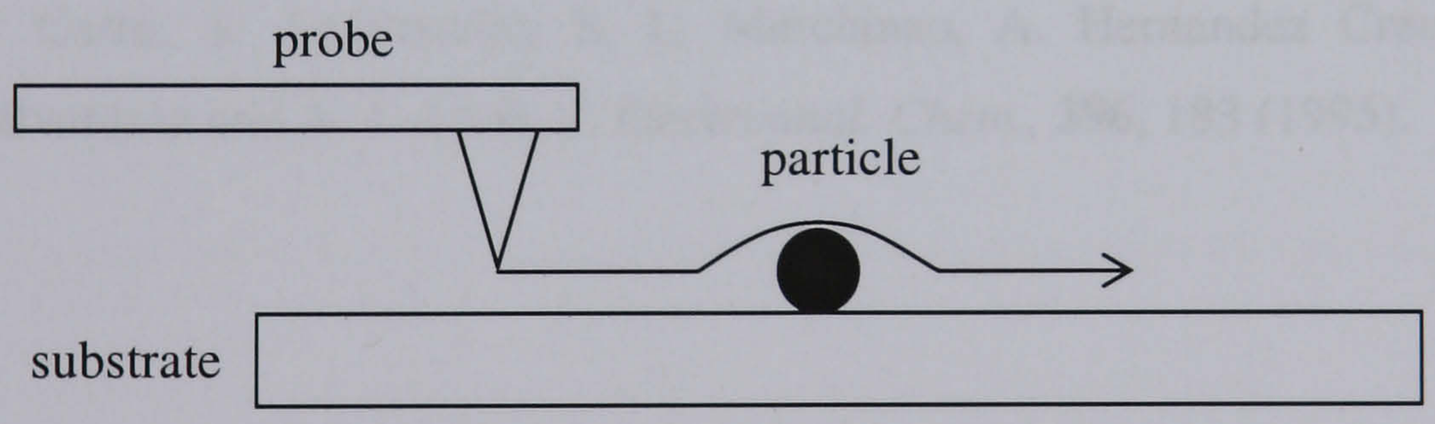

Figure 7.11: Tip convolution effect

7.4 References

7.1 D. Pletcher, R. Greef, R. Peat, L. M. Peter and J. Robinson, *Instrumental Methods in Electrochemistry*, Horwood Publishing (2001)

7.2 J. M. K. Donev, Q. Yu, B. R. Long, R. K. Bollinger and S. C. Fain, Jr., *J. Chem. Phys.*, **123**, 44706 (2005).

7.3 J. H. Weaver and V. N. Antonov, *Surf. Sci.*, **557**, 1 (2004).

7.4 T. Devers, I. Kante, L. Allam and V. Fleury, J. Non-Cryst. Solids, **321**, 73 (2003).

7.5 D. Barkey, F. Oberholtzer and Q. Wu, *Phys. Rev. Lett.*, **75 (16)**, 2980 (1995).

7.6 T. A. Written and L. M. Sander, *Phys. Rev. Lett.*, **47**, 1400 (1981).

7.7 S. C. Ferreira Jr., S. G. Alves, A. F. Brito and J. G. Moreira, *Phys. Rev. E*, **71**, 51402 (2005).

7.8 C. Monroe and J. Newman, *J. Electrochem. Soc.,* **151 (6)**, A880 (2004).

7.9 R. F. Sekerka, *Cryst. Res. Tech.*, **40**, 4/5 (2005).

7.10 F. Oberholtzer D. Barkey and Q. Wu, *Phys. Rev. E*, **57 (6)**, 6955 (1998).

7.11 H. Brune, K. Bromann, K. Kern, J. Jacobsen, P. Stolze, K. Jacobsen and J. Norskov, *Mat. Res. Soc. Symp. Proc.*, **407**, 379 (1996).

7.12 J. M. K. Donev, Q. Yu, B. R. Long, R. K. Bollinger and S. C. Fain, Jr., *J. Chem. Phys.*, **123**, 44706 (2005).

7.13 P. Carro, S. Ambrosolio, S. L. Marchinao, A. Hernandez Creus, R. C. Salvarezza and A. J. Arvia, *J. Electroanal. Chem.,* **396**, 183 (1995).

CHAPTER 8:

RESULTS:

METAL RECOVERY USING ELECTROLYTIC FLOW-BY CELL

8.1 Studies on Metal Ion Removal Process

Study on the feasibility of gold recovery from rinse waters from a gold thiosulphate-sulphite aged electrolyte was carried out in three stages. In the first stage, acidified copper sulphate solution was used as a reference electrolyte to characterise the mass transport property at a copper plate and RVC electrode. For this, 1, 5 and 10 mM of $CuSO_4$ in 0.1 M H_2SO_4 were used to test the effect of concentration on mass transport properties. Through these experiments, the limiting current and the product of mass transport coefficient, $k_m A_e$, for the RVC electrode were determined.

In the second stage, removal of copper (II) from 1 mM copper sulphate was carried out as a preliminary test of the cell performance. A theoretical plot of normalised copper concentration against time was constructed in order to estimate the number of steps needed to be taken to reduce the concentration of copper. Thereafter, controlled current analysis was carried out in which the current was adjusted to its limiting value corresponding to the estimated copper concentration at that instant and the current was allowed to flow for a specified time period. At the end of that time period, a sample of electrolyte was taken out and copper concentration in solution was quantified via ICP spectroscopy. Once this was accomplished, the current was adjusted to a new value which represented the value of limiting current at corresponding concentration.

In the third stage, the limiting current of gold (I) system was calculated using the diffusion coefficient of gold (I) [8.1], diffusion coefficient of copper (II) [8.2] and the limiting current of copper (II). Similar to that of copper (II) removal, a theoretical plot of normalised gold concentration was constructed from which the current at corresponding concentration was estimated. Subsequently, removal of gold from 1 mM gold thiosulphate-sulphite aged electrolyte was performed.

8.2 Removal of Copper (II) from Acid Sulphate Media

8.2.1 Mass Transport at a Copper Plate Electrode

Figure 8.1 shows the polarisation curves for two different electrolyte concentrations, 5 mM and 10 mM $CuSO_4$ in 0.1 M H_2SO_4 at a fixed electrolyte flow velocity. The area available for deposition was 60 cm^2.

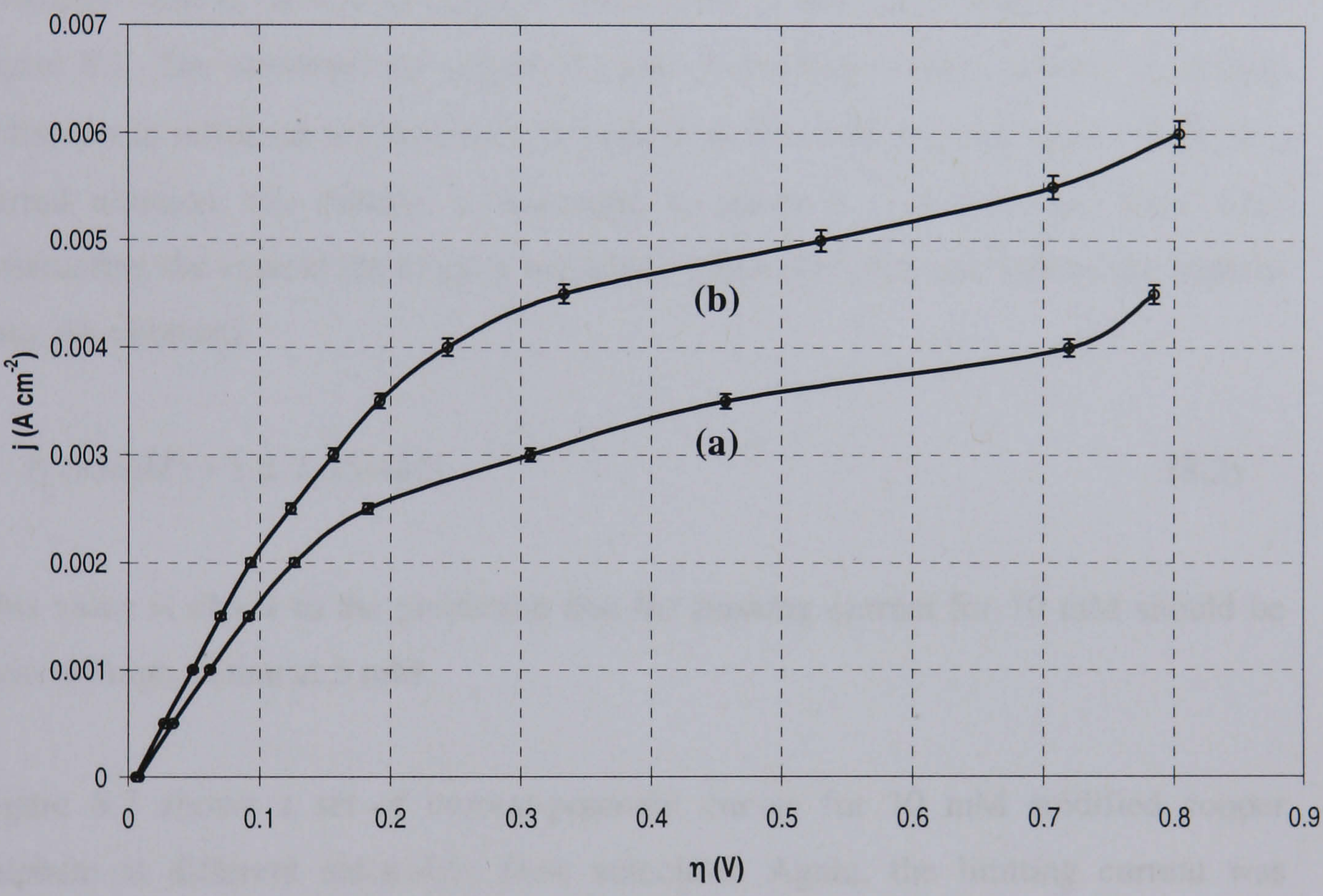

Figure 8.1: Limiting current of (a) 5 mM and (b) 10 mM $CuSO_4$ in 0.1 M H_2SO_4 at 0.222 m s^{-1}.

The limiting current for copper (II) reduction was estimated as the current measured at 0.5 V and was found to be 0.0035 A cm^{-2} and 0.0049 A cm^{-2} for 5 mM and 10 mM, respectively. Clearly, the limiting current increases with increasing metal ion

concentration and the correlation between the two electrolyte concentrations was found to be

$$I_L(10mM) = 1.4\ I_L(5mM) \tag{8.1}$$

According to the Nernst diffusion layer model, the limiting current for 10 mM should be twice as high as that at 5 mM. However, considering the fluctuation in electrolyte velocity observed during this experiment, the correlation obtained was of acceptable range. Furthermore, oxygen reduction was a parasitic reaction at the cathode and the diffusion limited current of oxygen contributes to the total observed currents in figure 8.1. The conventional accepted value of limiting current density of oxygen reduction in unstirred solution is in the range of 50 - 100 μA cm^{-2} [8.3 – 8.5]. In a stirred solution, the current is increased to about 1 – 5 mA cm^{-2} [8.5, 8.6]. Subtracting the current for oxygen reduction (taken as 1 mA cm^{-2}) from the original data, we obtained

$$I_L(10mM) = 1.6\ I_L(5mM) \tag{8.2}$$

This value is closer to the prediction that the limiting current for 10 mM should be twice as high as that at 5 mM.

Figure 8.2 shows a set of current-potential curves for 10 mM acidified copper sulphate at different electrolyte flow velocities. Again, the limiting current was estimated as the current measured at 0.5 V, and the values of limiting current at different electrolyte velocities are listed in table 8.1.

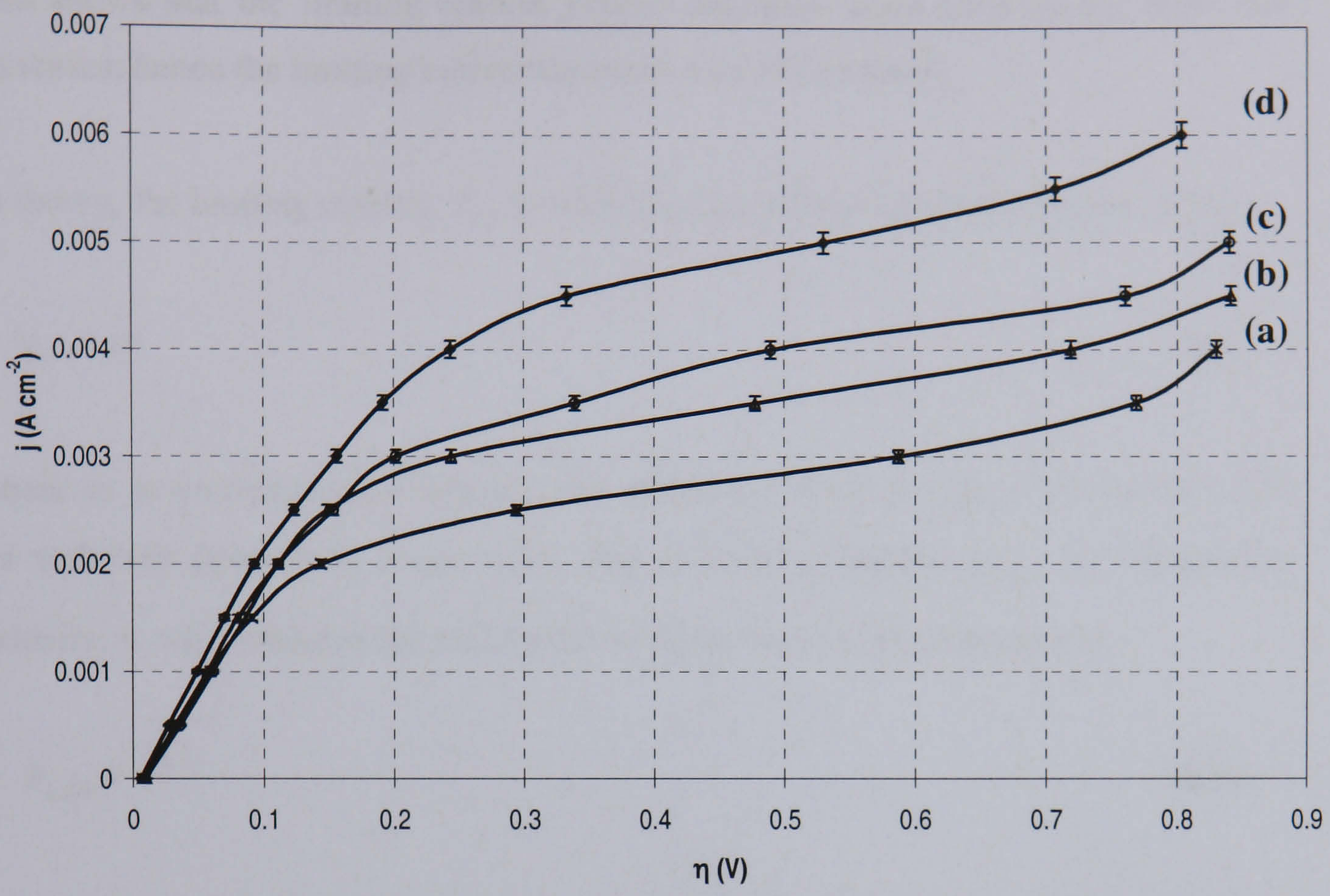

Figure 8.2: Limiting current of 10 mM $CuSO_4$ in 0.1 M H_2SO_4 at (a) 0.037 m s^{-1} (b) 0.074 m s^{-1} (c) 0.148 m s^{-1} and (d) 0.222 m s^{-1}.

υ (m s^{-1})	**$I_{L,Cu}$ (x 10^{-3}A cm^{-2})**
0.037	2.8
0.074	3.5
0.148	4.0
0.222	4.9

Table 8.1: Limiting currents of copper (II) deposition from 10 mM copper sulphate electrolyte at a copper plate electrode at different electrolyte velocities.

It can be seen that the limiting current increases with increasing electrolyte velocity, which is a characteristic behaviour of a mass-transfer controlled process. Figure 8.2

also shows that the limiting current plateau becomes more tilted as the flow rate increases; hence the limiting current becomes less well defined.

In theory, the limiting current, I_L, is related to the electrolyte flow velocity, υ, by

$$I_L \propto \upsilon^m \tag{8.3}$$

where m is a constant that theoretically equals to 0.5 for laminar flow or 0.8 – 0.9 for turbulent flow [8.7]. From a log plot of limiting current, $I_{L,Cu}$, *vs.* electrolyte velocity, υ, we found that the correlation between the two parameters was

$$I_{L,Cu} \propto \upsilon^{0.29} \tag{8.4}$$

The value of m ~ 0.3 indicates a laminar flow regime as expected.

8.2.2 Mass Transport at Reticulated Vitreous Carbon (RVC) Electrode

In order to establish the mass transport characteristic at porous electrode, current-potential data for copper (II) reduction with an RVC electrode using 1 mM and 5 mM acidified copper sulphate solutions was gathered. However, no clear limiting current was observed, as is observed in curve (a) of figure 8.3. This is due to the presence of H^+ ions contributed by H_2SO_4 in the electrolyte. Reduction of hydrogen takes place simultaneously with copper reduction, thus masking the limiting current plateau of copper (II) reduction. This behaviour is overcome by obtaining the current-potential curve for only 0.1 M H_2SO_4, which is shown by curve (b) in figure 8.3, and subtracting the current for hydrogen evolution from the original data, *i.e.* curve (a). The resulting curve for copper deposition is shown by curve (c) in figure 8.3.

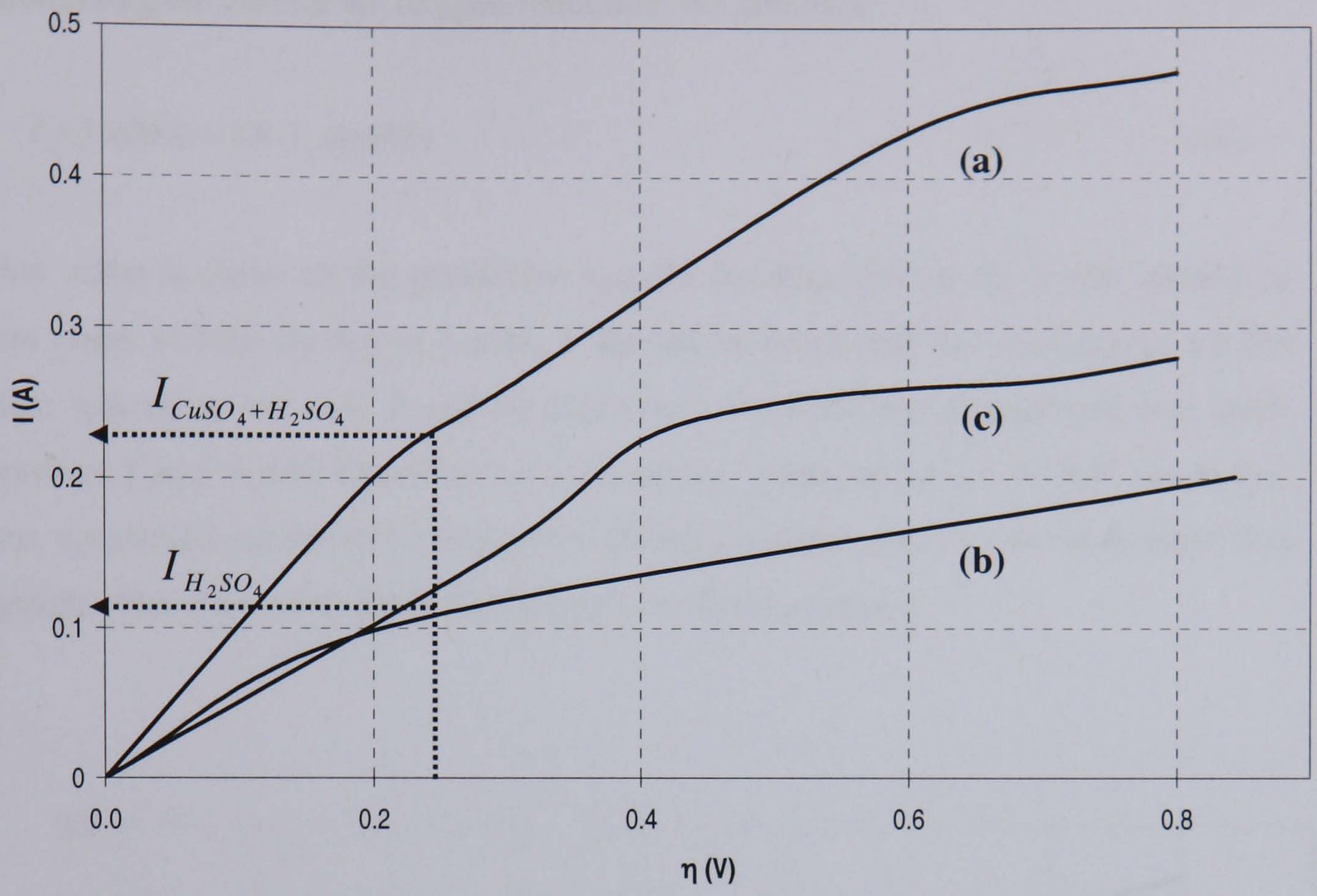

Figure 8.3: Current-potential curves at 0.037 m s^{-1} for (a) 5 mM $CuSO_4$ in 0.1 M H_2SO_4 (b) 0.1 M H_2SO_4 and (c) net current for copper deposition.

Figure 8.4 shows the limiting currents of 1 mM and 5 mM $CuSO_4$ in 0.1 M H_2SO_4 at electrolyte velocity of 0.037 m s^{-1} after subtracting the hydrogen evolution current from current-potential data obtained for ion reduction in acidified copper sulphate solution. This figure shows similar behaviour to that observed with a flat plate cathode, in which the limiting currents are proportional to the copper (II) concentration. A plateau, approximately at 0.25 A, was observed for 5 mM acidified $CuSO_4$ electrolyte and this value is more than twice as high as that obtained for 1 mM,

$$I_L(5mM) = 2.3\ I_L(1mM) \tag{8.5}$$

Subtracting the current for oxygen reduction, we obtained

$$I_L(5mM) = 3.8\ I_L(1mM) \tag{8.6}$$

This value is closer to the prediction that the limiting current for 5 mM should be five times as high as that at 1 mM. It should be noted that the comparison for flat plate was made between 5 and 10 mM while for RVC the comparison was made between 1 and 5 mM electrolyte concentrations. Experiment for 10 mM electrolyte was not carried out for RVC because no limiting current plateau was observed in that system even after subtracting the hydrogen evolution current.

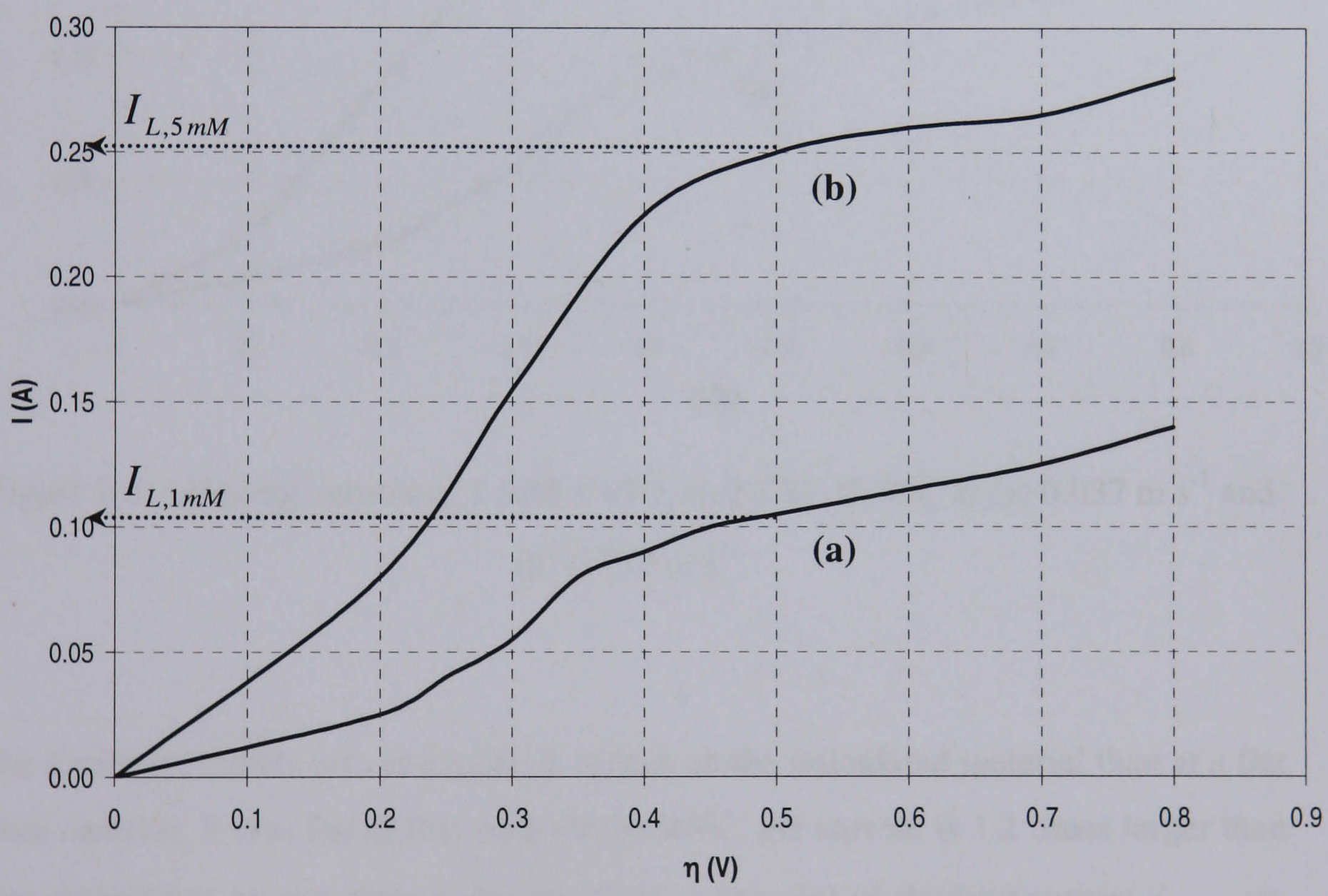

Figure 8.4: Limiting current of (a) 1 mM and (b) 5 mM $CuSO_4$ in 0.1 M H_2SO_4 at 0.037 m s^{-1}.

Figure 8.5 demonstrates that, in agreement with results obtained at a flat plate electrode, the limiting current increases with increasing electrolyte flow velocity. Similar observations were also found by other researchers studying metal recovery using porous electrodes [8.8, 8.9].

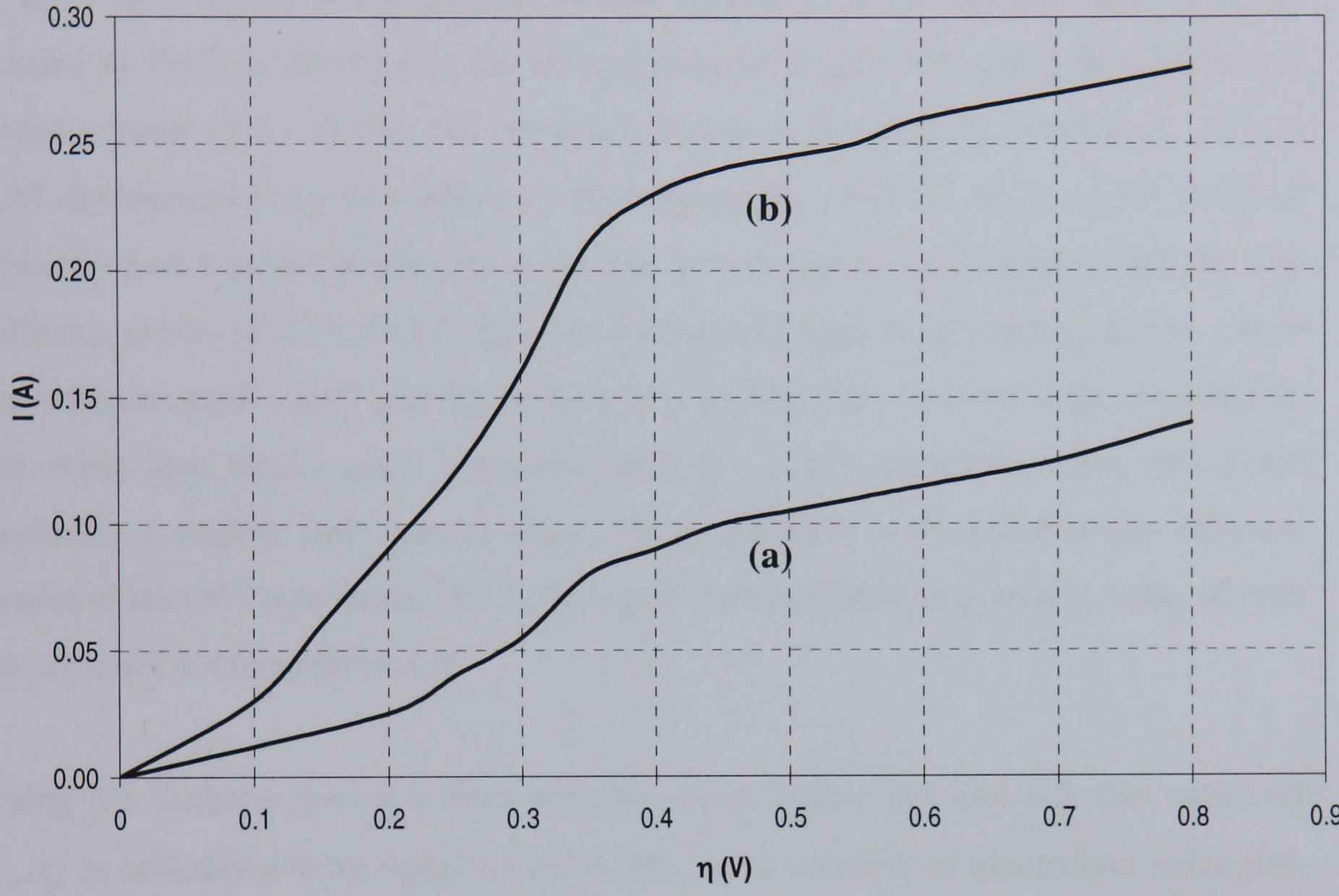

Figure 8.5: Limiting current of 1 mM $CuSO_4$ in 0.1 M H_2SO_4 at (a) 0.037 m s^{-1} and (b) 0.222 m s^{-1}.

The limiting currents are, as expected, higher on the reticulated material than at a flat plate cathode. It was found that with 60 ppi RVC, the current is 1.2 times larger than that obtained at copper plate electrode. From a log plot of limiting current, $I_{L,Cu}$, vs. electrolyte velocity, υ, the correlation between the two parameters was found to be

$$I_{L,Cu} \propto \upsilon^{0.44} \tag{8.7}$$

The value of $m = 0.44$ shows improvement from that obtained at a flat plate cathode. where $m = 0.29$. This improvement is due to the reticulated structure of the RVC which promotes turbulence in the system compared against those of flat plate electrode. Prior work on RVC material have shown that the mass transfer limiting current is proportional to the flow velocity with an exponential factor m in the range of 0.4 – 0.7, which is comparable to that obtained for our system. Mass transfer studies by Podlaha and Fenton for the reduction of copper (II) and ferricyanide ions found a value of 0.7 [8.10]. The exponent found in the study by Pletcher *et. al.* was 0.48 determined from data taken at different grades of RVC [8.2]. In the work of Tentorio and Casolo-Ginelli, the exponent was found to be 0.49 and 0.53 for two different grades of RVC [8.11]. Hor and Mohamed report values between 0.44 – 0.69 for different grades and specific surface area of RVC [8.12]. The value obtained by our study also shows good agreement with the values found for other reticulated materials. Langlois and Coeuret report values between 0.45 and 0.48 for different grades of nickel foam stacks [8.13]. Hor and Mohamed have reported a value of 0.69 for carbon felt electrode [8.12].

Using the limiting current values obtained from figures 8.4 and 8.5, the values of $k_m A_e$ is calculated from equation 8.8 below, as a function of electrolyte velocities. The values are listed in table 8.2. Plots of $k_m A_e$ as a function of electrolyte velocities are shown in figure 8.6.

$$k_m A_e = \frac{I_L}{nFV_e c_o} \tag{8.8}$$

υ (m s^{-1})	I_L **(A)**	$k_m A_e$ **(s^{-1})**
0.037	0.12	0.0829
0.222	0.25	0.1796

Table 8.2: Limiting currents and $k_m A_e$ of copper (II) system at reticulated vitreous carbon (RVC) electrode.

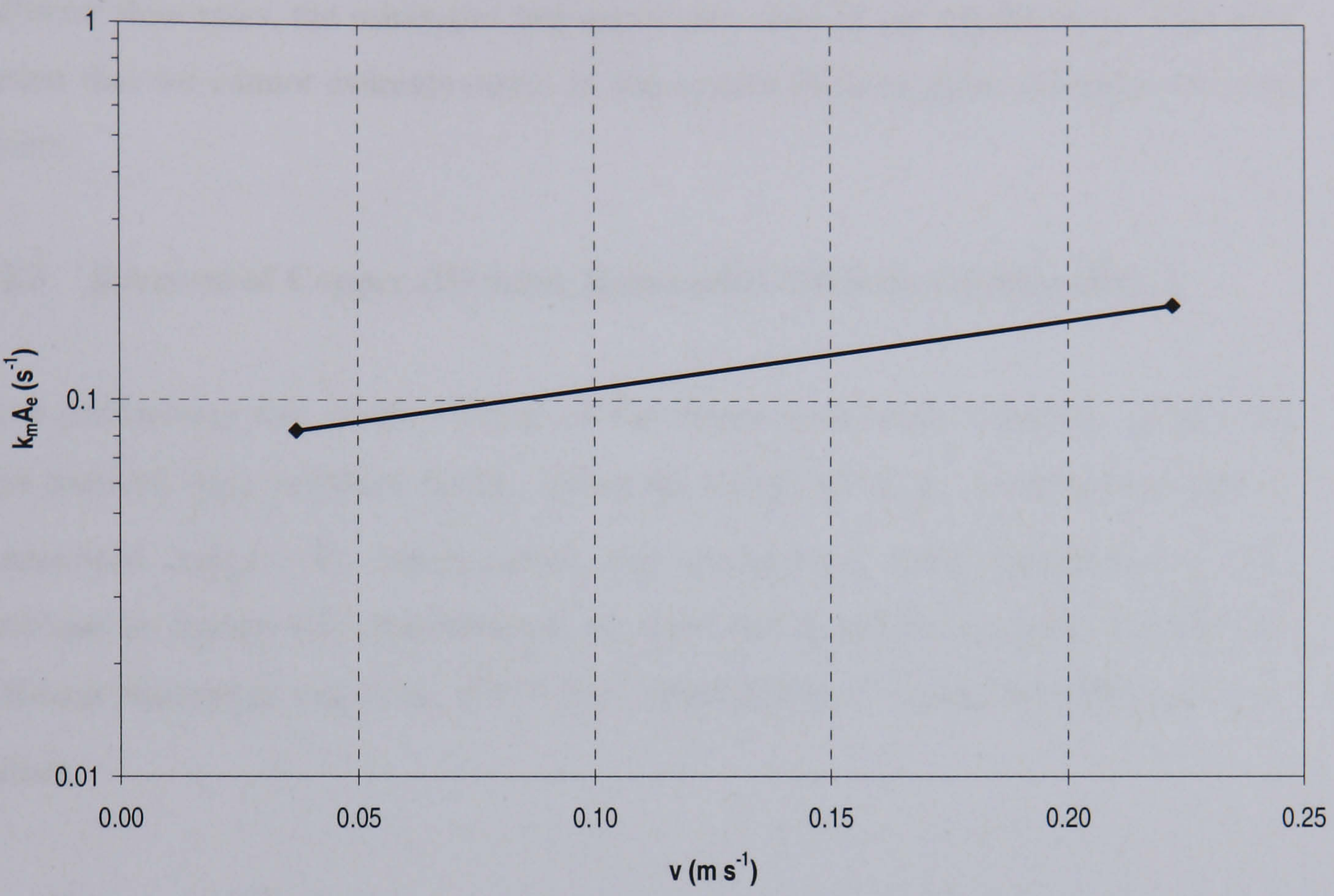

Figure 8.6: Variation of $k_m A_e$ with electrolyte velocities for acidified copper sulphate system.

The plot of $k_m A_e$ for acidified copper sulphate system shows reasonable agreement to those reported by other researchers [8.2, 8.14]. It was also found that the $k_m A_e$ plot as a function of electrolyte concentrations (1 and 5 mM) is similar to that in figure 8.6, as the limiting current obtained at electrolyte velocity 0.037 m s^{-1} with 5 mM electrolyte concentration is similar to that obtained for electrolyte velocity 0.222 m $s^{-1}$with 1 mM electrolyte concentration. The $k_m A_e$ values obtained in this analysis are later used to predict the concentration depletion of metal ions during the removal process.

Although, in a system such as ours one would collect $k_m A_e$ values at about four to five different velocities, due to time restrictions, we have shown values for only two different flow rates, the minimum and maximum, used in our experiments. This also means that we cannot estimate errors in our system because there are only two data points.

8.2.3 Removal of Copper (II) using Reticulated Vitreous Carbon (RVC)

As a preliminary test of the validity of our theory form metal removal, copper (II) was reduced from sulphate media. Using the values of $k_m A_e$, a theoretical plot of normalised copper (II) concentration was constructed using equation 8.9. The decrease in copper (II) concentration vs. time and is shown in figure 8.7 for two different electrolyte velocities, 0.037 m s^{-1} and 0.222 m s^{-1}, using two different $k_m A_e$ values.

$$\frac{c(t)}{c(o)} = \exp\frac{-V_e k_m A_e}{V_R} t \qquad (8.9)$$

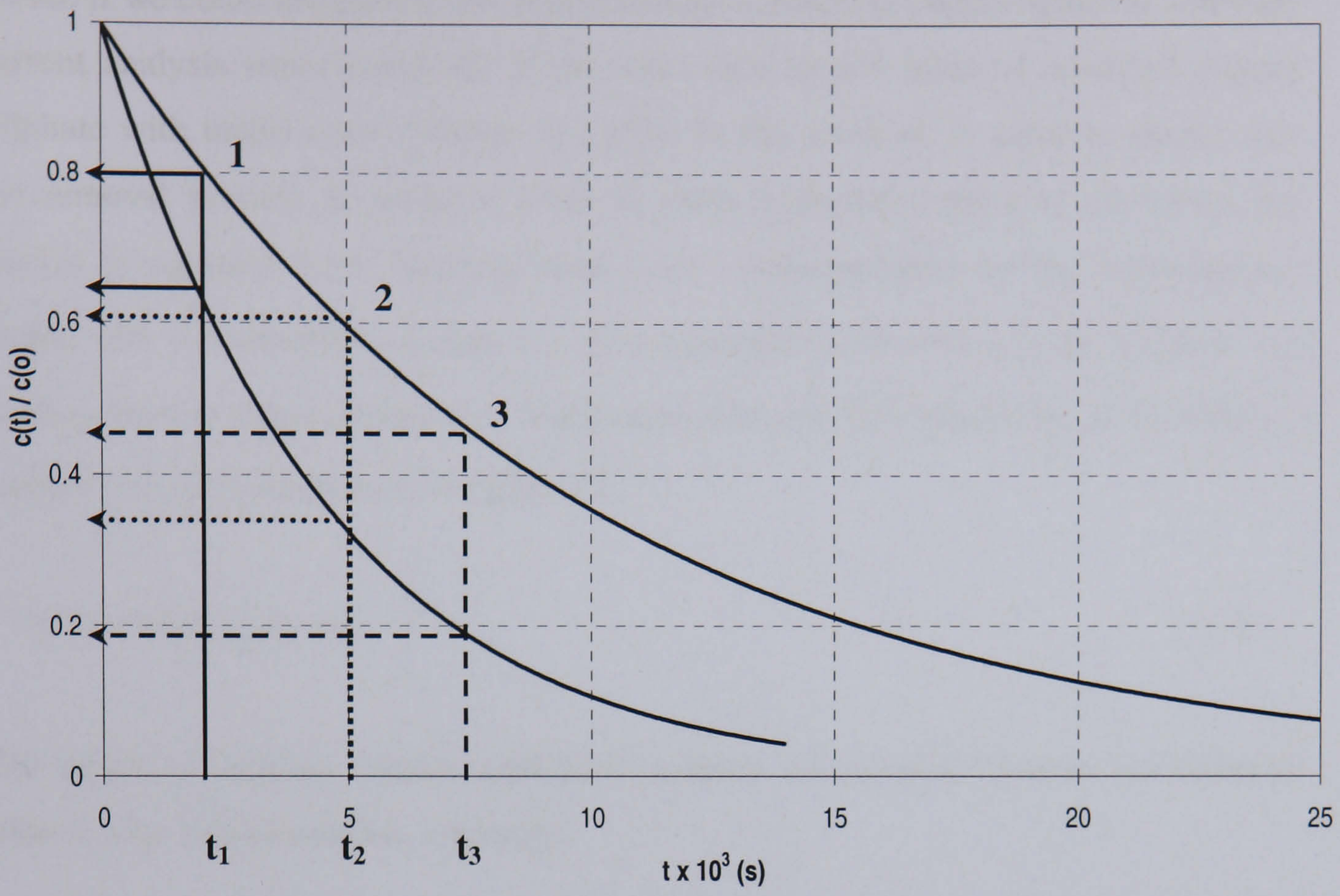

Figure 8.7: Theoretical plot of normalised copper (II) concentration against time at electrolyte velocities of (a) 0.222 m s^{-1} and (b) 0.037 m s^{-1}.

Figure 8.7 predicts that the copper (II) concentration decays exponentially with time and that the rate of copper (II) removal is faster at higher electrolyte velocity. This prediction is simply a solution of equation 8.9, which was originally shown by Pletcher *et. al.* [8.2]. The time taken for 90% removal of copper from the initial value, $t_{90\%}$, was calculated to be nearly 3 hours at 0.222 m s^{-1} and almost 6 hours at 0.037 m s^{-1}.

As shown in the figure, one can choose different current densities corresponding to points 1, 2, 3 and so on. If the reduction current is fixed at the limiting current corresponding to the concentration at 1 for a time period t_1, the metal will plate very close to its limiting current for that time period. At the end of this time period, the reduction current is reduced to the limiting current value at point 2 and so on.

To see if we could implement our approximation method to copper removal, constant current analysis was carried out in the cell containing 6 litres of acidified copper sulphate with initial concentration of 1 mM. In this method, in order to ensure that the removal process is operated close to mass transport control at all times, the current is adjusted to its limiting value, $I_L(t)$, corresponding to the instantaneous copper (II) concentration at time t, $c(t)$. Equation 8.10 was used to estimate the limiting current values using $c(t)$ determined from the theoretical plot of normalised copper concentration shown in figure 8.8.

$$I_L(t) = nFV_e k_m A_e c(t) \tag{8.10}$$

The values of limiting current applied throughout the removal process are listed in table 8.3 for two electrolyte velocities.

0.037 m s^{-1}			**0.222 m s^{-1}**		
t x 10^3 (s)	**c (t) (mM)**	**$I_{L,Cu}$ (mA)**	**t x 10^3 (s)**	**c (t) (mM)**	**$I_{L,Cu}$ (mA)**
0	1.00	120	0	1.00	260
1	0.90	108	1	0.80	208
2	0.81	97	2	0.64	166
5	0.59	71	3	0.51	133
7	0.48	58	4	0.40	104
9	0.39	47	5	0.32	83
15	0.21	25	7	0.21	55
17	0.16	19	10	0.10	26

Table 8.3: Estimated limiting currents of 1 mM acidified copper sulphate electrolyte at electrolyte velocities of 0.037 m s^{-1}and 0.222 m s^{-1}.

As an example, when a current of 120 mA is applied at an electrolyte velocity of 0.037 m s^{-1} for duration of 1000 s, the concentration of copper (II) is expected to reduce to 0.9 mM. In order to reduce this concentration to 0.8 mM, a current of 108 mA is then needed. In this experiment, overall seven steps were taken in order to reduce the concentration to below 0.1 mM. Samples of electrolyte were taken at predetermined intervals during the experiment. The remaining concentration of copper (II) ions in the electrolyte was monitored as a function of time and plotted in figures 8.8 and 8.9 for electrolyte velocities of 0.037 m s^{-1} and 0.222 m s^{-1}, respectively.

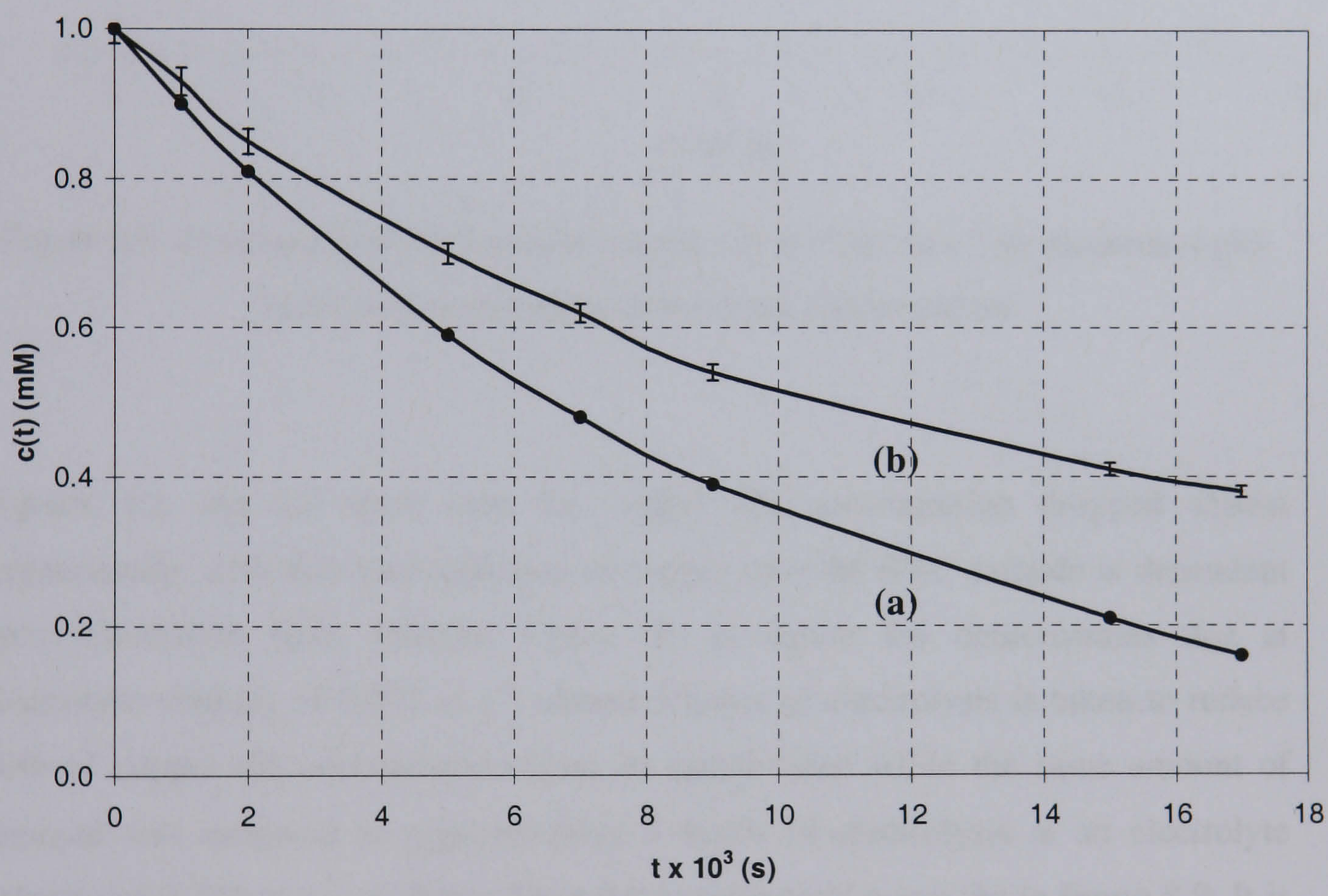

Figure 8.8: Concentration depletion of copper (II) at 0.037 m s^{-1} (a) theoretical plot and (b) experimentally determined concentration

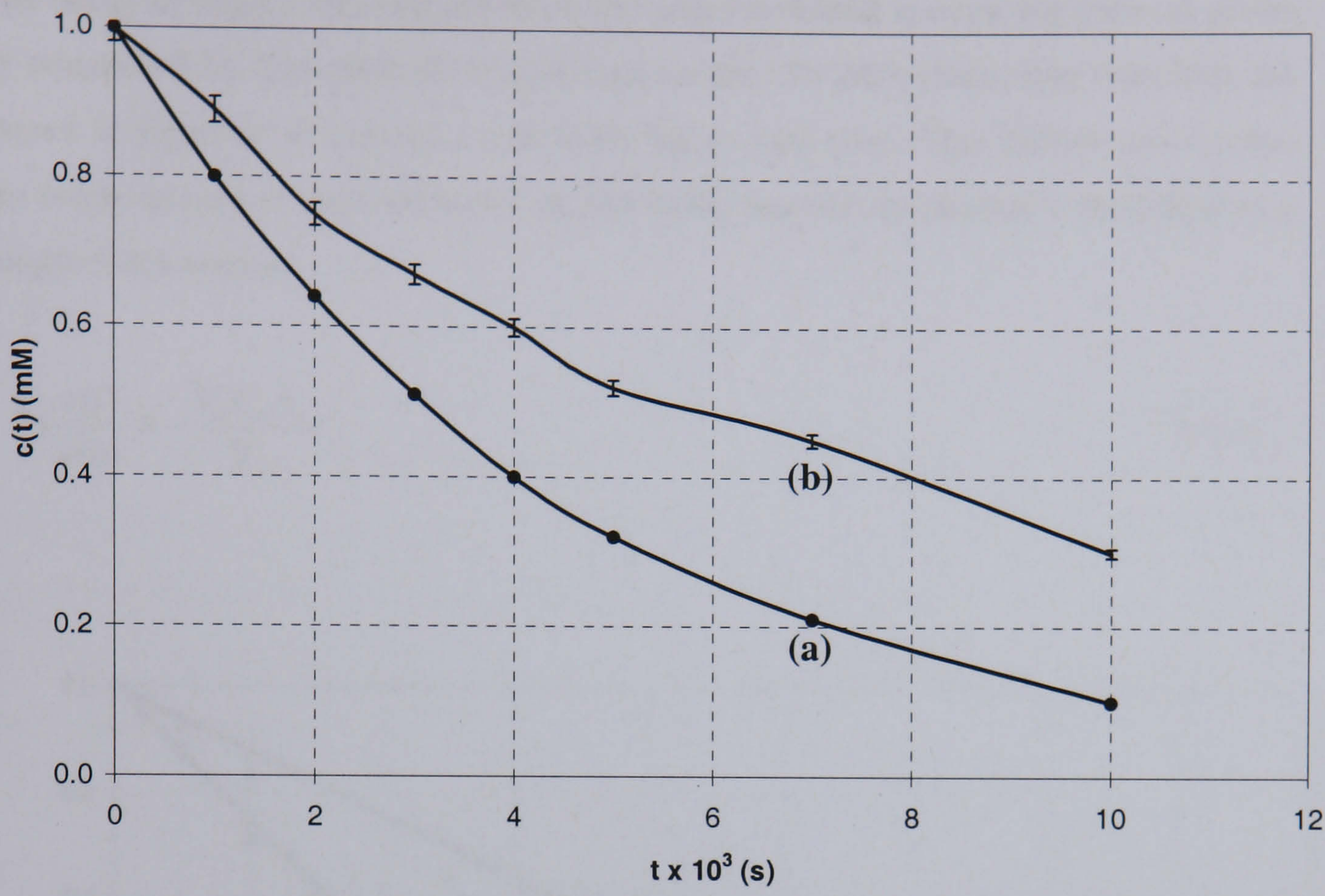

Figure 8.9: Concentration depletion of copper (II) at 0.222 m s^{-1} (a) theoretical plot and (b) experimentally determined concentration

Figures 8.8 and 8.9 show that the copper (II) concentration dropped almost exponentially with time and reduction of copper onto the RVC cathode is dependent upon electrolyte flow velocity. Curve (b) in figure 8.8 demonstrates that at electrolyte velocity of 0.037 m s^{-1}, almost 5 hours of electrolysis is taken to reduce 60% of copper (II) concentration from its initial value while the same amount of removal was achieved in approximately 2 hours of electrolysis at an electrolyte velocity of 0.222 m s^{-1}, as shown from the experimental curve (b) in figure 8.9. It is evident that the copper concentration decreases more rapidly with an increase in electrolyte velocity. Such results show clearly that at higher flow velocities, the reactor performance is better. The transport of electroactive species to the cathode surface is enhanced and this results in faster rate of concentration decay [8.15, 8.16].

The decay in copper (II) concentration can also be plotted in semi-log form as given by equation 8.11. The plots of ln [c(t)/c(o)] *vs.* time for both electrolyte velocities are shown in figure 8.10 and are found to be linear with time. This further proved that the batch recycle system employed in this study may be satisfactorily modelled as a simple batch reactor

$$\ln \frac{c(t)}{c(o)} = -\frac{V_e k_m A_e}{V_R} t \qquad (8.11)$$

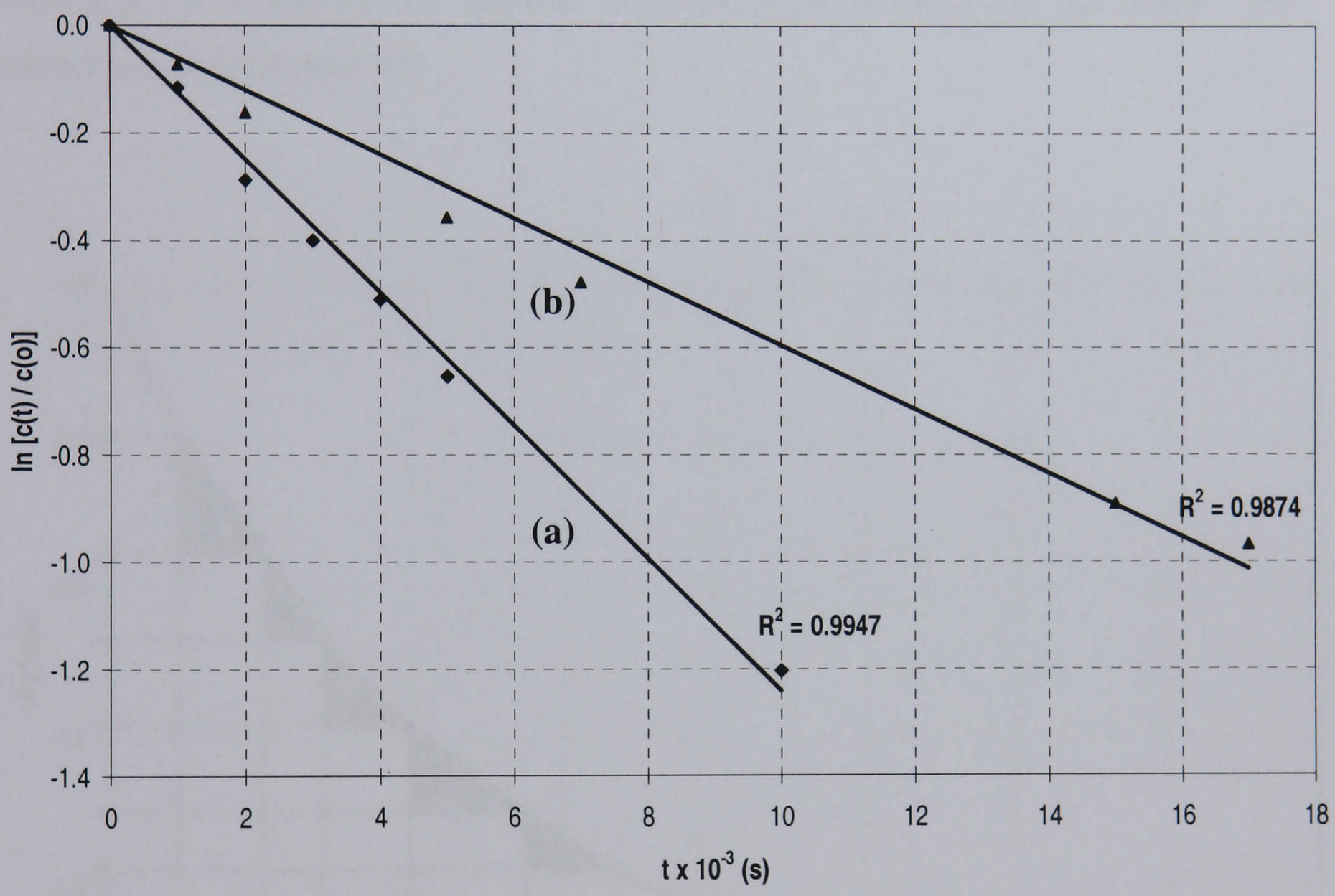

Figure 8.10: Plot of $\ln \frac{c(t)}{c(o)}$ *vs.* time at electrolyte velocities of (a) 0.222 m s^{-1} and (b) 0.037 m s^{-1}

In this process, the rate of copper (II) removal never reached 100% primarily due to the reduction of dissolved oxygen as a secondary reaction. Several authors have reported the influences of dissolved oxygen towards metal ion reduction. Walsh

reported the current through the cell is much higher when oxygen is present, which leads to a decrease in current efficiency [8.17]. Reade *et al.* has also attributed the low in current efficiency during copper (II) removal to the reduction of residual dissolve oxygen, an increase in the current efficiency was achieved after oxygen was removed from the electrolyte [8.18].

The low rate of copper (II) removal can also be due to the experimental error associated with the estimation of limiting current. As shown in figure 8.11, the calculated limiting current does not take into consideration the concentration of remaining metal ion in the highlighted area under the curve. This error can be eliminated by increasing the number of steps taken in reducing the copper (II) concentration to lower level.

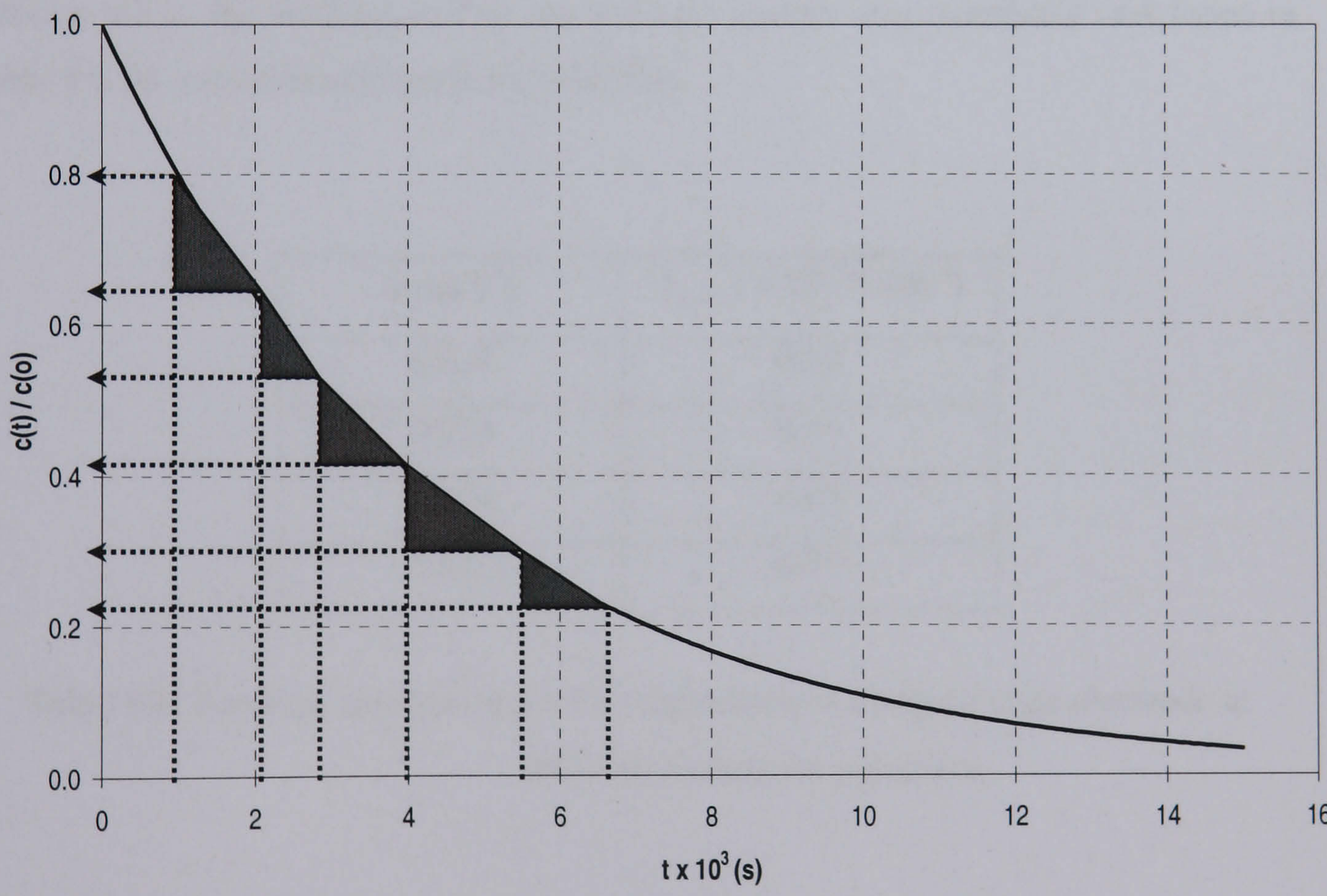

Figure 8.11: Experimental error associated with the estimation of limiting current.

8.3 Removal of Gold from Thiosulphate-Sulphite Aged Electrolyte

8.3.1 Estimation of Gold Reduction Current at a Flat Plate Cathode

Figure 8.2 provides the limiting current values for copper (II) system which are then used to estimate the limiting current for gold thiosulphate-sulphite system, using equation 8.12 shown below. The relationship for gold copper system has been derived from the Nernst diffusion layer model, as described in section 3.1.4 of chapter 3, and it was found that the limiting current of gold is approximately 16% of limiting current of copper.

$$I_{L,Au} = 0.158 I_{L,Cu} \tag{8.12}$$

Using this correlation and the limiting currents for copper (II) system obtained in section 8.2.1, the limiting current for gold (I) system was calculated and listed in table 8.4 for varied electrolyte flow velocities.

υ (m s^{-1})	$I_{L,Au}$ (x 10^{-3}A cm^{-2})
0.037	0.43
0.074	0.55
0.148	0.63
0.222	0.77

Table 8.4: Limiting currents of gold (I) deposition at a copper plate electrode at different electrolyte velocities.

8.3.2 Estimated Limiting Current for Gold Reduction at a Reticulated Vitreous Carbon Electrode

Using the limiting current values for copper (II) system at RVC electrode obtained in section 8.2.2, limiting current and $k_m A_e$ values for gold (I) system was calculated and listed in table 8.5. The $k_m A_e$ values are later used to construct the theoretical plot of normalised gold concentration against time at two electrolyte velocities.

υ (m s^{-1})	I_L **(A)**	$k_m A_e$ **(s^{-1})**
0.037	0.019	0.0262
0.222	0.042	0.0568

Table 8.5: Limiting currents and $k_m A_e$ of gold (I) system at reticulated vitreous carbon (RVC) electrode.

8.3.3 Removal of Gold using Reticulated Vitreous Carbon (RVC)

The experimental procedure used in copper (II) removal was repeated with 1 mM gold thiosulphate-sulphite aged electrolyte. Figure 8.12 shows the theoretical plot of normalised gold concentration *vs.* time calculated using the $k_m A_e$ values obtained from current-potential analysis. The time taken for 90% removal of gold from the initial value, $t_{90\%}$, was calculated to be nearly 9 hours at 0.222 m s^{-1}and twice as much time is needed to remove the same amount of gold at 0.037 m s^{-1}. The much longer time period required for gold removal indicates that the process may not be implementable.

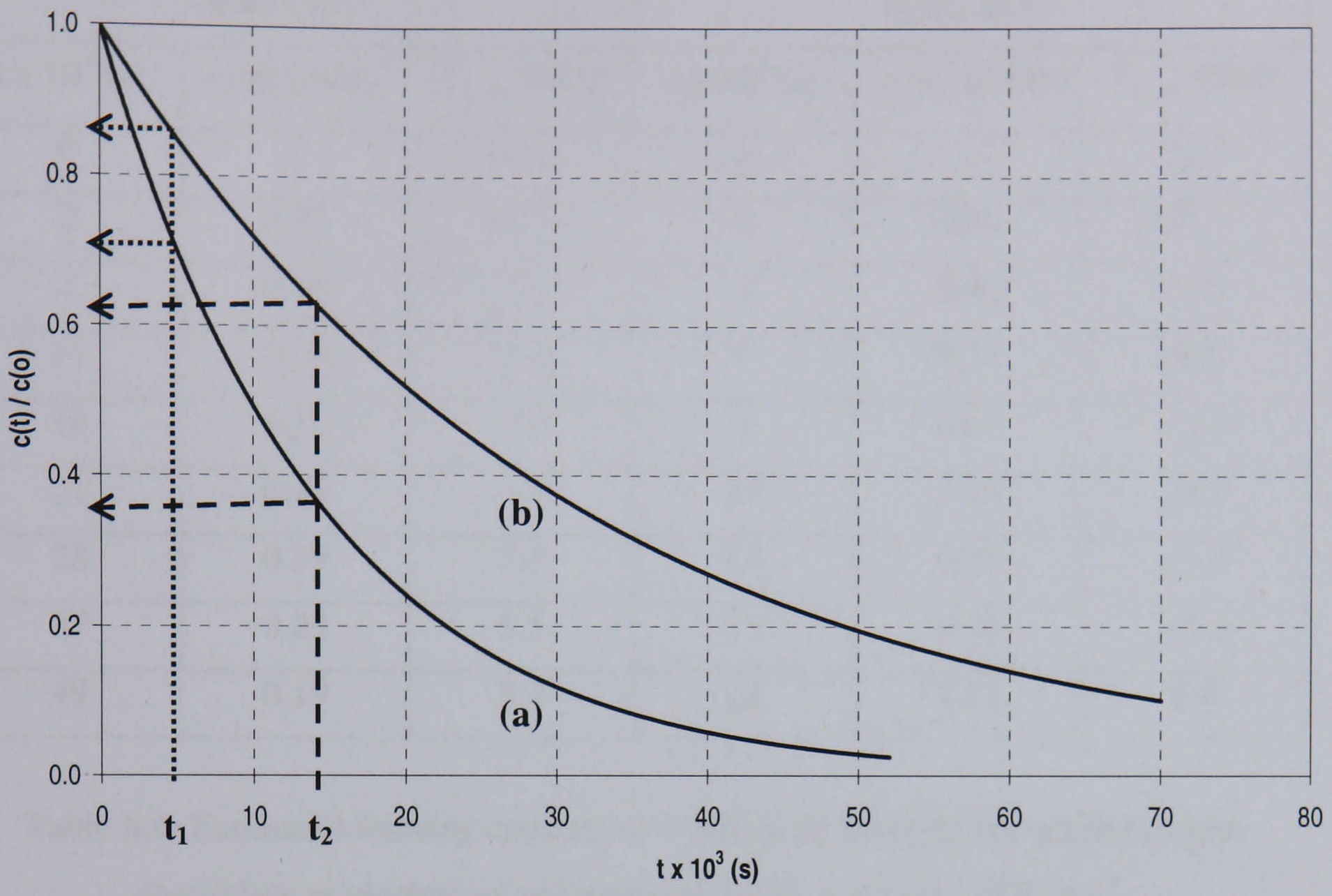

Figure 8.12: Theoretical plot of normalised gold concentration against time at electrolyte velocities of (a) 0.222 m s^{-1} and (b) 0.037 m s^{-1}.

Subsequently, a series of controlled current analysis were carried out aiming at highest possible gold recovery from a dilute waste stream. Similar to copper (II) removal process, the currents applied throughout the removal process are adjusted to its limiting values; as listed in table 8.6. Overall eight steps are needed to be taken in order to reduce the concentration of gold (I) ion to below 0.2 mM.

0.037 m s^{-1}			0.222 m s^{-1}		
t x 10^3 (s)	c (t) (mM)	$I_{L,Au}$ (mA)	t x 10^3 (s)	c (t) (mM)	$I_{L,Au}$ (mA)
0	1	18.9	0	1	41.1
3	0.91	17.1	1	0.93	39.1
7	0.79	15.1	3	0.80	34.5
11	0.70	13.2	5	0.70	28.9
16	0.59	11.2	7	0.61	25.0
21	0.49	9.5	10	0.49	20.2
28	0.39	7.5	13	0.40	16.3
37	0.29	5.5	17	0.30	12.3
49	0.19	3.7	22	0.21	8.6

Table 8.6: Estimated limiting currents of 1 mM gold thiosulphate-sulphite aged electrolyte at electrolyte velocities of 0.037 m $s^{-1}$and 0.222 m s^{-1}.

The variation of cell potential with time is plotted in figures 8.13 and 8.14 for electrolyte velocities of 0.037 m $s^{-1}$and 0.222 m s^{-1}, respectively. It can be seen that at each flow velocity, the overpotential decreases for the initial 10 seconds, indicating that the active surface area for metal deposition is increasing. The potential transient then exhibit a hump-shaped response, however this was only observed when higher concentration of metal ions are present in the solution, before it dropped to a certain level. With decreasing amount of metal ion in the solution and lower applied current, the peaks diminish. The potential then reached the steady state, characterised by a plateau. Although the concentration of gold decreases very slowly with time, the steady state potential is reached after 10 - 20 seconds of operation.

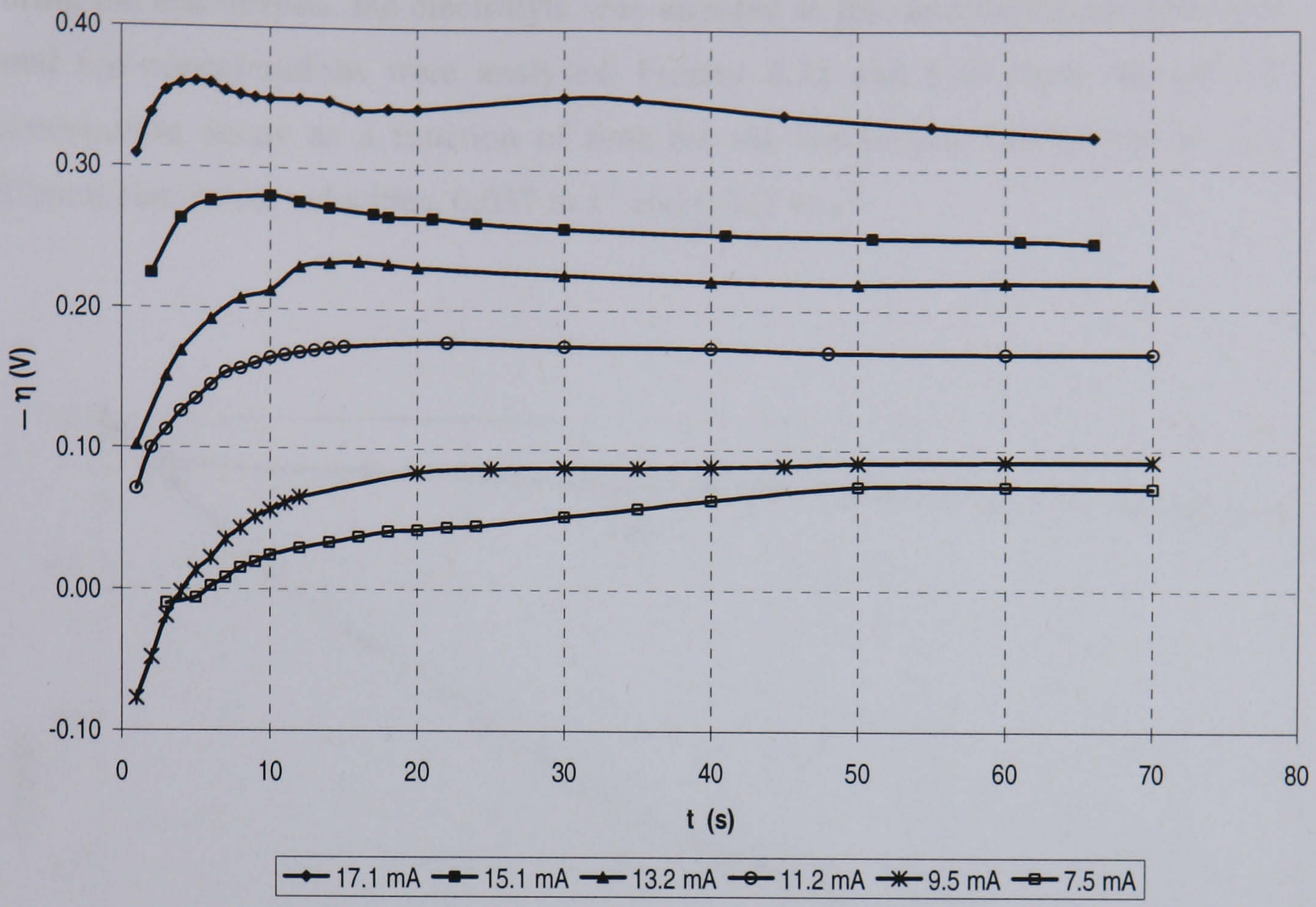

Figure 8.13: Initial cell potential *vs.* time at electrolyte velocity of 0.037 m s^{-1}.

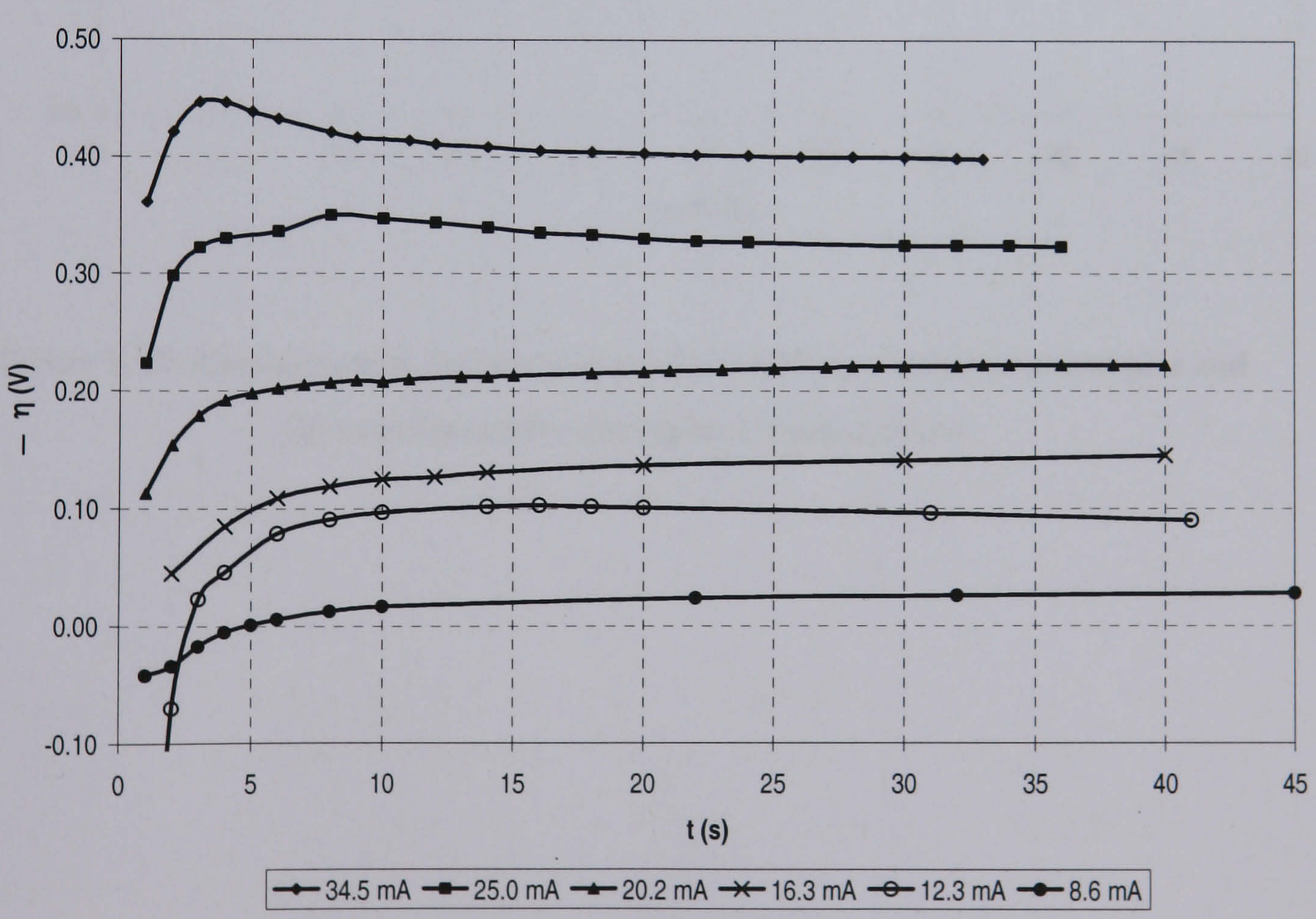

Figure 8.14: Initial cell potential *vs.* time at electrolyte velocity of 0.222 m s^{-1}.

During the electrolysis, the electrolyte was sampled at pre-determined intervals and metal ion concentrations were analysed. Figures 8.15 and 8.16 show the plot of concentration decay as a function of time for the electrolysis carried out at two different electrolyte velocities, 0.037 m s^{-1} and 0.222 m s^{-1}.

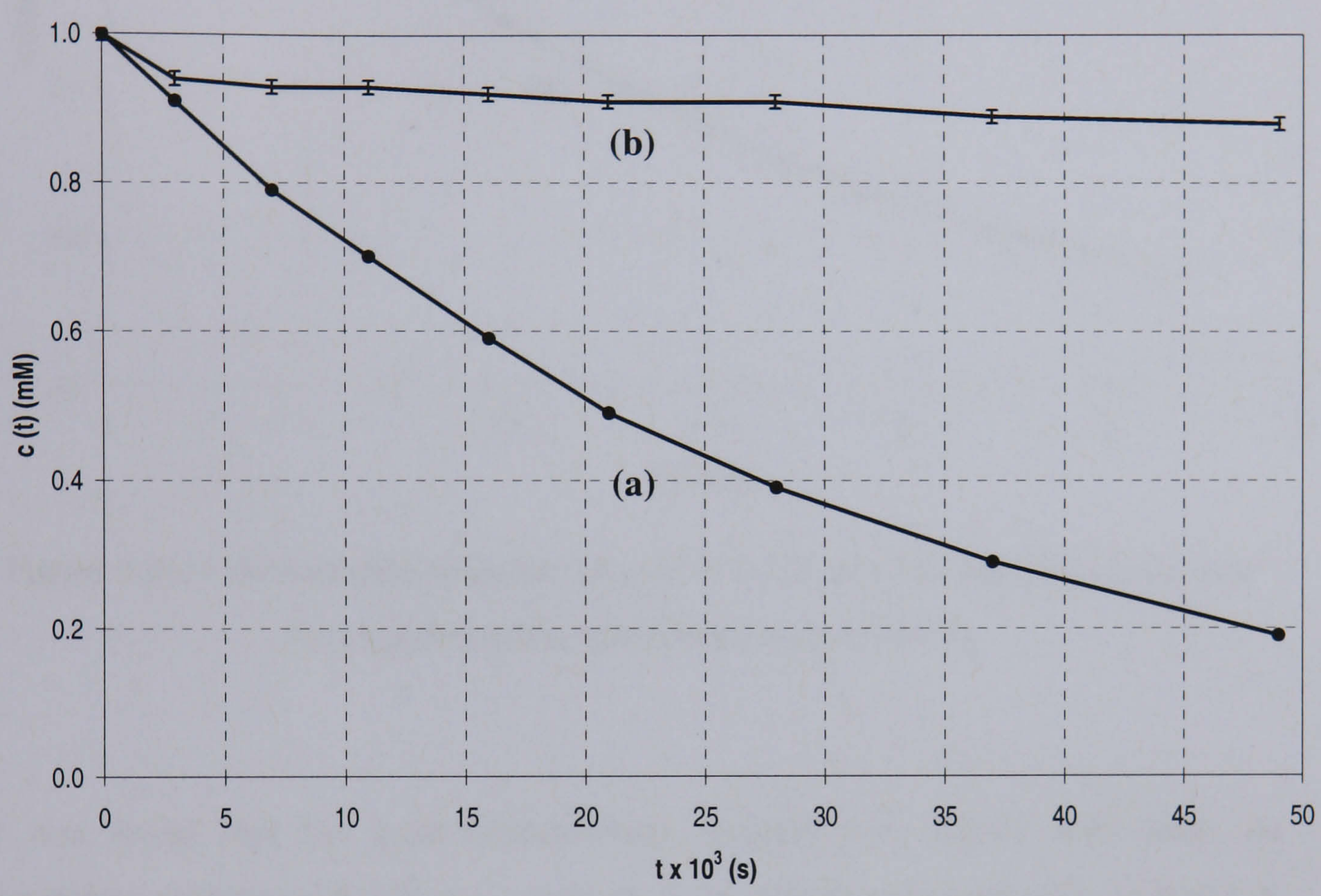

Figure 8.15: Concentration depletion of gold at 0.037 m s^{-1} (a) theoretical plot and (b) experimentally determined concentration

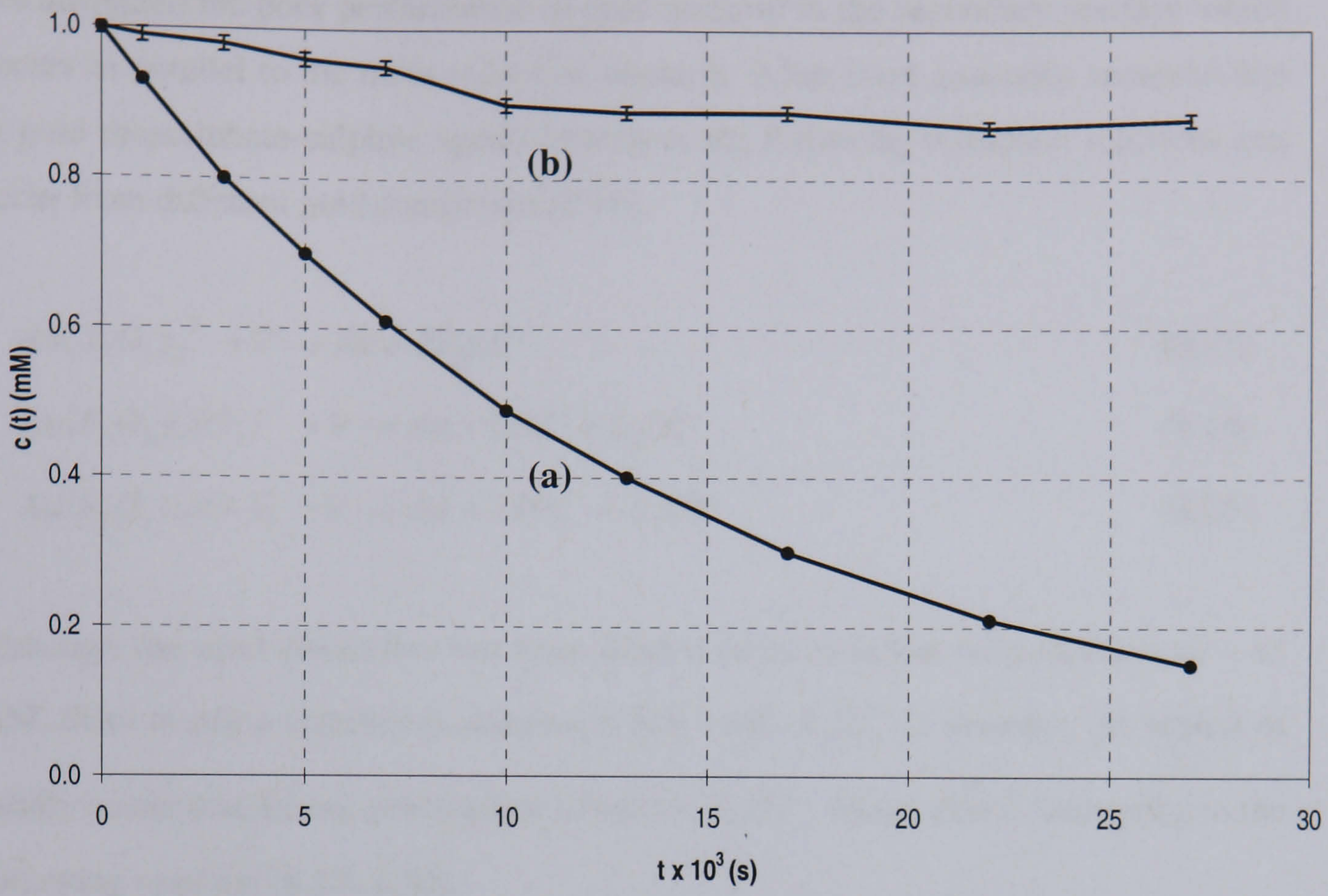

Figure 8.16: Concentration depletion of gold at 0.222 m s^{-1} (a) theoretical plot and (b) experimentally determined concentration.

It was found that the gold concentration depletes very slowly with time. At electrolyte velocity of 0.037 m s^{-1}, only 12 % of gold is recovered after 12 hours of processing. By increasing the electrolyte velocity to 0.222 m s^{-1}, the time taken to remove the same amount of gold was significantly reduced; however the amount of gold removed was still considerably low. The difference between the predicted and experimentally determined concentration depletion was nearly 85 % and there was no definitive evidence that the concentration of gold could be reduced to low levels.

As shown in both figures, the decay in gold concentrations does not follow the predicted exponential behaviour. This shows that the reduction of gold was not fully mass transfer limited and, therefore, the proposed method using batch decay model is unsuitable to recover gold.

We attributed the poor performance of gold removal to the secondary reaction which occurs in parallel to the main reduction reaction. It has been generally accepted that in gold thiosulphate-sulphite aged electrolyte, the following reduction reactions can occur from different gold complexes [8.19].

$$Au(S_2O_3)_2^{3-} + \bar{e} \rightarrow Au + 2S_2O_3^{2-} \tag{8.13}$$

$$Au(S_2O_3)(SO_3)^{3-} + \bar{e} \rightarrow Au + SO_3^{2-} + S_2O_3^{2-} \tag{8.14}$$

$$Au(S_2O_3)(SO_3)_2^{5-} + \bar{e} \rightarrow Au + 2SO_3^{2-} + S_2O_3^{2-} \tag{8.15}$$

Although the aged electrolyte has been diluted from its initial concentration of ~ 45 mM, there is still a significant amount of SO_3^{2-} and $S_2O_3^{2-}$ in solution. At neutral or mildly acidic conditions, protonation of excess $S_2O_3^{2-}$ forms HSO_3^- according to the following reaction [8.19, 8.20],

$$H^+ + S_2O_3^{2-} \leftrightarrow HSO_3^- \tag{8.16}$$

The following reaction can also occur depending on the pH of the electrolyte [8.21]. The more acidic the pH, the more HSO_3^- ions are formed.

$$H_3O^+ + SO_3^{2-} \leftrightarrow HSO_3^- + H_2O \tag{8.17}$$

The cathodic reduction of bisulphite ions, HSO_3^-, leads to the formation of dithionite ions, $S_2O_4^{2-}$.

$$2HSO_3^- + 2\bar{e} \leftrightarrow S_2O_4^{2-} + 2OH^- \tag{8.18}$$

The formation of the dithionite ion, which is a strong reducing agent, leads to a gradual reduction of the gold complex to form colloidal gold [8.19. 8.22].

8.4 References

8.1 S. Sobri and S. Roy, *J. Electrochem. Soc.*, **152**, C593 (2005).

8.2 D. Pletcher, I. White, F. C. Walsh and J. P. Millington, *J. Appl. Electrochem.*, **21**, 659 (1991).

8.3 M. B. Vukmirovic, N. Vasiljevic, N. Dimitrov and K. Sieradzki, *J. Electrochem. Soc.*, **150**, B10 (2003).

8.4 G. Fontana and D. Greene, *Corrosion Engineering (2nd Edition)*, McGraw-Hill Inc. (1978).

8.5 R. Trethewey and J. Chamberlain, *Corrosion*, Longman Group UK Limited (1988).

8.6 N. Masse, J. St-Pierre and M. Bergeron, *J. Appl. Electrochem.*, **25**, 340 (1995).

8.7 S. A. Bradford, *Corrosion Control*, Chapman and Hall (1993).

8.8 R. S. Wenger and D. N. Bennion, *J. Appl. Electrochem.*, **6**, 385 (1976).

8.9 M. Matlosz and J. Newman, *J. Electrochem. Soc.*, **133**, 1850 (1986).

8.10 E. J. Podlaha and J. M. Fenton, *J. Appl. Electrochem.*, **25**, 299 (1995).

8.11 A. Tentorio and U. Casolo-Ginelli, *J. Appl. Electrochem.*, **8**, 195 (1978).

8.12 Y. P. Hor and N. Mohamed, *J. Appl. Electrochem.*, **35**, 609 (2005).

8.13 S. Langlois and F. Coeuret, *J. Appl. Electrochem.*, **19**, 51 (1989).

8.14 C. Ponce de Leon and D. Pletcher, *Electrochim. Acta*, **41 (4)**, 533 (1996).

8.15 L. A. D. Barbosa, L. G. S. Sobral and A. J. B. Dutra, *Minerals Eng.* **14 (9)**, 963 (2001).

8.16 R. Bertazzoli, R. C. Widner, M. R. V. Lanza, R. A. Di Iglia and M. F. B. Sousa, *J. Braz. Chem. Soc.*, **8 (5)**, 487 (1997).

8.17 D. Pletcher, I. White, F. C. Walsh and J. P. Millington, *J. Appl. Electrochem.*, **21**, 667 (1991).

8.18 G. W. Reade, A. H. Nahle, P. Bond, J. M. Friedrich and F. C. Walsh, *J. Chem. Tech. and Biotech.*, **79**, 935 (2004).

8.19 T. A. Green and S. Roy, *J. Electrochem. Soc.*, **153** C157 (2006).

8.20 M. J. Liew, S. Roy and K. Scott, *Green Chem.*, **5,** 376 (2003).

8.21 P. C. Hydes and H. Middleton, *Gold Bull.*, **3 (12)**, 90 (1979).

8.22 P. Wilkinson, *Trans. Inst. Met. Fin.*, **59**, 57 (1981).

CHAPTER 9:

CONCLUSION AND FUTURE WORK

9.1 Conclusion

Gold thiosulphate-sulphite electrolyte has been developed in Newcastle University which is used as electrolyte to electrodeposit gold for microelectronics applications. At the end of the electrodeposition process, the spent electrolyte can contain a significant amount of gold in solution. Since the discharge of gold with effluent is a major economic as well as environmental concern, this study is aimed to investigate if gold can be recovered from aged thiosulphate-sulphite electrolyte

Initially, chemical and electrochemical properties of the aged electrolyte were studied. As the bath aged, pH of the electrolyte slowly decreased from 7.5 to 5.2. Changes in electrochemical behaviour of the electrolyte were observed, mainly the formation of gold particles which precipitated from solution. Polarisation curves showed that gold reduction occurred at lower cathodic overpotentials than the fresh electrolyte, presumably due to the lower sulphite content which is known to adsorb on the gold surface. A Tafel analysis showed that the charge transfer coefficient was higher than the fresh plating bath due to irreversible changes within the electrolyte.

In order to study the electrocrystallisation of gold, we have used flat plate glassy carbon and graphite as electrodes. The two different forms of carbons were chosen mainly because they are easily available and used for metal recovery in industry. Furthermore, the choice of glassy carbon allows us to examine the microstructure when the substrate has no preferred texture, whereas the graphitic electrode allows us to examine when the substrate has a well-established structure.

Cyclic voltammetry investigation suggests that the nucleation of gold on carbon electrodes occurs at a significant rate only at overpotentials more negative than –0.75 V. Current-time transients of gold on glassy carbon show that during the early stages of reduction process, the deposition exhibits an instantaneous nucleation of non-overlapping particles. With increasing time, the diffusion zones begin to overlap and the deposition follows the classical progressive nucleation phenomenon. On the

other hand, current time transients of gold on graphite electrode do not follow the classical nucleation phenomena.

Microscopy observations demonstrate that the particle size and density can be controlled by varying the deposition potentials and time. Deposition at less cathodic overpotentials yields a smaller number of large particles. As the applied potential is lowered, homogeneous Au crystals ranging in diameter from 80-100 nm are obtained. The particle density on both carbon surfaces increases with overpotential, signifying the increase in number of nucleation sites. It is also evident that single crystals can be obtained shortly after applying a potential whereas at longer times the particle tend to coalesce and form larger aggregates having diameter ranging from 100 to 300 nm. X-ray diffraction show peak characteristics of a face-centred cubic (FCC) and the preferred orientation of gold deposits on both carbon surfaces is (111).

In order to study the growth of gold with time, a set of current-time transients were obtained by applying the potentials of – 0.925 V and - 1.20 V *vs.* SMSE, for duration of 1, 10, 100, 500 and 1000 seconds. It was found that the initial deposition of gold at lower overpotential, - 0.925 V, corresponds to an electrochemical diffusion controlled of Au^+ discharge from which spherical nuclei are obtained. When a certain induction time for spherical growth has passed, the initial growing nuclei become unstable and the thin Au deposit begins to develop tips which eventually grow larger and produced dendrites. However, at more cathodic overpotentials, - 1.20 V, dendrites are produced as soon as the driving force is applied to the system.

A flow cell operated in a flow-by mode was constructed to study the removal of gold (I) ions from rinse waters, which used a three-dimensional reticulated vitreous carbon (RVC) electrode. A new approach to recovery method has been developed. In this work, metal removal was carried out close to the mass transfer limiting value by adjusting the current to its limiting value, $I_L(t)$, corresponding to the concentration of metal ion at that instant, $c(t)$. The method was tested by removing copper (II) from acidified copper sulphate solution and it was found that operating near the mass transfer limiting rate was a suitable method to recover copper. However, in the case

of gold (I) removal, the concentration of gold depleted very slowly with time and there was no significant evidence that the gold could be recovered from solution by this method. This was attributed to secondary reactions occurring at the electrode which consumed most of the applied current. Therefore, the 'approximation' method developed in this study was found to be an unsuitable method to recover gold.

From this work, we conclude that glassy carbon is a suitable electrode material for obtaining homogeneous gold nanoparticles. However, reticulated vitreous carbon works best for metal ion recovery by electrowinning.

9.2 Future Work

Future work with respect to gold nanoparticles obtained by electrochemical deposition on glassy carbon involves investigating their appropriate applications in tailored and novel processes such as in new catalysis materials, sensor development and in the electronics industry.

Also, future work on the currently available electrochemical reactor will be carried out to reduce limiting current estimation errors. It is also necessary to continue the development of a more suitable recovery method for gold (I) from an aged thiosulphate-sulphite electrolyte. This work will focus on elucidating the existence of different gold complexes in the aged electrolyte as well as clarifying the secondary reactions occurring at the electrode, as these are believed to be the likely cause of the encountered problem in the recovery process.